2018

The characterisation of MP512 for 2D/3D dose reconstruction for small beams

Nauljun Stansook

Follow this and additional works at: https://ro.uow.edu.au/theses1

Recommended Citation

The characterisation of MP512 for 2D/3D dose reconstruction for small beams

Nauljun Stansook

This thesis is presented as part of the requirements for the conferral of the degree:

Doctor of Philosophy

Supervisor:

Distinguished Professor Anatoly Rosenfeld

The University of Wollongong

Centre for Medical Radiation Physics,

School of Engineering Physics,

Faculty of Engineering and Information Sciences

Month, Year

Abstract

Stereotactic radiation therapy such as SRS and SBRT utilise multiple beams delivery with a small radiation field and high dose gradients. A quality assurance tool with high stability and linearity of radiation response that can map a 2D dose read out in real time and with a high spatial resolution is needed to accurately verify two-dimensional (2D) pre-treatment dose distributions. This thesis describes two 2D monolithic diode arrays based on different silicon substrates called MagicPlate-512 (MP512) designed and developed by the Centre for Medical Radiation Physics to verify small field dosimetry. The first substrate is based on bulk p-type silicon known as MP512-Bulk and the other is based on the high resistivity of a thin epitaxial layer known as MP512-EPI. MP512 allows real time 2D dose mapping with a high spatial and temporal resolution. Both detector arrays consist of 512 0.5x0.5 mm^2 active pixels with a 2 mm pitch that covers an area of 52x52 mm^2. The angular response of MP512-Bulk as well as its correction factor were investigated for various field sizes and photon energies. It showed a maximum variation of relative angular response normalised to an incidence beam angle zero at a beam angle of 90° of approximately 18.5±0.5% and 15.5±0.5% for 6 MV and 10 MV photon beams. These results indicate that the angular response is sensitive to the energy, whereas the variation of angular response is less affected by field size. The packaging and intrinsic asymmetry of the monolithic silicon detector array structure are the major elements that affect the angular dependence of an MP512-Bulk. A comparison of the cross-plane profiles measured by the

corrected MP512-Bulk and EBT3 shows an agreement within ±2% for all field sizes, which proves that its correction factor and procedures can be applied to small field sizes.

A full dosimetric characterisation of an MP512-EPI was carried out in terms of the radiation hardness, percentage depth dose, dose linearity, dose per pulse dependence, output factors for small field sizes, segmental dose linearity measurement, and the angular response for 6 MV and 10 MV photon beams; it was also studied for the dose rate dependence of 6 MV photon and 6 MeV electron beams. The results were then compared to a number of cylindrical ionisation chamber (Farmer and Wellhoefer CC13), PTW Markus chamber, gafchromic EBT3 film, MO*Sk*in detector, and MP512-Bulk detector. The MP512-EPI had excellent full dosimetric characterisation and very stable response for a high irradiation gamma dose of 60 kGy with a sensitivity degradation of 0.3%/10 kGy.

The ability of MP512-EPI to measure 2D dose distributions was evaluated using small IMRT and VMAT fields and a combination of homogeneous and inhomogeneous insertions and a CMRP cylindrical phantom, and then compared to EBT3 dose measurements and treatment planning system (TPS) dose calculations. A Pinnacle[3] version 14 TPS was used to optimise and calculate all the plans using an adaptive convolution superposition algorithm. A comparison of the dose distribution measured by MP512-EPI, EBT3 film and TPS dose calculation in a homogeneous phantom revealed a gamma pass rate of 97.11%±1.62 (1SD) and 99.72%±0.55 (1SD) for 2% /2 mm and 3%/3mm criteria for all plans. The similar results demonstrated in the heterogeneous phantom, a reconstructed MP512-EPI dose compared to EBT3

film and TPS dose calculation revealed a gamma pass rate of 97.58%±1.07 (1SD) and 99.60%±0.41 (1SD) for 2%/2mm and 3%/3mm criteria, respectively. Whereas the reconstructed MP512-EPI doses compared to the measured EBT3 films dose and TPS dose calculation revealed a gamma pass rate of less than 85% for criteria of 1%1 mm for both phantoms. The reconstructed MP512-EPI doses at smaller gantry angular increments showed slightly improved passing rate criteria of 2%/2mm for gamma and a VMAT plan delivery within ±2% (1SD).

This MP512-EPI detector will be used for 3D dose reconstruction in conjunction with rotating phantoms and it will be evaluated in terms of 3D gamma analysis and dose volume histogram (DVH). Future work will be devoted to the development of a Quadro MP512-EPI detector with four tiled MP512-EPI that will enable a sensitive area of 10×10 cm^2 to maintain the same spatial and temporal resolutions.

Acknowledgements

Contents

List of figures

List of tables

Peer reviewed journal papers and conference proceedings

1. **N. Stansook**, M. Petasecca, K. Utitsarn, M. Newall, P. Metcafe, M. Carolan, M. Lerch, A.B. Rosenfeld, "The angular dependence of a two dimensional monolithic detector array for dosimetry in small fields," Journal of Physics:Conf.Series MMND&ITRO2016. 777, 012020 (2017).

2. K. Utitsarn, Z.A. Alrowaili, **N. Stansook**, M. Lerch, P. Metcafe, M. Carolan, A.B. Rosenfeld, "Optimisation of output factor measurements using the MagicPlate 512 silicon dosimeter array in small megavoltage photon fields" Journal of Physics:Conf.Series MMND&ITRO2016. 777, 012022 (2017).

3. **N. Stansook**, K. Utitsarn, M. Petasecca, M. Newall, M. Duncan, K. Nitschke, M. Carolan, P. Metcafe, M. Lerch, A.B. Rosenfeld, "Angular dependence of a 2D monolithic array dosimeter and correction required for small field dosimetry" Poster presentation at Engineering and Physical Sciences in Medicine (EPSM) conference 2016, 6-10 November 2016, Sydney, Australia.

4. K. Utitsarn, **N. Stansook**, Z.A. Alrowaili, M. Lerch, P. Metcafe, M. Carolan, A.B. Rosenfeld, "Beam Perturbation characteristic of 2D monolithic silicon Diode MagicPlate 512 (MP512)" Poster presentation at Engineering and Physical Sciences in Medicine (EPSM) conference 2016, 6-10 November 2016, Sydney, Australia.

5. **N. Stansook**, M. Petasecca, K. Utitsarn, M. Carolan, P. Metcafe, M. Lerch, A.B. Rosenfeld, "Validation of the influence of M512 substrate resistivity on sensitivity degradation of radiation" Poster presentation at European Society for Radiotherapy and Oncology (ESTRO36) conference 2017, 5-9 May 2017, Vienna, Austria.

6. K. Utitsarn, **N. Stansook**, Z.A. Alrowaili, M. Lerch, P. Metcafe, M. Carolan, A.B. Rosenfeld, "The effect of air gaps on Magic Plate (MP512) for small field dosimetry" Poster presentation at European Society for Radiotherapy and Oncology (ESTRO36) conference 2017, 5-9 May 2017, Vienna, Austria.

7. **N. Stansook**, M. Petasecca, K. Utitsarn, P. Metcafe, M. Carolan, M. Lerch, A.B. Rosenfeld, "The characteristic of 2D monolithic epitaxial detector array as a quality assurance dosimeter for small field" Oral presentation at Innovation in radiation applications (IRA) conference 2017, 20-22 April 2017, Wollongong, Australia.

8. K. Utitsarn, **N. Stansook**, M. Lerch, P. Metcafe, M. Carolan, A.B. Rosenfeld, "A real time QA system with variable spatial resolution for volumetric modulated arc therapy" Poster presentation at Innovation in radiation applications (IRA) conference 2017, 20-22 April 2017, Wollongong, Australia.

9. **N. Stansook**, K. Utitsarn, M. Petasecca, M. Newall, M. Duncan, K. Nitschke, M. Carolan, P. Metcafe, M. Lerch, A.B. Rosenfeld, "Technical Note: Angular dependence of a 2D monolithic silicon diode array for small field dosimetry" *Med. Phys.*, pp. 1–29, 2017., DOI: 10.1002/mp12377.

10. K. Utitsarn, Z.A. Alrowaili, **N. Stansook**, M. Petasecca, M. Carolan, V.L. Perevertaylo, M. Lerch, A.B. Rosenfeld, "Technical Note: Impact of a monolithic silicon detector operating in transmission mode on clinical photon beams" Physica Medica., volume 43, pp. 114-119, 2017., https://doi.org/10.1016/j.ejmp.2017.10.017

List of abbreviation

1D	One dimensional
2D	Two dimensional
3D	Three dimensional
4D	Four dimensional
AAPM	American Association of Physicists in Medicine
ADC	Analog to digital converter
ASTRO	the American Society of Therapeutic Radiology and Oncology
BED	biologically effective dose
BEV	Beam eye view
CBCT	Cone beam computed tomography
CMRP	Centre for Medical Radiation Physics
CP	control point
CT	Computed tomography
DAQ	Data acquisition system
DICOM	Digital Imaging and Communications in Medicine
Dmax	Maximum dose
DMG	Dose magnifying glass
EBRT	external beam radiation therapy
EPID	Electronic Portal Imaging Devices

EPI	Epitaxial
eV	Electron volt
FPGA	Field programmable gate array
FWHM	Full Width of Half Maximum
GTV	Gross tumour volume
HU	Hounsfield units
IC	Ionization chamber
ICCC	Illawarra Cancer Care centre
ICRU	The International Commission of Radiation Units and Measurements
IGRT	Inage guide radiotherapy
IMRT	Intensity modulated radiation therapy
KV	Kilovoltage
Linac	Linear accelerator
MLC	Multi-leaf collimator
MP	Magic plate
MRI	Magnetic resonance imaging
MU	Monitor unit
MV	megavoltage
MVCT	Megavoltage computed tomography
OF	Output factor
PCB	Print circuit board
PDD	percentage depth dose
PMMA	Polyemethyl methacrylate
PTV	Planning target volume

QA	quality assurance
RTP	Radiation treatment planning
SABR	stereotactic ablative radiotherapy
SAD	source to axis distance
SBRT	stereotactic body radiotherapy
SRS	stereotactic radiosurgery
SSD	Source to surface distance
TERMA	Total energy imparted or released in the medium
TG	Task group
TMR	Tissue Maximum Ratio
TPS	Treatment planning system
USB	Universal serial bus
VMAT	Volumetric modulated arc therapy
WED	Water equivalent depth
UOW	University of Wollongong

Chapter 1

Introduction

1.1 Introduction

Since external beam radiation therapy (EBRT) is now an effective option in cancer treatment, new equipment and techniques have been developed to provide high quality therapy. The treatment must deliver the highest conformal dose to a tumour while sparing healthy tissue; the methods used to minimise complications are stereotactic localisation techniques such as stereotactic radiosurgery (SRS), stereotactic body radiotherapy (SBRT) or stereotactic ablative radiotherapy (SABR). While stereotactic radiation therapy provides much better radiobiological effectiveness than conventional photon therapies [1]. This technique is so complex that quality assurance devices are becoming more of an issue. More than 150 accidents with stereotactic radiotherapy have been reported, of which almost 62% stemmed from the quality assurance (QA) process [2][3]. The complicated treatment field due to a small field size and intensity modulated dosimetry means that point dose measurement cannot verify pre-treatment plans, and therefore planar dose (2D) and three-dimensional (3D) dosimetry is needed to verify the full plan delivery, including the penumbra or low dose region. Moreover, QA devices require small active volumes with high spatial resolution, water equivalence, dose rate and energy independence, and linear dose responses to achieve sufficient accuracy [4].

This thesis focuses on the development and characterisation of a two-dimensional (2D) monolithic diode array MagicPlate-512 that is based on epitaxial silicon; it is an efficient and accurate quality assurance tool for small field intensity modulated radiotherapy.

1.2 Objective of the study

The objective is to examine the feasibility of using a 2D monolithic detector array (MP512) based on epitaxial (MP512-EPI) and bulk (MP512-Bulk) silicon substrate as a 2D and 3D QA dosimeter for small field dosimetry in SRS and SBRT. The detector arrays were designed and developed by the Centre for Medical Radiation Physics (CMRP) at the University of Wollongong. For this purpose the full characterisation of a 2D monolithic detector array (MP512-EPI) and the small IMRT and VMAT plans were highlighted and validated. The parameters measured with MP512 were investigated and extended for use with an adaptive 3D dose reconstruction to verify it for patient pre-treatment.

1.3 Outline of the thesis

The general background and project goals are introduced in **Chapter 1** while **Chapter 2** describes and summarises the literature review of small field dosimetry. This review focused on stereotactic body radiotherapy (SBRT), the technique used to locate tumours, SBRT equipment, and a critique of QA in small fields. This chapter also discusses the benefits and drawbacks of current QA tools. **Chapter 3** focuses on the intrinsic directional dependence of 2D monolithic diode arrays based on a bulk silicon substrate (MP512-Bulk). It also studies the effects that photon energy and field sizes have on the angular response; the various field sizes were delivered using 6 MV and 10 MV photon

beams. This chapter also introduces a developing angular correction factor to improve the accuracy of MP512 measurements, and its verification procedures using the small static fields employed in SRS and SBRT. **Chapter 4** explores the full dosimetric characterisation of MP512-EPI for external radiotherapy using a Varian Clinac iX (linear accelerator). Characterization is studied in terms of radiation hardness, percentage depth dose (PDD), dose rate (MU/min) dependence, the dose per pulse response, dose linearity, as well as the angular response and segmental dose linearity. This chapter also presents an electrical characterization of IV characteristics of detector before and after irradiation. **Chapter 5** explores the validation of using MP512-EPI for quality assurance in an SBRT plan in combination with a cylindrical PMMA phantom developed by the Centre for Medical Radiation Physics (CMRP), at the University of Wollongong. Patient pre-treatment verifications for homogeneous and heterogeneous phantoms were examined for IMRT and VMAT. The MP512-EPI measurements were reconstructed using the angular correction factor to mitigate the effect of angular dependence before comparing it to EBT3 film dose measurements and TPS dose calculation. This chapter also examines how the treatment couch influences the patient dose verification where an actual gantry was performed. **Chapter 6** describes a method for reconstructing a 3D dose to verify patient pre- treatment using companies with 2D monolithic arrays and cylindrical PMMA phantoms. The MP512- EPI measured the significant parameters using a 3D algorithm such as the off-axis ratio (OAR), and the PDD and tissue maximum ratio (TMR). **Chapter 7** summarises the study outcomes, including the advantages and disadvantages of the MP512 detector.

Chapter 2

Literature Review

Since external beam radiation therapy (EBRT) is now an effective option for treating cancer, new equipment and techniques have been developed to provide high quality treatment for patients. It is desirable that the treatment method can deliver the highest conformal dose to a tumour while sparing normal tissue and minimising complications. Over the past decade, stereotactic radiosurgery (SRS) and stereotactic body radiotherapy (SBRT), or stereotactic ablative radiotherapy (SABR) has been increasingly used in the field of external radiation field because they are much better than conventional external beam therapy.

This chapter focuses on SBRT/SABR because it is used for small field dosimetry and this technique requires effective quality assurance (QA). There is also a discussion of current QA tools and their limitations, as well as the problem of small field dosimetric verification.

2.1. Stereotactic Body Radiotherapy (SBRT) /SABR

2.1.1. Overview

Stereotactic body radiotherapy (SBRT) or stereotactic ablative radiotherapy (SABR) is defined by the American Society of Therapeutic Radiology and Oncology (ASTRO) as an external beam radiation therapy method for delivering very precise high dose radiation per fraction to an extracranial tumour target, using one to five fractions [5]. Since the

SBRT target has a small margin, the prescribed dose is specified at an approximately 80% isodose lower than a conventional technique, while the heterogeneous dose and hot spots within PTV have been accepted under clinical consideration [6]. In a fractionated regimen, SBRT/SABR offers better outcomes in terms of a biologically effective dose (BED) relative to conventional external beam radiotherapy [1], and whereas a conventional technique delivers doses of 1.8 to 2.0 Gy per fraction and total doses of 60-70 Gy, SBRT applies a lower dosage using a hypo-fractionated scheme of five or less fractions between 10 to 20 Gy per fraction. Moreover, the small number of radiation fractions make SBRT more comfortable and convenient for the cancer patient.

The general concept of SBRT was developed from single fraction intracranial radiosurgery. In 1951, Lars Leksell [7] introduced the term radiosurgery where he delivered a single high dose fraction to a small intracranial lesion using a rigid metal frame for localised targets. The extracranial stereotactic frame and three-dimensional coordinate system for spinal lesion was developed by Hamilton *et al.* in 1995 [8]. This technique works on the principle of a rigid immobilisation of the brain by screwing a frame to the spinous processes, and although it is accurate within 2 mm, it is also time consuming and inconvenient. At the same time, Lax *et al.* constructed a stereotactic body frame with a vacuum bag that immobilises the body from caudal to tarsal with non-invasive patient fixations [9]. The author found that patients could be placed in the same position within 5-8 mm. Since body lesions are more complicated and difficult to irradiate than brain lesions due to organ movement, extracranial lesions can be displaced during and between fractions of irradiation by internal organ motions such as breathing, gastrointestinal peristalsis, and cardiac contraction. This means that the relative position of a tumour and the external marker is not reliable enough to ensure accurate radiation,

which is why improved image-guidance and software are crucial to allow for accurate delivery of SBRT.

Treatment machines have recently been improved with a collimator that provides more accurate dose conformation for stereotactic plans and very efficient image-guidance for more accurate localisation. This technology has led to increased confidence in implementing SBRT in multi-centres around the world. In fact SBRT is now an effective treatment for curative and palliative indications [2][10], with the three most frequent sites for treatment being spine, lung, and liver.

2.1.1.1. SBRT for spinal tumours

Spinal SBRT is a more challenging technique than traditional external beam radiation because it delivers a higher dose of radiation to spinal tumours without exceeding the cord tolerance. The spinal cord is a critical organ for spine irradiation because a high dose of radiation to the spinal cord can induce myelitis [6]. The spinal cord dose is limited to 10 Gy in 10% of the spinal cord, defined as 6 mm maximum above and below a planned target volume according to radiation therapy protocol oncology group number 0631 (RTOG0631) [7]. A typical regimen of conventional external beam therapy for spine metastasis is 30 Gy in 10 fractions whereas radiosurgery irradiates with a target dose of 8 to 25 Gy in one to five fractions [8]. The selected dose per fraction depends on factors such as the dimension and location of lesions, a patient's histological status, previous treatment, and which device is available. Tumour(s) on the spine are either extradural (vertebra bodies or in paraspinous regions) or intradural (extramedullary or intramedullary) [2], most of which are spinal metastases (up to 40%) that commonly occur at vertebral bodies in about 35% of cases [9][10]. Radiosurgery for spinal metastases is focused on the reduction of pain, improving sensory and motor function, and controlling the growth rate of local tumours [10].

2.1.1.2. SBRT for lung tumours

Lung SBRT/SABR is treatment offered to patients who are high-risk for surgery due to the location or size of the tumour(s) and their health. Lung SBRT is commonly used for early stage non-small cell lung cancer (NSCLC), oligometastasis, and the early stage of small cell lung cancer [13][14]. The single biggest problem with treating lungs is respiratory motion where tumours can move from 3-5 cm [15]; respiratory motion therefore limits the treatment outcomes due to the intra-fraction motion due to errors generated acquiring the images, planning the treatment, and delivering the radiation. The effects of respiratory motion can be minimised using a vacuum bag to immobilise and limit abdominal compression and movement, by respiratory gating to treat each specific respiratory phase or track the tumour in real time with MLC tracking as the tumour moves [16][17]. 4D CT scanning is proving to be a major technique for accurately delineating a tumour using physiologic movement for a specific phase of the respiratory cycle [18]. Treatment with lung SBRT is normally carried out with a non-opposing beam, with non-coplanar multiple beams (7-11 beams) or a combination of arc delivery and online image-guided radiation therapy (IGRT) to accurately locate the position of a tumour. The dose delivery limit to a lung with a volume of 10% (V_{10}) is less than 20 Gy of the total dose of 60 Gy (20 Gy/Fx) following the RTOG protocol number 0236, 0813 and 0631 [19] [20].

2.1.1.3. SBRT for liver tumours

The common SBRTs used for livers are primary hepatocellular carcinoma (HCC) and liver metastases [1]. SBRT is primarily used to maintain the systemic cytoreduction response of a liver as well providing systemic therapy to reduce the tumor without resorting to surgery. The margin of gross tumor volume (GTV) plus up to 5 mm for radial and 10 mm for the superior-inferior can be treated as the planning target volume (PTV), where the normal dose delivery is 14-26 Gy for one fraction or 30-36 Gy in three fractions

[21][22]. The VMAT or non-coplanar multiple static beams delivered using photon energies of up to 15 MV depends on the size of the patient's body. The dose used to treat liver cancer that a patient can tolerate is based on the dose a normal liver can receive, so the accumulated dose must less than 15 Gy (an overall treatment dose) for a liver with a volume 700 mL. To reduce respiratory motion and target the liver precisely, SBRT delivery must utilise custom body immobilisation with radiopaque markers or combine with 3-5 gold fiducials implanted around or within the tumour tissue. Moreover, respiratory motion can be minimised by abdominal compression, breath holding techniques, and respiratory gating.

2.1.2. SBRT equipment

There are at present many commercial delivery treatments which can deliver a steep dose gradient to a tumour lesion while sparing the critical organ; they include a compact imaging system that provides extreme accuracy and precision for localised targets. These treatment delivery methods are classified into three groups (2.1.2.1, 2.1.2.2, and 2.1.2.3, below), according to the capability of the image and delivery application system [23].

2.1.2.1. Irradiation with micro-stationary fields by cylindrical collimator

Stereotactic radiation is delivered with a micro cylindrical collimator and a robotic system (CyberKnife®, Accuray, Inc., CA, USA) (Figure 2.1). A 6 MV linear accelerator is mounted on a robotic arm that can rotate with six degrees of freedom, and the delivery system and verification of the set-up position for the patient operates through two orthogonal kV images and two 3D camera arrays [24]. The circular fields can emit non-coplanar and non-isocentric beams at large angles around the patient, this enables high doses to be delivered directly onto a target while avoiding normal tissue; the average delivery per plan is 100-300 beams [25]. To treat a target at an accurate sub-millimetre

level, a specialised tracking systems such as Xsight[TM] spinal tracking, Synchrony[TM], and Xsight[TM] Lung are used [26].

Figure 2.1: CyberKnife Treatment components [27]**.**

2.1.2.2. Irradiation with stationary fields shaped by a multileaf collimator (MLC) with gantry-based systems

The most common equipment used to deliver radiation for stereotactic tumours are linear accelerators (LINAC) with intensity-modulated radiation. This machine normally uses a 2.5 mm to 5 mm leaf-width MLC attached to a conventional LINAC such as ClinacIX (Varian Medical System, CA, USA) and Elekta (Stockholm, Sweden). While a LINAC such as the Novalis system (BrainLAB, Inc., Munich, Germany) can be dedicated with a built-in micromultileaf (Figure 2.2), all treatment machines are equipped with image-guidance to verify pre-treatment targets, where the image information can originate from an orthogonal x-ray or a cone beam CT. These treatment machines deliver a series of small segment radiation or sub-beams by modulated intensity photon fluence by changing the shape and speed of the MLC to produce a steep dose reduction at the targets. This delivery technique is known as Intensity Modulated radiotherapy (IMRT), and with SBRT, a patient is usually treated with four to twelve IMRT beams [28][13][29].
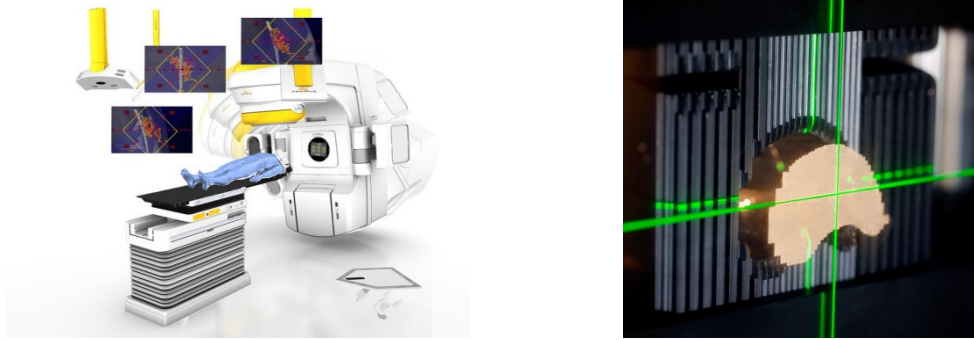
(a)   (b)

Figure 2.2: Gantry-based systems (a) Novalis machine [30] and (b) Built in micro multileaf [31].

2.1.2.3. *Irradiation with a circular approach from a moving source or table (Arc treatment)*

Arc treatment is a delivery radiation system where a circular method is used to rotate the source (linear accelerators base) or move the table (TomoTherapy Hi-Art System). Volumetric Modulated Arc Therapy (VMAT) is a common technique that delivers a dose to patients with a rotating gantry of linear accelerators (LINAC) such as RapidArc® (Varian Medical Systems, CA, USA) that surrounds a patient's body with a stable couch. The dose is modulated by changing the speed of the gantry, and the dose rate and multileaf (MLC) shapes, while the gantry is rotating [32][33]. The colours of the dose washes for the IMRT and VMAT plans for SBRT are shown in Figure 2.3.
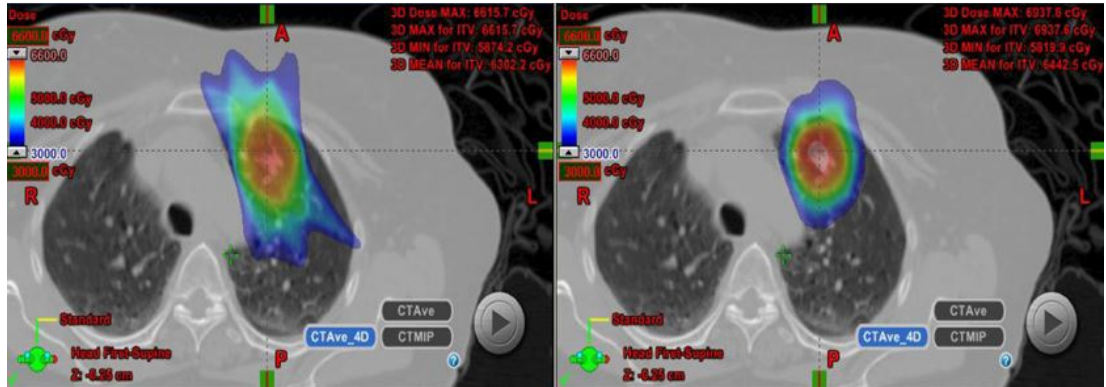
Figure 2.3: Colours of dose washes for IMRT and VMAT plans for pulmonary SBRT using LINAC base [33].

Tomotherapy Hi-ART (TomoTherapy, Inc., Madison, WI) is a CT-based delivery technology that can provide information from megavoltage computed tomography (MVCT) images. This imaging system enables high set up accuracy and will determine and correct patient position before delivering radiation; it can also modulate the intensity of the dose distribution via a binary multileaf (MLC) mounted on a slip-ring gantry (Figure 2.4). A helical fan beam emits radiation at 360^0 around a patient with a source to axis distance (SAD) of 85 cm, while the table moves into the gantry in a superior-inferior position and the selected pitch depends on the size of the target [34][35]. The precise table index and movement have a significant effect on the accuracy of the dose delivered.
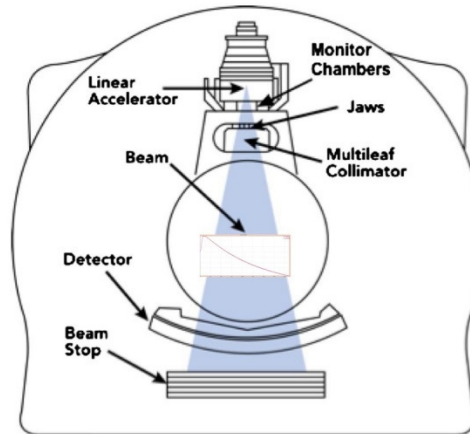
Figure 2.4: A schematic configuration for Tomotherapy systems [36].

2.2. Critique of QA

SBRT delivers a very high dose per fraction and provides a steep dose gradient in a small field which usually places the margin of the boundary tumours in close proximity to the organ at risk (OAR). Therefore, this technique requires effective quality assurance in the overall process, from patient immobilisation, target delineation, the treatment planning system (TPS), and throughout delivery. The American Association of Physicists in Medicine (AAPM) has given practical guidelines (task group 101: TG101) for SBRT quality assurance procedures for medical physicists, oncologists, and therapists [6]. There are two primary dosimetric verifications in the entire quality control of small field delivery treatment; the first part is the accuracy of beam data measurement used for calculating and optimising the dose distribution such as the percentage depth dose (PDD), the tissue maximum ratio (TMR), output factors, and the off-axis ratio (OAR); the second is a patient-specific quality assurance phase that verifies the accuracy of dose distribution from the planning system to the dose delivered to patients.

2.2.1. Small field: Overview and definition of field size

The charge particle equilibrium (CPE) is where the number and energies of photons or particles entering a volume of interest are the same as those leaving the volume. A CPE is a significant situation condition used in conventional dosimetry, according to Technical report series No.938 and ICRU 1980 [37]. The most critical issue of small field dosimetry is a lack of CPE where the dimensions of the collimator field are less than the lateral range of secondary electrons and the source of partial radiation is obscured by the collimator. Variations in the range of secondary electrons depends on the photon energy and spectrum because the electron range increases as the photon energy increases; the approximate range of secondary electrons for a 6 MV photon beam is normally 16 mm [38]. Moreover, the density and composition of the medium have a significant impact on the penumbra and effective beam size, and the range of electrons in a low density medium such as air is longer than the range of electrons in water [39]. This phenomenon can be defined as a small field where the dimensions of the beam are smaller than the range of secondary or charge particles at the central axis of radiation beam [40]. According to these theoretical and clinical data measurements, fields that are smaller than 4×4 cm^2 are small field sizes whereas conventional fields are defined with sizes ranging from 4×4 cm^2 to 40×40 cm^2 [38]. Figure 2.5 shows the effect of overlapping penumbra on the full width of half maximum (FWHM) achieve form small field collimator setting [38].
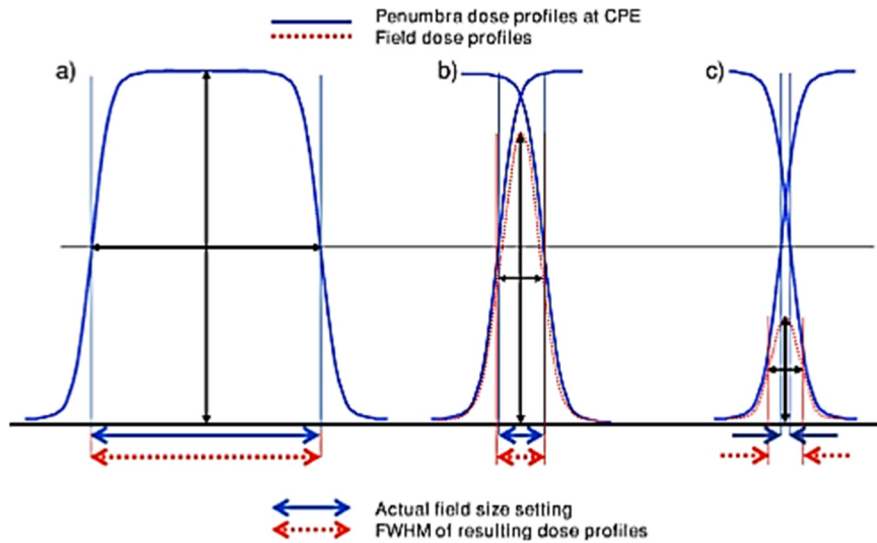
Figure 2.5: The effect of penumbra overlapping on the full width of half maximum (FWHM) achieve from small field collimator setting [38].

2.2.2. Detector size, spatial resolution, and density

The use of small fields in stereotactic radiosurgery combined with intensity-modulated delivery creates a challenging scenario for accurate dosimetry because the two most significant concerns for small field dosimetry are the averaging effects of detector volume and the spatial resolution of detectors [41] [42]. Laub W.U. *et al.* found a significant difference in the absolute dose measurements when using the different size detectors for IMRT fields; they were up to 6% between a 0.6 cm^3 Farmer chamber and a 0.015 cm^3 pinpoint chamber. The same results appeared in other reports, where a drop in the output factors for small field occurred in a central beam due to a partial source combined with electronic disequilibrium and decreasing scatter. These effects caused the under response signal of the detector to respond and a blurred penumbra due to a too large detector (Figure 2.6) [42][4][43]. Inaccurate output factors and broadened penumbra measurements are basic parameters for a treatment planning system, so inaccurate monitor unit calculations and planning optimisation resulted in an incorrect dose being

delivered to a patient [43][44]. To avoid the effects of volume a detector should be small enough to measure the uniform dose region of a small field, therefore its maximum size should not be greater than half the full width of half the maximum (FWHM) of the beam profile, and furthermore, the spatial resolution of the device should be the same size as the calculation grid used in the treatment planning system (less than or equal to 2 mm) for end-to-end testing [6].
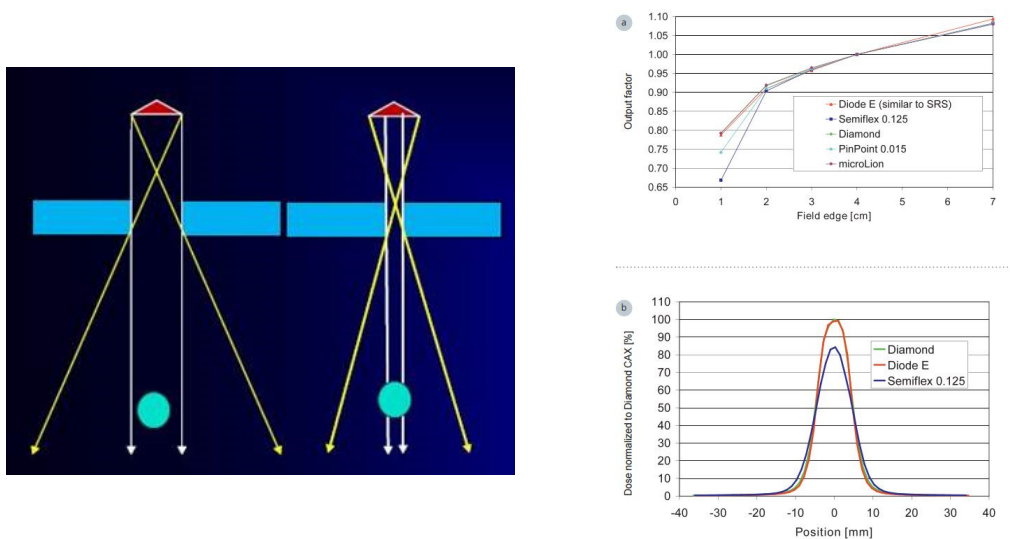
Figure 2.6: The volume averaging effect (a) a schematic diagram of a detector inside a broad and narrow beam [38] (b) a comparison of output factors and dose profiles measured by various detectors [45].

The density perturbation effect stems from detector measurements in small field dosimetry; it can be explained using Fano's theorem that states the effect of particles emitted per unit mass [46] is the difference in mass density compared to the influence of water and the uniformity of the fluence of charged particles in the medium. A low-density detector such as an ionisation chamber can produce fewer electrons than water, so electrons with a longer range can exit the cavity and lead to a lower dose in the detector. However, a detector of high Z material such as a diode emits higher number of secondary

electrons in the detector than water material measurement due to a shorter electron range where most electrons are absorbed in the medium and fewer in the exit cavity.

2.2.3. Ideal detector for small field dosimetry

Since small field dosimetry is complicated it is difficult to find a perfect detector. An ideal detector for small field dosimetry should have the following attributes:

(i).   A stability response within ±0.1 % for short-term measurements of large doses and multiple beam irradiation, as well as long term stability that does not require frequent recalibration.

(ii).   It should have a linear response to a clinical dose range of 1-1000 cGy.

(iii).   A stable response independent of dose-rate measurements because treatment machines such as LINAC can change the dose rate (MU/min) during VMAT delivery.

(iv).   Since the dose per pulse varies depending on the distance measured and the medium, the detector should be stable when measuring in a typical dose per pulse range of 0.2-0.4 mGy per pulse.

(v).   An ideal detector should respond to a wide photon energy range and not be affected by attenuation of low energy photons and low electrons.

(vi).   Volume averaging by a large detector can cause penumbra boarding, so small spatial resolutions are needed in small dosimetry where a high dose gradient is presented.

(vii).   A high temporal resolution to accurately verify the time-resolved dosimetry for 4D IMRT and VMAT delivery in combination with respiratory gating or a tumour tracking system. A high temporal resolution detector can reduce the burling effect of an integrated gantry and moving MLC.

(viii). It should be water equivalent to avoid any extreme electron perturbation from its composition and density due to the ratio of the mass energy absorption coefficient and the stopping power of water and the detector medium.

(ix). It should respond isotropic ally to the direction of the radiation beams while the gantries rotate around the detector.

There is no ideal detector that IPEM could recommend other than the detector used to measure in small dosimetry [47].

2.3. The quality assurance currently available and its limitations

In recent years many commercial QA tools have been used in radiotherapy. The following examples are devices currently available for measuring relative dose parameters such as beam profiles, PDD, output factors including patient pre-treatment and in-vivo verification. This section will give a general description of detectors including their specific configurations, functions, and limitations. The detectors will be classified into four categories based on their basic dose measurements.

Table 2.1: A summary of dosimeters used for megavoltage photon beam dosimetry

Dosimeter	Applications	Advantages	Limitation
Ionisation chamber	Absolute and relative dosimetry measurement, QA testing, commissioning measurement (1D, 2D and semi-3D)	High level of accuracy and reproducibility, dose rate and energy independence	Volume averaging effect
Silicon diode	Relative and *in-vivo* dosimetry measurement (1D, 2D and semi-3D)	High sensitivity and good spatial resolution	Sensitive to low dose (High Z), directional dependence and response sensitivity depend on accumulated dose
Diamond detector	Relative dosimetry (1D)	High sensitivity and spatial resolution, tissue equivalent, less dependence on dose per pulse and dose rate	Cost expensive, high Z of electrode increases electron scattering
Scintillating fibre	Relative dosimetry measurement, intracavitary therapy (1D)	High sensitivity and spatial resolution, tissue equivalent, wide dose range measurement, flexible	Cherenkov effect (high noise within system)
Radiochromic films	Relative dosimetry measurement (2D)	High sensitivity and spatial resolution, tissue equivalent, energy and dose rate independent and directional independent	Not real-time read-out, scanner system and film batch dependent
Gel dosimeter	Relative dosimetry measurements (1D, 2D and 3D)	High sensitivity and spatial resolution, near tissue equivalent, actual 3D dosimetry	Not real-time read-out and sensitive to the preparation (chemical proportion) and read-out procedure (image artefact)
Flat panel electronic portal imaging device (EPID)	Relative dosimetry measurements (2D and semi-3D)	High sensitivity and spatial resolution, dose rate independent, no extra phantom requirement	High Z, signal is nonlinear to dose measurement, suffer from radiation backscatter (supporting arm), ghosting and image lag effect

2.3.1. Point dose

2.3.1.1. Ionisation chamber

Ionisation chambers (IC) are commonly used in EBRT due to their directional independence (cylindrical shape), dose linearity, dose rate and energy independence (kV energy range), and sensitivity to stability [48][49]. An IC can measure an absolute or relative dose, and it can verify output factors and point dose in the central axis of beams. The major components of an IC are its air or liquid filled cavity and the chamber electrode (anode and cathode). An IC measures the current in proportion to the electron-ion pair generating from the interacting ionisation proceeding from the medium in the cavity. A voltage must be supplied to the detector electrode to make the pairs of electron ions move across the detector which created a current through the IC. The appropriate voltage depends on the size of the chamber; this means a large chamber must supply up to 400 Volts. The numbers of electrons depend on the energy deposited within the volume (EX: 1 MeV produce 30000 ion pairs), the distance between electrodes, and the voltage supply and the density of the detector (either gas or liquid). ICs come in various sizes as defined by the average sensitive volume; a standard IC volume of 0.6 cm^3 is generally used as a reference chamber and an IC volume of 0.13- 0.14 cm^3 is generally used for beam scanning [50][37]. However, the volume averaging effect of a large IC can underestimate the dose in the central and broadening penumbra in the steep dose region of a small field [51][42]. To minimise this effect, the PTW31016 PinPoint (0.016 cm^3), Wellhofer/Scanditronix compact ionisation chamber, model CC01 (0.01 cm^3) and CC04 (0.04 cm^3), were introduced into radiosurgery and small field (Figure 2.7) [52][53]. The preferred chamber size should be compromise between its sensitivity and its signal to noise ratio response. Since CC01 and PinPoint have a small volume the anode is made from a high-Z material to maintain appropriate signal to noise ratio so the response of

both detectors depends mainly on the low energy photons [54]. Apart from which the polarity, cable, and stem effects of small ICs is of more concern that an IC with a large volume, particularly when they must perform in the regions of homogeneity or where the dose across the detector is less than 5- 10% [48].
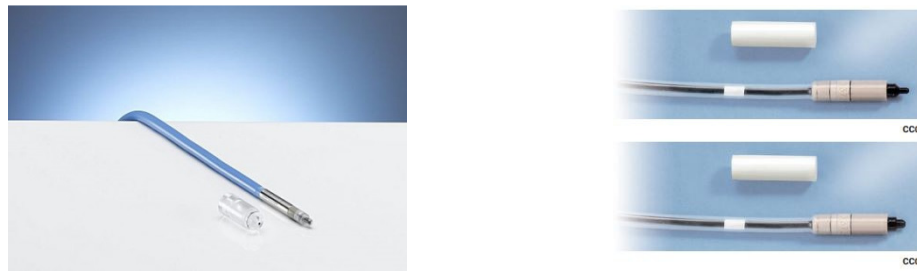
(a)   (b)

Figure 2.7: The ionisation chamber used in small field dosimetry: (a) Pinpoint (PTW31013)[55] and (b) CC01 and CC04 (Wellhofer)[56].

2.3.1.2. Single-Point silicon diode

The p-n junctions are commonly used in a semiconductor detector because the built in electrical field is greater than 10^3 V/cm and it can be operated in a passive mode (without external bias supply) [57]. There are two types of diodes based on bulk silicon wafers, n-types and p-types. A p-n junction is obtained by doping the opposite impure material onto a silicon substrate, so a p-type is doped with boron and an n-type is doped with phosphorus. The basic operating principals of a silicon diode are similar to those within an ionisation chamber, where the electrometer detects the diode current emanating from electron-hole pair diffusion. Radiation energy that exceeds 3.6 eV produces an electron-hole pair within the silicon, while the excess minority carriers within the diffused lengths of p-side (electrons) and n-side (holes) diffuse to the opposite side of the depleted region (p-n junction) and are collected by the anode and cathode (Figure 2.8) [58]. A silicon diode has a higher response per volume than other detectors, for instance, with the same volume the sensitivity of a diode is approximately 18000 times greater than the ionisation

chambers [59]. These characteristics of diodes enables detector to be manufactured in sizes less than 3 mm, such as SFD stereotactic, and PFD photon (IBA Dosimetry), both of which have a diameter with an active area of 0.6 mm and 2 mm, respectively [56]. The diode used in small field dosimetry is shown in Figure 2.8. While diodes are generally used in relative dosimetry such as scanning beam profiles, depth doses, and measuring MLC penumbra, they can perform within phantom or *in-vivo* dosimetry such as MO*Skin*, which is one type of Metal Oxide semiconductor field-effect transistors (MOSFET). MO*Skin* was designed by CMRP and using drop in technology for MOSFET chip packaging in a tissue equivalent kapton tail making MO*Skin* suitable for small field dosimetry, especially measuring surface doses in real time at water equivalent depth (WED) 0.07mm [60]. However, silicon diodes should not be used for measurements of absolute dose because while their response is almost MeV photon energy range independent , their sensitivity increases if low energy photons are present due to their high atomic number; these diodes still induce a perturbation effect and provide directional dependence due to their high-Z material and asymmetrical orientation of the sensitive volume [61]. The sensitivity of a diode also depends on the accumulated dose, and the temperature and dose rate [62][63][64][65].

(a)   (b)
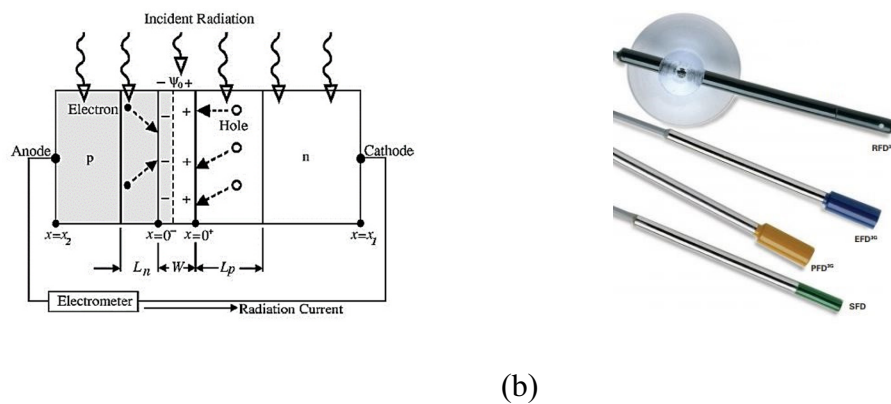
Figure 2.8: A schematic of p‑n junction of silicon diode and the commercial p‑type silicon diode detectors for use in small field dosimetry (IBA Dosimetry) [56][58].

2.3.1.3. Diamond Detector

A diamond detector is an outstanding QA detector for small field dosimetry because its atomic number is almost tissue equivalent to $Z = 6$ (Z_{eff} of tissue approximately 7.42) [66][67], and it has a small sensitive volume ranging from 0.004 to 6 mm^3 that provides an excellent high spatial resolution suitable for measuring in the penumbra region of small fields. Traditionally, a diamond detector uses a naturally grown diamond plate or dice with a specific contact system embeds in a cylindrical PMMA capsule which made a detector difficult to reproduce in the same sensitive volume. Recently, the synthetic diamond detector has been developed based on chemical vapour deposition (CVD) by embedding the CVD intrinsic layer on a highly conductive boron-dropped CVD diamond film and grown on high-pressure high temperature single crystal substrate (HPHT) [68], [69]. A diamond detector can also act like an ionisation chamber (TM60003 diamond) or as a solid state diode (T60019 microDiamond) (Figure 2.9) [55][70] because its basic operating principles are similar to an ionisation chamber and a diode detector. Similar to silicon diode ionizing radiation interact with the diamond to create electron-hole pairs which migrate towards the anode and cathode respectively and generate a signal current that is measured by the electrometer. A microDiamond detector is a synthetic single crystal which operating in the photovoltaic regime that can be operated at zero voltage so no external voltage is required. These detectors are almost independent on energy of photon beams because they provide a constant of the mass stopping power detector to water ratio [71]. Diamond detectors will also indicate radiation hardness and long term stability, as well as directional and temperature independence; they also less dependent on varying the dose per pulse and the dose rate (MU/min) [72][73]. A micro-Diamond can also measure an insignificant signal variation of absolute dose to water when measuring a large field size of 40×40 cm^2 or a small field size of 0.5×0.5 cm^2 [74]. These

advantages mean that a diamond detector can be used in PDD, output factors, and measuring beam profiles for conventional and small field sizes (SRS and SBRT fields) in all photon energy ranges, including electron energy [75]–[77]. However, diamond detectors are is more expensive than diode and ionisation chamber detectors. The composition and density of detector material such as the high-Z of an electrode or silver conductive glue increases electron scattering so the dose absorbed by the detector's sensitive volume also increases [66].

(a)   (b)
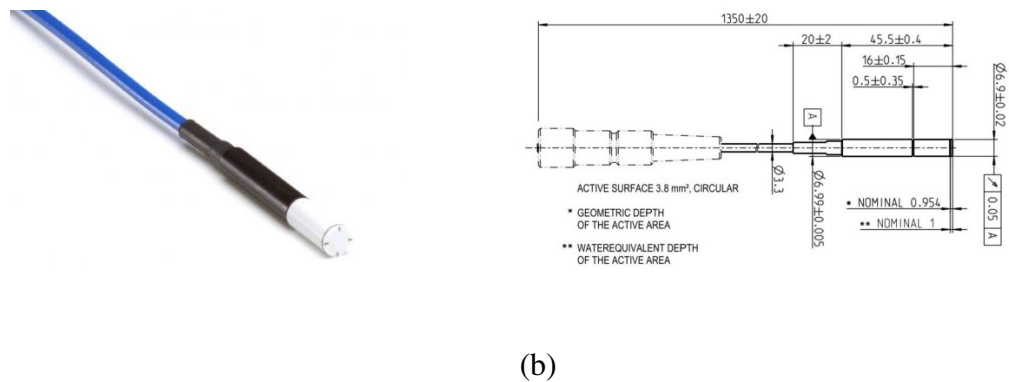
Figure 2.9: A single crystal diamond detector (SCDD) and its configuration (PTW-Freiburg) [78].

2.3.1.4. Single Scintillating fibre

Scintillation detectors have been developed and used in radiotherapy for past 15 years. Common scintillation dosimeters using in radiotherapy are organic scintillators; they have a low atomic number and are almost tissue-equivalent to plastic scintillators [79][80]. When irradiated photons or particles interact with the scintillating medium they stimulate atoms into excited states and fall back to a ground state emitting photons into visible light. The transfer of light through fibre optic is collected and converted into an electronic signal by a photodetector [81]. Scintillators can read signals in real-time and have a linear response to a broad dose range of photon and electron energy. The fibres in a scintillator are flexible and small enough to enable it to measure a dose in intra-cavitary

brachytherapy and intra-operative therapy. Scintillators have a high spatial resolution (approximately 1 mm diameter), there is less degradation of the radiation dose and dose rate, and they are energy and temperature independent [79], [80]. However, Cherenkov in the fibre guide is the significant effect of inducing noise within the system [82], and scintillators that combine with a silicon photomultiplier (SiPM) tend to show a higher noise [83].

2.3.2. 1D array dosimetry

A point dose detector cannot distribute the entire planned dose or the beam profile in a single irradiation, which is why a 1D array is usually based on an ionisation chamber or diodes which fabricate the detector in a linear direction such as CA 24 scanditronix Welhofer and an LDA-99 that provide a resolution of 2 cm and 0.5 cm, respectively. 1D arrays are generally used for data commissioning and measuring a dynamic wedge [84][85]. In 2010, Wong *et al.* introduced an innovative 1D diode array called a Dose Magnifying Glass (DMG), which implanted 128 phosphor n^+ on a p-type silicon wafer with a high spatial resolution of 0.2 mm; this detector array was designed by CMRP for use as a QA verification tool in SRT delivery [86].

2.3.3. 2D dosimetry

Point dose verification is no longer adequate for stereotactic RT once the beam shape has been modulated, particularly for delivering a high conformal dose. 2D dosimetry was developed to evaluate the full dose distribution measurement for IMRT and VMAT plans dose delivery. There are several 2D detectors available, such as radiochromic film, IC, and silicon diode arrays with EPID.

2.3.3.1. Film dosimetry

The film dosimetry process is based on changing its optical density (OD), which is proportional to the dose of irradiation that interacts with the film. The scanner measures the dose using the light transmitted through the darkening films. Silver halide (AgH) film or radiographic film was the first type of film dosimetry used to verify a relative dose in the megavoltage energy range. Radiographic films have successfully validated two-dimensional IMRT dose distributions by providing a permanent two-dimensional dose distribution mapping with a high spatial resolution. However, they have many drawbacks due to their varying sensitivity within each batch of film batch, a film process that produces chemical, and artefacts caused by the densitometer (scanner) [87][88]. The emulsion of radiographic film is based on high Z material, response of which depends mainly on low photon energy (<1MeV) [48]. In 1980, radiochromic films were introduced and widely used for dosimetry in radiotherapy because film processing is not required and they are almost tissue equivalent. Gafchromic EBT3 film is the last generation of radiochromic film used in radiotherapy due to its high sensitivity for radiotherapy dose between 0.01 and 8 Gy [89]. EBT3 films has a uniformly thin active layer that is sandwiched between symmetrical thicknesses of matte polyester [90]. Gafchromic films has become a standard tool for verifying small field dosimetry because their high spatial resolution provides two-dimensional (2D) dose mapping with sub-millimetre accuracy, and they are energy and dose rate independent, as well as angular independent and tissue equivalent [91][92][93][94]. However, radiochromic films cannot be read out in real-time because they require at least 24 hours to stabilise [90], and they are dependent on film scanning orientation, scanner uniformity, and the temperature of scanner bed, and that makes film dosimetry depend on the read-out procedure adopted [95]. In addition, the accuracy also depend on the colour channels and scanner resolution [94], [96].

Radiochromic films can be used for measuring relative dose distributions and the relative outputs in a small field such as the stereotactic field (4 to 30 mm^2) provide on a Novalis Trilogy [96], [97]; they are not recommended for measuring an absolute dose and verifying monitor unit outputs [98].

2.3.3.2. Array detectors

Detector arrays are increasingly used in patient-specific verification for delivering IMRT and VMAT plans because they provide a two-dimensional dose distribution in real-time and are easy to setup. The two main commercial detector arrays are, 1) an ionisation chamber-based detector and 2) silicon diode based detector. Table 2.2 is a summary of the current commercial detector arrays.

(i). Ionisation chamber (IC) array

Amerio *et al*. introduced the initial design of pixel-segmented ionisation chambers array (PXC) for verifying 2D doses distributed in complex shaped field delivery [99][100]. This device contains independent cylindrical ionisation chambers with sensitive volumes of 0.07 cm^3, i.e., 1024 IC that cover a 24×24 cm^2 area at 0.75 cm spacing between them. This PXC has excellent long and short term stability, as well as integral dose independence and linear to dose measurements. Moreover, the output factor measured by this device agrees within 0.4 % compared to a Farmer IC; this detector array has evolved into an ImRT MatriXX (IBA Dosimetry, Bartlett, TN), which uses a combination with specific software. The ImRT MatriXX has fabricated 1020 parallel plate ionisation chambers with volumes of 0.08 cm^3 and pitches of 0.76 cm that cover an active area of 24×24 cm^2 [101][102]. These detector arrays performed very well in terms of field size and independent SSD distance for 6 MV and 18 MV photon beams, they also had good long and short term reproducibility, and an independent dose rate between 0.02 to 20 Gy/min and dose linearity [103]. Although the detector arrays had a gamma passing rate

of more than 95% for IMRT and VMAT plans with 3%/3mm criteria, their wide resolution showed a large discrepancy in the penumbra region (20%-80%) of a 2×2 cm^2 field that was greater than 1 mm, unlike the beam profiles measured with the CC03 ionisation chamber [102][101][104]. Moreover, this device requires a pre-irradiation dose of up to 10 Gy and a 15 minute warm up before it can be used. Another commercial 2D detector array base on an ionisation chamber was designed and developed by PTW-Freiburg; the seven29 PTW model T10024 has 729 air-vented ionisation chambers, each with a sensitive volume chamber 0.125 cm^3 by 0.5 cm in diameter. These IC chambers cover an active area of 27×27 cm^2 and have a 1cm spacing between them [105][106]. These devices are less dependent on energy and dose rate for a given range of radiotherapy energy, but they do have good long and short term reproducibility and uniform sensitivity across the arrays. The arrays also have a good agreement between the beam profiles and wedge-modulated field measurements, unlike results measured by an ionisation chamber in water [106]. Although the seven29 PTW requires a pre-irradiation dose of only 100 MU, it needs more time to warm up before being used and it cools down quickly. Moreover, the large spacing of two adjacent chambers and its large diameter limits the potential of the seven29 PTW for stereotactic radiotherapy or in a gradient with a high steep dose. To mitigate its spatial resolution limitations PTW-Freiburg introduced a higher sampling density within an array called Octavius 1500 (OD1500). This new prototype has 1405 ionisation chambers, each of which has a sensitive volume of 0.058 cm^3, arranged in a checkerboard pattern covering an area of 27×27 cm^2 [107][108]. The OD1500 was designed for a higher range of dose rates with a flattening filter free (FFF) beam (up to 48 Gy/min) [108]. This detector arrays have a very stable signal without needing pre-irradiation and have excellent dose linearity within ±1% for doses ranging from 5 to 1000 MU. The increased spatial sampling frequency of this detector array

occurs when two measurements of couch shifting 5 mm merge to show a high agreement of dose distributions with a gamma passing rate up to 99.6% and 96.9% for 3%/3mm criteria, compare with dose predicted by radiation treatment planning system (RTP) and measured by film, respectively. Although the output factors of the OD1500 agreed with a field size above 4×4 cm^2 within 1%, compared to a Semiflex chamber (CC13) and Si diode, the output factors measured for a small field showed more deviations from the reference detectors [107]. To meet the standard required of detectors for small field dosimetry in SRS and SBRT technique, PTW-Freiburg introduced the first liquid filled ionisation chamber array called Octavius 1000SRS (T0036). This detector array has the highest spatial resolution of 2.5 mm in the inner area of 5×5 cm^2 and 5 mm in the outer area [109]. The 1000 SRS detector has 977 liquid filled ionisation chambers with a small sensitive volume of 0.003 cm^3 and covers an area of 10×10 cm^2. This detector has less energy dependence, good dose sensitivity linearity, good long and short term stability and reproducibility, and has excellent agreement when measuring the output factors in a small field down to 1×1 cm^2. The gamma passing rate agreement between the detector measurement and TPS calculation for IMRT verification is approximately 95.2% for 3%/3mm criteria, but the liquid filled ionisation chambers depend mainly on the dose rate and dose per pulse because of the high incidence of ion-pair recombination. The detector array signal dropped more than 3.5% when measuring a dose per pulse that was less than $1.7×10^{-4}$ Gy/min, and the cross calibration procedure must consider the pressure and the temperature applied.

(ii). Silicon diodes array

The MapCHECK (Sun nuclear crop, Melbourne, FL) is the first commercial of 2D array base on arrays of silicon diodes. The first MapCHECK prototype was model 1175 with 445 n-type diodes fabricating with a resolution of 7.07 mm in the central area of 10x10
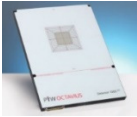
cm^2 and 14.14 mm close by [110]. The MapCHECK2 has improved by increasing the number of diode to 1527 and maintaining a resolution of 7.07 mm over an area of 32×26 cm^2 [111]. The n-type diode used to fabricate the detector array was designed to depend less on accumulated dose of radiation and small intrinsic build-up of 0.1 gm/cm^2 for measuring surface doses [112]. MapCHECK2 is better at verifying IMRT than films, with excellent gamma passing rates for 6 MV and 18 MV photon beams and allows it to calibrate using absolute dose measurements [103][113]. However, detector arrays based on silicon diodes still have a high dose per pulse and directional dependence [114], and MapCHECK2's wide resolution is not suitable for measuring the steep dose gradient of small fields

Table 2.2: Specifications of a commercial 2D detector array [115][116][55].

	Detector type	Detector size (mm)	Detector volume (mm^3)	Resolution (mm)	Number of detector	Active Field size(cm^2)
MapCHECK2	n-type diode (cubic)	0.8×0.8×0.03	0.0192	7.07	1527	32×26
ImRT Matrixx	Pixel ionisation chamber (disc shaped)	4.5 diameter × 5height	80	7.62	1020	24.4×24.4
PTW seven29	Plane-parallel ionisation chamber (cubic)	5.0×5.0×5.0	125	10	729	27×27
OCTAVIUS 1500	Plane-parallel Ionisation chamber	4.4×4.4×3.0	58	7.1	1405	27×27

OCTAVIUS	Liquid-filled	2.3×2.3×0.5	2.6	2.5 in central	977	10×10
1000SRS	ionisation			area of		
	chamber			5.5×5.5		
	(cubic)			cm^2		
				5 mm outer		
				area		

2.3.3.3. Flat panel Electronic Portal Imaging Device (EPID)

EPIDs were designed and developed to verify patient localisation in radiotherapy and then analyse and store the images in a DICOM file format. However, their use as a dose verification tool has expanded rapidly over the last decade so they now provide high spatial and temporal resolution (approximately 0.7 mm and readout 10 frames/sec), a real time 2D mapping image and accurate positioning perpendicular to beam irradiation while being mounted and rotating on the gantry arm [117][118]. EPIDs are now used for pre-treatment verification and measuring directly onto the EPIDs without a phantom or patient, and *in-vivo* dosimetry using transit dosimetry and back projection. EPIDs can be based on fluoroscopy (video based), matrix liquid filled ionisation chambers and amorphous silicon (a-Si) systems [119][120][121]. EPID dosimetry is where scintillation is used to convert radiation dose to a signal. The radiation generates electrons within the Cu plate which create a visible light in the phosphor screen which is then detected and integrated into charge captures by the photodiode array implanted onto an a-Si panel. The aSi-based systems such as aS500/ aS1000 (Varian system), iView GT (Elekta) and OptiVue (Siemens) have become popular and are commonly used to verify portal doses because a lower dose can be delivered per portal frame; moreover, their long term stability and reproduction over two years, independent dose rate, spatial resolution and image quality are much better than other EPIDs. However, the response relationship between EPID signal and dose is nonlinear scale the correction factor for effects of the acquisition process are need to be consider [122]. In addition, EPID signal to dose conversion must

to be calibrated for the various field sizes, beam energies, and distances from a central axis due to their high atomic number that increases the photoelectric effect that makes EPID signal beam energy and field size dependent [123]. Furthermore, the doses measured by EPIDs usually suffer from radiation backscatter due to its extra layers and supporting arm. The inadequate accumulation of material above the detector layer also indicates the lack of an electronic equivalent in the phosphor scintillator layer [124][117][125]. This means the charge trapped within the detector layer has a significant influence on the ghosting and image lag effect for EPIDs.

2.3.4. 3D dosimetry

The significant issue with measuring 2D dose distribution is interpreting the results because although 2D dose measurement can ensure that the dose delivered to a patient is the same as the dose from TPS calculation, the patient's corrected isocentre and the MLC positioning error means that the data is only provided at that particular plane of measurement. Calculating the advanced algorithms of a treatment planning system create a complicated delivery plan which then provide a large amount of sub-field and irregular shapes. This then requires a method that can evaluate and verify a large number of dose points in three- dimensional (3D) treatment volume. A 3D dose distribution such as dose volume histograms (DVH) is needed for dose verification and clinical interpretation, so this section will classified 3D dosimetry into three categories; actual 3D dosimetry which will measure the dose in its entire volume; semi-3D dosimetry that will measure particular dose points within a specially designed phantom, and then use the dose calculation method to predict the dose for the entire volume; and virtual 3D dosimetry which will calculate the dose using fluence measurements.

2.3.3.1. Gel dosimetry

In recent years measuring the gel dose is the only one of actual 3D dosimetry. Gel dosimetry was introduced in 1950 to verify clinical doses [126]. A gel dosimeter monitors and analyses the chemical changes in the interaction between radiation and the chemical chain using external quantitative readout such as Magnetic resonance imaging (MRI), computed tomography (CT) and spectrophotometric. The first generation of gel dosimeters was the Fricke solution based on bulk water, ferrous sulphate (Fe^{2+}) and gelatin or agarose [126][127]. Although Fricke gels are easy and convenient to prepare and the results can be read soon after irradiation, the ion diffusion effect reduces the spatial dose information through the gel [128] [129]. Polymer gels dosimeter (PAG) such as bis acrylamide nitrogen and gelatin (BANG) is a tissue equivalent material developed to reduce diffusion via an infusion of monomers and cross linked servants in a gelatin matrix [130][131]. The free radicals of water radiolysis induce a chain polymerisation reaction as the monomers are cross linked in proportion to the absorbed dose. The polymer gels reveal that 3D dosimeters can provide permanent 3D dose distributions within millimetres, while the liquid form can be manufactured in an irregular shape such as an anatomical phantom; these gel dosimeters also deliver independent dose rates and energy in a clinically relevant range [130][132]. PAG is limited by oxygen which inhibits polymerisation [133]. The normoxic polymer gel dosimeter known as MAGIC gel is a new PAG which contains oxygen scavengers in the gel matrix to mitigate oxygen inhibition. In 2003, a new polymer gel dosimeter called PRESAGE^{TM} was introduced; it is a plastic radiochromic dosimeter that is not affected by oxygen. It consists of polyurethane, leuco-dye leucomalachite green (radiochromic components), hydroxyl reactive polyol, and alkyl diisocyanate prepolymer [134], [135]. The changing optical density inside the PRESAGE^{TM} dosimeter is suitable for readouts with an optical based

scanner such as He-Ne laser-based and an optical-CT scanner [136]. Unfortunately gel dosimetry is sensitive to the conditional preparation of gel matrices such as the chemical compound rate (type and radical initiator concentration), the light and temperature, and the amount of time needed to prepare a procedure and then read the results [137], [138]. Moreover, the imaging artefacts from the readout system (MRI or CT) such as image distortion, and ring and streak artefacts are important factors in determining the accuracy of the dose measurements [127].

2.3.3.2. Semi 3D dosimetry

Semi-3D dosimetry is where multiple point doses are measured using built-in detector arrays in a cylindrical phantom such as ArcCHECK (helical shape) and Delta^4 (cross-plane array). As well as dose measurements using 2D detector arrays (seven29, 1000SRS, OC1500) combined with rotating phantom such as OCTAVIUS 4D system (PTW), dose measurements are combined with the specific dose calculation algorithm to create a 3D dose volume. The following section is a commercial semi -3D dosimeter system.

(a)   (b)   (c)
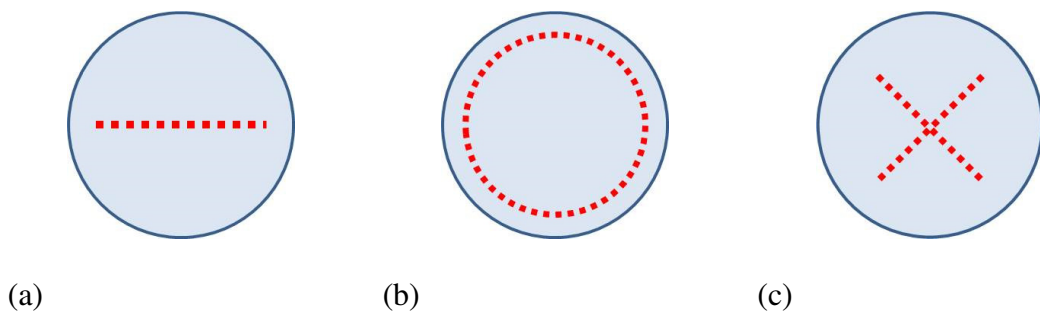
Figure 2.10: The general shape detector within the phantom for a commercial semi-3D dosimetry system

(i). ArcCHECK

ArcCHECK (Sun Nuclear Corp, Melbourne, FL) is the first semi-3D cylindrical phantom; it has 1386 diode detectors in a helical pattern at 1 cm spacing on the surface around the PMMA phantom with the equivalent depth of 3.3 g/cm^3 [139][140][141]. Each active

diode is 0.8×0.8 mm^2 and the active area is 21 cm in diameter 21 cm long. This device was designed to deliver dynamic volumetric treatment; it is a time-resolved measurement that acquires real-time data for each gantry at 50 ms updates using a virtual inclinometer algorithm. The semi-3D dose calculation of AcrCHECK is used in combination with 3DVH (Sun Nuclear) software where the 3D dose reconstruction is calculated by scaling the radiation ray traced through the phantom using a particular point dose measurement at the entrance and exit detector which is then renormalised using dose distribution calculated from TPS. The ArcCHECK has field size dependence and an ionisation chamber that compares the over-response when the field size is less than 10×10 cm^2 and under-response when the field size is larger due to its spiral configuration and the thickness of the build-up above the detectors [141][142]. This means a field size correction factor must be applied while interpreting the 3D dose distribution. Furthermore, calculating the dose of the ArcCHECK system also requires angular correction and background correction [143]. Although the ArcCHECK detector is arranged in a spiral pattern to improve its special resolution, a beam eye view (BEV) spacing of 1.12 cm at SAD 89.6 cm is too coarse to analyse a small field size and small MLC offset [141]. Moreover, since the detectors are arranged into a spiral shape there is no detector in the isocentric of the phantom result so the device can only measure the dose near the surface and cannot detect the scattered dose.

(ii). Delta$^{4®}$

The Delta$^{4®}$ (ScandiDose AB, Uppsala, Sweden) is a 3D phantom manufactured from two orthogonal p-type diode arrays arranged in an asymmetrical "X" shape ($+50°$ and $-40°$) within a PMMA cylindrical phantom with a diameter of 22 cm. Each active detector is 0.1 cm in diameter, and the 1069 diodes are fabricated at 0.5 cm and 10 cm spacing in the centre of 6×6 cm^2 and the remaining area of 20×20 cm^2, respectively [144][145]. This

device can measure a continuous sampling of dose per pulse at approximately 3 ms pulse separation and 3 ms pulse width; the data is then stored to synchronise with the linac pulses using the inclinometer attached to the treatment gantry. Since there is no measurement between pulses there is a high signal to noise ratio so the device can be utilised for 4D treatment delivery and segment-by-segment analysis. The Delta$^{4®}$ operated combination with Delta^{4DVH} (ScandiDos) software calculates the dose measurement at particular points into a semi-3D dose distribution. The 3D dose has calculated the dose along the radiation ray path using the dose detected by two diode detector arrays. The Delta^4 has good short term reproducibility and stability, dose linearity, dose rate and dose per pulse independence [144][146], but it does show a different angular response to gantry angles of 0° up to ±5% at a parallel detector plane angle [146]. To reduce measurement uncertainty due to fluctuating beam outputs and density values, the Delta^4 the field measurements must be calibrated daily before using it for pre-treatment verification [147].

(iii). OCTAVIUS and 2D array

The OCTAVIUS 4D$^®$ system (PTW, Freiburg, Germany) is a rotating cylindrical phantom 32 cm in diameter by 34.3 cm long and is combined with 2D arrays such as seven29, 1000SRS and OC1500 [108]. It was designed to deliver a modulated arc by eliminating the influence of angular dependence on the accuracy of QA; this phantom can rotate with a full angular range of ±360° [148]. The 2D array is always measuring perpendicular to each incident beam angle, the rotation of the phantom is synchronised with the linac using the inclinometer attached to the treatment gantry. The OCTAVIUS 4D$^®$ is a stand-alone verification system which does not require information from the TPS dose distribution for calculations. The 3D dose distribution was reconstructed using the summary of doses along the ray trace in each plane and the dose measured at a particular
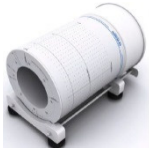
angle and the PDD curves installed in the PTW Verisoft software [149][148]. Since the calculation is based on PDD data implementation, the accuracy of the measurement is sensitive to the source of the phantom distance.

Semi-3D dosimetry does not directly measure a 3D dose distribution of treatment delivery and is therefore not allowed to be used as an *in-vivo* dosimeter. The accuracy of 3D dose reconstruction relies on the detector's characteristics and depends on the accuracy of the calculation algorithm which calculates the full 3D dose from the limited point dose measured within the phantom. The system must be validated before being used for the recommended pre-treatment verification. Moreover, the accuracy of the dose calculation is associated with the efficiency of the inclinometer because it is also used to store data and phantom movements; therefore this inclinometer must be validated before being used.

Table 2.3: Summary of commercial semi-3D dosimeter specifications [139][144][148].

	Detector arranging	Detector spacing	Detector Volume (mm³)	Detector size (mm²)	Number of detector	Software
ArcCHECK	Spiral shape	10 mm	0.19	0.64	1386	3DVH
Delta⁴	Bi-planar	5 mm in inner (10×10 cm²) 10 mm in peripheral	0.39	0.78	1069	Delta⁴ᴰⱽᴴ
OCTAVIUS 4D system	2D plane	Depend on 2D array combination (the summary is shown in Table 2.1)				VeriSoft

2.3.3.3. Virtual 3D dosimetry

Virtual 3D dosimetry does not measure dose delivery within the phantom volume or in a patient; it uses beam fluence to measure before or after radiation beam entry to calculate the 3D dose distribution, as shown in Figure 2.11. Dosimeters are generally attached to the machine so they can rotate with the treatment gantry. This kind of dosimeter can operate as either before or during treatment delivery.
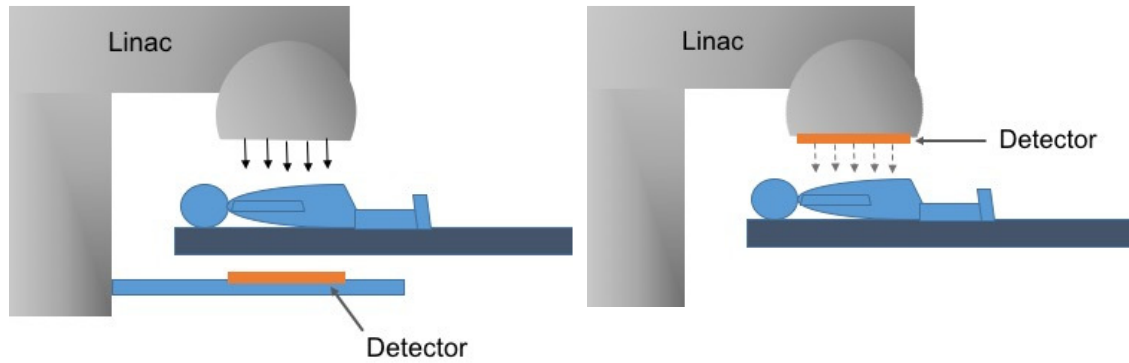
(a)   (b)

Figure 2.11: A detector used for patient verification during treatment; (a) downstream of the patient, and (b) upstream of the patient.

(i). A portal dose EPID

Portal dosimetry using EPID is a type of virtual 3D dosimetry that uses the transit dose measurement. EPID generally uses the portal image to do a QA by comparing it with the image predicted from the TPS but this type of verification cannot interpret the actual difference in dose between treatment delivery and TPS dose calculation. EPID measures the dose transmitted through a patient and calculates the dose inside the volume using a back projection algorithm and the iterative method [150][151]. Commercial software EPIdose[TM] is designed for use in combination with conventional EPID; so the EPIDose algorithm converts the EPID image into a dose by projecting the image to the simulated dose plane or extended phantom (CT image), multiplies the output factor correction, and then convolves the corrected EPID dose response with a redistribution kernel. A field calibration map is then applied to the relative dose to reconstruct the 3D dose distribution inside the volume [152].

Another virtual 3D dosimetry is where the entrance dose measurements use the 2D arrays dosimeter mounting on the treatment gantry head such as the COMPASS® device, Dolphin detector, and the DAVID, and Delta[4AT] system. The photon fluence

measurements are used in conjunction with a unique algorithm to derive the 3D dose distribution within a patient's volume.

(ii). COMPASS® system

The COMPASS® system (IBA Dosimetry, Germany) is an independent dose engine that uses a collapsed con convolution/superposition algorithm in conjunction with 2D detector arrays such as MatriXX, a novel pixel segment IC transmission detector (COMPASS device) and wireless IC (Dolphin®) [153][154][155]. COMPASS arrays fabricate 1600 parallel ionisation chambers spaced 0.65 cm apart and with a sensitive volume of 0.02 cm^3 [156]. Since this detector measures the fluence dose by being placed between the radiation beam and the patient, the transmitted dose and surface dose is of concern. Sankar *et al*. examined how the COMPASS device affected the dose surface and transmission using 6 MV photon beams and found a significant difference in the dose at the surface depth of 11.9%, with respect to the open beam measurement. However the dose transmitted from the device had no effect on the depth beyond d_{max} in terms of the beam profile and PDD curves, and showed a mean transmission factor of 0.967 for field sizes ranging from 3×3 cm^2 to 20×20 cm^2. Similar results were found in the pixel-segmented IC detector array Dolphin® transmission device (DTD). A DTD is a wireless device that fabricates a small active area detector of 0.24×0.24 cm^2 and 1513 air-vented ICs. It gives a high resolution of 5 mm at the detector level (gantry head) and 8 mm at the beam isocentre (SAD100 cm). It had a maximum surface dose of almost 11% at a 30×30 cm^2 field and 80cm SSD. These results indicate that the influence of this device on the transmission dose depends on its field size and the distance between the detector and the surface. The surface dose decreased as the field size decreased and the SSD increased. Furthermore, the device had less effect on PDDs beyond the maximum depth where different doses were compared to an open beam of only 1% [157]. The DTD was a good

agreement when used to verify the transmission mode during treatment for 2D and 3D dose distribution compared to pre-treatment verification with MatriXX measurements and TPS dose calculations [158]. Because the COMPASS® system is independent and uses a complicated dose engine algorithm, it needs commissioning data such as beam profiles, PDD curves, output factors, and absolute doses to model the calculation algorithm [153].

(iii). DAVID system

The DAVID system (PTW) is an advanced real-time method of verifying modulated treatment during delivery. This device consists of transparent multi-wire ionisation chambers placed inside the accessory tray of the linac and aligned parallel to the MLC leaf pair [159]; the number of wire chambers depends on the number of MLC leaf pairs. The chambers are collected charge in a 2 mm thick volume of air and sandwiched by two 4 mm thick PMMA covers. This device monitors the shelf dose area product (DAP) with an Integral Quality Monitor (IQM) [160][161]. Here, patient doses are monitored at each MLC opening along the wire and the measured signal at each moment is determined the length of the wire chamber not blocked by the leaf of MLC and integrated during treatment delivery [162]. The total signal comes from the secondary electron and the primary photon beam within the radiation field, with some secondary electron scattering from the nearby chamber and background scattering from the linac head components. The signal information is transferred to the control unit via a Bluetooth interface so it cannot lose the signal due to its connecting cable problems [159]. The products from the dose area is compared to the pre-recoded data. The presence of DAVID in the beam does not interfere with the relative dose measured in the phantom, which showed insignificant difference in the PDD curves with and without the device for 6 MV and 18 MV photon beams. However, since the instrument is 14mm thick, the surface dose is enhanced by a

factor of 1.13 and a transmission factor of 0.939 and 0.955 for the 6 MV and 10 MV beams, respectively. Therefore, the transmission factor of the DAVID system is considered to be a true factor that should be used to calculate the monitor unit (MU) for all segments during the documentation process [163].

(iv). Delta^{4DT} system

ScandiDos has developed an ultra-thin transmission detector called Delta^4 Discover (Delta^{4AT}). It has 4040 p-type silicon diodes, each of which is 1 mm in diameter. The detectors are arranged parallel to the MLC leaf pair trajectories (X direction) at 2.5 mm spacing along the leaf and 5 mm spacing at the beam isocentre. The detector is fabricated on a 0.5 mm PCB that relies on a 1.1 mm globe top embedded between two 0.3 mm thick carbon fibres. This device has less attenuation and transmission factor closer to 1 and provide less surface dose enhancement. It has an attenuation factor of 1% and the surface dose only increases by 1 % for a 10×10 cm^2 field. However, the scattering from the collimator increased the surface dose by almost 9% when field was larger than 30×30 cm^2. This device tracks MLC motion during treatment and also verifies the MU of each segment. The Delta^{4AT} has a built-in inclinometer that can verify the gantry and collimator rotation, while the integrated laser can verify a patient's position during beam delivery. This device can analyse the 3D dose distribution in a patient by generating a virtual patient dose using correlation of signal measured by transmission device with the Delta^4 phantom dose measurement [164][165].

2.4. Bulk Epitaxial Silicon diodes.

SBRT and SRS are complex radiotherapy treatments that involve multiple small segment fields and angles irradiating around patients. These techniques require efficient 2D and 3 D dose verification with high spatial and temporal resolution. Although the ionisation

chamber is used as a gold standard and practical radiation detector for external radiotherapy, volume averaging has a significant effect in small field dosimetry. A silicon diode is an outstanding candidate for use as an efficient dosimeter for sophisticated radiotherapy delivery techniques, because their high sensitivity means they can be manufactured to a small sensitive volume and still provide a good sensitivity and high spatial resolution. As a consequence, CMRP has designed and developed several spectacular silicon diode detectors based on p-type wafers that are used as a radiation dosimeter. A p-type silicon diode was selected due to its superior characteristics compared to n-type diodes in terms of linearity of the response with dose per pulse and higher radiation hardness [166][167]. CMRP has developed various silicon detector prototypes such as for surface point dose measurements (MO*Sk*in), 1D diode array (DMG), 1D orthogonal diode array (DUO) including 2D diode array (MP121 and MP512) [60][86][168][169][170]. These detectors have been studied and are useful for external beam radiation therapy dosimetry.

However, the silicon diodes exhibit angular, temperature, and dose per pulse dependence, as well as being sensitive to accumulated radiation [171][57]. Marre *et al.* studied the effect of an accumulated dose on several commercial diodes and found the detector lost approximately 20-25% sensitivity at an accumulative dose of 1 Mrad for electron and photon beams [172]. The degradation of sensitivity from radiation depends mainly on the quality of radiation and the type of silicon [173][174]. Radiation can damage the mass bulk and surface regions of silicon detector when energy that is greater than the threshold energy is imparted, the point defects and clusters within the silicon lattice are created ; this increases the leakage current, induces the growth of full depletion voltage and degrades detector sensitivity. The effect of increasing of leakage current can be minimised by using silicon diodes in a passive mode or no biased application [175].The sensitivity

of silicon detectors is proportional to the active volume, and that depends on the area of the detector (A) and the diffusion length (L). The diffusion length (L) depends on the minority carrier time (τ) as shown by $L = \sqrt{D\tau}$, where D is the diffusion constant. The lifetime of the minority carrier will decrease the concentration of crystal defects increases; these defects at a high and deep level create a recombination-generation (RG) centre which reduces the lifetime of the minority carrier, decreases detector sensitivity, but makes it more sensitive to dose per pulse and temperature [65][176][64]. An RG centre can be managed using the oxygen doping technique or specific silicon growing technology; with the silicon growing technique, the silicon substrate is doped with impure material to modify the transport mechanism in the silicon lattice.

Brookhaven National Laboratories has developed oxygenated devices known as oxygen-enriched floating zone (DOFZ) substrates where the oxygen is doped in the substrate to form a vacancy-oxygen (V-O) complex in a deep level of the forbidden gap where the energy is approximately 0.55 eV. This V-O complex resulted in the creation of the RG centre. This technique is perfect for minimising the effect of radiation damage from gamma irradiated by Co-60; it only creates point defects with no generating cluster defects. However, the detector was still sensitive to degradation due to higher energy irradiation. Besides, the process of manufacturing DOFZ makes is difficult to reproduce the same macroscopic property and effective doping concentration [177], [178].The same concept was used when doping n-type Czochralski silicon with platinum (Pt); Pt-doping delivered a short diffusion range of charge carriers approximately 20 μm but this reduced the sensitivity of detector in the low dose rate range [58].

In 2006, Lindstrom *et al*. studied the thin layer of low resistivity of an n-type silicon detector using for tracking charged particles in hadron field and found its sensitivity had improved [179]. The epitaxial layer is limited an active depth of detector which is shorter

than the diffusion length and keep the active volume constant even after being irradiated with high radiation. Santos *et al.* investigated the effect of clinical electrons with energy ranging from 6 MeV to 21 MeV and photons with energy of 6 MV and 18 MV beams onto the thin n-type epitaxial layer with a resistivity of 50 Ω cm, which had been grown on 300 µm thick n-type silicon substrate. They found excellent characteristics in terms of long and short term repeatability, electron PDD measurements, dose linearity for electron and photon beams , and measurements of electron beam profiles, however the detector also showed electron energy dependence and increasing current leakage current [180][181]. Bruzzi *et al.* investigated the sensitivity of an epitaxial silicon detector to radiation damage delivered from a Co-60 gamma source; they found that the n-type silicon diodes decreased in sensitivity more than the p-type silicon diodes with an 83% and 58% drop, respectively. Their study also showed the effect of epitaxial thickness and guard ring distance to active area of the diode on radiation damage. A 50 µm thick epitaxial layer provided high constancy and stability of sensitivity, with sensitivity reduced by only 7% at a dose of 1.5 kGy and stability within 1.8% at 10 kGy. However, the larger guard ring distance of 50 µm resulted in more stable sensitivity at a dose of 1.5 kGy [182]. These results mean that a p-type epitaxial silicon detector with a thin layer and wide guard ring is better for a radiotherapy dosimeter, and moreover, p-type silicon is not affected by changes in the absolute value of space charge by increases in fluence [183]. Talamonti *et al.* investigated the first prototype of 2D arrays when the p-type epitaxial layer was used as a dosimetric detector for pre-treatment verification [184]. The prototype 2D detector arrays consisted of 21×21 pixels that achieved a resolution of 3 mm; this resulted in good dose linearity, excellent repeatability and reproducibility, as well as less dependence on the dose rate. As a consequence, CMRP developed an IMRT patient verification dosimeter based on the epitaxial p-type diodes with silicon epitaxial

layer thickness of 50 µm and using drop-in technology for packaging of the diode called magic plate 121 (MP121). An MP121 has 11×11 diodes with a sensitive volume of each 0.5×0.5×0.05 mm^3 and 1 cm pitch. The sensitivity was stable within 2.1% after a pre-irradiation dose of 41.5 kGy and the excellent dosimetric characteristics for photon beam irradiation remained. The detector showed good dose linearity and good agreement of PDD measurements with CC13, ionisation chamber however the sensitivity of MP512 decreased as the dose per pulse increased [168]. However the 1 cm pitch of MP121 is too coarse for use in small field dosimetry. Therefore, CMRP has designed a novel monolithic detector fabricated on epitaxial p-type layer and providing a high spatial resolution of 2 mm they call MagicPlate512-epitaxial (MP512-EPI), it will be described and investigated in this thesis.

Chapter 3

Angular dependence and the correction factor

3.1. Introduction

This chapter focuses on the characterisation of the 2D monolithic p-type detector array called MagicPlate-512 (MP512-Bulk) in terms of its intrinsic directional dependence and the effects that energy and field size have on its angular response. This chapter also presents a procedure for an angular correction factor development to improve the accuracy of a dose map measured in a particular plane using small fields, as used in SBRT and SRS.

This MP512-Bulk was designed and developed by the Centre for Medical Radiation Physics (CMRP) to investigate dosimetric characteristics in terms of their output factor, percentage depth dose, dose linearity and dose per pulse dependence, and the uniformity of detector response by Aldosari *et al.* [170]. The beam profiles and penumbra for field sizes less than 4×4 cm^2 that are relevant to stereotactic radiation therapy were measured and shown to be feasible for small field dosimetry. The Full Width of Half Maximum (FWHM) of square radiation fields measured by the MP512-Bulk for field sizes down to 1×1 cm^2 matched within 2% compared to the gafchromic EBT3 film data measurements [170], but the critical aspect of a silicon diode is its directional dependence due to asymmetry in the detector packages and the high-Z material generates

different attenuations of secondary electrons in different directions [185][186]. Variations of detector response can be more than 10% due to anisotropy and detector assembly; the results have been reported in several studies [70][187][188][189][190]. Paul *et al.* examined the angular dependence of *p*-type semi-conductor surface diodes with an active volume of 1.6×1.6×0.05 mm³ that were mounted on a 0.051 mm thick copper contact pad of PCB. They showed that the detector varied in sensitivity between ±12% when normalised to a normal incidence of the beam at a range of angles between ±45 degrees [61]. The angular dependence of an n-type 2D diode array, MapCHECK (SunNuclear, Melbourne, Florida, USA) was evaluated and compared with ionisation chambers, and a maximum difference of almost 20% was found at the beam angle of 90 degrees [189]. Hosang *et al.* also investigated the angular dependence of a MapCHECK for verifying RapidArc plans and found a significant difference in dose as large as 30.6±6.6% and 33.4±5.8% for field sizes of 10×10 cm² and 3×3 cm², respectively [190]. This phenomenon affected the accuracy of angular dependence of the detector used in rotational radiotherapy where many modulated irradiation fields surround the patient.

3.2. Material

3.2.1. MagicPlate-512 (MP512-Bulk) design and fabrication

The MP512-Bulk is a monolithic silicon detector array with 512 square diodes, an active area of $0.5×0.5$ mm² and a pitch of 2 mm; it was fabricated by ion implantation onto a 470 μm thick *p*-type silicon substrate (Figure 3.1). The MP512-Bulk is wire bonded to a 500 μm thick fibreglass printed circuit board (PCB) with plugs for connection to a fast readout DAQ system. The detector and the wire bonding are covered by a thin layer of protective epoxy for mechanical robustness. The MP512-Bulk was pre-irradiated with a total water equivalent dose of 80 kGy from Co-60 gamma source to stabilise its response;

the MP512-Bulk array operates in a passive mode where no bias voltage is applied to the diodes.

The MP512-Bulk detector array was embedded between two 5 mm thick PMMA slabs with an air gap above silicon pixels entrance surface. This packaging arrangement (Figure 3.1b) is needed to protect the silicon detector and optimise the detector response to small radiation fields by adjusting the air gap to match the detector's response for small radiation fields to radiochromic film [170], [191]. The air gap is 0.5 mm and 1.0 mm for 6 MV photon beam and 10 MV photon beam, respectively [192].

(a)   (b)
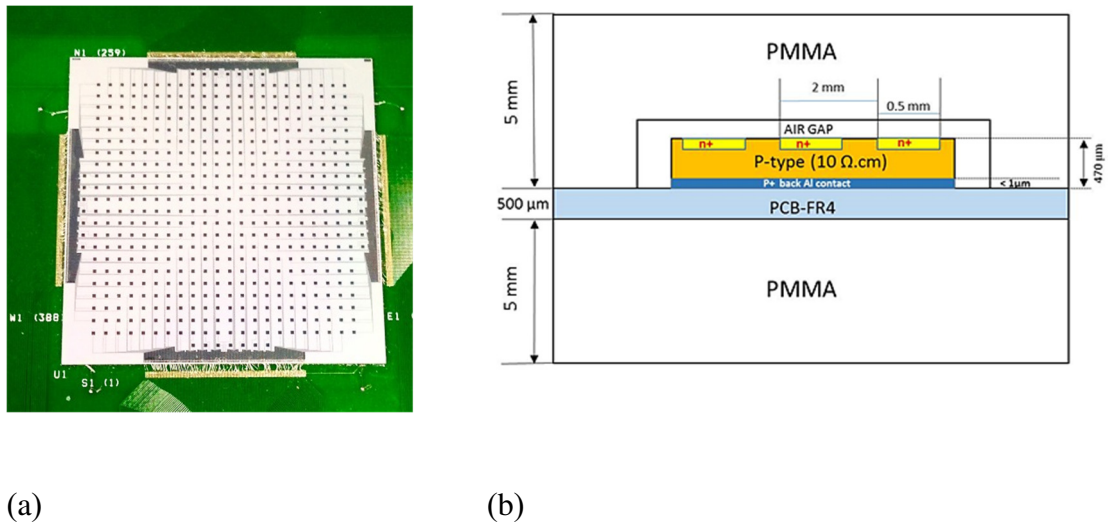
Figure 3.1: A schematic of the cross section of an MP512 detector component and its packaging (not to scale).

3.2.2. Data acquisition system (DAQ)

The MP512 data acquisition system (DAQ) is based on a 64-channel analogue front-end electrometer ASIC chip that provides an analog differential output that is proportional to the charge that accumulates in a capacitor during a pre-selected time frame that is set electronically through a software interface. The gain adopted in this work was set to span a full scale range up to 9.6 pC max with a resolution of 16 bits and an integral linearity of approximately 0.006% [193]. The baseline of each current integrator is subtracted

using a double sampling approach: this feature is very important for maintaining accuracy in a medical instrument which requires a high signal to noise ratio (Figure 3.2). Each chip is interfaced to a quad analogue-to-digital converter (ADC), and the ADC output is synchronised and the channels de-randomised by a field programmable gate array (FPGA). The FPGA also synchronises the sync pulse of the LINAC to acquire a detector current only when the electron gun injects electrons into the accelerator (for approximately 3.7 µs every 2.7 ms at 600 MU/min on a Varian Clinac iX). The ADC system can also acquire the detector array signal by an internal trigger generator with frequency up to 10 kHz in case dosimetry on the source of isotopic radiation radiated intensity in all directions.

The data is transferred from FPGA via USB2.0 to a host computer where the in-house developed program interface (Magic Suite) operates. This program was designed to perform real time signal processing where the signal from the detector is manipulated immediately and the users can monitor in real time. Moreover, the Magic Suite interface was designed to be convenient and easily accessible. The software enables a user to set the acquisition parameters such as the integration time (µs) to match the detector, and the acquisition length (s) and acquisition frequency (kHz) that synchronises with the radiation time and machine, respectively. The program provides instantaneous and integral detector response as an output, and this can be visualised using a map and histogram response (Figure 3.3). The tool also provides an equalisation function that can be stored and calculate the equalisation factor of the detector. Moreover, each acquisition parameter and detector signal are recorded as log files that can be used for further offline analysis. An overview of DAQ workflow is shown in Figure 3.4.

(a) (b)
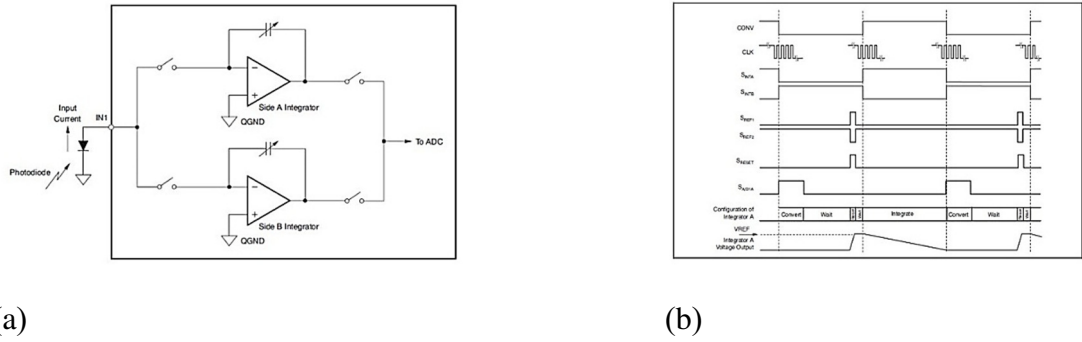
Figure 3.2: The general operation schematic of ASIC ship (a) Dual switched integral architecture and (b) Integration Timing [193].
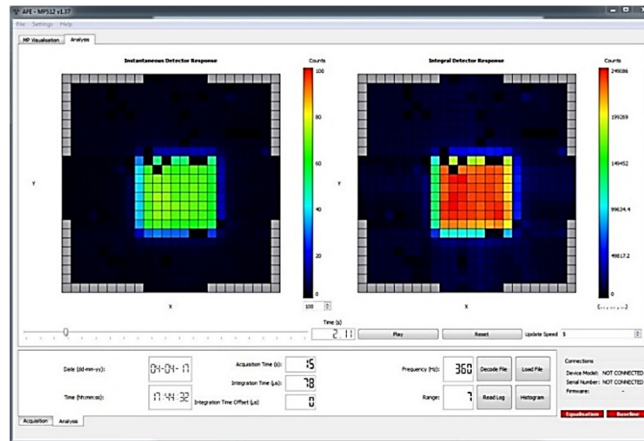
(a)
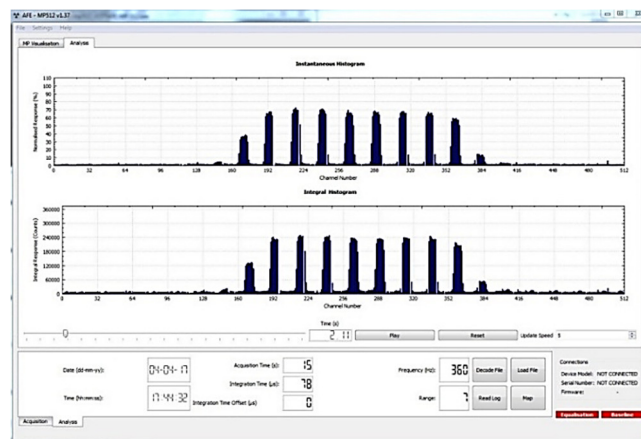
(b)

Figure 3.3: Magic Suite interface (a) Map response display and (b) Histogram response display.
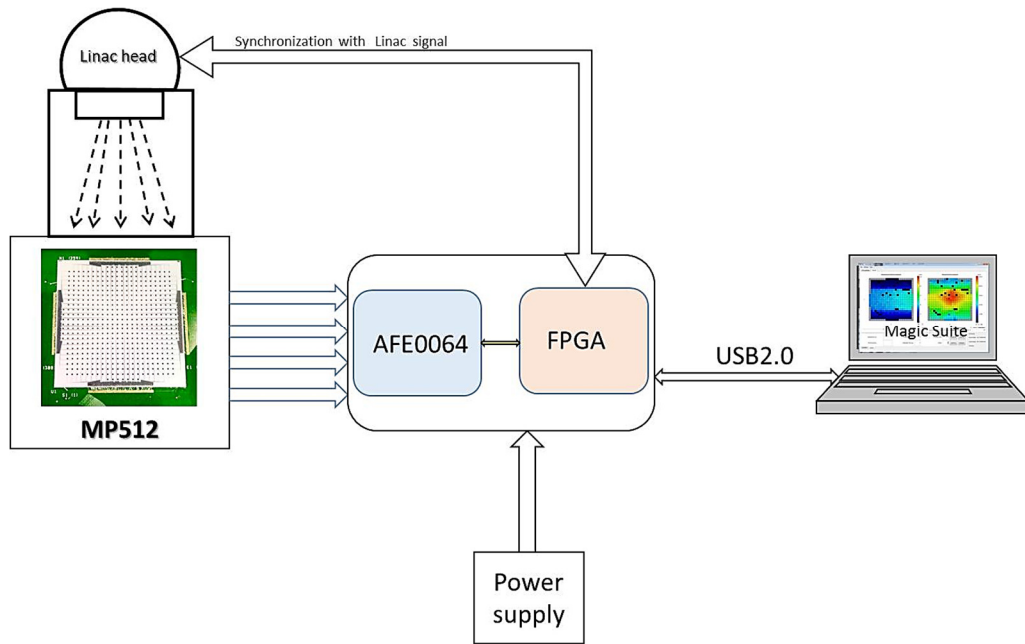
Figure 3.4: Flow chart of data acquisition (DAQ).

3.2.3. CMRP Cylindrical phantom

A CMRP cylindrical phantom is shown in Figure 3.5**.** It was built by CMRP using polymethyl methacrylate (PMMA) material, also known as acrylic glass. The physical density of PMMA is approximately 1.15-1.19 g/cm^3 [194]. The phantom is a 30 cm diameter by 40 cm long cylinder [170], and has a central PMMA insertion slot of 15.5 $\times$20.5 $\times$5 cm^3, into which the detector array can be inserted.
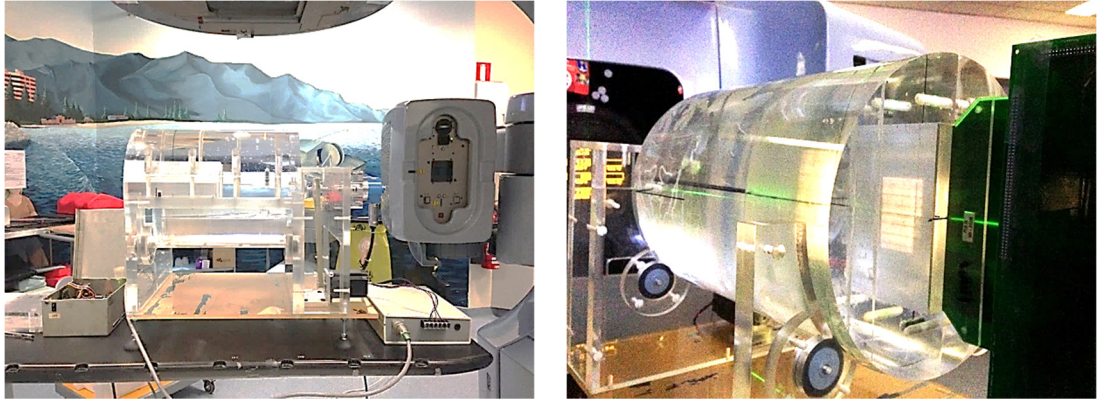
(a)   (b)

Figure 3.5: PMMA cylindrical phantom (a) Lateral view of phantom and (b) MP512 inside the phantom.

3.3. Methods

All the experiments in this chapter were carried out on a Varian Clinac iX (Varian Medical System, Palo Alto, CA) at the Illawarra Cancer Centre (ICCC), Wollongong hospital.

3.3.1. Equalisation and calibration factors

Before taking any measurements the MP512 must be equalised to correct for any sensitive non-uniformity in the detector array and ASIC readout chips channels. This equalisation factor was carried out by irradiating the MP512 using a 20×20 cm^2 square field of 6 MV photon beams and 200 MU. The detector was placed into water at a depth of 10 cm and full scatter conditions by fixing the source to the isocentre of the detector (SAD) at 100 cm. This procedure has been investigated and used to obtain equalisation factors that were calculated by following Equation (3.1) and (3.2) [168][170]. The equalisation coefficients can be stored in the DAQ software interface.

$$F_i = \frac{X_i}{(\overline{X})} \tag{3.1}$$

$$X_{eq-1} = \frac{X_i}{F_i} \tag{3.2}$$

Where F_i is the correction factor vector, X_i is the pixel response, $\overline{X}$ is the average response of detector and X_{eq-1} is the equalized detector response.

Each pixel for the calibration factor was calibrated against a 0.6 cm^3 Farmer NE2571 ionisation chamber that refers to the relative calibration MU/min of the machine [50]. The detector was set to a maximum depth of 1.5 cm for 6 MV photon beams with a full back scatter of 10 cm solid water phantom and a fixed source to skin distance (SSD) of 100 cm. A 10×10 cm^2 field was irradiated to the detector delivering 100 MU and a dose rate of 600 MU/min. The calibration factor for each pixel is defined by Equation (3.3).

$$CF_i = \frac{D_{IC}}{R_{MP512}} \tag{3.3}$$

Where CF_i is the calibration factor, D_{IC} is the ionisation dose (cGy) measurement. The detector was calibrated to 1 MU = 1 cGy and R_{MP512} is its response.

3.3.2. Angular response

The angular response is examined by inserting an MP512 into a CMRP cylindrical phantom. The detector is in a vertical position and the treatment gantry is horizontal (Figure 3.6). The central pixel of the detector array is aligned to the machine's isocentre; a 5×5 mm^2 size field is used for fine alignment as the couch is moved in 1 mm steps vertically and laterally to identify the maximum response of the central pixel. The gantry's horizontal position is defined as the zero incident beam angle because the beam incidence is perpendicular to the detector surface. This setup enabled the angular response

of the MP512 detector to be examined from 0 to +180 degrees without any interference from the couch. The Linac gantry was rotated clockwise at 15° increments from the incidence beam angle 0° to +180°. For a beam with a 10×10 cm^2 field the gantry was rotated at 1° increments for angles of incidence between 85° to 95° to finer characterise the detector around the expected variations of maximum response. The MP512 was irradiated five times with 100 MU for each angular position at a dose rate of 600 MU/min, while keeping the central pixel at the isocentre (at a depth of 15 cm for PMMA and 85cm for SSD). The square beams are defined by the primary collimators (jaws) field sizes of 1×1 cm^2, 2×2 cm^2, 3×3 cm^2, 4×4 cm^2 and 10×10 cm^2. The relative angular response is the ratio at which the pixel responds at a given angle of irradiation that is normalised to the same pixel with a beam incidence of 0 degrees.
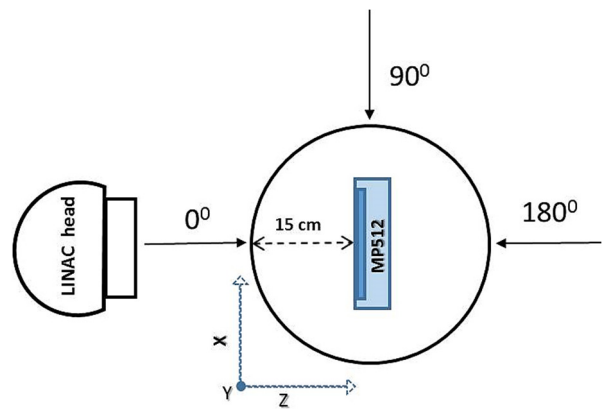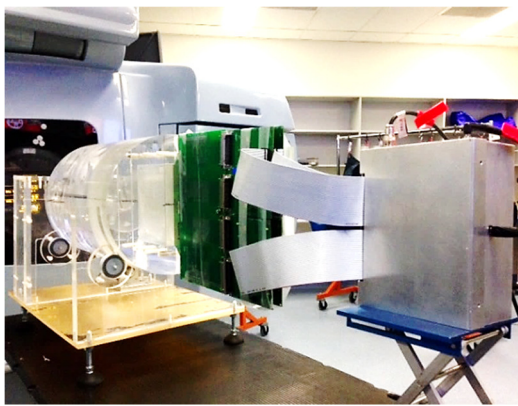
(a)   (b)

Figure 3.6: The experiment setup; (a) The MP512 embedded inside the phantom, (b) Schematic diagram of angular response measurement (not to scale).

3.3.3. Gafchromic EBT3 film measurement

Gafchromic EBT3 film was used as the reference dosimeter to evaluate and correct the angular response of MP512 by assuming that its response has no significant angular

dependence. This EBT3 film was designed to minimise its angular response by using two 30 µm thick active layers stacked with two 125 µm thick matte polyester layers to protect them from mechanical damage [195]; this configuration of EBT3 film is shown in Figure 3.7. The normalisation of the MP512 detector to EBT3 film response helps minimise the mechanical tolerances as the LINAC gantry rotates around the phantom and the non-homogeneous effects of the phantom.
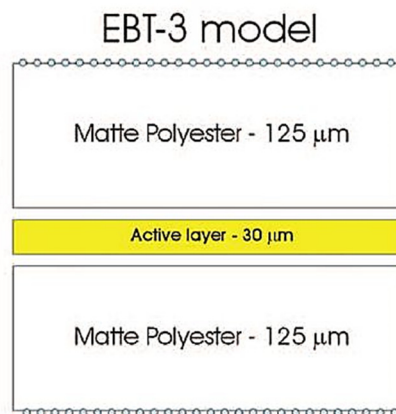
Figure 3.7: The structure of gafchromic EBT3 film [195].

Films were calibrated by using 12 pieces from the same film lot, with each having areas of 3×3 cm^2; they were irradiated with 6 MV photons and an open 10×10 cm^2 field at d$_{max}$ (1.5 cm) at SSD 100 cm that was placed on a 10 cm thick slab of solid water for back scatter equilibrium. The films were exposed to doses from 0.25 Gy to 5 Gy, although one film was retained to have its optical density baseline evaluated. A 0.6 cm^3 farmer ionisation chamber (model 2571) was used to measure the actual dose delivered for a given MU setting under the same irradiation conditions. In this study, a Microtex ScanMaker i800 was used for films scan procedure. Microtex ScanMarker model i800 is the flatbed scanner with a staggered trilinear CCD array and a built-in transparency adapter [196]. The set of calibration films were scanned six times at the same position in the centre of a scanner with 48 bits of colour depth and spatial resolution of 72 dpi

(equivalent to 350 μm size pixels). All the correction image parameters of the scanner were set to disable. The last three scans were used to carry out the analysis needed to ensure the scanner was thermally stable and the inter-scanning was consistent [89]. Data analysis was carried out using the red channel which had been extracted using ImageJ V1.48 (National Institute of Health, USA). The mean pixel values were calculated for a region of interest (ROI) of 2×2 cm^2 at the centre of each film patch to determine the net optical density (net OD) according to Equation (3.4); this was then converted to dose by fitting it with a fourth degree polynomial function [197][198][199]. The calibration curve of EBT3 film is shown in Figure 3.8. The calibrated dose response curve of EBT3 film was energy independent on the photon energy from 6 MV to 15 MV, so the same calibration curve was used to analyse the 6 MV and 10 MV irradiation [198].

$$netOD = OD_{exp} - OD_{bckg} = log_{10}\left(\frac{I_{pre}-I_{bckg}}{I_{post}-I_{bckg}}\right) \tag{3.4}$$

Where I_{pre}, I_{post}, and I_{bckg} are the optical intensities for pre and post irradiation, as well as the transmitted background intensities.

To calculate the correction factor, samples from the same lot of EBT3 films were cut into 7.0×7.4 cm^2 patches to fit the PMMA holder used for MP512 packaging (Figure 3.9). The films were irradiated inside the cylindrical phantom, in the same position as the detector array, with 6 MV and 10 MV photon beams and a 10×10 cm^2 open field at incident beam angles of 0°, 45°, 90°, 135°, and 180°; the films were then analysed by following the same procedure for film calibration. A median 3×3 pixels filter was used to reduce noise. An ROI with 137×137 pixels matches the active area of an MP512 corresponding to 5.2×5.2 cm^2. MATLAB 2014b (Math Works Inc., Natick, MA) and the

polynomial function obtained during the calibration step were used to convert pixels to doses.

The equation shown in the figure is $y = -2190.5x^4 - 900.53x^3 + 2285x^2 + 736.15x + 0.6113$
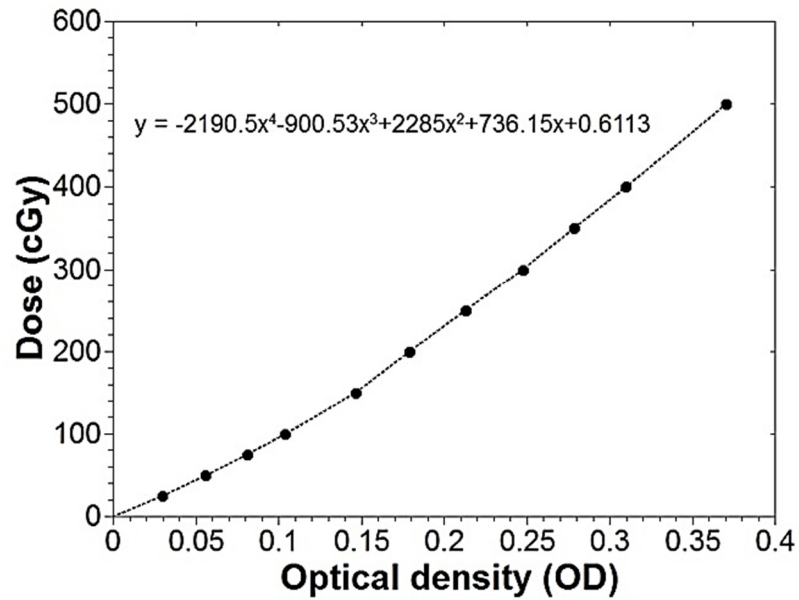
Figure 3.8: The calibration curve of gafchromic EBT3 films using a red channel.
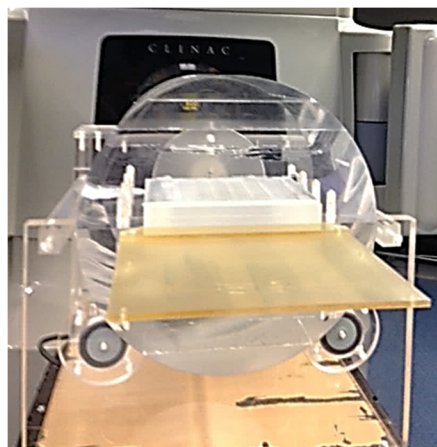
Figure 3.9: The experiment setup of gafchromic EBT3 films using MP512 packaging to fit the PMMA holder**.**

3.3.4. Angular correction factors

Data collected by the MP512 and EBT3 film with an open 10×10 cm^2 field were used to determine the correction factor for each detector pixel. Increasing the field size beyond 10×10 cm^2 for angular calibration does not change the field uniformity or electron equilibrium within the active area of MP512 that determines the angular response calibration when 10×10 cm^2 field irradiation is used. The angular dependence of MP512 was evaluated in an azimuthal direction (along the *x*-axis) because the rotation was longitudinal (*y*-axis), as shown in Figure 3.6. Because the spatial resolution of the detectors is different, the (*i,j*)-*th* pixel of the EBT3 dose profiles in the *x* and *y* direction was aligned with the (*i,j*)-*th* pixel of MP512 using a curve function that obtained a second order polynomial fit [168]. The response of film at the angular increments 15^0 needed to determine an angular correction of MP512 was achieved by interpolating between the values of films irradiated at 0°, 45°, 90°, 135°, and 180°. The calibration matrix a_{ij} is the conversion factor from counts to dose; it was calculated from the ratio between the response of MP512 in counts for each pixel (*i,j*) to the dose measured by the EBT3 film in each pixel (*i,j*) as a function of the gantry angle θ, defined as Equation 3.5 and expressed in units of counts/cGy.

$$a_{ij}(\theta) = \frac{MP_{ij}(\theta)}{EBT3_{ij}(\theta)}$$

(3.5)

Where *i* is the row index along the *x*-axis, i.e., the axis perpendicular to the phantom rotation, and *j* is the column index of pixels along the *y*-direction parallel to the axis of rotation. For each column along the *y*-coordinate the detector and film did not very much.

For the open 10×10 cm^2 field, the angular response calibration tensor for MP512 ($C_{ij}(\theta)$) was calculated by dividing the calibration factor at an arbitrary gantry angle θ by the calibration factor at a gantry angle of 0 (Equation 3.6)

$$C_{ij}(\theta) = \frac{a_{ij}(\theta)}{a_{ij}(0)} \qquad (3.6)$$

3.3.5. Validating the angular response correction factor for a small field

The angular response of MP512 was verified by irradiating it with open field sizes of 1×1 cm^2, 2×2 cm^2, 3×3 cm^2 and 4×4 cm^2, and at gantry angles of 0°, 45°, 90°, 135° and 180° using 6 MV and 10 MV photons, and by fixing 100 MU and dose rates at 600 MU/min at each position. At each pixel (i,j), the dose response $MP_{ij}^{corrected}(\theta)$ measured by the MP512 and corrected for angular dependence, was obtained by dividing the measured response $MP_{ij}^{'}(\theta)$ by the calibration tensor $C_{ij}(\theta)$ for a 10×10 cm^2 field (Equation 3.7). The methodology used to measure the MP512 response was similar to that described above.

$$MP_{ij}^{corrected} = \frac{MP_{ij}^{'}(\theta)}{C_{ij}(\theta)} \qquad (3.7)$$

Where $MP_{ij}^{'}(\theta)$ is the MP512 response signal (counts) for a particular angle, and $C_{ij}(\theta)$ is the calibration tensor for the 10×10 cm^2 open field.

3.4. Results

3.4.1. Angular response

Figure 3.10 shows the difference in angular response at the central pixels for MP512 and EBT3 film. Figure 3.11 shows the intrinsic detector response between 0^0 and 180^0 as a function of the incidence angles collected from the four central pixels with various field sizes. These responses are the combined effect of beam attenuation through the silicon substrate and the fibreglass supporting the detector crystal. The error bars are calculated as one standard deviation (1SD) for the five measurements repeated in a test state, and the measurement uncertainty with a maximum variation of ±0.2% at a 95% confidence interval. The relative response of MP512 decreased as the incident beam angle increased, giving an average change per degree of 0.18±0.03%. The relative angular response of MP512 decreased by less than 5% for incident angles between 0^0 and 60^0, whereas the minimum response (largest deviation) of 18.5±0.5% for 6 MV and 15.5±0.5% for 10 MV was achieved at incidence beam angles between 90^0-95°. The relative angular response increased again when it moved towards larger angles, which led to underestimating the response of 14.3±0.6% and 9.4±1.8% at 180^0 for the 6 MV and 10 MV photon beams, respectively. The data in this study was not distributed normally and the sample size per group was less than the criteria (n<15), so a non-parametric statistical analysis such as a Kruskal-Wallis test and a Mann-Whitney U test were used. A Kruskal-Wallis test is commonly used to compare the difference for three or more independent groups, in this study, it was carried out to determine the effect of various field sizes ($1{\times}1$ cm^2 to $10{\times}10$ cm^2) for the same photon energy. While Mann-Whitney U-test is suitable for comparison of the difference between two independent groups, in this study, it used to find out for the effect of energy (6 MV and 10 MV) for same field size. There was no significant

difference in an angular response with values of p = 0.9985 for 6 MV and p = 0.5359 for 10 MV, although the angular response for 1×1 cm^2 and 10×10 cm^2 field size for a 10 MV photon beam at incidence angles between 135° to 180° changed by more than 3%, and a Mann-Whiney U test showed no significant difference with p = 0.5214. Hence, the angular response of MP512 is not sensitive to field size. However, Figure 3.12 shows the intrinsic detector response for a 10 ×10 cm^2 open field was between 0^0 and 180^0 as a function of the incidence angle collected from the four central pixels and the beam energy. The relative angular response for higher energy 10 MV photon beams was less than for 6 MV photon beams. A Mann-Whitney U test to compare the angular response between 6 MV and 10 MV photon energies revealed a significant difference in the angular response as a function of the beam energy with p = 0.04.
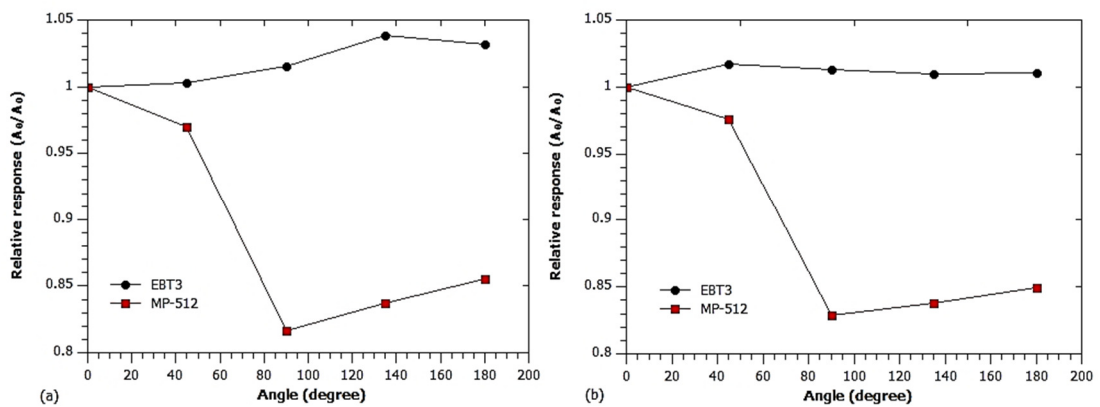
Figure 3.10: A comparison of the central pixel response between MP512 and EBT3 for 6 MV (a) Field size 3×3 cm^2, (b) Field size 10×10 cm^2.
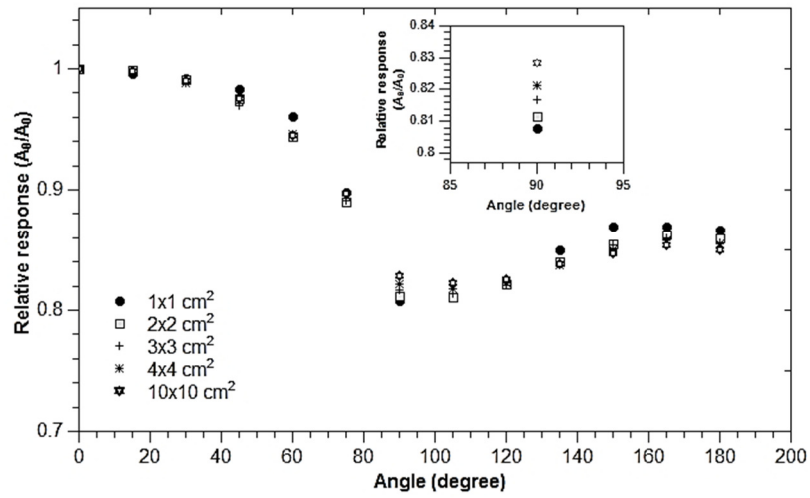
(a)
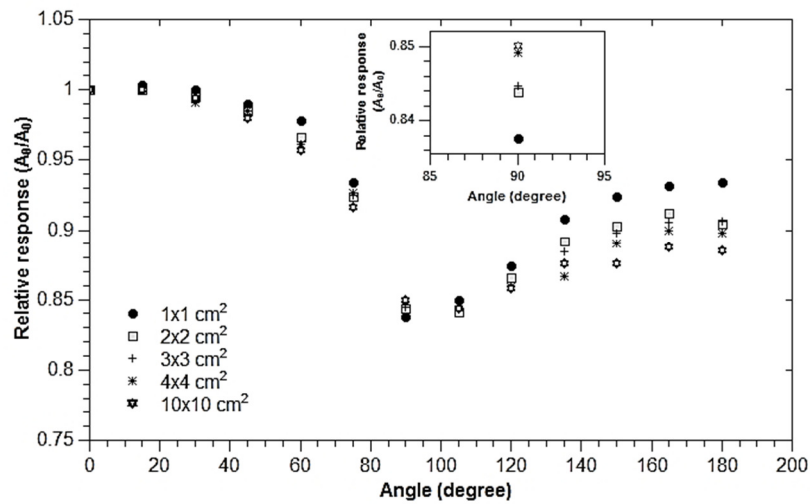
(b)

Figure 3.11: Angular dependence of the averaged four central pixels of the MP512 detector array shown as a function of incident gantry angle for (a) 6 MV and (b) 10 MV photons.
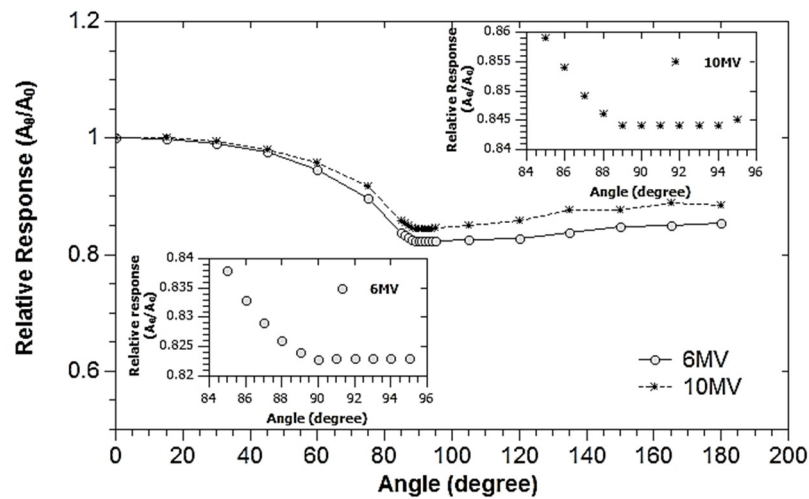
Figure 3.12: Angular dependence of the averaged four central pixels of the MP512 detector array shown as a function of incident gantry angle for an open field size of 10×10 cm^2 for 6 MV and 10 MV photons.

3.4.2. Validating the angular response correction factor for a small field

The beam profile comparisons were evaluated using the shape-preserving interpolant curve fitting tool in MATLAB which provides 0.01 mm precision that is reflected in a Table 3.1. The beam profiles of field sizes from 1×1 cm^2 to 4×4 cm^2 measured with an MP512 at an incidence angle of 0 degrees were compared to EBT3 films; there was agreement with the Full Width of Half Maximum (FWHM) and penumbra (20%-80%) for 6 MV and 10 MV beams within ±1% and 1 mm for FWHM and penumbra, respectively (

Table **3.1**). When the angular dependence is not corrected the MP512 response to beams at incidence angles other than 0 degrees has a dose profile that is similar in shape to EBT3 film but with a lot of attenuation. This result confirms that underestimating the dose for angled beams due to the extracameral silicon surrounding each pixel cannot be avoided for a monolithic solid state detector. After correcting the MP512 measured doses using

the $C_{ij}(\theta)$ factor (Equations 3.6 and 3.7), the agreement between MP512 and EBT3 films improved significantly for field sizes of 2×2 cm^2, 3×3 cm^2, and 4×4 cm^2. The dose profiles from 2×2 cm^2 to 4×4 cm^2 measured with the MP512 detector after correction match the EBT3 dose profiles for all angles within ±2% (Figures 3.13 to 3.18) for 6 and 10 MV photon beams. However, with 6 MV photons and a field size of 1×1 cm^2 the cross-plane depth-dose profiles corresponding to a 90^0 gantry angle were wrong by almost 6% out compared to EBT3 film [Figure 3.19(c)]. This larger error occurred because the partial response of MP512 for small a 1×1 cm^2 field for beam incident along the detector plane is due to secondary electrons generated by photons interacting along the silicon substrate about 400 micron thick and attenuating stronger that in a phantom. In case of 10×10 cm^2 field the contribution of electrons generated in silicon is much smaller because the response of the detector is mostly due to secondary electrons generated by photons from the phantom where their (photon) attenuation is less than in silicon. However, with a 10 MV photon beam, the discrepancy between MP512 and film after correction was within 2% for the 1×1 cm^2 size field [Figure 3.20(c)] because the scattered electrons have higher energy which is not absorbed by the printed circuit board and the silicon substrate.

Table 3.1: The difference in FWHM and penumbra width (20%-80%) between MP512 and EBT3 films for various field sizes.

FS (cm^2)	6 MV						10 MV					
	FWHM(mm)			Penumbra(mm)			FWHM(mm)			Penumbra(mm)		
	EBT3	MP512	Diff (%)	EBT3	MP512	Diff (mm)	EBT3	MP512	Diff (%)	EBT3	MP512	Diff (mm)
1×1	9.84	10.06	2.31	2.44	2.82	0.38	10.19	10.41	2.18	2.84	3.14	0.30
2×2	19.85	20.02	0.83	2.85	3.57	0.71	19.86	20.29	2.17	3.43	3.83	0.39
3×3	29.80	30.33	1.81	3.18	3.69	0.52	29.92	30.37	1.49	4.01	4.25	0.24
4×4	40.01	40.32	0.79	3.40	3.79	0.39	40.06	40.54	1.19	4.30	4.39	0.09

Figure 3.13: Dose profiles of 2×2 cm^2 beam measured with EBT3 films and MP512 with and without a correction factor for 6 MV photon as a function of distance (mm) and dose (cGy); (a) 0°, (b) 45°, (c) 90°, (d) 135° and (e) 180°
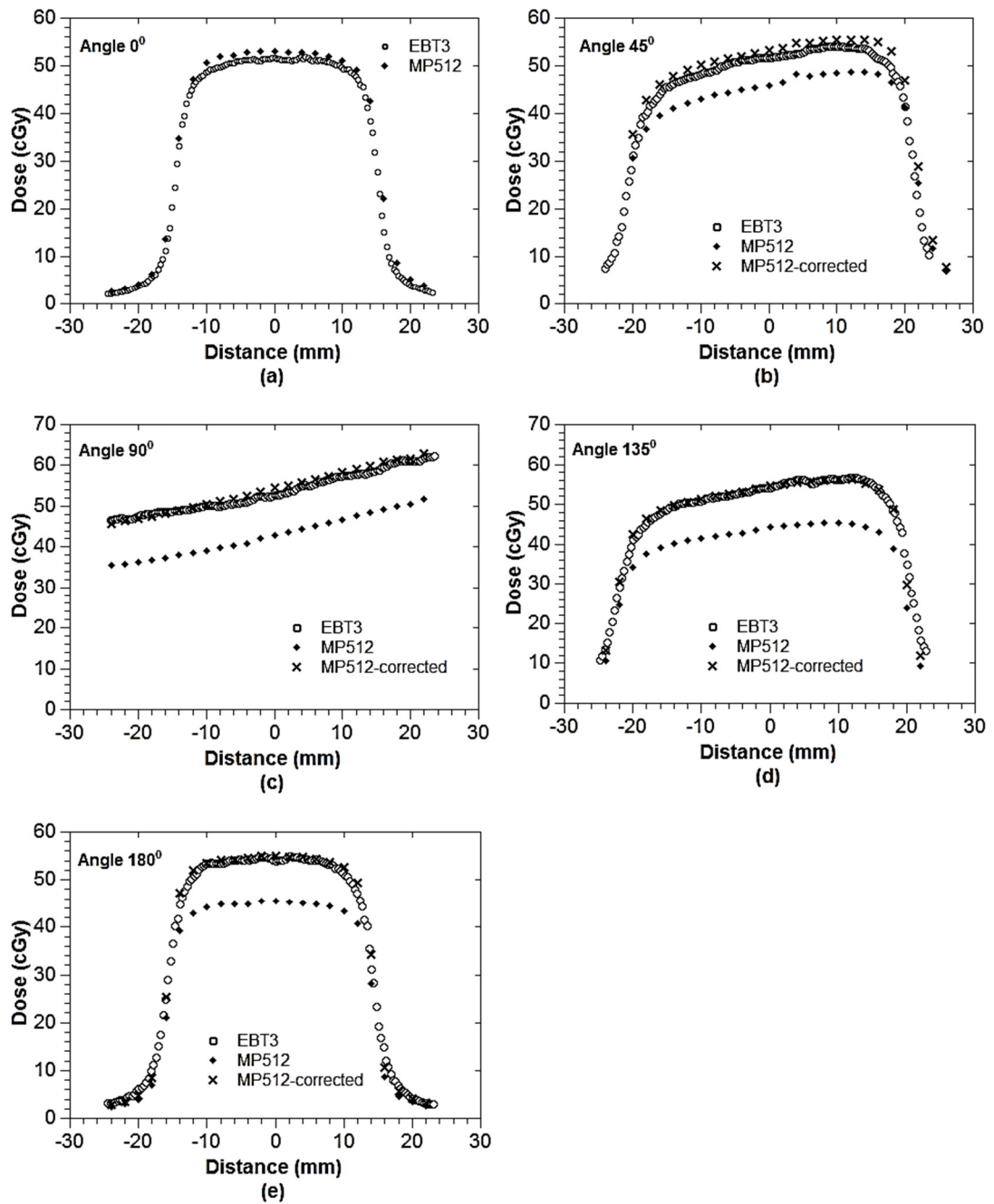
Figure 3.14: Dose profiles of 3×3 cm^2 beam measured with EBT3 films and MP512 with and without a correction factor for 6 MV photon as a function of distance (mm) and dose (cGy); (a) 0°, (b) 45°, (c) 90°, (d) 135° and (e) 180°

Figure 3.15: Dose profiles of 4×4 cm^2 beam measured with EBT3 films and MP512 with and without a correction factor for 6 MV photon as a function of distance (mm) and dose (cGy); (a) 0°, (b) 45°, (c) 90°, (d) 135° and (e) 180°

Figure 3.16: Dose profiles of 2×2 cm^2 beam measured with EBT3 films and MP512 with and without a correction factor for 10 MV photon as a function of distance (mm) and dose (cGy); (a) 0°, (b) 45°, (c) 90°, (d) 135° and (e) 180°

Figure 3.17: Dose profiles of 3×3 cm^2 measured with EBT3 films and MP512 with and without a correction factor for 10 MV photon as a function of distance (mm) and dose (cGy); (a) 0°, (b) 45°, (c) 90°, (d) 135° and (e) 180°

Figure 3.18: Dose profiles of 4×4 cm^2 beam measured with EBT3 films and MP512 with and without a correction factor for 10 MV photon as a function of distance (mm) and dose (cGy); (a) 0°, (b) 45°, (c) 90°, (d) 135° and (e) 180°
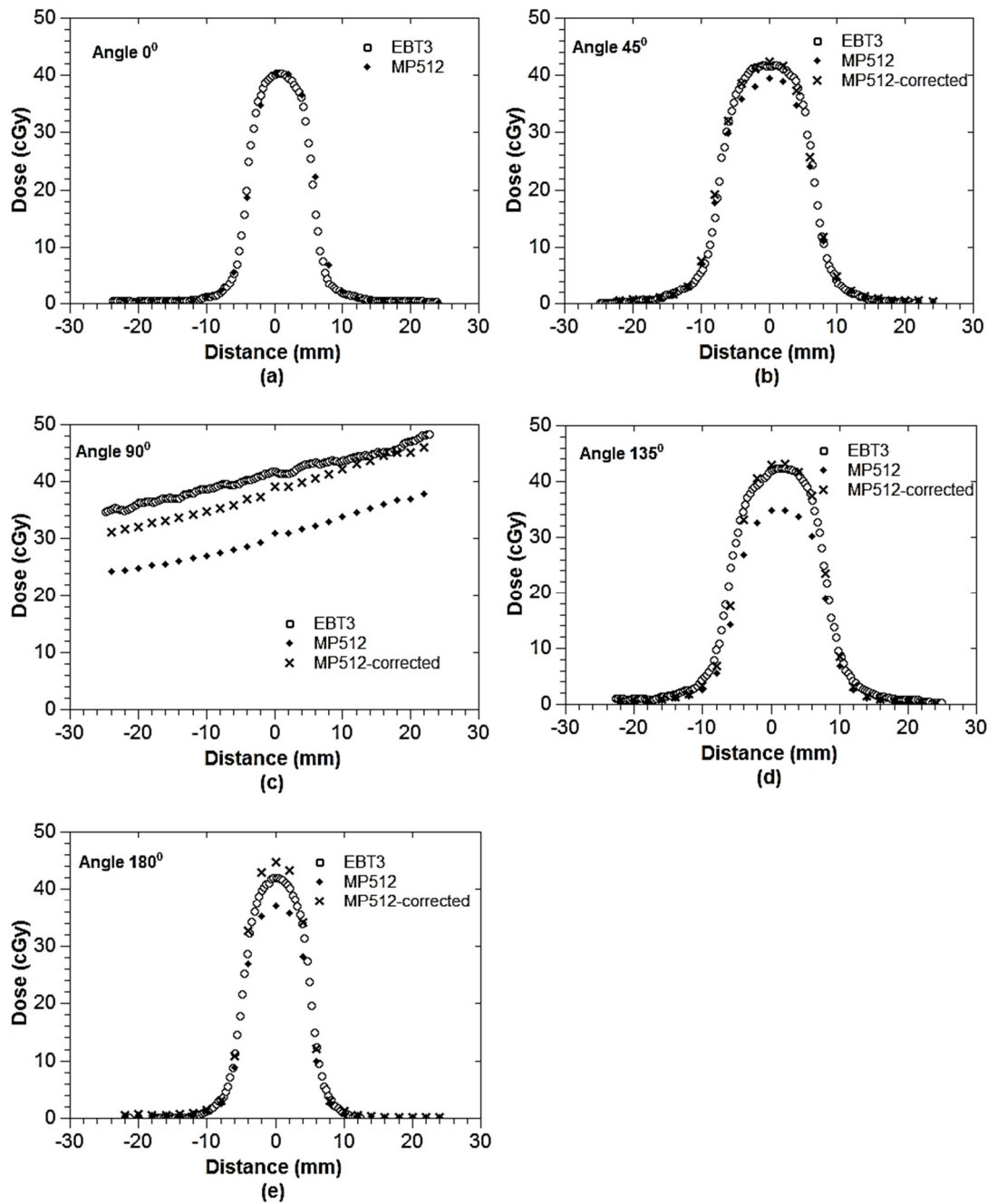
Figure 3.19: Dose profiles of 1×1 cm^2 beam measured with EBT3 films and MP512 with and without a correction factor for 6 MV photon as a function of distance (mm) and dose (cGy); (a) 0°, (b) 45°, (c) 90°, (d) 135° and (e) 180°

Figure 3.20: Dose profiles of 1×1 cm^2 beam measured with EBT3 films and MP512 with and without a correction factor for 10 MV photon as a function of distance (mm) and dose (cGy); (a) 0°, (b) 45°, (c) 90°, (d) 135° and (e) 180°

3.5. Conclusions

This study examined how the field size and photon energy affected the angular response of MP512, a monolithic detector arrayed with 0.5×0.5 mm^2 pixels and a 2 mm pitch; the angular response of MP512 was almost independent of the field size. Our results suggest that a using a 10×10 cm^2 reference field to calculate the correction factor and apply it to any field size larger than 1×1 cm^2 is feasible. This makes the MP512 a viable option for small field dosimetry in intensity modulated SBRT or VMAT where the fields shape is modulated. The method used to calculate the angular correction vector is based on comparing the EBT3 mapped dose and MP512 detector response to a 10×10 cm^2 field and beam incidence angles between 0 degrees and 180 degrees. When the developed angular correction vector was used the dose profile measured by MP512 and EBT3 film for all field sizes at 6 MV and 10 MV photons agreed within 2%, except for the 1×1 cm^2 field at 6 MV where the agreement was within 6%. The angular dose of MP512 decreased by increasing the beam incidence angle to $18.5 \pm 0.5\%$ and $15.5 \pm 0.5\%$ for 6 MV and 10 MV photon beams, rather than the normal beam incidence (zero degree) where the minimum was between $90°$ to $95°$. While the MP512 is a large monolithic 2D array detector, its angular response is similar to or less than of the single diodes presented in other studies [61], [114], [200], whereas its directional dependence is attributable to the intrinsic anisotropic configuration of the MP512 silicon detector where each pixel is surrounded laterally by extra-cameral silicon and by a thin fibreglass printed circuit board on the back. This packaging creates differences in beam angle dependent attenuation of the secondary electrons which causes the pixels to become sensitive to angular dependency; and since the silicon surrounding the pixels is denser than water, secondary electrons are produced with an energy distribution that differs to that generated in water which affect the dose measured by the pixels under different beam angles [186], [201]–

[203]. For 10 MV photon beams, the scattered electrons have more energy than 6 MV photon beams, which leads to a less pronounced angular response by the MP512.

The discrepancy between the MP512 and EBT3 films of up to 6% for 6 MV beams and a 1×1 cm² field at an incidence angle of 90^0 are due to the different radiation fractions for a 1×1 cm² field compared to a 10×10 cm² field. The partial fraction of photons attenuated by 0.47 mm thick and 52 mm long silicon substrate has more influence on how the pixels embedded in silicon with depth respond, whereas the response of pixels with depth for a 10×10 cm² field is driven mostly by secondary electrons scattered from the PMMA to silicon. With the 1×1 cm² field and 10 MV photon beams, this effect was less pronounced because the scattered electrons had more energy, leading to a smaller asymmetry due to PCB and extra-cameral silicon. At field sizes less than 2×2 cm² for 6 MV photon beams, when a beam is irradiated parallel to the silicon detector array such as at an incident beam angle of 90^0 a small field correction factor rather than generic one for a 10×10 cm² field should be considered to achieve higher accuracy.

The applicability of MP512 for the developed correction vector was studied using the case of arc delivery in VMAT and IMRT for small lesions. Here, the gantry angles measured with an inclinometer and synchronised with the MP512 DAQ are the basis of the list mode data which, in conjunction with the angular correction vector, will provide corrected integral 2D dose mapping in a particular plane [204]. Measurements using MP512 will be compared with the EBT3 response for the same VMAT and IMRT delivery and TPS prediction and will be discussed in Chapter 5.

Chapter 4

The characteristics of a 2D monolithic epitaxial detector array as a quality assurance dosimeter for small field

4.1. Introduction

After being investigated the MP512-Bulk proved to be an excellent QA dosimeter in a small field, but it is sensitive to degradation from accumulative doses of radiation [205][63]; this means it requires frequent recalibration to maintain a measurement accuracy within 2%. Although epitaxial silicon technology has been introduced into conventional radiotherapy, investigations showed it suffered from radiation hardening [182][206][207]. To improve the radiation hardness and provide long term recalibration of the MP512 detector arrays, the CMRP has modified the MP512 base on epitaxial technology so it is now called MP512-EPI.

This chapter presents a complete dosimetric characterisation of an MP512-EPI by describing its design and fabrication, and the experimental techniques and setup. The dosimetric characteristics of this detector were investigated in terms of radiation hardness, percentage depth dose (PDD), dose per pulse and dose rate (MU/min) dependence, dose linearity, segmental dose linearity, long term reproducibility, cross-plane profiles in small fields, and directional dependence. MP512-EPI measurements were compared to the

Markus ionisation chamber, to gafchromic EBT3 films, and to MO*Skin*. The result of MP512-EPI in term of radiation degradation was compared to MP512-Bulk to understand benefit of epitaxial silicon detector technology can be utilized for development of radiation hard quality assurance dosimeters. The chapter also presents the detector's I-V characteristic measurements to show the leakage currents as the function of the accumulated dose of irradiation.

4.2. Materials and Methods

4.2.1. MP512-EPI design and fabrication

The MP512-EPI (Figure 4.1) detector has flat array planes with 512 phosphorus n+ implanted pixels fabricated on a 34.13-35.67 µm thick epitaxial layer with a high resistivity of 100 Ohm·cm (Ω·cm) and grown on top of a low resistivity p+ substrate of 0.001 Ω·cm resistivity and thickness 525±25 µm. This thin epitaxial layer limits the thickness of detector's sensitive volume to less than the length of the minority carrier diffusion while maintaining the stability of the detector's sensitive volume with the dose of irradiation. Each sensitive area is 0.5×0.5 mm^2 as defined by an n$^+$ phosphorous ion-implant that covers an area of 52×52 mm^2 with a high resolution of 2 mm. The p-stop (p+) is implanted between the sensor pixels to minimise the coupling effect due to conductive channels being generated between the boron implantations. MP512-EPI is wire-bonded onto a 5 mm thick tissue equivalent printed circuit board (PCB) that is connected to the readout system via the connector pins (Figure 4.2). The thin layer of epoxy covers the entire active area of the detector to protect it from accidental damage and dust. The MP512-EPI is sandwiched between two 5 mm thick PMMA slabs, while the covering piece provides an air gap of 0.5 mm for 6 MV photon and 1.2 mm for 10 MV photon measurements [192].
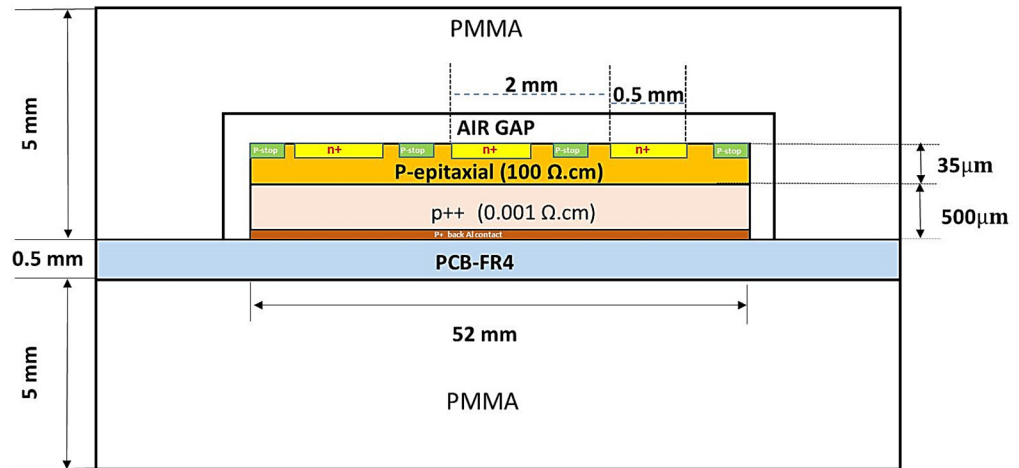
Figure 4.1: Schematic of the MP512-EPI fabrication and packaging (not to scale).
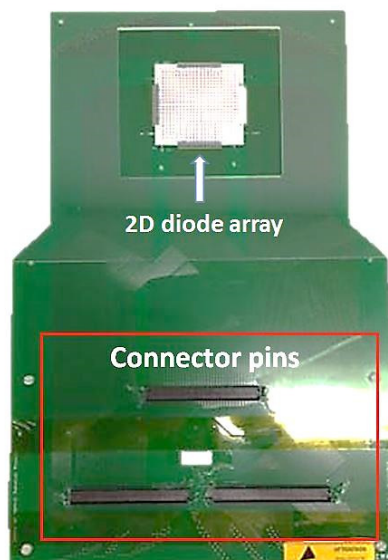
Figure 4.2: MP512-EPI wire-bonded onto a PCB and the

connector pins.

4.2.2. Data acquisition system (DAQ)

The FPGA data acquisition system was used for the measurements, as discussed in Chapter 3, Section 3.2.2.

4.2.3. Electrical characterisation: Current-Voltage (IV) characteristic.

The current-voltage (IV) characteristic or radiation hardness characteristics were investigated to determine the quality of the p-n junction and the effects of radiation damage. Radiation can increase the leakage current of silicon detectors which limits the sensitivity of the silicon diode used to optimise the signal/noise ratio. The IV characteristic of MP512-EPI was performed before and after irradiation with a high dose Co-60 gamma source for a total dose of 60 kGy, and an increment 20 kGy per step dose. A Keithley 230 programmable voltage source was applied to the detector bias, and a Keithley 199 System DMM/scanner and Keithley 614 electrometer were used to measure the reverse current (Figure 4.3). The IV measurements and parameters were controlled using software called LabVIEW (Figure 4.4).
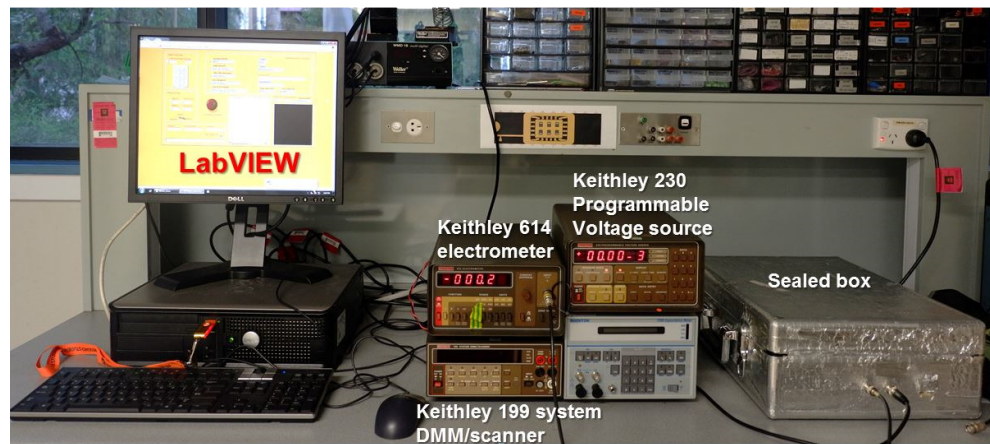
Figure 4.3: I-V characteristic measurement setup.
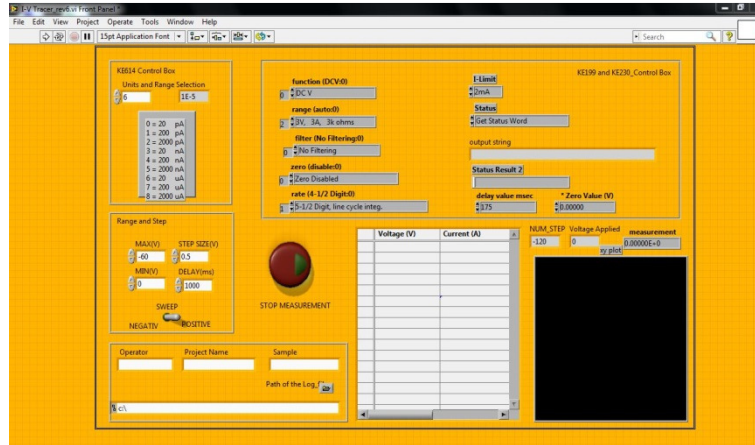
Figure 4.4: LabVIEW software interface.

The 14 diodes were randomised to cover the central and peripheral area on the MP512-EPI and to determine how detector geometry affected the leakage current. The location of the selected diodes is shown in Figure 4.5 (yellow highlight). A reverse voltage was applied to the sensor on the p+ substrate via the bias pins, and the current across the junction was measured with an ammeter connected to the n+ region of each diode pixel (Figure 4.6). The voltage ranged from 0 to -60 V, in increments of -0.5 V per step. The time interval needed to stabilise the current transient measurement was fixed at 1000 msec. The variable scale was set for a current between 2 kpA to 200 nA. Light disturbance can generate a photocurrent so the detector was kept in a dark environment or sealed box, as shown in Figure 4.3. The leakage current measurement depended on the temperature due to electromagnetic interference, so the selected diodes were measured at room temperature of approximately 298 K (24.85 °C).

	0	1	2	3	4	5	6	7	8	9	10	11	12	13	14	15	16	17	18	19	20	21	22	23	
23										457	467	319	289	301	311	323									23
22		416	418	420	424	428	434	440	448	456	468	287	**288**	300	310	320	328	337	340	347	348	353	352		22
21		415	417	419	423	427	433	439	447	455	466	477	290	302	312	322	331	336	343	346	**351**	355	354		21
20		412	413	414	422	426	432	438	446	**454**	465	476	291	303	313	325	330	339	342	349	350	357	356		20
19		409	410	411	421	425	431	437	445	453	464	475	292	304	314	324	333	338	345	359	358	361	360		19
18		404	405	406	407	408		436	444	452	462	474	293	305	315	327	332	341	344	**363**	362	365	364		18
17		399	400	401	402	403	429	435	443	451	463	473	294	306	316	326	335	367	366	369	368	371	370		17
16		392	393	394	395	396	397	398	442	450	461	472	295	307	317	329	**334**	373	372	375	374	377	376		16
15		385	386	387	388	389	390	391	**441**	449	460	471	296	308	318	379	378	381	380	383	382	256	255		15
14	7	4	5	2	3	0	1	62	63	384	459	470	297	309	321	254	253	252	251	250	249	248	247	246	14
13	17	14	15	12	13	10	11	8	9	6	458	469	298	245	244	243	242	241	240	239	238	237	235	236	13
12	26	29	27	24	25	22	23	20	21	18	19	**16**	299	234	233	232	231	230	229	228	227	226	**224**	225	12
11	31	**28**	30	33	32	35	34	37	36	39	38	**41**	**155**	213	214	215	216	217	218	219	220	221	223	222	11
10	43	40	42	45	44	47	46	49	48	51	89	100	152	202	203	204	205	206	207	208	209	210	212	211	10
9	53	50	52	55	54	57	56	59	58	61	90	101	**153**	165	175	193	194	195	196	197	198	199	201	200	9
8	123	60	122	121	120	119	118	117	72	80	91	102	150	162	172	130	131	128	129	127	126	124	192	125	8
7		116	115	114	113	112	111	110	73	81	92	103	151	**163**	173	183	188	136	137	134	135	132	133		7
6		511	510	509	508	507	481	66	74	82	93	104	148	160	170	180	189	258	257	140	141	138	139		6
5		506	505	504	503	502	480	67	75	83	94	105	149	161	171	181	186	284	279	262	261	260	259		5
4		501	500	499	489	485	479	68	76	84	95	106	146	158	168	178	187	285	280	266	265	264	263		4
3		498	497	496	488	484	478	69	77	85	96	107	147	159	169	179	184	286	281	276	273	268	267		3
2		495	493	491	487	483	64	70	78	86	97	108	144	156	166	176	185	190	282	277	274	270	269		2
1		494	492	490	486	482	65	71	79	87	99	143	142	154	164	174	182	191	283	278	275	272	271		1
0										88	98	109	145	157	167	177									0
	0	1	2	3	4	5	6	7	8	9	10	11	12	13	14	15	16	17	18	19	20	21	22	23	

Figure 4.5: Location of selected diodes on the MP512-EPI (yellow highlight).

Diode — Ammeter (A) — Ground — Variable voltage source from 0 V to -60 V
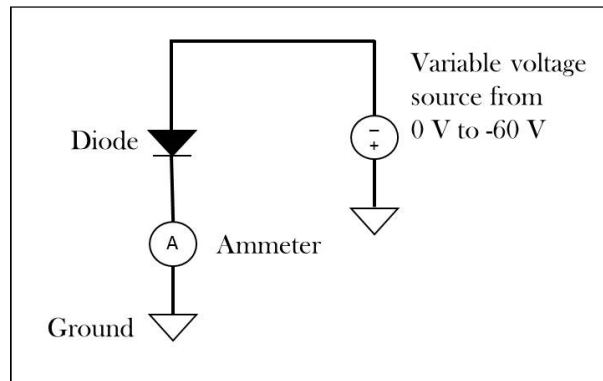
Figure 4.6: Schematic of I-V test for MP512-EPI.

4.2.4. Radiation hardness.

Silicon diode are sensitive to degradation when the accumulated dose of radiation increases [205][63], but the extent of damage to the diode depends on the quality of beam radiation. Typically, a higher energy photon beam such as 15 MV can cause more damage than 6 MV or 10 MV due to contamination with fast neutrons [208] [209]. Photon radiation mostly induces point defects in a lattice of silicon crystal, this leads to traps in the forbidden gap of silicon that acts as centres for generation and recombination. The length of the minority carrier diffusion decreases which reduces a diode's sensitivity and

dose per pulse response modification [173]. The damage caused by radiation also increases the silicon diode detector's dark current and temperature dependence. In this study the MP512-EPI was irradiated with a 2.28 kGy/hr (approximated at the time of irradiation) from a Co-60 gamma source that provided a mean energy spectrum of 1.25 MeV. All the gamma irradiated by Co-60 was held at the Gamma Technology Research Irradiator (GATRI), Australia Nuclear Science and Technology Organisation (ANSTO). The MP512-Bulk and MP512-EPI were irradiated with a total water equivalent dose of 40 kGy and dose increments 10 kGy and 60 kGy with dose increments 20 kGy, respectively. The 6 MV photon beams (Varian Clinac iX) at the Illawarra Cancer Centre (ICCC) were used to investigate the detector's sensitivity to degradation before and after irradiation. The detector array was placed perpendicular to the iso-centre of the radiation beam with a solid water phantom of 30×30 cm^2 depth of maximum dose (1.5 cm) and 10 cm phantom slab downstream for full back scattering, by fixing the source to surface distance (SSD) at 100 cm (Figure 4.7). All these experiments were carried out with 10×10 cm^2 square filed while delivering 100 MU at a constant dose rate of 600 MU/min. The measurements were repeated five times to study the detector's consistency and data acquisition system. The response of MP512-EPI to radiation was normalised to the response of the non-irradiated detector (0 kGy).
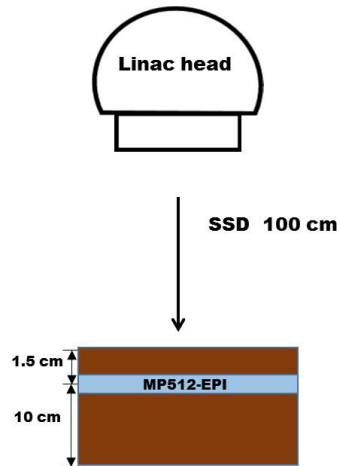
Figure 4.7: Schematic of the setup for measuring radiation

degradation.

4.2.5. Percentage depth dose (PDD)

The percentage depth dose is the radiation beam absorbed at the central axis measured at

any depth and normalised to the dose at a depth of maximum (d_{max}). This curve depends

on the depth of measurement, the beam energy (beam quality), the field size, the source

to surface distance (SSD), and the detector used in the measurement [210]. The PDD

curves show a reduction in the depth and dose functions. The PDD curve is an important

parameter in radiotherapy, and this measurement is needed to ensure the detector is a

suitable quality assurance dosimeter. The PDD were carried out in a solid water phantom

with an MP512-EPI. Because the detector array was covered by 0.5 cm thick PMMA the

PDDs were measured by varying the phantom depth from 0.5 cm to 30 cm. The PDD

curves were measured with 6 MV and 10 MV photon beams and a $10{\times}10$ cm^2 square field

where the SSD was fixed at 100 cm. The detector was irradiated using 100 MU and a

fixed dose rate at 600 MU/min. The results were compared with MP512-Bulk

measurements under the same conditions. The PDD curves were also compared with the

standard PDD data measured by the Wellhofer CC13 ionisation chamber (cavity volume

is 0.13 cm^3, length 5.8 mm and radius 3.0 mm) in water at depths ranging from 1.5 to 30

cm while the Markus chamber Model N23343 (PTW-Freiburg, Germany) measured the solid water phantom at depths ranging from 0.5 cm to 10 cm. The overdose measured by the Markus chamber was due to its small guard ring and large separation; this was corrected by following the Velkley and Rawlinson Method [211][212][213], [214]. The dimensions of the Markus chamber obtained from Chen *et al*. were used to correct the calculations [215].

4.2.6. Dose linearity

The complexity radiotherapy such as VMAT or IMRT usually delivers the dose range covers a large variation of MU per segment and fraction. The response of detector arrays should have linearity with the dose or MUs increasing. The MP512-EPI was placed at a depth of 1.5 cm in a solid water phantom and 10 cm slab behind detector for full back scattering condition of 10 cm, fixing SSD at 100 cm. The measurement obtained for both 6 MV and 10 MV photon beams. The doses were delivered ranging from 1 MU to 500 MU using a 10×10 cm^2 radiation field.

4.2.7. Dose rate (MU/min) dependence

The advanced technique VMAT and IMRT modulated the dose to deliver a conformal dose to a tumour by changing the monitor's unit rate (MU/min), gantry position, and MLC shapes during radiation. The silicon diode sensitivity on dose per pulse dependence is on a LINAC that delivers radiation with a pulsed beam and a high instantaneous dose rate [65][216]. The characteristics of this new detector must be examined in terms of its dose rate (MU/min) dependence. The pulse base frequency of a Varian accelerator for 6 MV is 360 Hz, this dose rate delivers a different pulse period and number of pulses per minute, as shown in Figure 4.8 [217]. To investigate how the duration between pulses affects

detector sensitivity, an MP512-EPI was irradiated with dose rates ranging from 100 to 600 MU/min and 100 to 400 MU/min for 6 MV photon beams and 6 MeV electron beams, respectively. The set up for this experiment followed the reference conditions of a 10×10 cm^2 size field and SSD at 100 cm at D_{max} (1.5 cm) and z_{ref} (1.2 cm) for 6 MV photon beams and 6 MeV electron beams, respectively. By following the TRS-398 protocol, 1 MU was calibrated to a dose of 1 cGy to deliver a water equivalent material at the reference condition [37]. According to this protocol, the dose rate (MU/min) measurements corresponded to dose rate from 100 cGy/min to 600 cGy/min. The sensitivity of MP512-EPI at a particular dose rate was averaged for four central pixels and average sensitivity was normalised to the maximum dose rate for both energies.
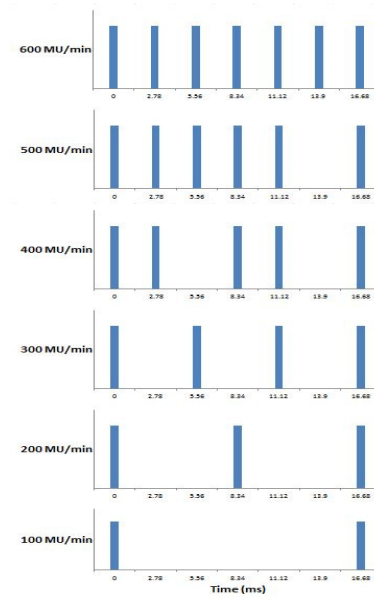
Figure 4.8: The dose rate time-sequence of 6 MV photons for Varian Clinac IX.

4.2.8. Dose per pulse (DPP) dependence

Dose per pulse (DPP) is an integration of the instantaneous dose rate over the pulse width. Co-60 is a continuous beam that is equal to the instantaneous dose rate and the average dose rate. A LINAC delivers radiation in a pulse beam series with a high instantaneous dose rate. The silicon diode is sensitive to dose per pulse so there is some concern when

a silicon diode is used for measurements in a LINAC machine [65][216]. The DPP decreased as the SSD increased. The nominal energies of 6 MV x-ray beam (Varian Clinac iX) were used to study the dose per pulse dependence on the sensitivity of a silicon diode. The front of the detector array was perpendicular to the horizontal radiation beam (gantry 90°) at a 1.5 cm depth (d_{max}) and with a 10 cm solid water slab behind for full back scattering (Figure 4.9). The MP512-EPI was irradiated using a 10×10 cm^2 beam and by varying the SSD from 100 cm to 370 cm. The frequency pulse timing for 6 MV photon beams for the Varian accelerator was 360 Hz, giving a dose per pulse ranging from 2.78×10^{-4} to 0.21×10^{-4} Gy/pulse. The thimble ionisation chamber Farmer 0.6 cm^3 (NE2571) was used for comparison under the same conditions. Charges from the ionisation chamber were measured using a PTW UNIDOS electrometer with a supply voltage of -300 volts (V). The MP512-EPI sensitivity (pC/Gy) S was a ratio of the charge collected (pC) from an average of the four central pixels of MP512-EPI per unit absorbed dose (Gy) as measured by the ionisation chamber at the same SSD (Equation 4.1). The dose per pulse response was calculated by normalising the sensitivity ratio at any SSD to the detector sensitivity at SSD 100 cm (2.78×10^{-4} Gy/pulse) (Equation 4.2) [218].

$$S_{SSD} = \frac{(M512\ response)_{SSD}}{(Dose)_{SSD}} \tag{4.1}$$

$$DPPresponse_{SSD} = \frac{S_{SSD}}{S_{100}} \tag{4.2}$$
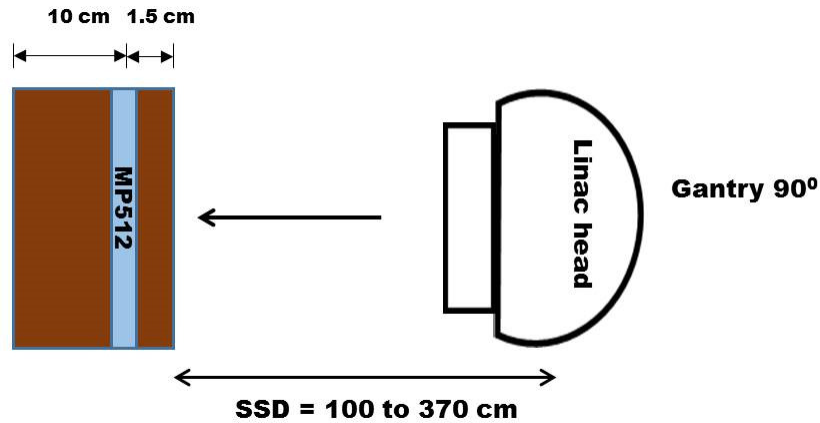
Figure 4.9: A schematic of the gantry angle orientation for measuring dose per pulse.

4.2.9. Output factor for small field size

The output factors are defined as a dose for a particular field size ratio to the dose from the reference field size of 10×10 cm^2 [50]. The output factors decrease as the field size decrease and decrease even faster in a small field due to lateral electron disequilibrium, source occlusion, and detector perturbation. The output factor measured by the detector in small radiation fields is a function of the averaging effect of the sensitive volume and the electronic density of the surrounding material [219]. The output factors were measured at a depth of 10 cm RMI 457 solid water phantom and fixed SSD at 90 cm (Figure 4.10). The detector array was irradiated on 6 and 10 MV photon beams with fixed 100 MU and a dose rate of 600 MU/min. The detector array was irradiated using open square fields ranging from 10×10 cm^2 down to 0.5×0.5 cm^2. To avoid the dose averaging volume effect the response of the central pixel (0.5×0.5 mm^2) at specific field size was used to calculate the output factors by comparing the OF measured with the MO*Skin* and gafchromic EBT3 film measurements under the same conditions.

Figure 4.10: The MP512-EPI in the output factors measurement setup.

4.2.10. Angular response

The MP512-EPI is a planar detector array whose active sensitivity consists of a monolithic substrate. This configuration is mainly concerned with the angular response when the beam is not perpendicular to the detector (Refer to Chapter 3)[220][221]. In this study, the angular response of MP512-EPI was under the same orientation discussed in Chapter 3 where irradiation was carried out by rotating the gantry from 0° to 180° at increments of 10° and finer increments of 1° at incidence beam angle of 90°±10° using a 10×10 cm^2 square field. The response at a particular angle was normalized to the detector response at an incidence beam angle of zero. The results were compared to the MP512-Bulk in order to understand how substrate affects the angular response.

4.2.11. Segment linearity

Step and shoot IMRT is a series of low MU delivery where the maximum segment is approximately 15 segments per each field [48], therefore the innovation detector is used as a verification dosimeter and the measured linearity of segmental beam delivery should

be investigated. An MP512-EPI was placed at a depth of 1.5 cm of a water equivalent solid phantom and full backscatter, fixing the SSD at 100 cm. A series of 10×10 cm^2 beams were carried out at a dose rate of 600 MU/min. The constant dose of 50 MU was irradiated by varying the segments from 1 to 25; the MP512-EPI response for each segment was normalised to the one segment of 50 MU deliveries.

4.2.12. Long-term reproducibility

This experiment set out to estimate the long term sensitivity and stability of MP512-EPI over 12 months with the average dose of photons of 500 Gy. Irradiation was measured after pre-irradiation at 60 kGy and was repeated for one to twelve months. In this experiment an MP512-EPI was placed at a depth of 1.5 cm in a solid water phantom and delivered a fixed beam of 10×10 cm^2 with 100 MU and at a dose rate of 600 MU/min; the SSD was fixed at 100 cm, and all the measurements used 6 MV photon beams. The response from an average of four central pixels was normalised to the primary irradiation time using the uncorrected calibration factor; standard deviation was calculated using five consecutive exposures.

4.2.13. Measuring the cross plane profiles

The cross plane profiles of MP512-EPI were measured in a solid water phantom at a depth of 10 cm. The central pixel of the detector array was aligned perpendicular to the central axis of the beam, and the set up position was tuned with a 0.5×0.5 cm^2 beam. 6 MV photon beams irradiated a series of small fields collimated by the jaw from 1×1 cm^2 to 4×4 cm^2 with a constant dose rate of 600 MU/min and a fixed 100 MU. In this study the MLC was completely retracted from the irradiation fields. The central beam profiles of MP512-EPI were evaluated with reference to gafchromic EBT3 films in terms of full width and half maximum (FWHM) or at a 50% isodose and penumbra region (20%-80%

isodose). The EBT3 films were cut into 7×7 cm^2 sizes and performed under the same conditions. Each film was scanned by the Microtrex ScanMaker i800 flatbed scanner with 48-bit depth of colour and a spatial resolution of 72 dpi (equivalent to a pixel size of 350 µm). The difference in the FWHM between MP512-EPI and EBT3 films was calculated as shown by the equation below.

$$\Delta FWHM = \frac{MP512 - EBT_3}{EBT_3} x100\%$$ (4.3)

4.3. Results

4.3.1. I-V Characteristics

Figure 4.11 shows the I-V characteristics of selected diodes of MP512-EPI in the function of logarithmic scale reverse current (pA) and reverse voltage (V). This characteristic was measured before irradiation and then compared to post irradiation for each pixel. With non-irradiation, the I-V curves show that the current has increased rapidly as the voltage increased until it reached approximately -10 V after which it continued to increase slowly. The I-V curves showed a breakdown voltage of approximately of -58 V. Increased radiation led to an increase in the leakage current of the diode but there was a large variation between the non-irradiated and an irradiated 2 Mrad (20 kGy). However, this increased dose of radiation after a 20 kGy did not effect the leakage current. I-V curves also exhibited a small variation for all selected diodes, whereas the MP512-EPI had excellent uniformity and a slight variation between each irradiated diode at the same accumulated dose (Figure 4.12).
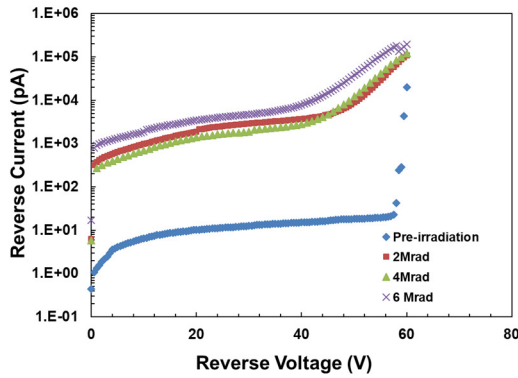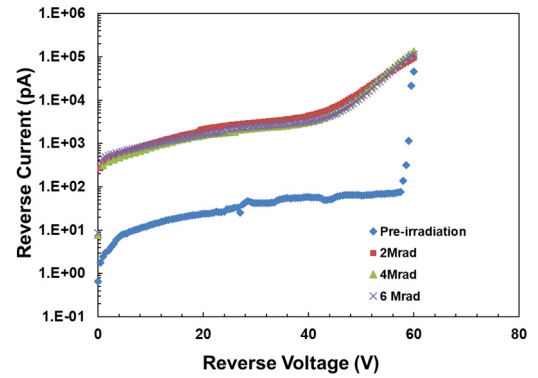
(a) channel 16

(b) channel 28
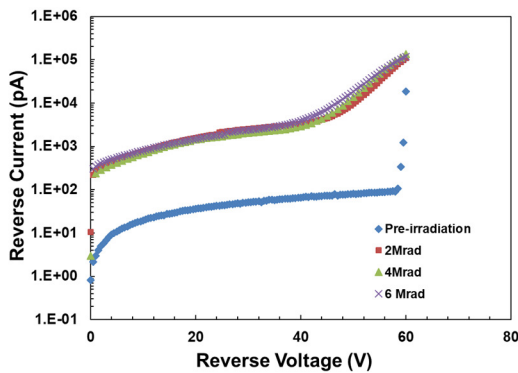
(c) channel 41
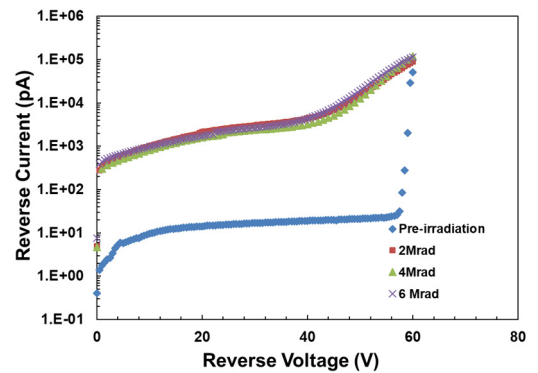
(d) channel 153
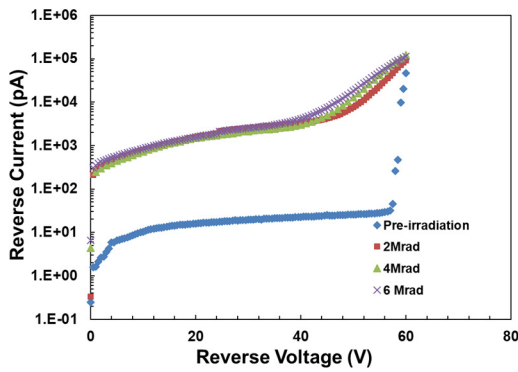
(e) channel 155
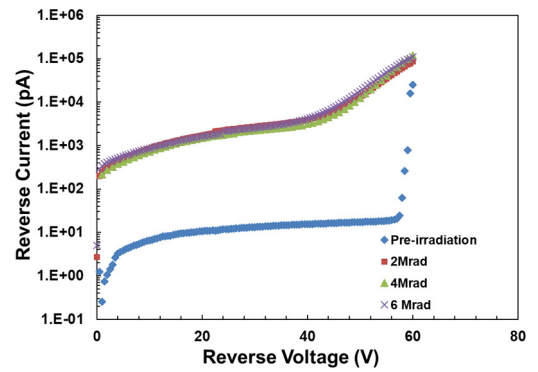
(f) channel 163

Figure 4.11: Leakage current measured in reverse direction on selected channels of MP512-EPI comparison between prior-irradiation and after irradiation.
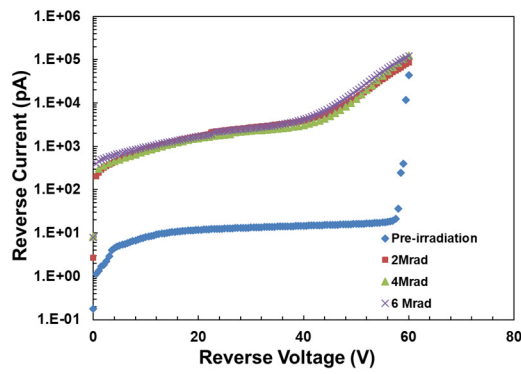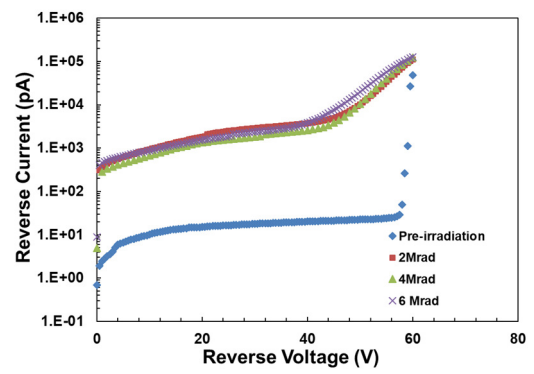
(g) channel 224

(h) channel 288
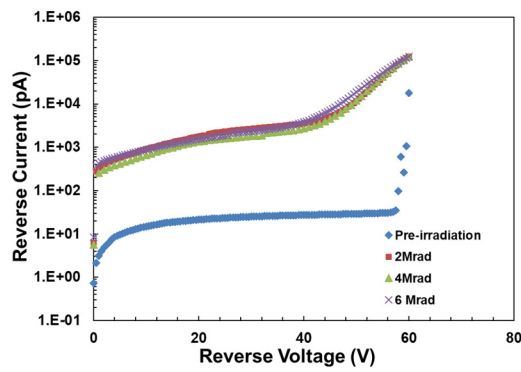
(i) channel 299
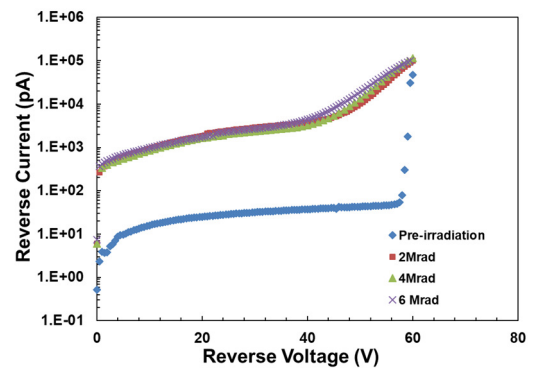
(j) channel 334
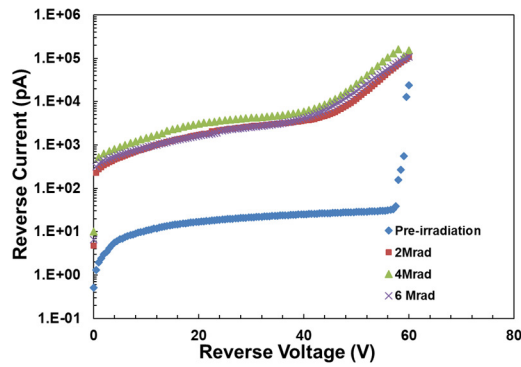
(k) channel 351
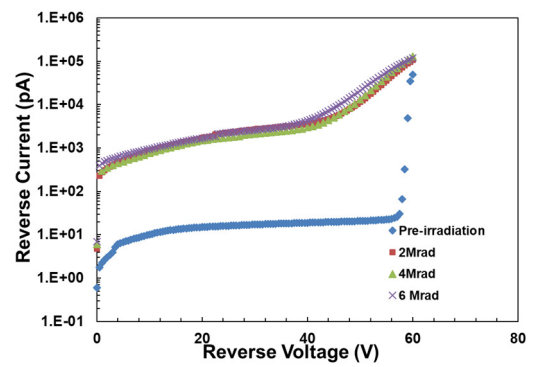
(l) channel 363

Figure 4.11: Leakage current measured in reverse direction on selected channels of MP512-EPI comparison between prior-irradiation and after irradiation.
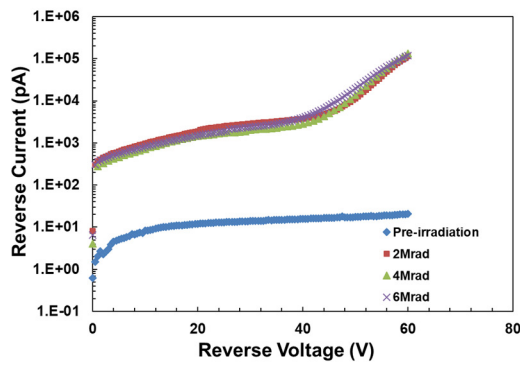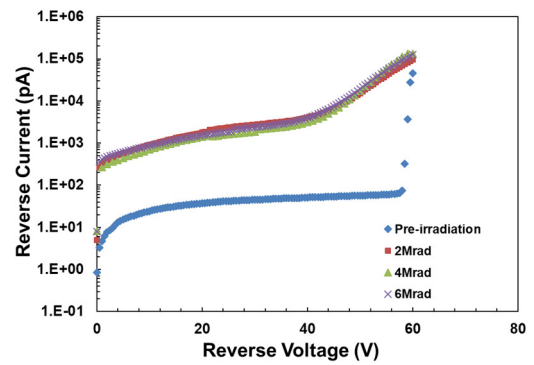
(m) channel 441   (n) channel 454

Figure 4.11: Leakage current measured in the reverse direction on selected channels of MP512-EPI comparison before and after irradiation.
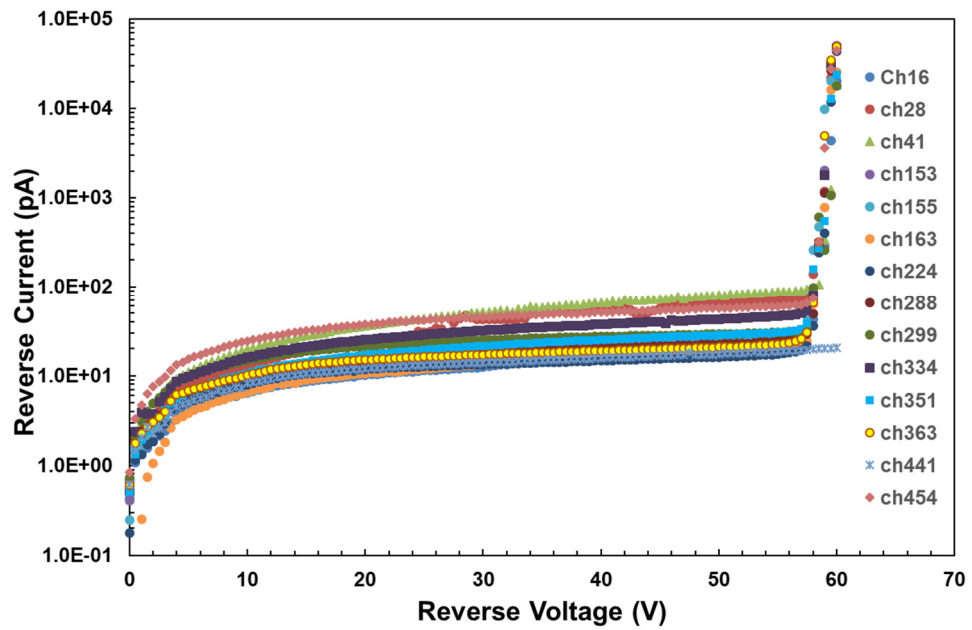
(a) Prior-irradiation

Figure 4.12: The results of I-V characteristic comparison of each channel for (a) Prior irradiation, and (b) After 20 kGy irradiation.
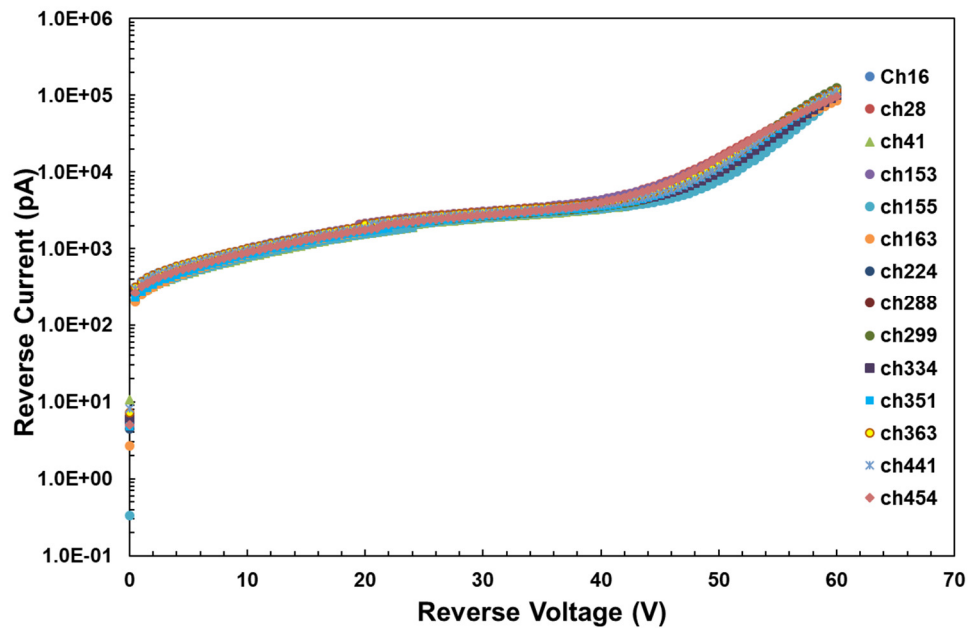
(b) After 20 kGy dose of irradiation

Figure 4.12: The results of I-V characteristic comparison of each channel for (a) Prior irradiation, and (b) After 20 kGy irradiation.

4.3.2. Radiation hardness

Figure 4.13 shows the response of MP512-EPI and MP512-Bulk as a function of relative sensitivity and accumulated dose of radiation. The error bar represents the ±1SD of five repeated measurements (<2%). The sensitivity of MP512 dropped rapidly after irradiation with 10 kGy, while stability after irradiation with 20 kGy was then obtained. The detectors fabricated on a thin p-Si epitaxial layer with a high resistivity of 100 Ω cm (MP512-EPI) show a higher constant sensitivity than the detectors fabricated at a low resistivity of 10 Ω cm p-Si (MP512-Bulk). The response of MP512-EPI decreased less than 3% and was constant within 0.3% after a given dose of 40 kGy. The MP512-EPI demonstrated excellent sensitivity and stability after pre-irradiation with a sensitivity

degradation of 0.3%/10 kGy while the degradation response of MP512-Bulk was 5%/10 kGy.
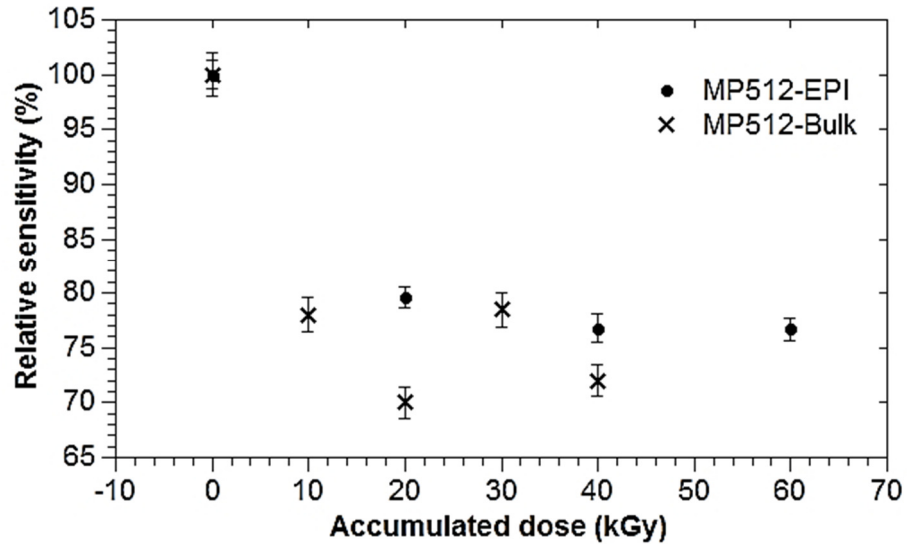
Figure 4.13: The relative sensitivity of MP512- Bulk and MP512- EPI as a function of the accumulated dose for Co- 60 gamma source, normalised to a zero dose response.

4.3.3. Percentage depth dose (PDD) measurement

Figure 4.14 shows a good agreement of percentage depth dose (PDD) for 6 and 10 MV photon beams between MP512-EPI and CC13, Markus chamber, and MP512-Bulk. The PDD curves measured by MP512-EPI were slightly lower than those measured with CC13 and MP512-Bulk. The maximum discrepancy between MP512 and IC for 6 MV beams was approximately 1.5% and 0.8% at a depth of 30 cm for MP512-EPI and MP512-Bulk relative to Dmax. Similar variations occurred when 10 MV beams were measured relative to Dmax; here the maximum discrepancies were 1.3% and 1% for MP512-EPI and MP512-Bulk. These results are commensurate with their dose per pulse response and are easy to correct, and the discrepancy is within allowable error of ±2%.

(a)   (b)
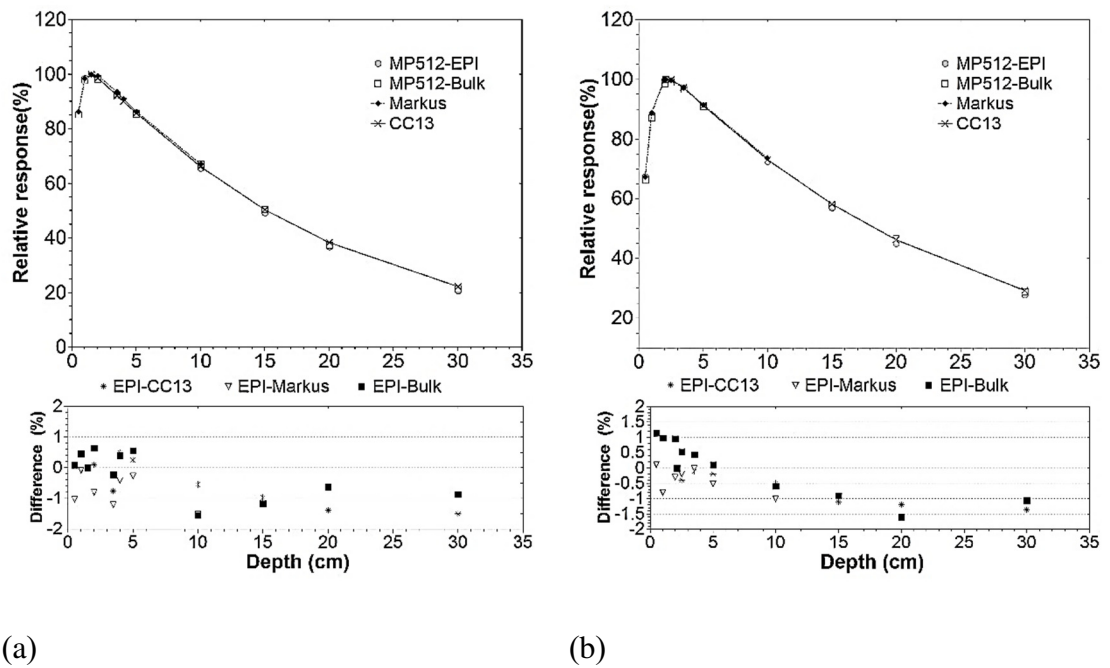
Figure 4.14: Percentage depth dose measurement of MP512 compared to the Markus and CC13 ionisation chambers for (a) 6 MV and (b) 10 MV photon beams.

4.3.4. Dose linearity

The response of MP512-EPI at doses ranging from 1 to 500 MU show an excellent linearity for the 6 MV and 10 MV photon energies, and the regression coefficient r^2 is almost equal to 1 (Figure 4.15). The linearity of MP512-EPI in this study had the same trend as the MP512-Bulk, as presented in Aldosari *et al* study [170].
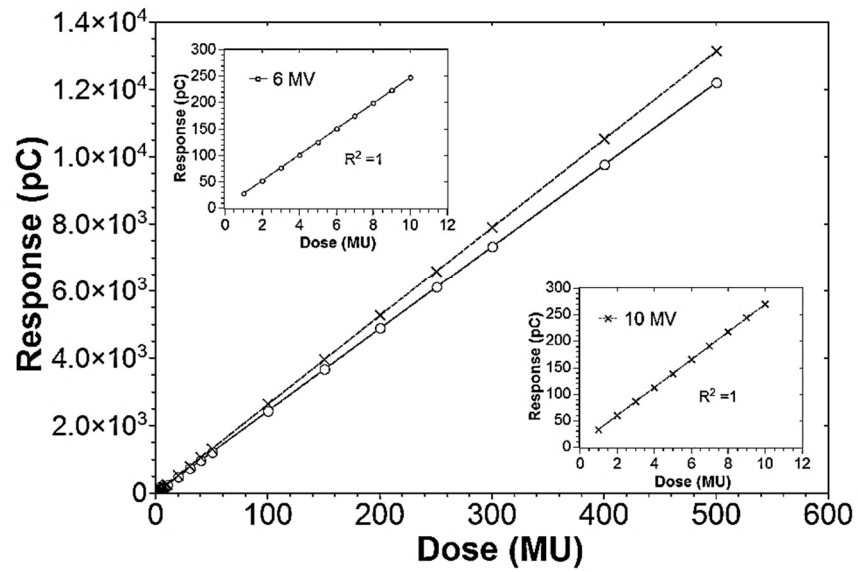
Figure 4.15: The average response of four central pixels of MP512-EPI as a function of the accumulated dose (MU).

4.3.5. Dose rate (MU/min) dependence

The change in MP512-EPI sensitivity as a function of the dose rate (MU/min) is shown in Figure 4.16; the error bar indicated the uncertainties after measuring the (1SD) five times. The maximum variation was within ±0.5% for the 6 MV photon and 6 MeV electron energies; this means the MP512-EPI response is independent of dose rate for the clinically relevant MU/min.
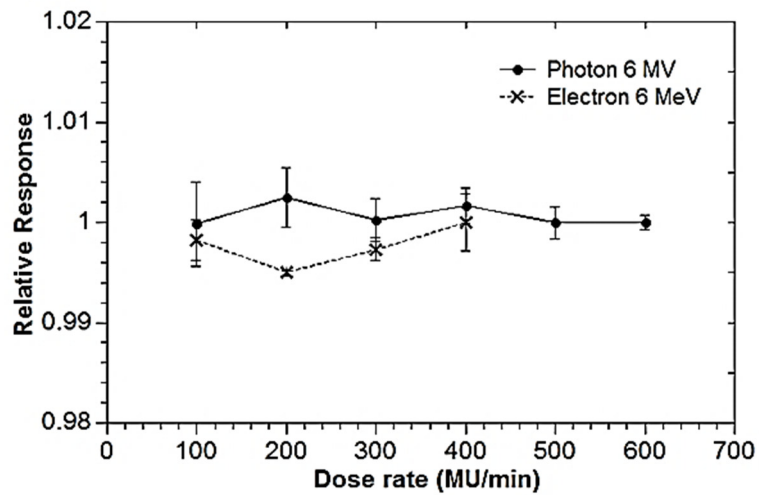
Figure 4.16: Variation of MP512-EPI response as a function

of the dose rate $(\mathrm{MU/\,min})$ for 6 MV photon and 6 MeV

electron beams.

4.3.6. Dose per pulse (DPP) dependence

Figure 4.17 shows the variation of detector sensitivity (pC/Gy) as a function of the dose

per pulse of MP512-Bulk and MP512-EPI at 6 MV with an average uncertainty of five

times the measurements was ± 2% (1SD). The sensitivity response decreased as the dose

per pulse of both detectors decreased. The MP512-EPI fabricated at a high resistivity of

a 100 Ω cm p-Si epitaxial layer had a reduced sensitivity of up to 8% while the MP512-

Bulk fabricated at a low resistivity 10 Ω cm p-Si had a reduced response of approximately

3% at a dose per pulse change of 10 times (at a minimum dose per pulse of 2.11×10^{-4}

Gy/pulse or SSD 370 cm). However, this reduction in sensitivity is within ±2% for both

detector arrays at a clinically relevant distance (SSD less than 150 cm).
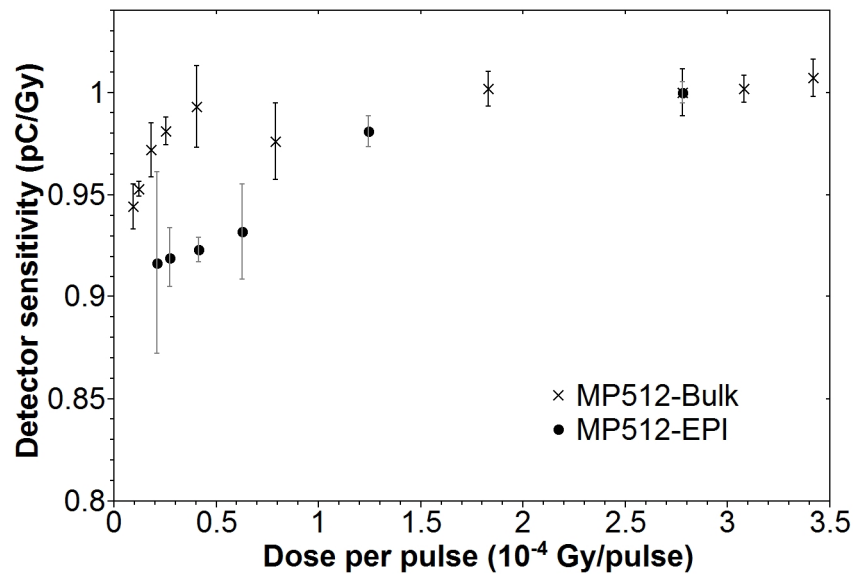
Figure 4.17: Sensitivity response of MP512-Bulk and MP512-EPI detectors as a function of dose per pulse for 6 MV photon beam. These responses were normalised to a dose per pulse of 2.8×10^{-4} Gy/pulse at the source to a surface distance of 100 cm.

4.3.7. Output factor for small field size

Figure 4.18 shows the output factors measured by MP512-EPI and MP512-Bulk compared to the MO*Skin* and gafchromic EBT3 films for 6 and 10 MV photon beams. The results show an excellent agreement within ±2% and ±3% for all field sizes ranging from 10×10 cm^2 down to 0.5×0.5 cm^2 for 6 MV and 10 MV photon energies. This is partially due to the small area of pixels of 0.5×0.5 mm^2 for MP512-EPI and a suitable optimised air gap above MP512-EPI.

(a)   (b)
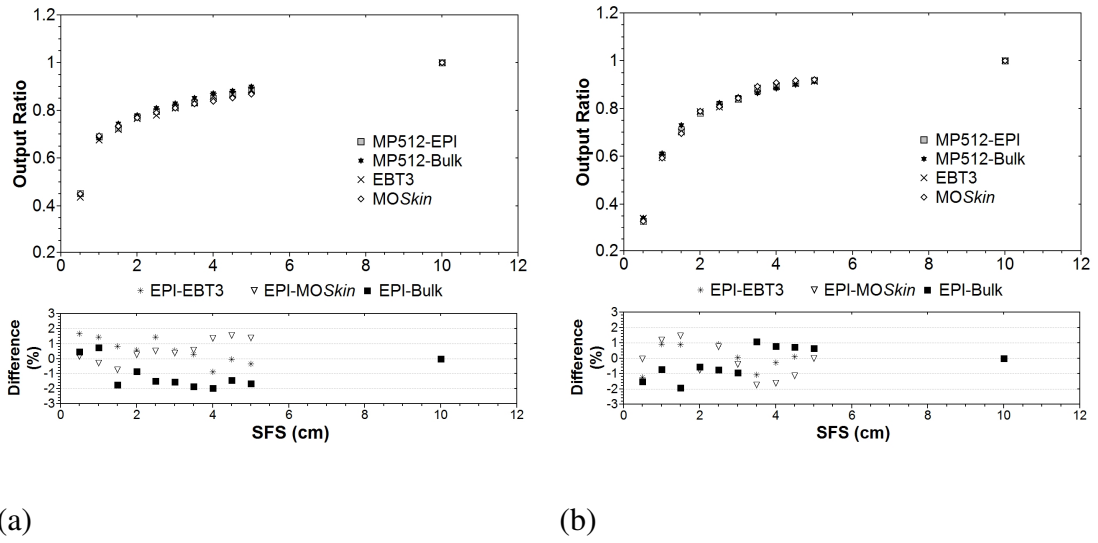
Figure 4.18: The output factors measured by MP512- EPI and normalised to a 10×10cm^2 field radiation compared to those measured by MP512- Bulk, MO*Skin* and EBT3 film for (a) 6 MV and (b) 10 MV photon beams.

4.3.8. Angular response

The angular response of MP512-EPI decreased as the incident beam angle decreased due to their intrinsic configuration and material; this resulted in a difference in attenuation and a scattering of photons and electrons that reached the active volume of the pixels while irradiating from different directions. Figure 4.19 and Figure 4.20 show that the relative angular response has normalised to the incident angle zero for MP512-EPI and MP512-Bulk as the incident beam angle increased from 0° to 180°. The angular response of both detectors was similar, with any difference being between ±2% (Figure 4.20). Maximum variation relative to incident beam angles of 17.55±0.32% and 16.11±0.40% were present at incident beam angles between 90° to 100° for 6 MV and 10 MV photon beams. The angular response depends on photon beam energy, as shown in Figure 4.19, as determined by the difference in the photon and electron scattering conditions.
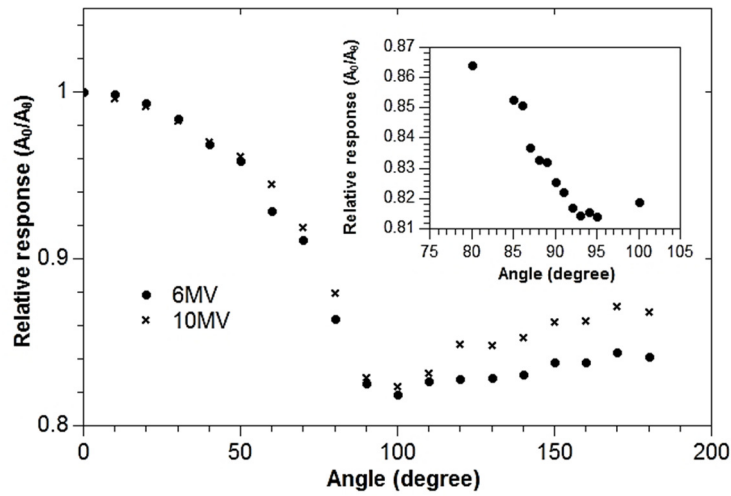
Figure 4.19: A comparison of the average response of four central pixels between 6 and 10 MV photon beams for MP512-EPI.

(a)   (b)
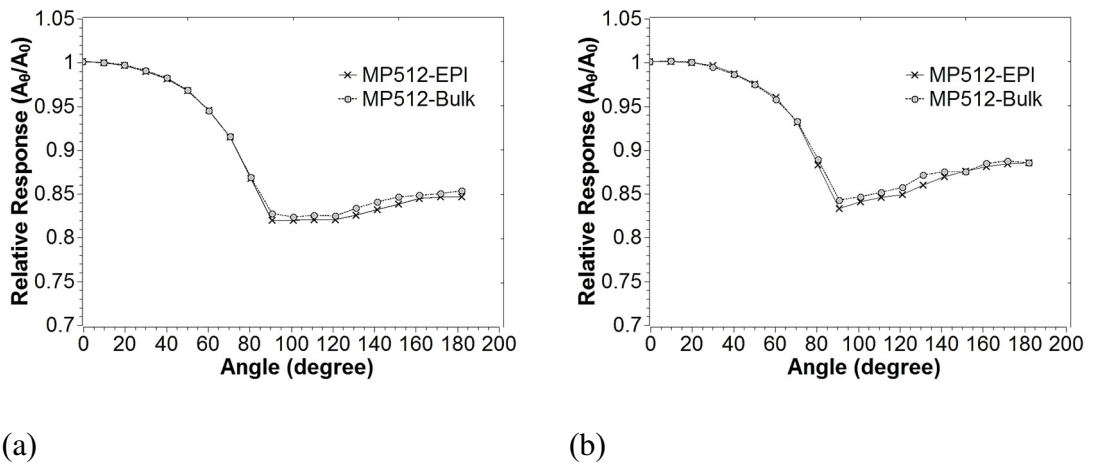
Figure 4.20: A comparison of the average response of four central pixels between MP512-EPI and MP512-Bulk for (a) 6 MV and (b) 10 MV photon beams.

4.3.9. Segment linearity

Figure 4.21 shows the response of MP512-EPI as a function of the dose segments of a constant 50 MU dose where the response increased with increasing irradiation segments. With segments of 2 MU or larger, MP512-EPI responded within ±2%. Figure 4.22 shows

the signal (pC) from the central pixel acquired during segmental beam irradiation where MP512-EPI had excellent uniformity and a repeatable dose response even after delivery with a low MU and large segments.
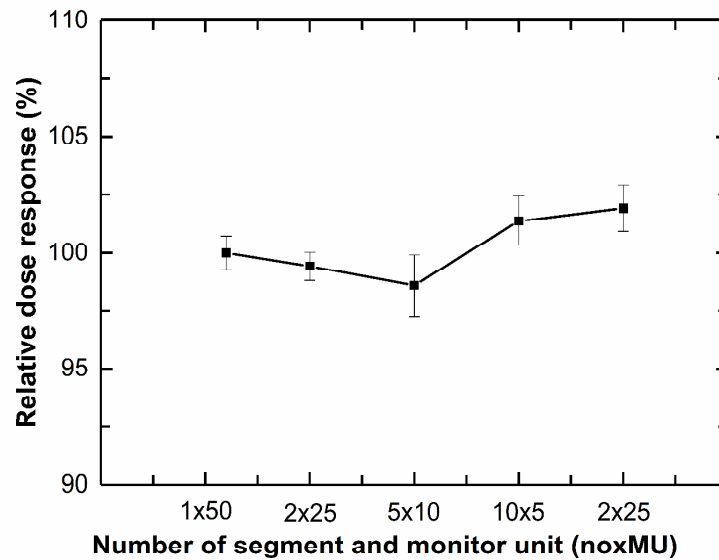
Figure 4.21: The response of MP512-EPI as a function of a segmental monitor unit (MU) normalised to 1×50 MU.

4.3.10. Long-term reproducibility

Figure 4.23 shows the relative sensitivity of MP512-EPI as a function of time measurements where sensitivity remained stable after photon irradiation up to 500 Gy over a period of 12 months. The change in reproducible sensitivity was within ±0.9%, with two standard deviations of 0.03; this result indicates that MP512-EPI could be used without recalibration for one year.

(a)

(b)

(c)

(d)

(e)
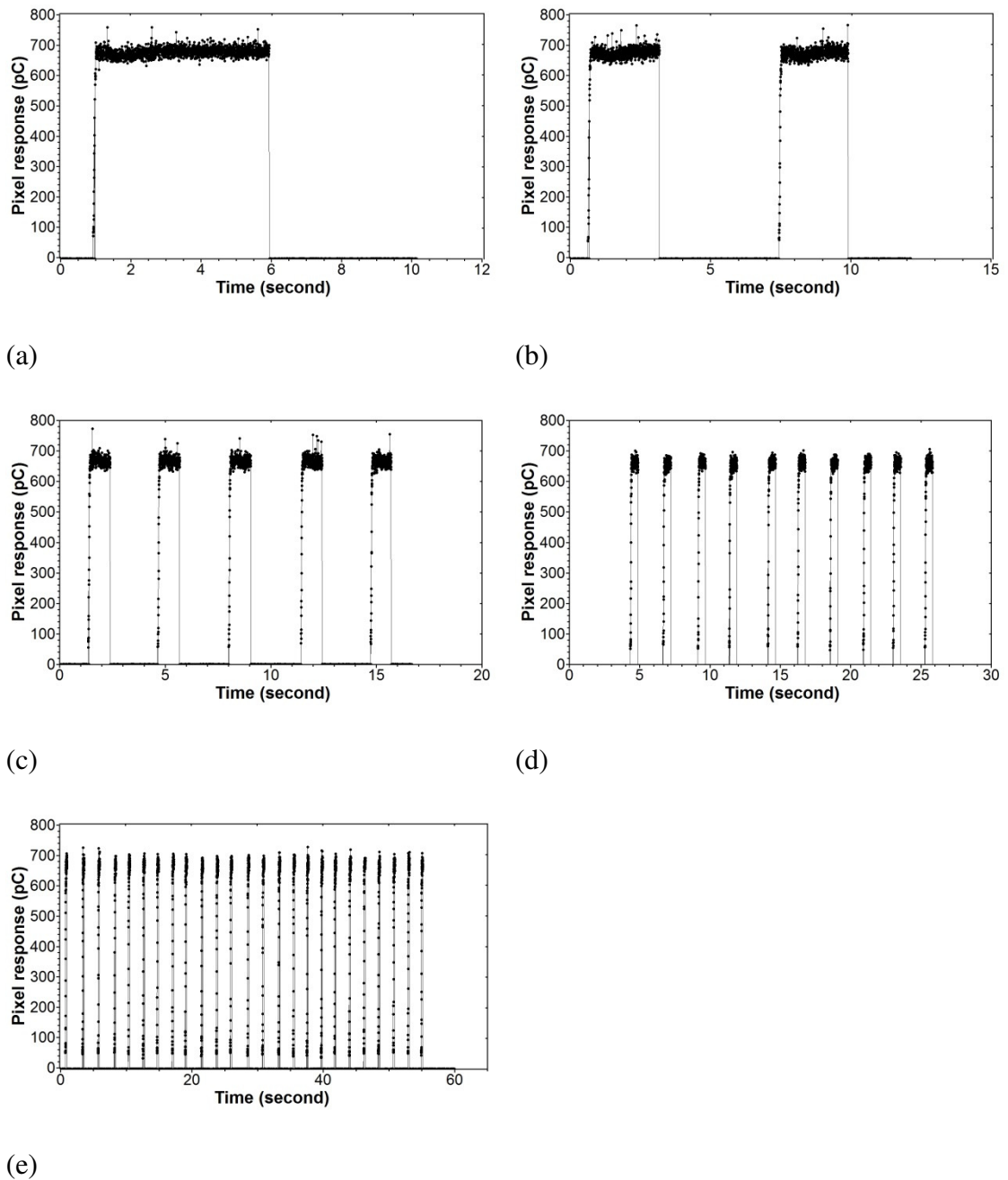
Figure 4.22: The response of MP512-EPI from the central pixel during segmental beam irradiation as a function of acquisition time; (a) One segment with 50 MU each, (b) Two segments with 25 MU each, (c) Five segments with 10 MU each, (d) Ten segments with 5 MU each, and (e) Twenty five segments with 2 MU each.
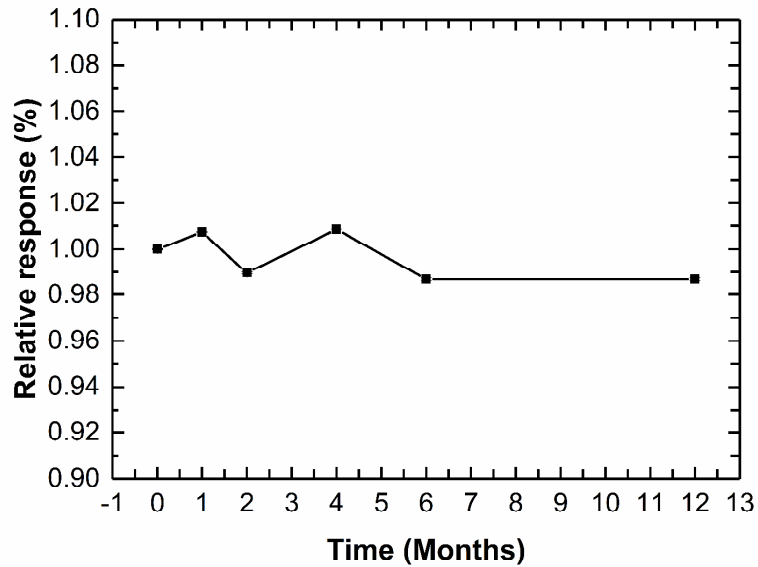
Figure 4.23: The average response of four central pixels of MP512-EPI as a function of time (months) normalised to the first acquisition after pre-irradiation of 60 kGy. The standard deviation is smaller than the marked symbol.

4.3.11. Measuring the cross plane profiles

Figure 4.24 and Figure 4.25 shows half of the cross plane profile measured by MP512-EPI and gafchromic EBT3 film for field sizes ranging from 1×1 cm^2 to 4×4 cm^2. These illustrations show more detailed resolutions. The cross plane profiles for 6 MV photons have excellent agreement between the MP512-EPI and EBT3 films within ±1% and 0.6 mm for FWHM and the penumbra region. These results are similar to the MP512-Bulk presented in a previous study. The cross plane profiles for 10 MV photons show a slight overestimation of FWHM, with a different value for a 1×1 cm^2 field of up to 1.5%, however the difference for the penumbra region is still within 0.6 mm; this percentage difference decreases as the field size increases. The FWHM, penumbra width and percentage differences are summarised in Table 4.1.

Table 4.1: The FWHM and penumbra width measured by MP512-EPI and gafchromic EBT3 films

Field size (mm)	6MV						10MV					
	EBT3		MP512-EPI		Differences		EBT3		MP512-EPI		Differences	
	FWHM (mm)	Penumbra (mm)	FWHM (mm)	Penumbra (mm)	FWHM (%)	Penumbra (mm)	FWHM (mm)	Penumbra (mm)	FWHM (mm)	Penumbra (mm)	FWHM (%)	Penumbra (mm)
10	9.95	2.43	10.04	2.95	0.94	0.52	10.18	2.83	10.34	3.37	1.57	0.53
20	19.95	2.85	30.02	3.35	0.33	0.50	19.86	3.43	20.13	3.72	1.40	0.29
30	29.91	3.13	29.95	3.66	0.14	0.53	29.92	4.01	30.11	4.58	0.65	0.57
40	39.94	3.23	39.99	3.84	0.15	0.60	40.06	4.30	40.20	4.87	0.36	0.57
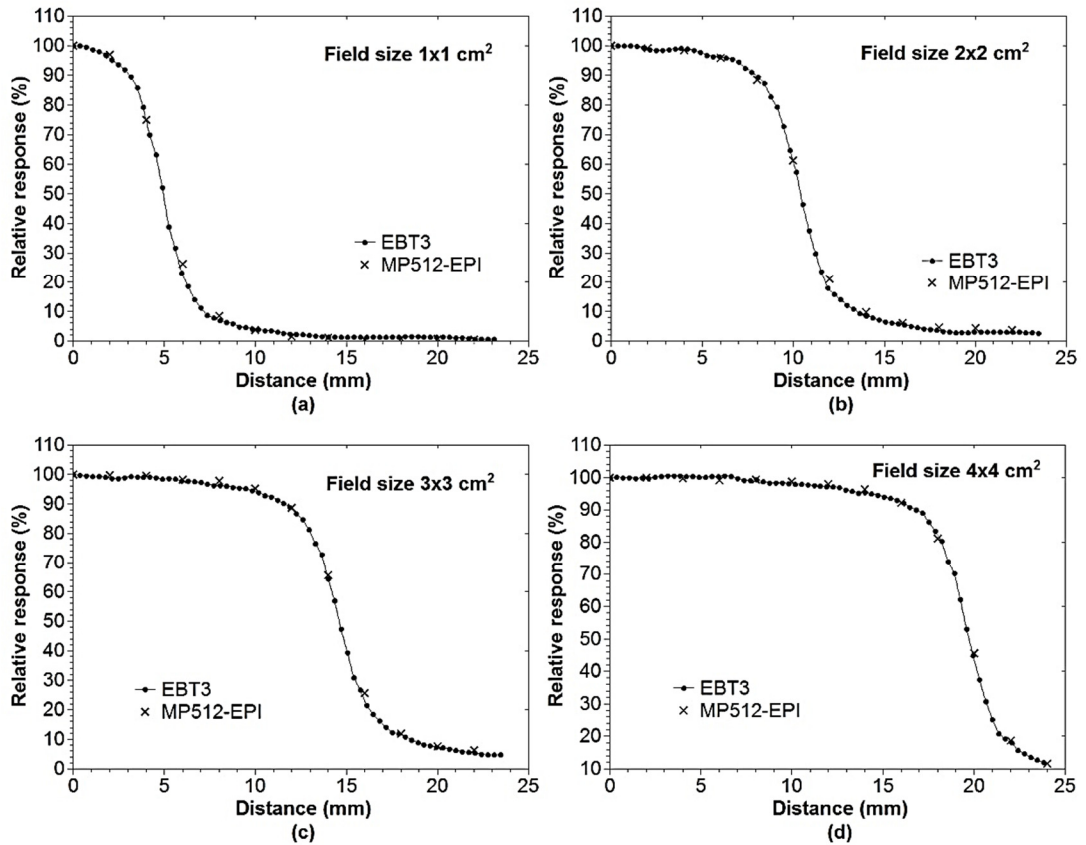
Figure 4.24: Cross plane profiles measured by MP512-EPI and EBT3 film for 6 MV photon beams; (a) field size 1×1 cm^2, (b) 2×2 cm^2, (c) 3×3 cm^2 and (d) 4×4 cm^2.
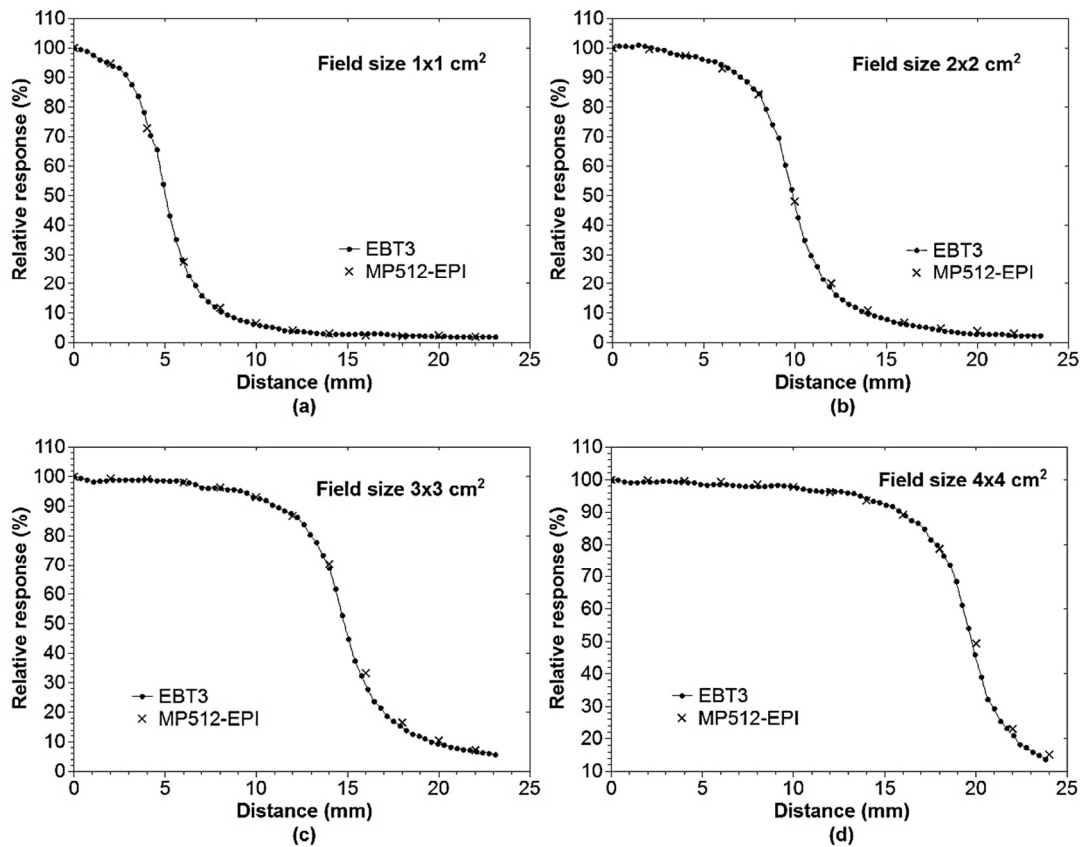
Figure 4.25: Cross-plane profiles measured by MP512-EPI and gafchromic EBT3 film for 10 MV photon beams; (a) field size 1×1 cm², (b) 2×2 cm², (c) 3×3 cm² and (d) 4×4 cm².

4.4. Conclusions

A 2D monolithic detector array MP512-EPI was developed and characterised by re-grading the radiation hardness, long term stability, PDD, dose per pulse measurement, output factor, dose linearity, angular response, cross plane profiles and segment linearity using 6 MV and 10 MV photon beams and 6 MeV electron beams for the dose rate response. The MP512-EPI characteristics demonstrated the usefulness of detector arrays as a quality assurance tool for radiation therapy. The detector's high spatial resolution of 2 mm and small active area of 0.5×0.5 mm² means it can be used in small field measurements without the effect of radiation perturbation from averaging volume

measurement. Moreover, silicon substrate resistivity and the thickness of an active silicon layer from which a charge is collected will determine the dosimetric response of MP512. A modified detector with epitaxial technology improved its long term stability and sensitivity with an accumulated dose of approximately 0.3%/10 kGy, unlike the MP512-Bulk fabricated on bulk silicon (5%/10kGy). This is because the initial diffused length of electrons in 100 Ω cm epi layer is longer than the 35 µm thick epitaxial layer. Degradation of the diffused length does not inherently depend on the collected charge until the diffused length is less than 35 µm. In the MP512-Bulk, any deterioration of the diffused length creates a deficit in charge collection, so the trade off is a higher variations of dose per pulse for an MP512-EPI pre-irradiated with 60 kGy compared to a MP512-Bulk pre-irradiated with 40 kGy. However, at a typical treatment distance corresponding SSD <150 cm (fixing source to iso-centric, SAD setup) and for all beam angles, the sensitivity of MP512-EPI and MP512-Bulk in terms of their dose per pulse varies within ±2%, although MP512-EPI provides good long term stability over a 12 month period or photon irradiation up to 500 Gy; these good characteristics means this detector does not need frequent recalibration.

The output factor measured by MP512-EPI with 0.5 and 1 mm thick air gaps above the detector surface for 6 and 10 MV photon beams, respectively, agreed with gafchromic EBT3 film and MO*Skin* within ±2% for 0.5×0.5 cm^2 fields, unlike in the previous study where MP512-Bulk had a 1.2 mm thick air gap for 6 MV photon beams had an over response of approximately 4% for fields less than 1×1 cm^2 [170]. This was partially due to 0.5×0.5 mm^2 area of pixels and the optimised air gap above MP512. The predominant electron scatter in the silicon diodes cause increased sensitivity to a small field size compared to the reference field because the density relative to water was higher [222]. Overestimating the diode detector due to a small field size can be mitigated by

providing a wide enough air gap above the detector, the wide of this air gap depends mainly on the design of the diode detector [223].

The packaging and intrinsic asymmetry of the 2D monolithic detector array MP512 affects its intrinsic angular dependence [220][221]. The angular response of MP512-EPI fabricated on an epitaxial layer with a high resistivity of varied by ±2% when compared to the low resistivity bulk subtract (MP512-Bulk); this means the angular response of MP512 is independent of its resistivity and substrate type bulk or epitaxial.. The angular correction factor must be applied where the detector is not perpendicular to the radiation beam in order to deliver accurate pre-treatment measurements (refer to **Chapter 3**). The MP512-EPI demonstrated excellent dose linearity for small mu range (1-10 MUs) and large dose range (10-500 MUs); it also responded very well to the dose segments, especially large segments and small MUs (25×2 MU) within ±2%. This result confirms that MP512-EPI is a suitable verification tool for step and shoots and dynamic IMRT. Conventional radiotherapy usually delivers dose rates from 100 to 600 MU/min, whereas advanced treatment machines such as True beam (Varian) which deliver beams using flattening filter free or Cyberknife, deliver dose rates of approximately 800 MU/min up to 2400 MU/min [24][224]. Although the dose rates range from 100 to 600 MU/min, the measurements were within ±1%, which cannot conclude that MP512-EPI can provide stable response at dose rates that are higher than 600MU/min. Further study of dose rates and doses per pulse is warranted, particularly for flattening filter free beams.

A high resolution MP512-EPI (2 mm) was needed to measure small fields of 1×1 cm^2 with an acceptable value in FWHM and the penumbra region for clinical use [60], whereas this study only investigated the sizes of simple square fields. Further study is needed using MP512-EPI in order to evaluate a patient qualification for small intensity

modulated treatment fields. A clinical QA using MP512-EPI in homogeneous and inhomogeneous phantoms will be presented in **Chapter 5**.

Chapter 5

Clinical implementation of a 2D monolithic epitaxial detector array for a small intensity modulated field

5.1. Introduction

SBRT is a complex treatment that uses the IMRT and VMAT technique with a high dose per fraction and a steep dose gradient. Verifying the dose is the major process needed to guarantee an accurate dose delivery to the patient. Pre-treatment QA or end-to-end test is used to verify treatment delivery, as well as calculating the treatment planning dose, the data transmission system from TPS to the linear accelerator, and the actual dose delivery [225]. The absolute dose and dose distributions of treatment planning are verified by comparing them with the actual dose measurements using a 1D, 2D, or 3D dosimeter. Several commercial 2D arrays have recently been used as a QA tool to measure the phantom such as MapCHECK (SunNuclear, Melbourne, Florida-USA), Octavius 1000 SRS (PTW-Freiburg-Germany) and MatriXX (IBA Dosimetry, Bartless, TN), but their 5 mm and 10 mm spatial resolutions are too coarse to detect any errors in the TPS, or the delivery system for small irradiation fields [226][225][227][102]. This lack of information can lead to an inaccurate treatment delivery. The MP512-EPI is designed for patient specific QA in small field treatments with a high spatial resolution of 2 mm pixel

pitch; a dosimetry characteristic that has proved it can be used as a quality assurance tool; as discussed in **Chapter 4**.

Although the MP512-EPI is angular dependent has a maximum deviation with respect to a zero angle up to 18% at a gantry incidence angle of 90°, the angular correction factor works well with cross-beam profiles between MP512-EPI corrected and gafchromic EBT3 films for small static irradiation beams down to 1×1 cm^2 fields within ±2%, as discussed in **Chapter 3**.

This chapter describes the clinical implementation of MP512-EPI as a patient specific quality assurance dosimeter for small intensity modulation fields of IMRT and VMAT delivery to a homogeneous and inhomogeneous phantom based on Pinnacle^3 version 14 treatment planning system (TPS). The planar dose reconstructions of MP512-EPI have verified a comparison to EBT3 film dose measurement and TPS calculation dose.

5.2. Materials and Methods

5.2.1. Two-dimensional monolithic epitaxial detector array (MP512-EPI)

The 2D monolithic epitaxial detector array used for the measurements was the MP512-EPI; it consists of 512 diode pixels over an area of 52×52 mm^2 with a high spatial resolution of 2 mm pixel pitch, as discussed in **Section 4.2.1.**

5.2.2. Data acquisition system (DAQ) and inclinometer

The MP512-EPI data acquisition system (DAQ) is based on a 64-channel analog front-end electrometer ASIC chip where each chip is interfaced to a quad analogue-to-digital converter (ADC). The ADC output is synchronised and the channel is de-randomised by

a field programmable gate array (FPGA) that also manages the synchronisation with the sync pulse of the LINAC to acquire the detector current discussed in **Section 3.2.2.** In this study, the inclinometer attached to the gantry stand utilised the angular correction of MP512-EPI during VMAT arc delivery for any gantry angle increment (Figure 5.1).

The ADIS16209 dual-axis digital inclinometer has 0.025° angular resolution and a very accurate measurement state within ±0.1° [228]. The inclinometer can operate at both single-axis (±180°) and dual-axis (±90°) using a standard power supply voltage of 3.3 V. The function block diagram of the inclinometer is shown in Figure 5.2. The inclinometer data of gantry rotation during irradiation was synchronised with the detector acquisition (ADC output) signal and de-randomised by FPGA using the same sync pulse of the LINAC. A schematic diagram of the DAQ system synchronised with the inclinometer is shown in Figure 5.3. Data acquisition is transferred via USB2.0 to the in-house software interface called Magic Suite version AFE_MP-512i. This software can store the inclinometer function and also display the instantaneous detector response for each gantry angle and integral detector for all the delivery angles (Figure 5.4). The acquisition data can be used for online and offline analysis and it can reset the parameter of the inclinometer in the actual experimental setup (Figure 5.5).

To validate the inclinometer measurement, the gantry angle measured was compared with the gantry angle indication stored by Varian MLC controller software. Gantry information is recorded in binary format every 50 minutes, and then exported to the DynaLog files that also contain essential treatment parameters such as the gantry angle, collimator angle, couch angle, jaw settings, and MU delivery and MLC leaf positions [229].
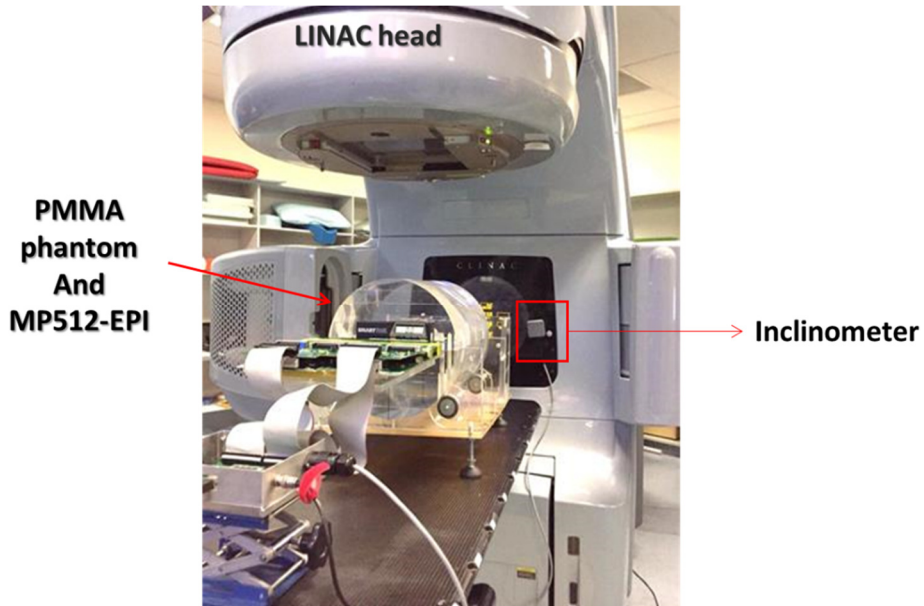
Figure 5.1: The CMRP phantom with the MP512-EPI inserted in the coronal plane and associated device, DAQ, and inclinometer**.**
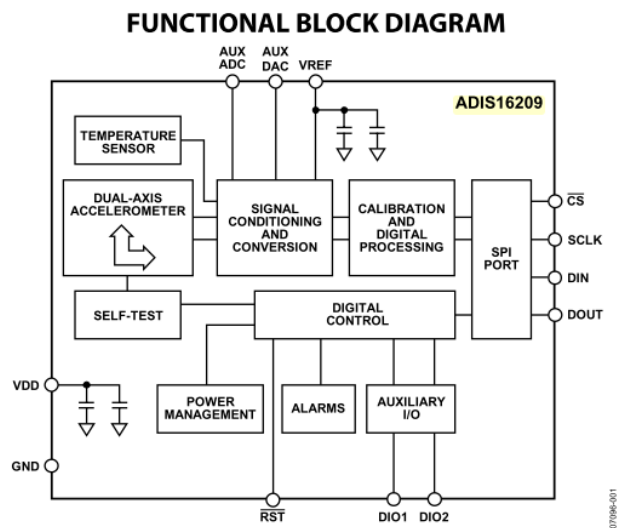
Figure 5.2: The function block diagram of ADIS16209 inclinometer [228].
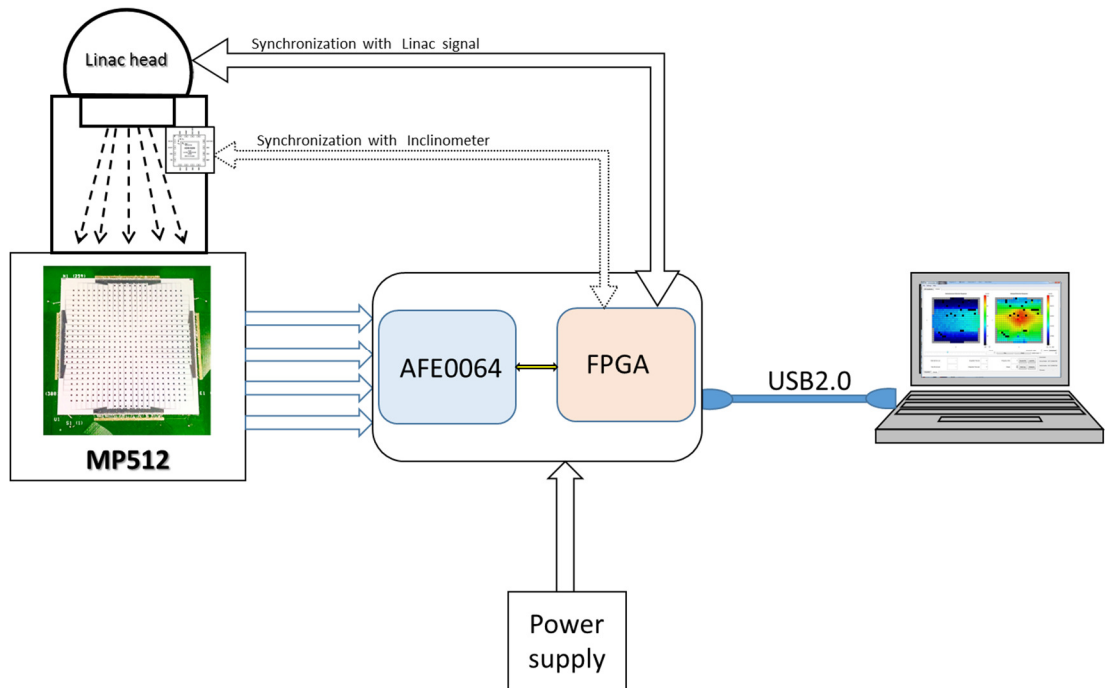
Figure 5.3: Schematic diagram of data acquisition system (DAQ) synchronised with the inclinometer.

(a)   (b)
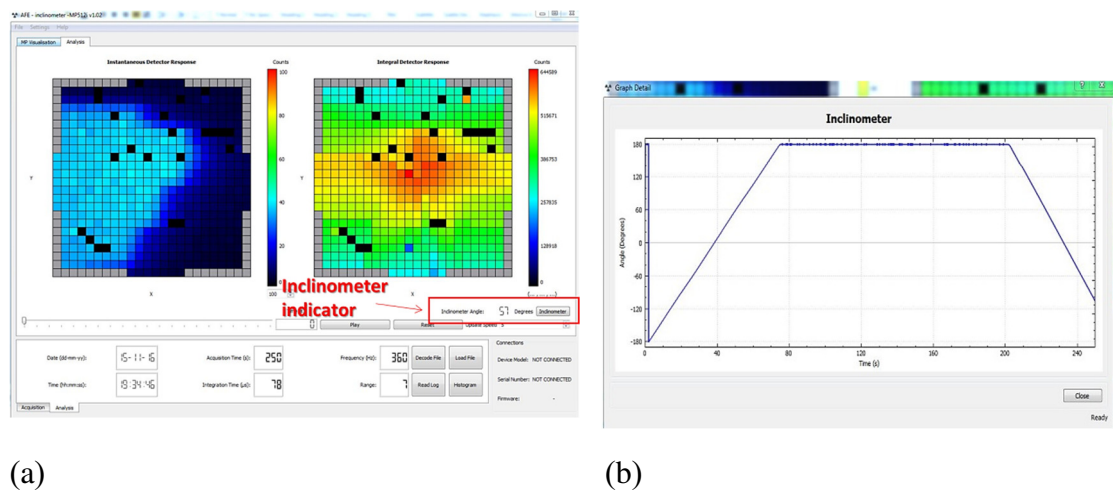
Figure 5.4: The software interface Magic Suite; (a) the inclinometer indicator and (b) the angle (degrees) as a function of time.
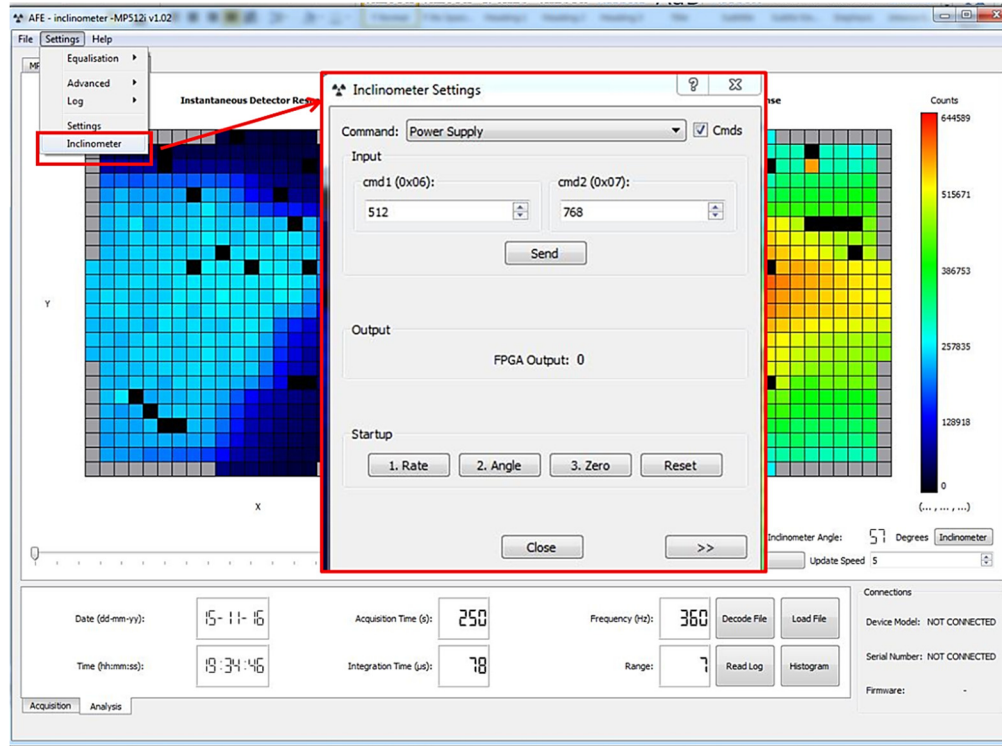
Figure 5.5: Inclinometer settings function

5.2.3. CMRP cylindrical phantom and insertions

The 30 cm diameter by 40 cm long CMRP cylindrical phantom was used to measure the clinical validation plans; it was designed and developed to fully verify an actual gantry beam delivery for IMRT and VMAT, where the phantom produced a PMMA density of 1.15-1.19 g/cm^3, as discussed in **Section 3.2.3.** This phantom has a 15.5×20.5×5 cm^3 central slot into which homogeneous and inhomogeneous holders can be inserted. Both holders were designed and developed in-house to allow the MP512-EPI detector and films to be positioned at the isocentre of the CMRP phantom.

5.2.3.1. Design and fabrication of the homogeneous insertion

The homogeneous holder was made from PMMA with the same specifications as the CMRP cylindrical phantom; it is 5 cm thick and has a 1 cm central cavity for an MP512-EPI and its packaging (Figure 5.6). The 18.5 cm length of the lower part of the holder

was designed to support the detector's electronic boarding to stop detector from shifting as the boarding sags due to gravity during experiments.
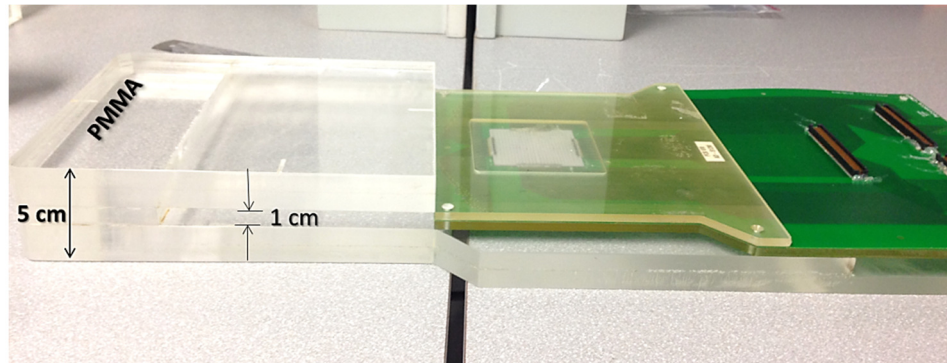
Figure 5.6: The homogeneous holder and MP512-EPI packaging.

5.2.3.2. Design and fabrication of an inhomogeneous insertion

Tissues with different densities pose a challenge in clinical calculation and optimisation because determining a steep dose gradient region and penumbra is complicated, as is delivering an accurate dose to the heterogeneous region such as the thorax with the lungs, heart, and bones. To use an MP512-EPI to diversify clinical treatment, a holder and insertions were designed and developed by CMRP. Both items were made from red cedar because its physical density of 0.38 g/cm^3 is equivalent to human lungs [230]. The holders have upper and lower parts that are connected with two pinpoints of carbon fibre inside two holds on the larger holder (Figure 5.7a). The inhomogeneous insertion section was established in two 1 cm thick squares that enable gafchromic EBT3 film and MP512-EPI to be placed inside, as shown in Figure 5.8. The MP512-EPI detector without a PMMA cover was sandwiched between two inhomogeneous slaps and fixed to the holder, as shown in Figure 5.7b. These insertions were moulded into two types, a spherical shape with a large water equivalent size of 1 cm^3 and 2 cm^3 (density of 1 g/cm^3) to represent a tumour in the lung, while the second insertion has no tumour representation (Figure 5.8).

(a)   (b)
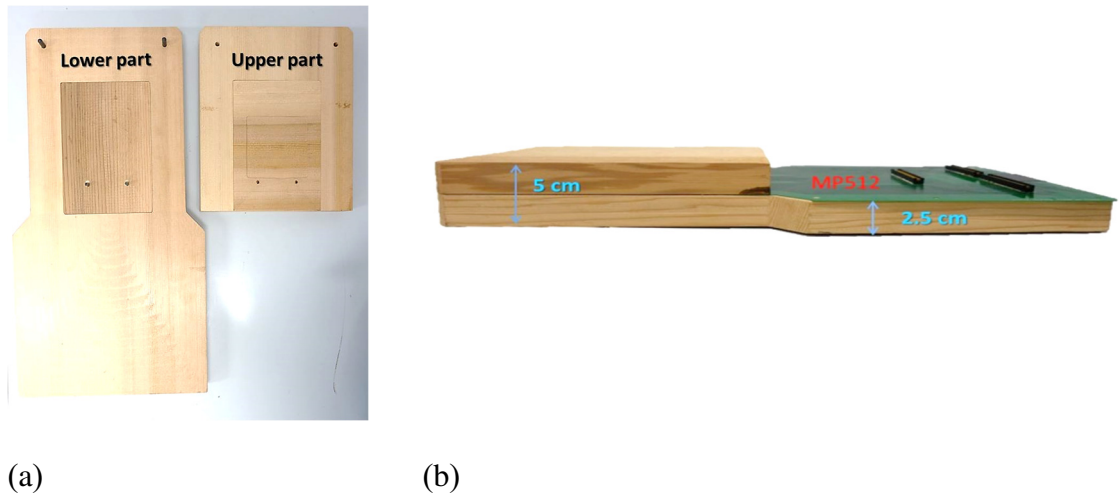
Figure 5.7: The inhomogeneous holder; (a) without and (b) with MP512-EPI.

(a)   (b)
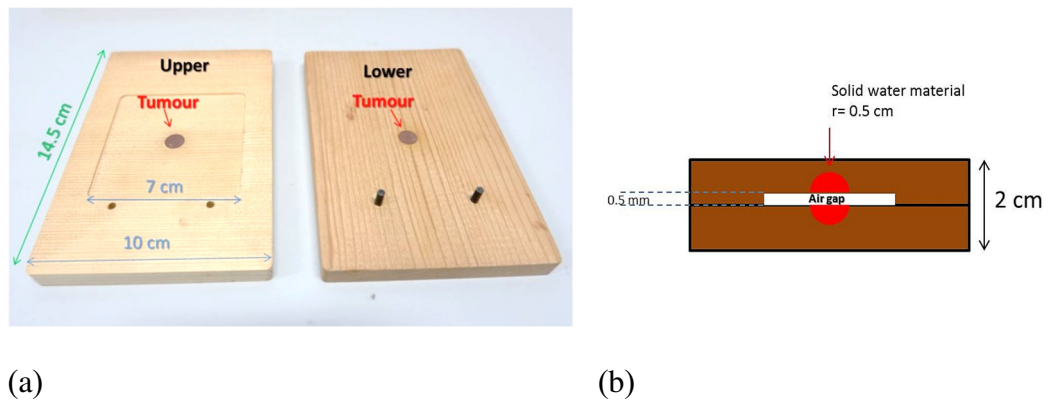
Figure 5.8: The inhomogeneous insertion; (a) The upper and lower part of the insert, and (b) schematic cross-section of the inhomogeneous insertion with a tumor inside (not to scale).

5.2.4. Computed tomography (CT) scan

Radiation therapy needs electron density data so that the treatment planning can be calculated precisely. CT image datasets provide patient anatomy and structure, including the CT number or Hounsfield units (HU) that can be converted to information on electron density. The CMRP cylindrical phantom with homogeneous and inhomogeneous insertions was carried out by computed tomography (CT) using SOMATOM (Siemens

Healthineers, Erlangen, Germany) at ICCC Wollongong hospital (Figure 5.9). Three small markers were placed on the phantom surface to correspond to the central detector reference. Two imaging datasets with and without a detector inside the phantom were carried out for each holder. Axial slices 2 mm and a 512×512 matrix resolution were acquired for the homogeneous and inhomogeneous holder insertions by following the CT scan protocol for radiation therapy [231][6]. Typical scanning extends over the length of the entire phantom by avoiding any electronic part of the detector. The CT images with and without detectors are shown in Figure 5.10 and Figure 5.11. The cylindrical phantom data sets were sent to the Pinnacle[3] TPS.
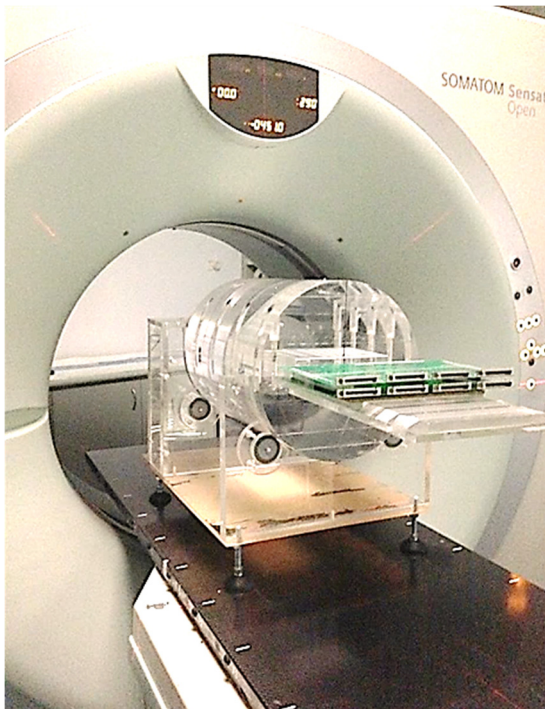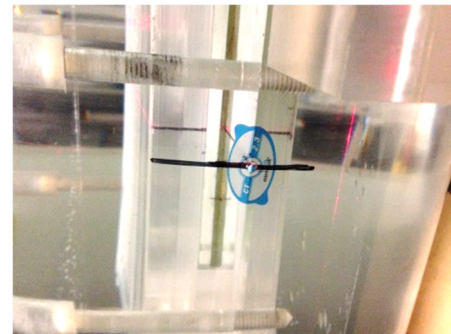
(a)   (b)

Figure 5.9: MP512-EPI and phantom setup for CT scan (b) the lead marker used for reference points.
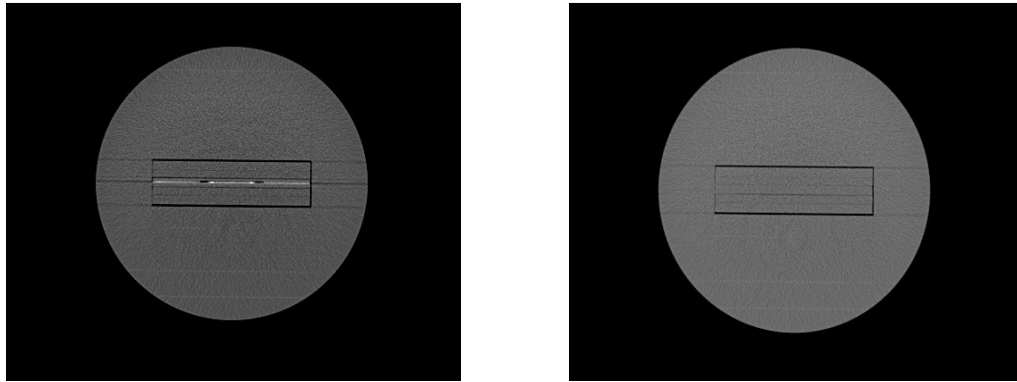
(a)   (b)

Figure 5.10: The CT images for the homogeneous holder (a) with MP512-EPI, and

(b) without MP512-EPI.
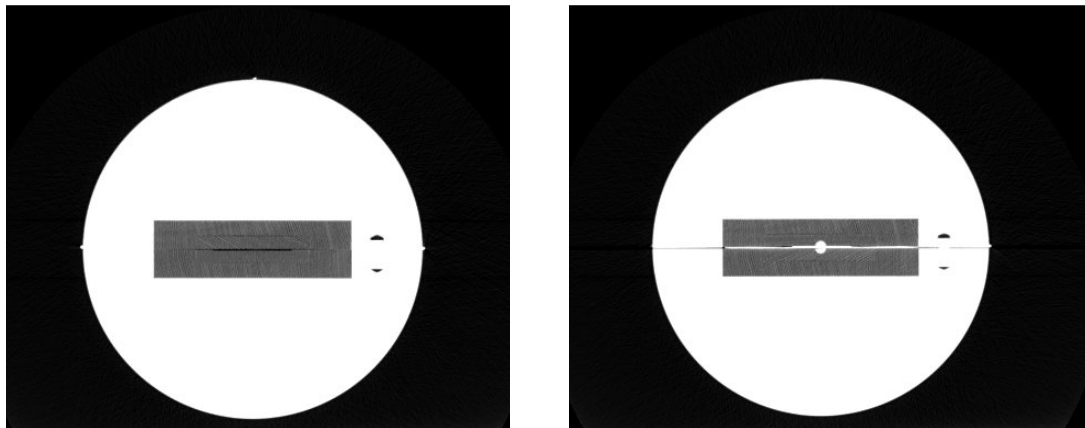
(a)   (b)

Figure 5.11: CT images of the inhomogeneous holder; (a) without MP512-EPI and

(b) with MP512-EPI and with a hidden tumour.

5.2.5. Clinical planning and optimisation

Pinnacle[3] version 14 (Philips Radiation Oncology Systems, Fitchburg, WI, USA) was

used as a treatment planning system to conduct clinical experiments. An adaptive

convolution superposition was used to calculate 6 MV photon beams on a 2 mm^3 dose

grid resolution. This algorithm is a fast model-based 3D dose calculation method

developed by Mackie *et al.* and AhnesjÖ based on dose spread array (kernel) convolved

with energy fluence through the medium volume (TERMA; Total Energy released per unit Mass) that accounted for the polyenergetic spectrum [232][233]. The algorithm accounts for beam attenuation, primary and secondary scattered electrons changing in heterogeneous medium, as well as the beam modifier and patient contour effects using a ray-tracing technique during the superposition [234]. To account for heterogeneities, the kernels are density-scaled during superposition by "collapsed cones" that using a single ray corresponding to the central axis of a cone model in space, the set of cone utilised a lattice of rays [235]. Several studies have been showed that collapsed cone convolution (CCC) using in Pinnacle provide a high accuracy calculation in the heterogeneity medium such as lung and bone by revealed insignificant differences between predicted dose distribution measured, and Monte Carlo simulated dose [236]–[238].

5.2.5.1. Homogeneity plan

The clinical IMRT and VMAT plans for a small brain tumour (GTV size 2.5-3 cm) were transferred to the CMRP homogeneous phantom CT datasets. The isocentre of the clinical plan was aligned with the isocentre of the detector, and each plan was recalculated without changing the clinical planning parameters. Both plans delivered a nominal 2 Gy per fraction to the target volume. Seven fixed gantries at 0°, 50°, 100°, 150°, 210°, 260° and 310° were to generate the step and shoot IMRT plans. The plan was delivered with a total of 369 MU. The VMAT plan consisted of a full arc (360°) using a four-degree control point (CP) angular increment with a total of 90 CP and delivered 410 MU.

5.2.5.2. Inhomogeneity plan

A small 1 cm^3 solid water equivalent within the inhomogeneous phantom was used to represent the GTV of a lung tumour for IMRT and VMAT delivery. The PTV was extended by 0.5 cm in every direction. A nominal 3.5 Gy per fraction was delivered to the target volume, and six fixed gantries of 0°, 50°, 120°, 180°, 240° and 310° were used

to generate the step and shoot IMRT plans. The plan was delivered with 757 MU. The VMAT plan consisted of a full arc (360°) using a four -degree control point (CP) angular increment with 90 CP and a dose delivery of 835 MU (2.32 MU/degree). A summary of the planning parameters for both phantoms is shown in **Error! Reference source not found.**. The dose distribution recalculated in a CMRP phantom is shown in Figure 5.12. The 3D dose volume was exported as a DICOM dose file, and MATLAB 2016b (Math Works Inc., Natick, MA) was used to extract the planar dose distributions that corresponded to the specified detector measured plane. The TPS dose distributions were compared to the MP512-EPI and EBT3 film dose measurement.

(a)   (b)
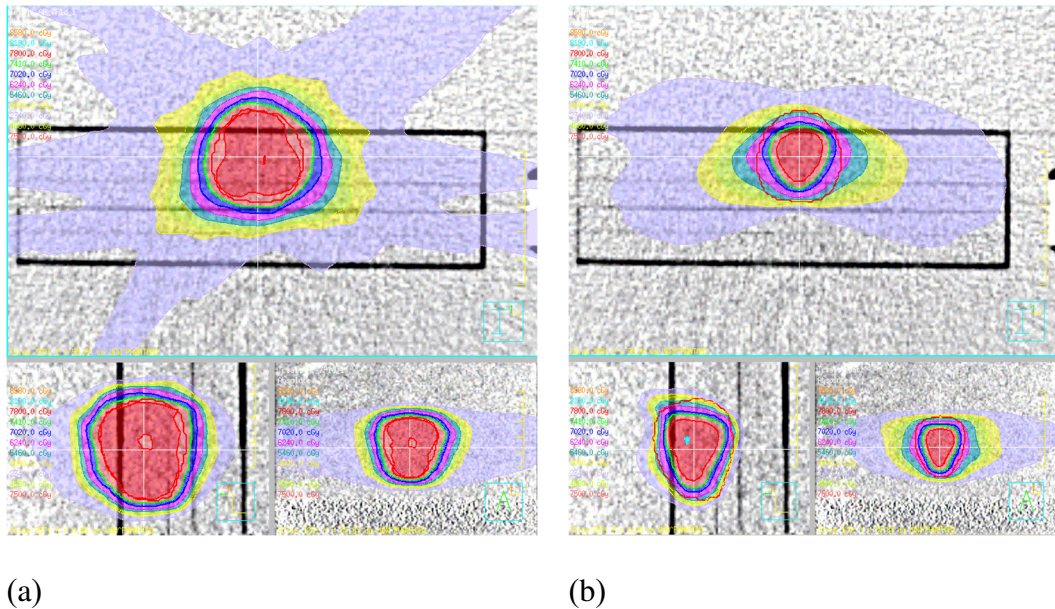
Figure 5.12: Pinnacle[3] version 14 TPS screenshots of the dose distribution cross-sections through the iso-centre of the CMRP cylindrical phantom for axial, sagittal and coronal plane; (a) IMRT plan and (b) VMAT plan.

Table 5.1: Treatment delivery parameters for homogeneous and inhomogeneous phantoms.

	Pinnacle^3 Planning parameters					
Phantoms	**Dose** (Gy/Fx)	**IMRT**		**VMAT**		
		Gantry	**MU**	**Gantry**	**CP**	**MU**
Homogeneity	2	0°,50°,100°, 150°,210°, 260°, 310°	369	360°	4°	410
Inhomogeneity	3.5	0°,50°,120°, 180°, 240°, 310°	757	360°	4°	835

5.2.6. Gafchromic EBT3 film

In this study, EBT3 film (Ashland Advanced Materials, Bridgewater, NJ) with batch numbers 04071601 and 05181502 were used as a reference dosimetry tool for comparison to MP512-EPI. The curves of these films were calibrated for each batch number, and then the films were cut into 7×7 cm^2 size pieces to fit into the homogeneous and inhomogeneous holders (Figure 5.13). The films were scanned before and after being irradiated for 48 hours by the Microtrex ScanMaker i800 flatbed scanner and Epson Expression 10000 XL. Each film was aligned in the centre of the scanner and scanned six times with 48-bit colour depth of RGB colour channels and a spatial resolution of 72 dpi (equivalent to a pixel size of 0.35278 mm). The process of calibrating and analysing the films was discussed in Chapter 3, Section 3.3.3.

(a)   (b)
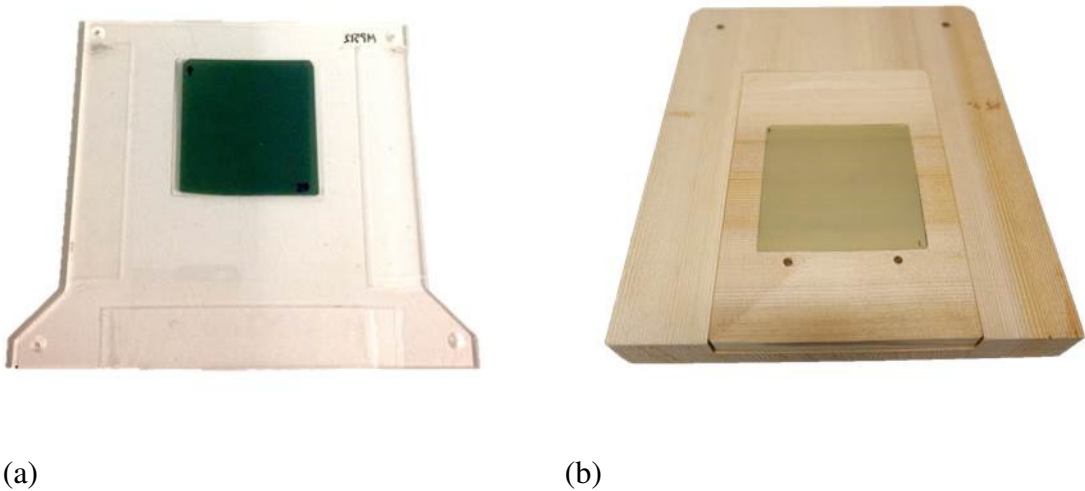
Figure 5.13: Gafchromic EBT3 film cutting pieces using for patient verification; (a) Homogeneity holder and (b) Inhomogeneity holder.

5.2.7. Verifying the clinical delivery

All measurements were carried out with a Varian Clinac iX (Varian Medical System, Palo Alto, CA) at ICCC Wollongong hospital. The LINAC is equipped with a 120-leaf Millennium multi-leaf collimator system where the inner 80 leaves provide a leaf width of 0.5 cm and 1 cm for the remaining outer leaves. Before the detector was used as a dosimeter in clinical verification, MP512-EPI had performed equalisation and relative dose calibration as discussed in **Section 3.3.1**. The MP512-EPI was inserted into the homogeneous and inhomogeneous holder to deliver head and lung treatment, respectively. The detector array inside the holder was placed in the coronal plane position of the PMMA cylindrical phantom (Figure 5.1). The phantom was put onto the middle of the couch to avoid colliding with gantry while rotating around the phantom. To minimise couch attenuation error, the phantom was place in the same location relative to its location when the couch attenuation factor was measured. The centre of the detector was aligned to the isocentre of the radiation beam using a 5×5 mm^2 field to reposition the vertical,

lateral and longitudinal axis to a setup uncertainty within ±1 mm. The inclinometer was attached to the gantry stand and aligned to zero to indicate a gantry angle of zero.

The clinical plans were delivered with the actual beam angles for IMRT and VMAT, and the angular dependence correction factors were applied to MP512-EPI measurements (the details will discuss in **Section 5.9**). Each IMRT and VMAT plan was delivered three times to justify the reproducibility of the detector measurement. Each plan was also measured using gafchromic EBT3 film at the same orientation setup. The composite dose measurements for MP512-corrected and EBT3 films were compared to the calculated dose exported from RTP using gamma analysis and by following criteria of 2%/ 2mm and 3%/3mm. The overall process of clinical validation is shown in Figure 5.14.
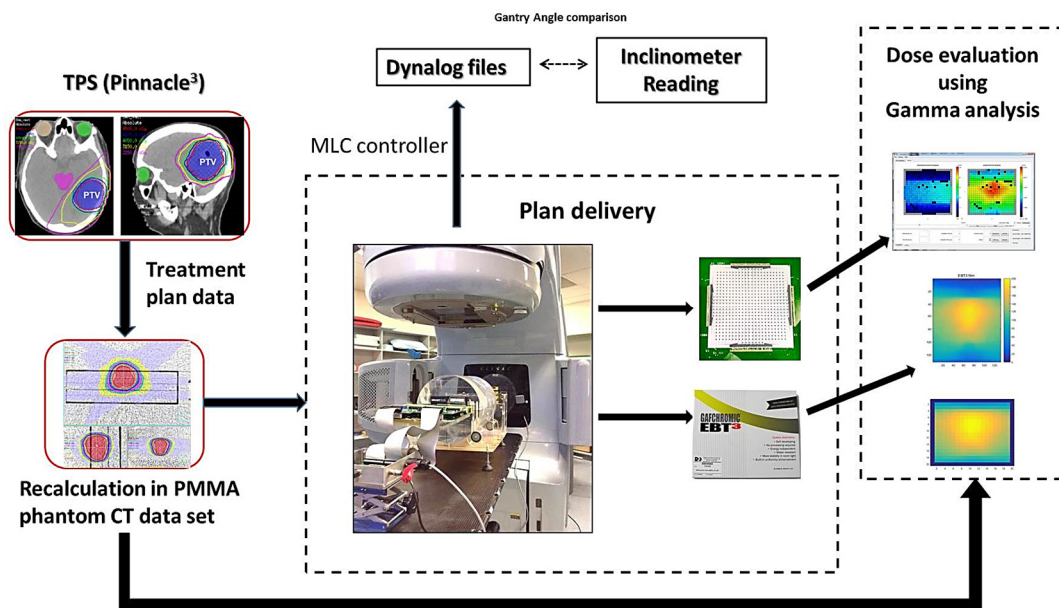
Figure 5.14: A schematic diagram of the clinically validated process.

5.2.8. The correction factor

5.2.8.1. Angular dependence correction factor

The MP512-EPI was investigated to determine how the detector response could be affected by angular dependence and to provide the maximum relative discrepancy with respect to the incident beam angle zero of approximately 18.6% and 17.7% for 6 MV and 10 MV photon beams (refer to **Chapter 4 section 4.3.8**). Since the angular dependence of MP512-EPI would affect the accuracy of the patient plan verification when using arc therapy modalities, its angular correction method was developed and has been proven that it can be used in small static fields due to good agreement (±2%) of the corrected dose to dose measured with gafchromic EBT3 films, as discussed in **Chapter 3**.

The angular correction factor of MP512-EPI was also calculated using the same method as MP512-Bulk (Chapter 3). The factor obtained as a function of the MP512-EPI responding measurement ratio to the EBT3 film dose measured at Θ and normalised to the zero incident beam angle (Θ = 0°). The dose correction of MP512-EPI was adopted as shown in Equation (3.1) (as present in Chapter 3).

$$MP_{ij}^{corrected} = \frac{MP_{ij}'(\theta)}{C_{ij}(\theta)} \tag{3.1}$$

where $MP_{ij}'(\theta)$ is the MP512 experimental measured response signal (counts) for the particular angle, and $C_{ij}(\theta)$ is the calibration tensor for the open 10×10 cm^2 field.

The angles measured during VMAT delivery with an inclinometer were used to correct the integral 2D-dose mapping in a particular plane. To correct the VMAT plan, the angular correction factors were applied to accumulated MP512-EPI responses at gantry

angle increments of 1°, 5° and 10°, respectively. The exported data files from Magic Suite software called VMAT_angle.aux and VMAT_Decoded.txt were used for the calculations in this study. The angles measured with an inclinometer (±180°) were converted to the same scale as the Varian IEC scale (360°). MATLAB 2016b (Math Works Inc., Natick, MA) was used to apply the angular correction factor to the detector measurement and convert the detector response to a relative dose (see Appendix B for MATLAB scripts). A schematic diagram of the angular correction factor applied to VMAT is shown in Figure 5.15. The reconstructed composite dose of MP512-EPI for VMAT and IMRT were compared to the EBT3 dose measurement and the TPS 2D-dose plane.
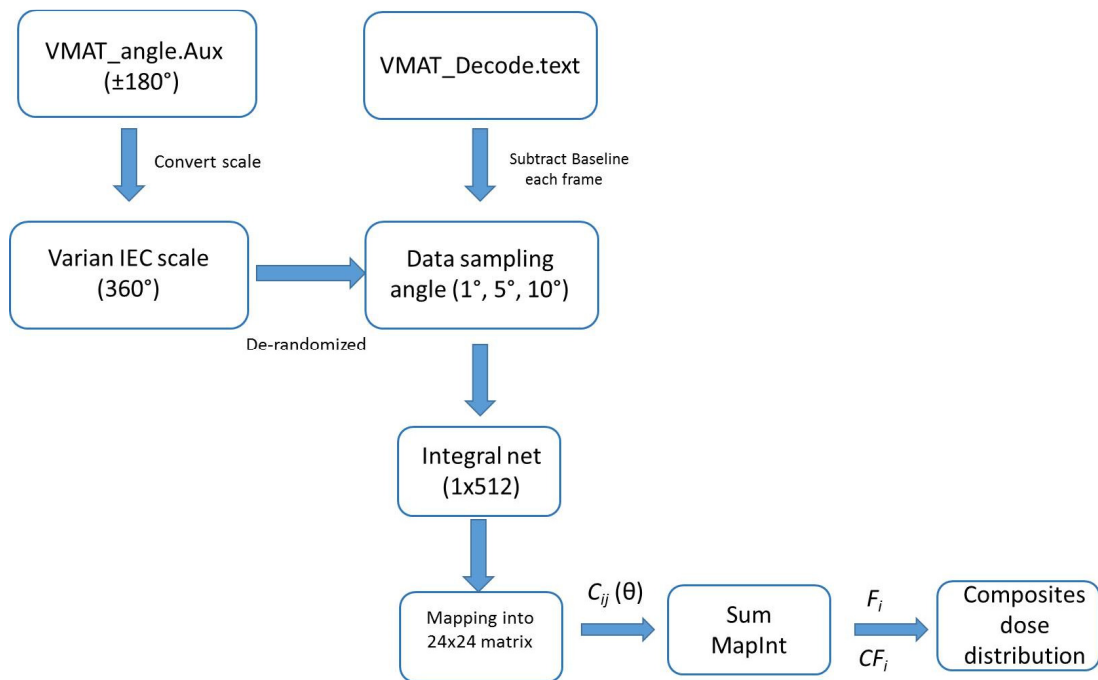
Figure 5.15: A schematic diagram of MP512-EPI dose reconstructed for VMAT delivery.

5.2.8.2. Couch attenuation effect

The treatment couch can have an impact on the TPS calculation and the treatment delivery. Some reports showed the influence that a couch build up has on skin reaction and underestimated of the target dose by ignoring this factor when calculating and optimising doses [239][240]. The angular correction factor discussed in **section 5.9.1** was calculated when the detector was in a vertical position, so the couch attenuation effect was not included. To ensure that the MP512-EPI dose reconstruction calculation is accurate, couch attenuation on patient dose verification should be investigated. The Varian Exact image-guide (IGRT) couch (Varian Medical Systems, Palo Alto, CA) was used. This couch was manufactured with less artefacts and radio-translucent material for image guidance radiation therapy such as Cone beam computed tomography (CBCT), or Megavoltage computed tomography (MVCT) [241][242]. The couch consists of 2 mm thick carbon fibre (density of 0.7 g/cm^3) wrapped around a 5.2 mm water equivalent thick homogeneous foam core (density of 0.1 g/cm^3) at 6 MV photons [243]. The couch was manufactured from materials with different thicknesses, as shown in Figure 5.16.

(a)

(b)

Figure 5.16: Photographs of the Varian Exact image- guide (IGRT) couch and construction cross-section [241].

The CMRP cylindrical phantom was used to measure couch attenuation and provide the equivalent depth for all the angles under investigation. The MP512-EPI was placed in the centre of the phantom, 15 cm deep. The detector array faced upwards to be perpendicular to the iso-centre of the radiation beam at a gantry angle of zero degrees (0°). Because the IGRT couch has different thicknesses and attenuation depends on the beam's angle of incidence, the posterior oblique angle was measured. A 10×10 cm^2 field of 6 MV photon beams was irradiated with the gantry at four different angles; 0°, posterior (180°), and posterior oblique (135° and 225°). To exclude the angular dependence of MP512-EPI, the measurements were repeated with the detector face down to the couch and irradiated with the gantry at 0°, 45°, 180° and 315°. All the gantry measurements were repeated

three times at dose rates of 600MU/min, and 100 MU delivered. The setup is shown in Figure 5.17. Couch attenuation was the ratio of the detector response measured with the couch ($MP512_{WC}$) and without the couch ($MP512_{W/o}$) (Equation 5.1).

$$C_{attenuation} = \left(1 - \frac{MP512_{WC}}{MP512_{W/o}}\right) * 100 \qquad (5.1)$$

(a)   (b)
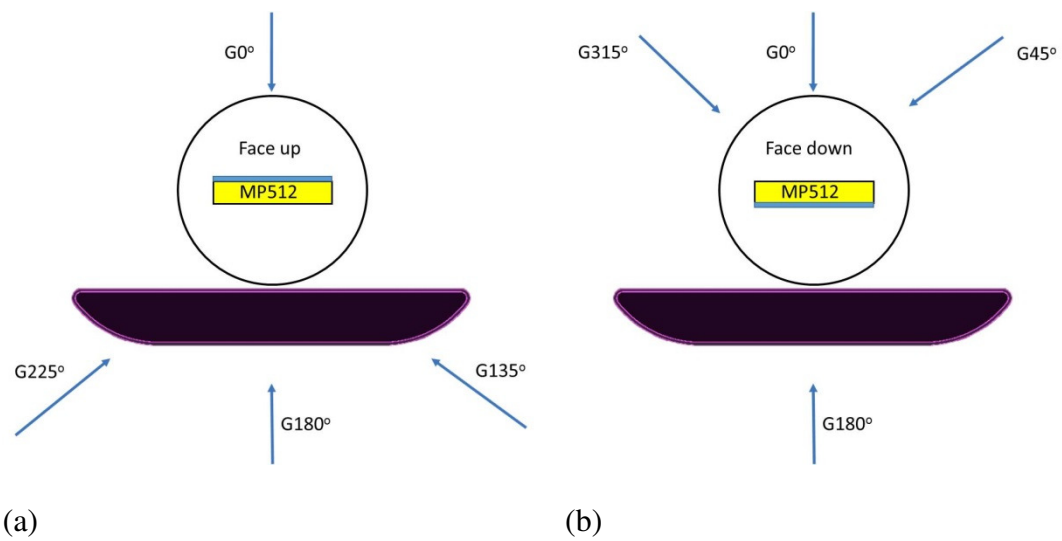
Figure 5.17: The setup used for the couch attenuation effect; (a) MP512-EPI face up and (b) MP512-face down.

5.2.9. Gamma analysis

A gamma map analysis is a valid quantitative tool for evaluating a 2D planar dose-agreement between the expected dose distribution of the treatment plan and the actual dose distribution measurement [244]. This method was introduced by Low *et al.* in 1998 [245][246]. The two principal factors using for comparing the dose distribution of a Gamma index are dose deviation (DD) or dose tolerance (ΔD), and distance-to-agreement (DTA). The point of interest is calculated within the acceptance of an ellipsoidal shape of DD and DTA (Figure 5.18) [247]. The gamma value (γ) is computed for all the points in

the area of interest by following Equation 5.2. The pass-fail criteria rely on the γ value, so if γ ≤1 the calculation passes, and if γ >1 the calculation fails.

$$\gamma_m = \sqrt{\left(\frac{\Delta r}{DTA}\right)^2 + \left(\frac{\Delta d}{DD}\right)^2} \qquad (5.2)$$

Where Δr is the distance between a point on the distribution A and B, Δd is the difference between the dose on distribution A and B. In clinical practice, it is accepted gamma criteria of 3%/3 mm for evaluation of dose delivered in comparison with planned. Dose delivery is acceptable if the passing rate exceed 90% [248]. However, the small field provides a high dose gradient leading to the fact that more robust tolerances criteria should be considered. The MP512-EPI has a high resolution of 2 mm and to evaluate suitability of MP512-EPI for for small field dose verification; the 2%/2mm and 1%/1mm, gamma index were used to quantify confidence limit of MP512-EPI to be useful tool for small field measurement. The gamma evaluation criteria using in this study were 1%/1mm, 2%/2mm and 3%/3mm with a threshold dose of 10% of the maximum.
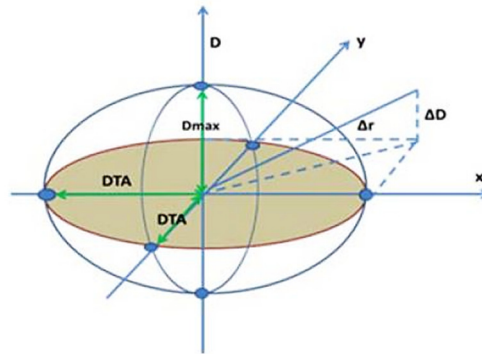
Figure 5.18: Schematic diagram of gamma evaluation [247].

5.3. Results

5.3.1. The couch attenuation effect

The couch attenuation value for a 10×10 cm^2 field size measured by MP512-EPI showed the average value to be within ±1.3% and a standard deviation of ±0.05 (1SD). Maximum attenuation was 1.4% at a posterior oblique angle (135° and 225°). These results showed that couch attenuation was within ±2% and had no effect on the MP512-EPI response. Couch attenuation depends on the angle of the incident beam, and the field size and photon energy [249][250]. For VMAT and IMRT, the treatments were delivered at a segment field less than 10×10 cm^2 and irradiated with an amount of treatment angles around the patients. The detector responses had an insignificant effect on the partial couch attenuation portion so the correction couch attenuation factors were not used to correct the dose reconstruction of MP512-EPI.

5.3.2. Inclinometer verification

The accuracy of dose reconstruction with MP512-EPI depends on the accuracy of gantry angle sampling during treatment delivery. Figure 5.19 shows the deviation for each gantry measurement during beam delivery as a function of time (ms). The accuracy of the inclinometer used in conjunction with our fast DAQ system was within ±1.5° (0.05%), unlike the particular data point extracted from the Dynalog files during full arc (360°) delivery of VMAT.
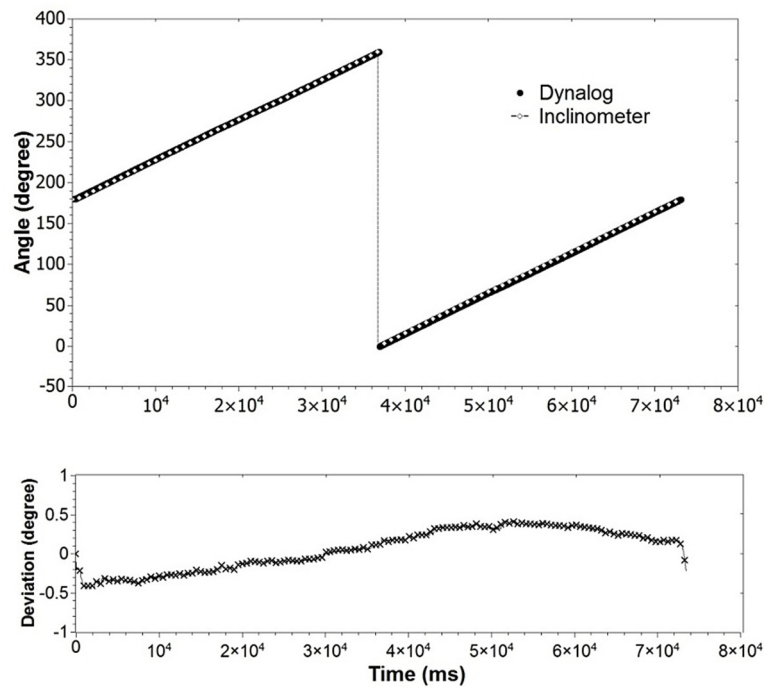
Figure 5.19: Comparison of the gantry angle measured by the inclinometer and extracted from Dynalog files over full arc (360°) delivery.

5.3.3. Clinical verification

5.3.2.1. Homogeneous phantom

A comparison of an MP512-EPI dose reconstruction, a gafchromic EBT3 film dose measurement, and a planar TPS dose for IMRT and VMAT are shown in Table 5.1. These results showed an excellent gamma passing rate of more than 95% (2%/2mm criteria) and 98% (3%/3mm criteria) for the IMRT and VMAT plans. However, a lower gamma passing rate of 60% for all cases with criteria of 1%/1mm emerged when the MP512-EPI dose reconstruction and EBT3 dose measurements were compared. The 1%1mm criteria had a better gamma passing rate of 80% compared to the MP512-EPI dose reconstruction and TPS dose calculation. Figure 5.20 shows the comparison of planar dose

reconstruction of MP512-EPI and EBT3 film dose measurement. For IMRT delivery, Figure 5.21 and Figure 5.22 show the *x*-axis and *y*-axis dose profiles through the isocentre (central axis) and indicated off-axis points reconstructed from MP512-EPI measurements with and without angular correction and EBT3 film. In all cases there was excellent agreement between the dose profiles measured using EBT3 film and those reconstructed from angular corrected MP512 measurements. Figure 5.23 and Figure 5.24 show the comparison of dose profiles measured using EBT3 film and those reconstructed from MP512-EPI measurements for the VMAT case. The gamma passing rate (2%/2mm) for the VMAT plan delivery improved slightly as smaller gantry angles were used for the MP512 dose reconstruction. The gamma pass rates were 95.04%, 95.23%, and 95.56% for gantry angles used for dose reconstruction at 10°, 5° and 1°, respectively. For example, at an off-axis of 2 cm, as shown in Figure 5.23(b) and (e), the agreement between the angular corrected MP512 and EBT3 film measurements can be improved using smaller angles because the dose can change rapidly over a small angular segment.

5.3.2.2. Inhomogeneous phantom

A comparison of MP512-EPI dose reconstruction, gafchromic EBT3 film dose measurement, and planar TPS dose for IMRT and VMAT for an inhomogeneous phantom are shown in Table 5.2, with similar results as those measured in homogeneity; they indicated an excellent gamma passing rate of more than 95% (2%/2mm criteria) and 98% (3%/3mm criteria) for IMRT and VMAT plans when MP512-EPI dose reconstruction was compared with EBT3 dose measurement and TPS dose calculation. MP512-EPI dose reconstruction compared to EBT3 dose measurements showed a lower percentage passing rate of 70% for 1%/1mm criteria but the pass rate was more than 85% when compared with the TPS dose calculation. Figure 5.25 shows a comparison of the planar dose reconstruction of MP512-EPI and EBT3 film dose measurement for the VMAT plan

delivery. Figure 5.26 and Figure 5.27 shows the *x*-axis and *y*-axis dose profiles through the isocentre (central axis) which indicated that off-axis points were reconstructed from MP512 measurements with angular correction and EBT3 film.

Table 5.1: Summary of the gamma passing rate of IMRT and VMAT plan delivery to CMRP homogeneous phantom

| Cases | Agreement Criteria | | | | | |
| | 1%/1mm | | 2%/2mm | | 3%/3mm | |
	MP512-EBT3	MP512-TPS	MP512-EBT3	MP512-TPS	MP512-EBT3	MP512-TPS
IMRT	69.97	89.47	96.25	98.46	98.38	100
VMAT-1°sampling corrected	56.21	82.70	95.56	98.77	99.79	100
VMAT-5°sampling corrected	55.28	81.39	95.23	98.77	99.79	100
VMAT-10°sampling corrected	53.73	80.13	95.04	98.77	99.79	100

(a)

(b)
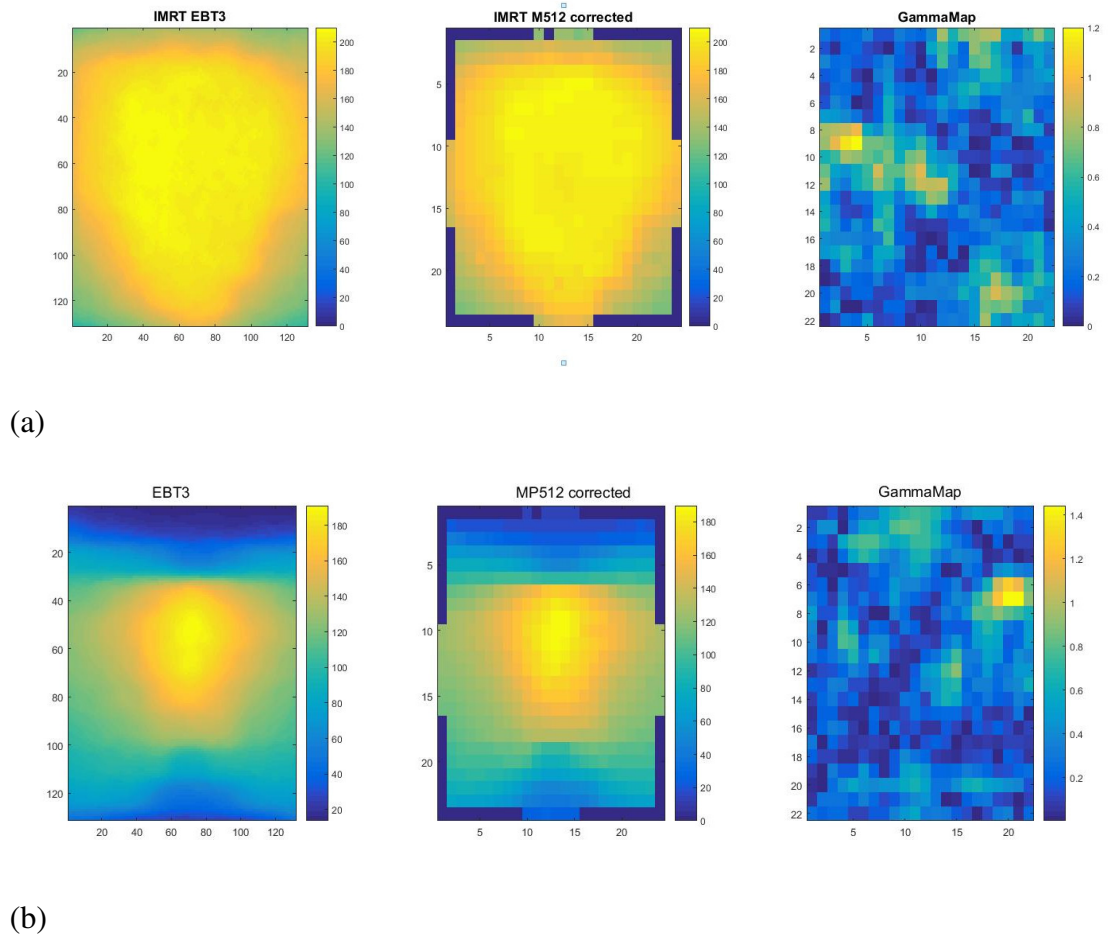
Figure 5.20: A comparison of planar dose reconstruction of MP512- EPI and gafchromic EBT3 film dose measurement for (a) IMRT and (b) VMAT plans delivery.
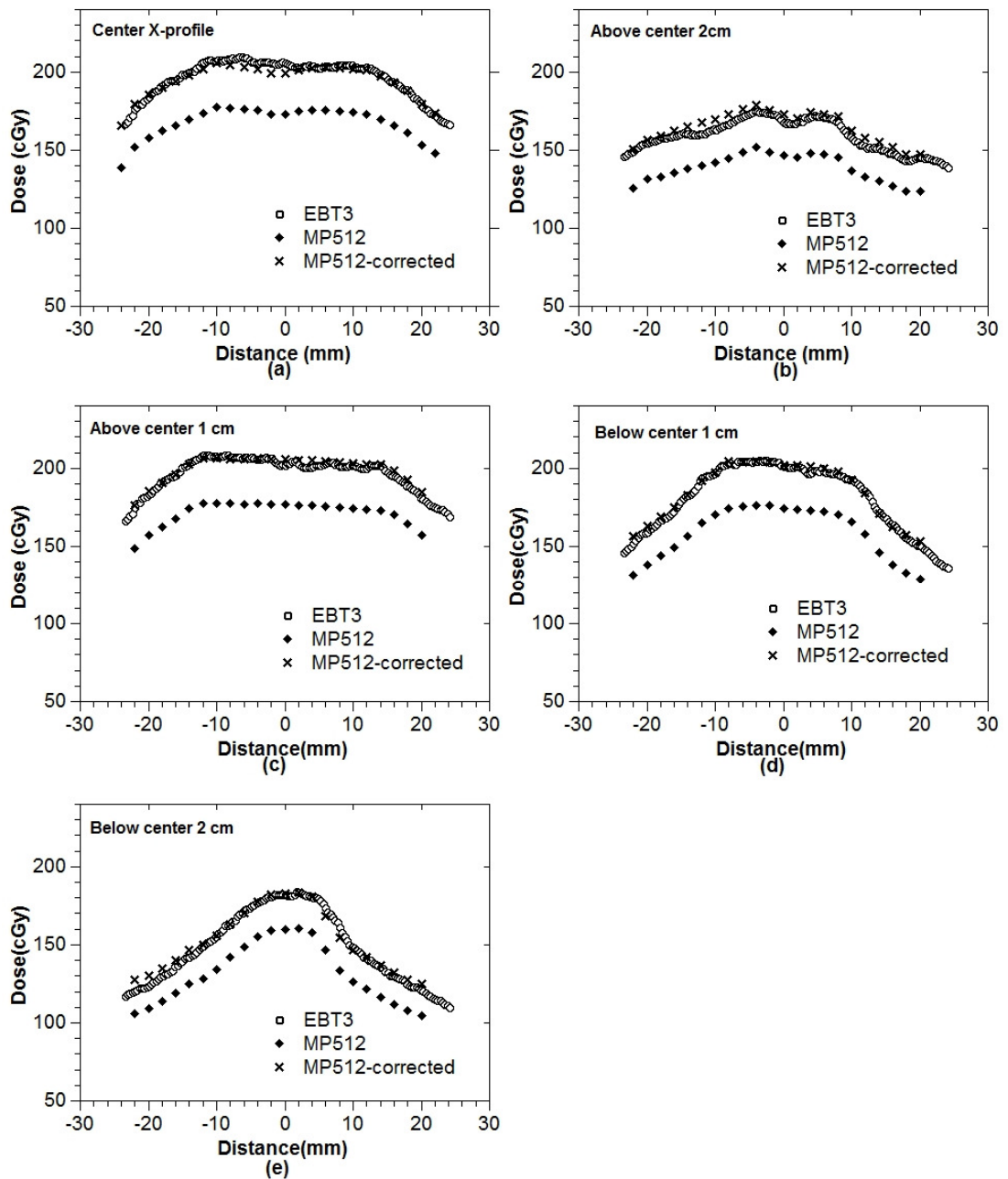
Figure 5.21: A comparison of Superior-Inferior dose profiles measured with gafchromic EBT3 films and reconstructed from MP512-EPI measurements with and without angular correction, to deliver an IMRT plan to a homogeneous phantom as a function of distance from the centre; (a) the beam profile at the centre, (b) the off-axis profile above the central 2 cm, (c) the off-axis profile above the central 1 cm, (d) the off-axis profile below the central 1 cm, and (e) the off-axis profile below the central 2 cm.
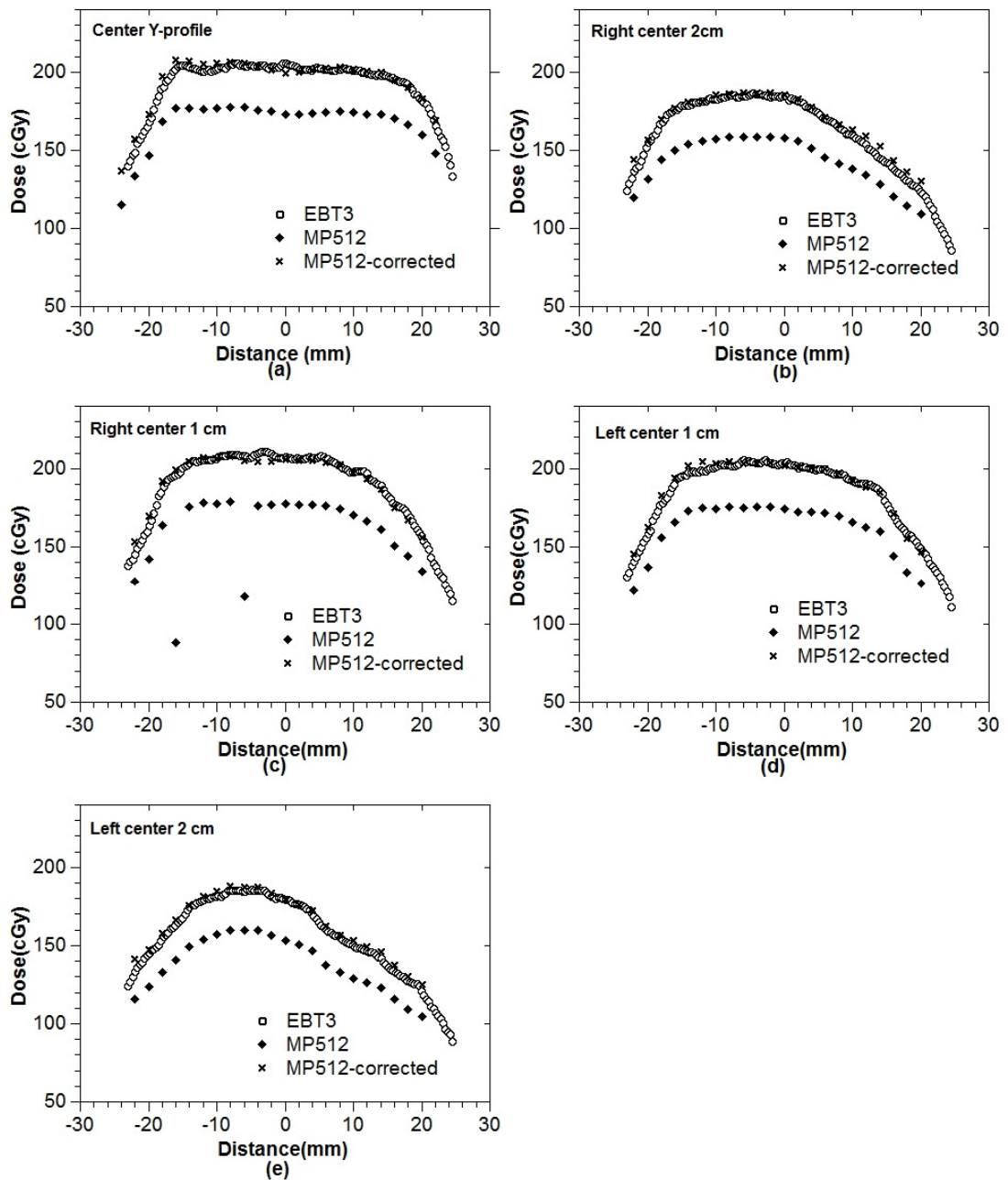
Figure 5.22: A comparison of Left-Right dose profiles measured with gafchromic EBT3 films and reconstructed from MP512 measurements with and without angular correction to deliver an IMRT plan to a homogeneous phantom as a function of distance (mm) from the centre; (a) the beam profile at the centre, (b) the off-axis profile 2cm right of centre, (c) the off-axis profile 1cm right of centre, (d) the off-axis profile 1cm left of centre, and (e) the off-axis profile left 2cm left of centre.
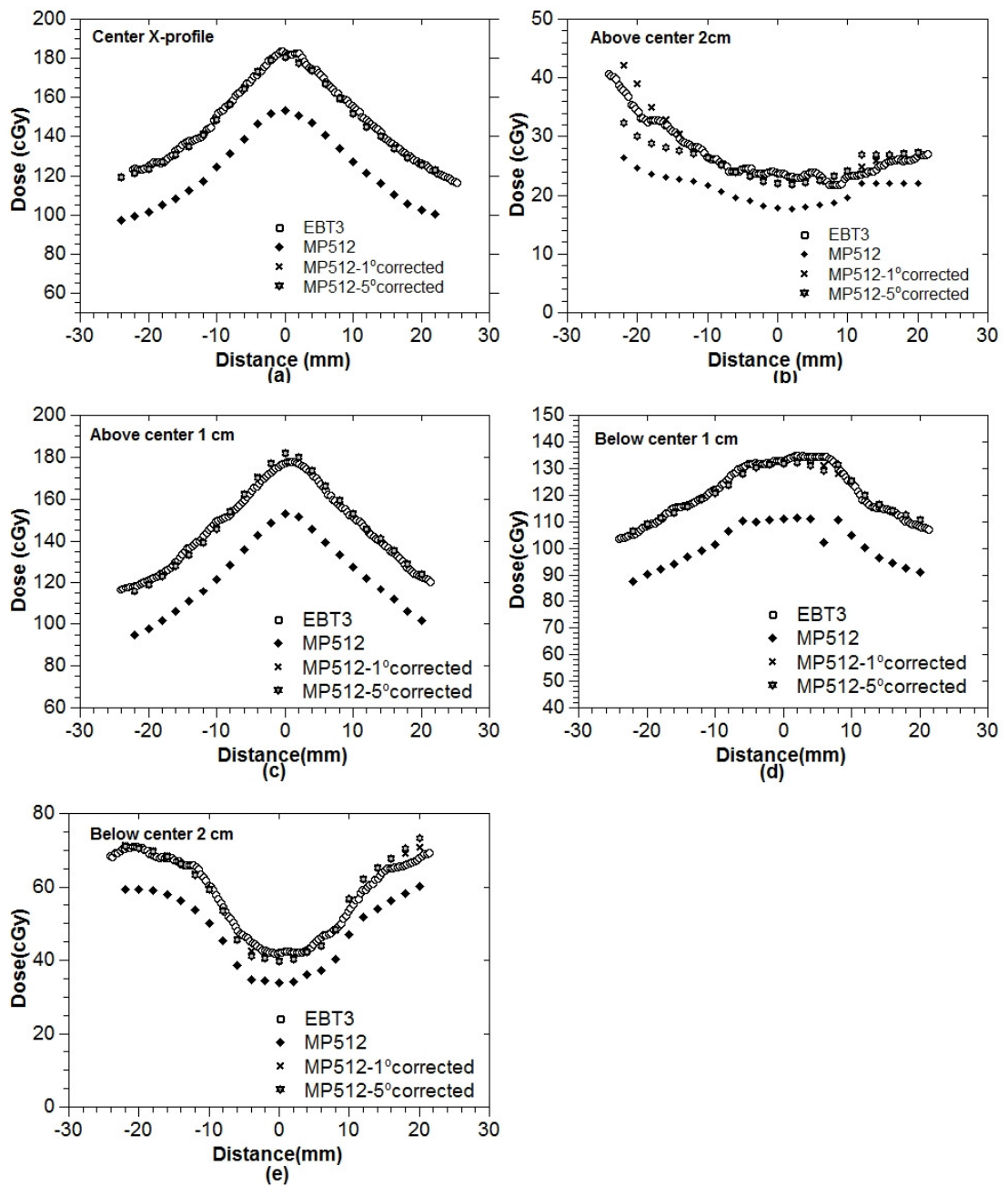
Figure 5.23: A comparison of Superior- Inferior dose profiles measured with gafchromic EBT3 films and reconstructed from MP512 measurements with and without angular correction, to deliver a VMAT plan to a homogeneous phantom as a function of distance (mm) from the centre; (a) beam profile at the centre, (b) the off-axis profile 2cm above the centre, (c) the off-axis profile 1cm above the centre, (d) the off-axis profile 1cm below centre, and (e) the off-axis profile 2cm below centre.
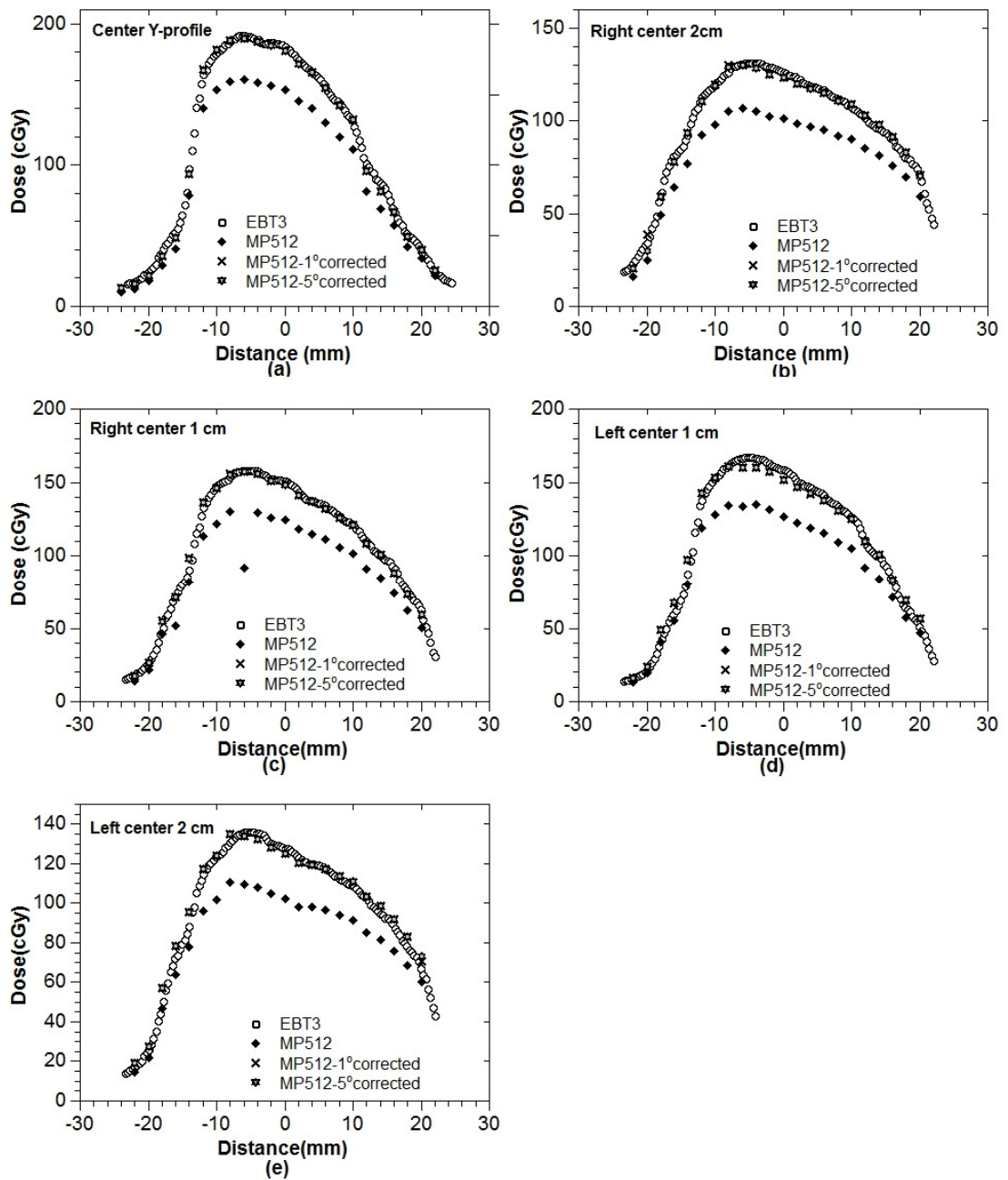
Figure 5.24: A comparison of Left-Right dose profiles measured with gafchromic EBT3 films and reconstructed from MP512 measurements with and without angular correction to deliver a VMAT plan to a homogeneous phantom as a function of distance (mm) from the centre; (a) beam profile at the centre, (b) the off-axis profile 2cm right of centre, (c) the off-axis profile 1cm right of centre, (d) the off-axis profile 1cm left of centre, and (e) the off-axis profile 2cm left of centre.

Table 5.2: Gamma passing rate of IMRT and VMAT for a CMRP inhomogeneous phantom

Cases	Agreement Criteria					
	1%1mm		2%/2mm		3%/3mm	
	MP512-EBT3	MP512-TPS	MP512-EBT3	MP512-TPS	MP512-EBT3	MP512-TPS
IMRT	69.97	89.47	96.90	96.17	99.40	100
VMAT-1°sampling corrected	73.53	83.33	97.06	99.17	99.12	100
VMAT-5°sampling corrected	72.94	83.75	97.06	99.17	99.12	100
VMAT-10°sampling corrected	72.65	79.58	96.76	98.33	99.12	100
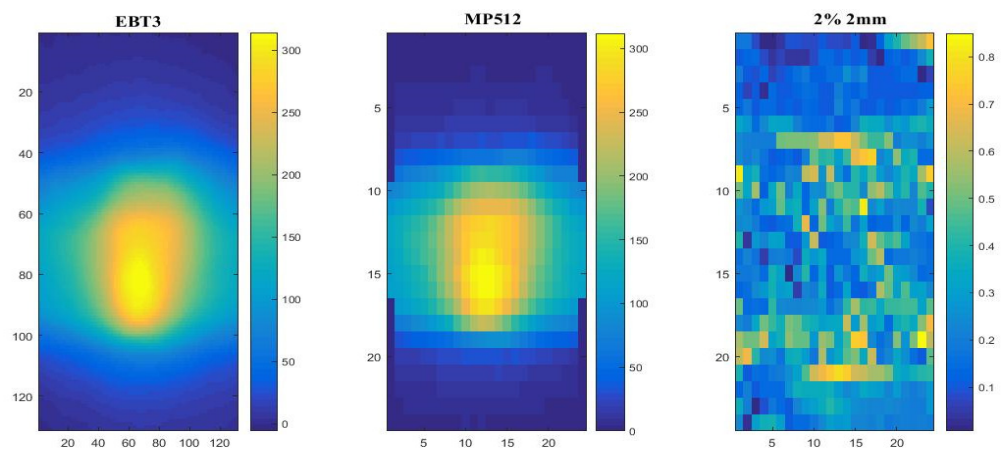
Figure 5.25: A comparison of planar dose reconstruction of MP512- EPI and gafchromic EBT3 film dose measurement to deliver VMAT plans.
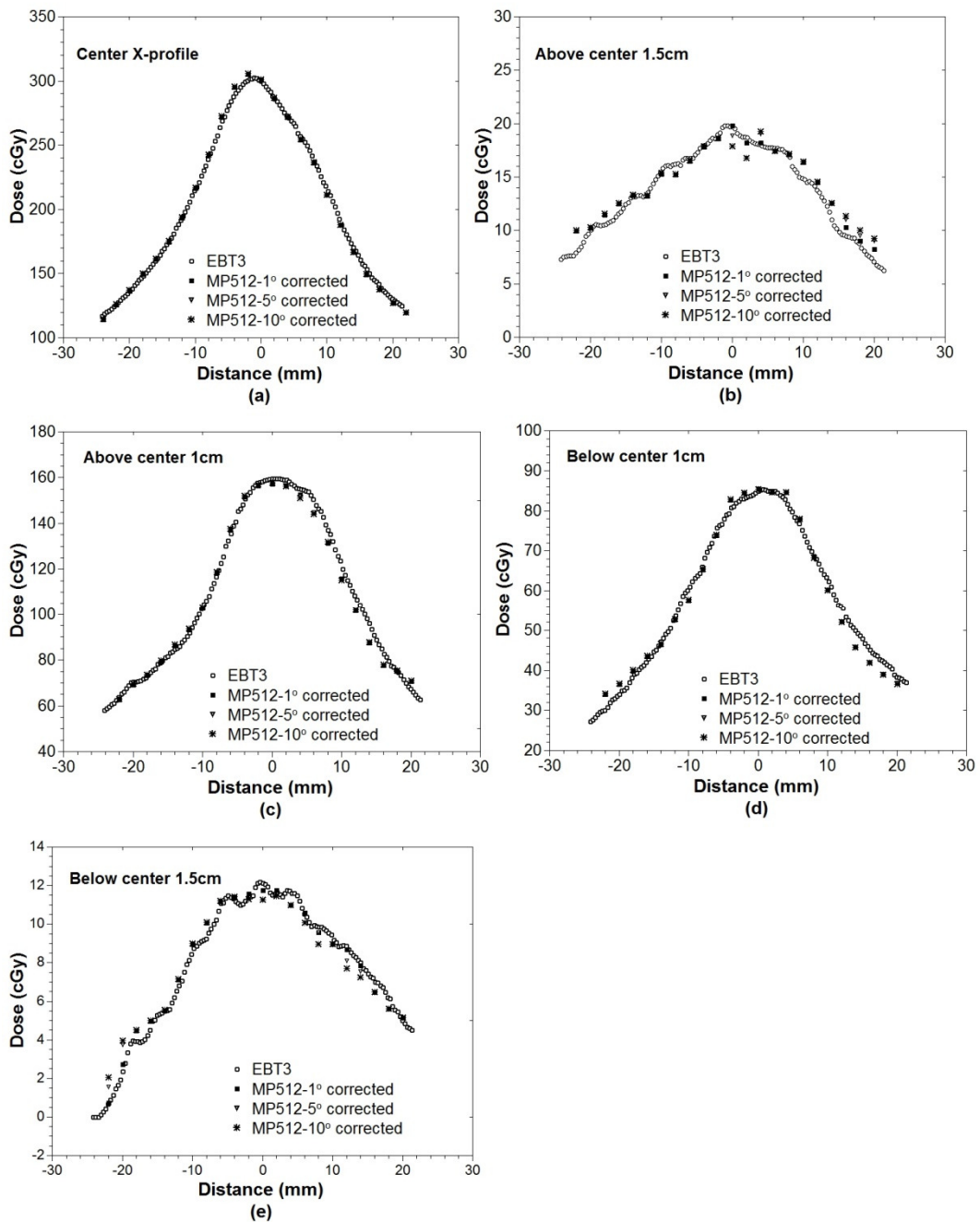
Figure 5.26: A comparison of Superior- Inferior dose profiles measured with gafchromic EBT3 films and reconstructed from MP512 measurements with an angular correction for a VMAT plan delivered to an inhomogeneous phantom as a function of distance (mm) from the centre; (a) beam profile at the centre; (b) the off-axis profile 1.5cm right of centre, (c) the off-axis profile 1cm right of centre, (d) the off-axis profile 1cm left of centre, and (e) the off-axis profile 1.5cm left of centre.
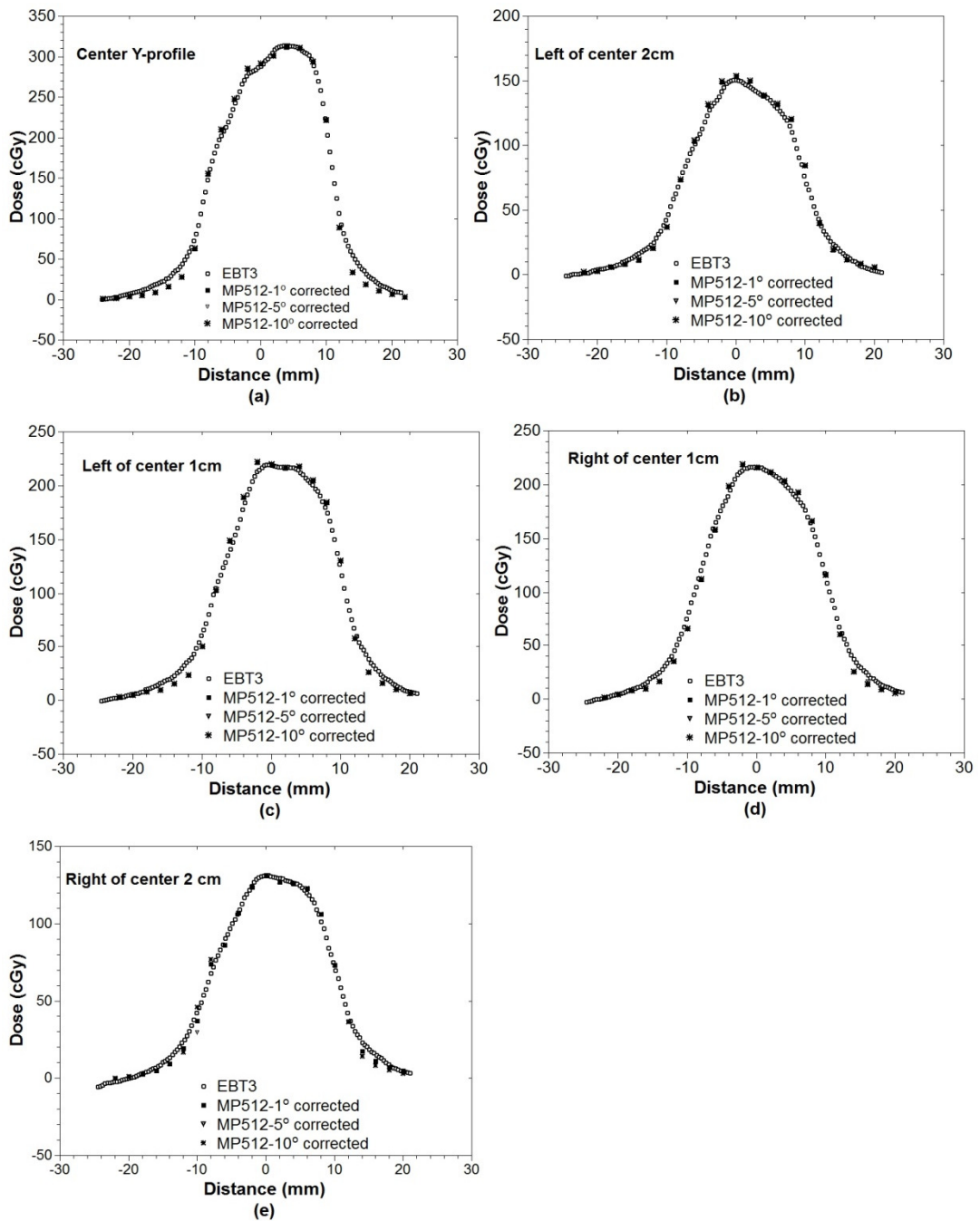
Figure 5.27: A comparison of Left-Right dose profiles measured with gafchromic EBT3 films and reconstructed from MP512 measurements with angular correction for a VMAT plan delivered as a function of distance (mm) from the centre; (a) beam profile at the centre, (b) the off-axis profile 2cm right of centre, (c) the off-axis profile 1cm right of centre, (d) the off-axis profile 1cm left of centre, and (e) the off-axis profile 2cm left of centre.

141

5.4. Conclusions

To compare a clinical plan, the percentage passing rate of IMRT compared to gafchromic EBT3 film and RTP dose calculation was almost 95% and 100% when following the 2%/2mm and 3%3mm gamma criteria for homogeneous and heterogeneous phantoms. With VMAT, the agreement between angular corrected MP512-EPI dose reconstruction and EBT3 film measurements can be improved using a smaller angular sampling interval because the dose can change rapidly over a small angular segment (Figure 5.23 and Figure 5.26). The accuracy of dose reconstruction with MP512-EPI depends on the accuracy of gantry angle sampling during treatment delivery, but with VMAT plans, the four degree control points of TPS dose optimisation were not a fine enough sampling point to perform different percentage passing rates when the MP512-EPI dose reconstructions, EBT3 films dose measurements, and RTP dose calculation were compared. The homogeneous and heterogeneous phantom measurements showed a lower agreement between MP512-EPI dose reconstruction and EBT3 films dose measurement than the TPS dose calculation for a gamma passing rate of 1%/1mm criteria. The set-up error may influence this result because EBT3 films positioned in the holder could experience misalignment during setup due to the holder being configured and the small gap shown in Figure 5.13; moreover the small radiation field in the heterogeneous medium means that the accuracy of the dose calculation algorithms is more important. The accuracy of dose perturbations within the inhomogeneity and at the interface region between two different mediums depends on the secondary electron transport modelling used during optimisation and calculation. Pinnacle[3] uses a convolution superposition algorithms so it tends to underestimate the dose to a low-density medium such as lung tissue [234][251], but the agreements between MP512-EPI dose reconstruction and TPS dose calculation were almost 98% at a tolerance

of 2%2mm, and maintained more than 99% at a tolerance of 3%/3mm, which could be acceptable for clinical practice.

These results demonstrated the clinical feasibility and accuracy of MP512-EPI as a real-time dosimetry QA tool with a high spatial resolution for small fields (less than $5x \times 5$ cm^2) as used for SBRT. The QA procedure is practical and convenient for routine patient specific verification for small intensity modulated fields. Future work will be devoted to the development of a Quadro MP512-EPI detector comprised of four tiled MP512-EPI to allow for a sensitive area 10×10 cm^2 while maintaining the same spatial and temporal resolution.

Chapter 6

3D dose reconstruction using MP512-EPI

6.1. Introduction

Current patient specific verification using 2D dose distributions comparison between the treatment planning (TPS) dose calculation and dose measurement in the phantom is the primary choice in approach to QA in IMRT and VMAT delivery. However, the 2D gamma agreement has weak correlation to be clinically meaningful, so 3D dose distribution verification was introduced as a powerful QA tool for advanced treatment delivery because the results can be correlated with the clinical dose distribution histogram (DVH). In principle, the actual 3D dose can only be measured by polymer gel developed from radiation-sensitive materials. The other commercial 3D dose distribution measurement in a phantom such as DELTA[4®], ArcCheck, and OCTAVIUS[®] 4D systems are known as a Quasi-3D dose reconstruction. DELTA[4®] and ArcCheck have a specific detector arrangement and reconstruct 3D dose measurements using the dose relative to the treatment planning dose calculation [139][144]. OCTAVIUS[®] 4D system is an independent QA tool that can calculate 3D dose distribution using the independent simple data input of a 2D planar detector array measure combination with a rotating phantom that rotates perpendicular to the irradiation beam delivery [227]. Although these devices have good results, 3D dose reconstruction based on coarse detector density (5 mm -10

mm) might not be suitable as the QA tool for small field dosimetry such as SRS and SBRT delivery.

This chapter extends the study described in **Chapter 5**, which demonstrated the excellent agreement of 2D dose distribution measurement using the MP512-EPI comparison to gafchromic EBT3 films and TPS dose calculation. This chapter aims to introduce the use of MP512-EPI as an independent 3D dose distribution reconstruction QA device for small field dosimetry based on the dose calculation method proposed by Allgaier *et al*. [149]. The second purpose is to review and discuss the potential of dataset measured by MP512-EPI and used for clinical 3D dose reconstruction.

6.2. Theoretical background of 3D dose reconstruction

The critical aspect of modelling the dose distribution in a patient is the interpolation and correction of measured data. ArcCheck and DELTA$^{4\circledR}$ using the 3D dose reconstruction that related to the TPS planning. ArcCheck combine with 3DVH software to reconstruct 3D dose distribution using the algorithm call ArcCheck Planar Dose perturbation (ACPDP). Due to the detector of ArcCheck placed on the cylindrical surface, the dose inside the phantom is estimated by convolving TERMA and 3D_kernel using the measured dose at entry and exit detector. Each dose voxel inside the phantom renormalizes to the same dose voxel calculated from the TPS then use those ratio data to generate 3D dose distribution [252]. The 3D dose verification and its comparison with dose predicted by TPS also provided by DELTA$^{4\circledR}$ system. DELTA$^{4\circledR}$ generate dose along radiation rays path by renormalizing the TPS calculation to fit the measured dose at intersect bi-planar diode then use this data to reconstruct 3D dose inside the phantom [253]. Both of these systems reconstruct 3D dose distributions relying on the TPS dose calculation dose while Octavius 4D system uses independence algorithm to reconstruct 3D dose.

The Octavius 4D system reconstructs 3D dose distribution using 2D planar detector (seven29, SRS1000 and 1500OC) in conjunction with a rotating able phantom (OCTAVIUS 4D phantom). To eliminate angular dependence, the detector plane is rotated and synchronised with the treatment gantry to keep the detector perpendicular to the radiation beam during delivery, as shown in Figure 6.1.

(a)   (b)
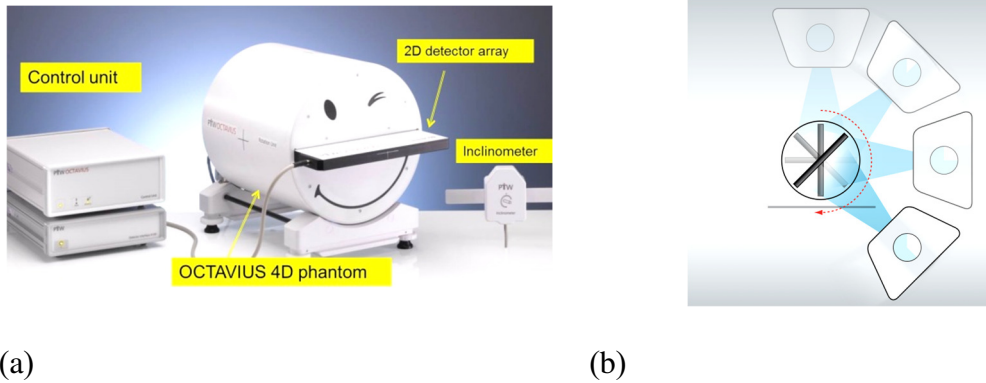
Figure 6.1: OCTAVIUS® 4D system; (a) the component of OCTAVIUS® 4D system and (b) the phantom rotates synchronised with the treatment gantry [254].

Allgaier *et al*. [149] investigated and demonstrated the simple algorithms of the 3D dose reconstruction based on PDDs data. The PDDs for different field sizes were measured at SSD 85 cm in a water phantom and implemented into the Verisoft software. The dose of each voxel along the ray line (D_r) at a distance r was calculated to correspond to the dose obtained from the current detector $D_{det}(0)$ at the current angle, as given by the Equation 6.1 [149][148]. With the non-central axis detector, the Tissue phantom ratio (TPR) correction factors were applied according to Tailor *et al*. [255] for flattening filter beams and Georg *et al*. [256] for flattening filter free beams. The dose was calculated for all detectors and summarised for all the angular measurements.

$$D(r) = D_{Det}(0)\frac{PDD(r)}{PDD(0)}$$ (6.1)

However, the patient densities are not as homogeneous as the phantom. The PDDs was converted to TPRs and the depth along the ray line in the patient CT was scaled to the depth in water. The patient dose (D_{CT}) calculation algorithm was modified based on the above equation and given by Equation 6.2.

$$D_{CT} = D_{Det} \frac{TPR(z_{CT})}{TPR(z_{Det})} \cdot \left(\frac{a_{Det}}{a_{CT}}\right)^2 \tag{6.2}$$

Where a_{Det} and a_{CT} are the distance from the source to detector and current voxel(z_{CT}), respectively.

6.3. Data measurement for commissioning and the factor involved in 3D dose reconstruction

All the data measurements were carried out on a Varian Clinac iX (Palo Alto, CA) at the Illawarra Cancer centre (ICCC), Wollongong Hospital, Australia. These measurements were implemented using 6 MV photon beams because this energy is commonly used in intensity modulated techniques such as IMRT and VMAT.

6.3.1. Percentage depth dose (PDD) measurement and off-axis ratio (OAR)

The important data implementation for 3D dose reconstruction using MP512-EPI is the PDD dataset because PDDs depend on the beam quality, depth, field size and SSD. The beam data implemented to some TPSs or physical validation software for radiotherapy is generally based on small ionisations or diodes measured in a water phantom, but this technique is limited to point measurents and appropriated detector selections that will markedly increase the inaccurate data implementation. In this study, MP512-EPI was

used to measure and generate the dataset for each active pixel MP $_{(ij,z,r)}$. Theoretically, it

is problematical to measure the PDD curves in the PMMA cylindrical phantom itself

because there is no slot that can provide a different depth within the phantom except at

the isocentre depth (z_{phy} = 15 cm). To simplify the PDDs measurement within the original

phantom, MP512-EPI was measured in a Gammex-RWI (Middleton, WI) solid water

phantom slap size 30×30 cm^2 and fixing the SSD at 85 cm, which corresponds to the SSD

of a CMRP phantom. The PDDs were measured by varying the depth of the detector from

0.5 cm to 30 cm (Figure 6.2) and the irradiating the detector at field sizes from 1×1cm^2

to 10×10 cm^2. Although, the solid water phantom RMI has a density ($\rho = 1.04\ g \cdot$

cm^{-2}) close to water equivalent ($\rho = 1.00\ g \cdot cm^{-2}$) the dose distribution within the

solid water phantom is not completely matched with the water phantom [257]. Moreover,

the MP512-EPI was sandwiched between 5 mm thick PMMA, so the depth measurement

must be scaled to the appropriate water-equivalent depth (z_{eq}) as shown in the Equation

6.3, using the mass density in Table 6.1.

$$z_{eq} = \frac{1}{\rho_{water}}\left(z_{sw}\rho_{sw} + z_{pm}\rho_{pm}\right) \tag{6.3}$$

Where z_{sw} and z_{pm} is the depth in a solid water phantom and PMMA, and ρ_{sw} and ρ_{pm} is

the mass density ($g \cdot cm^{-3}$) of the solid water material and PMMA, respectively.

This measurement also provides the off-axis ratio (OAR) of each pixel (MP512$_{ij,z,r}$) for

depth z and field size r, where i is the active pixel in the x-direction, and j is the active

pixel in the y-direction. The off-axis ratio ($OAR_{ij,z,r}$) is the ratio between a dose for

particular points ($D_{ij,z,r}$) and the dose at the central axis ($D_{(13,13),z,r}$) where the central

pixel ij is 13,13; this calculation is given by Equation 6.4.

$$OAR_{ij,z,r} = \frac{D_{ij,z,r}}{D_{(13,13),z,r}} \tag{6.4}$$
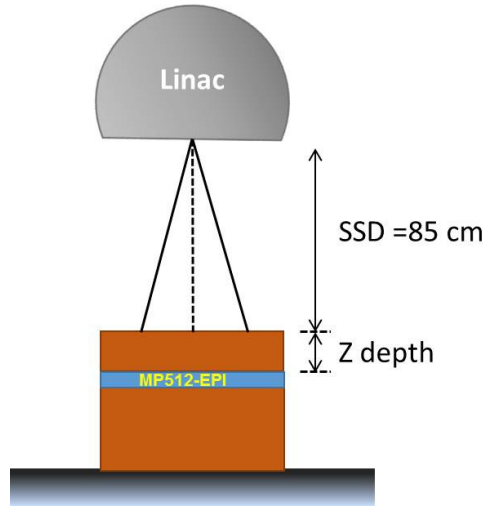
Figure 6.2: Geometry used for PDDs measured

by MP512-EPI at an SSD of 85 cm for 6 MV

photon beams.

6.3.2. Measuring the tissue maximum ratio (TMR)

The tissue maximum ratio (TMR) is the ratio between the dose measured in the phantom

at a particular depth (D_z) and the dose at maximum (D_{max}) at the same distance (SAD)

[37]. TMR is insensitive to the SSD set up and depends on the depth of measurement (z)

and field size at the depth of measurement (r_d). TMRs can generally be calculated by

Equation 6.5 based on the PDDs data while ignoring the peak backscatter factor (BSF),

where z is the depth of measurement, r_d is the field size at the isocentric, and hv is the

photon energy [258][259].

$$TMR_{(z,r_d,hv)} \approx \frac{PDD_{(z,r,SSD,hv)}}{100} \left(\frac{SSD+z}{SSD+z_{max}}\right)^2 \tag{6.5}$$

According to Equation 6.5, PDDs with a smaller field are recommended to calculate the TMRs because measuring PDDs with a field size of less than 3×3 cm^2 is difficult in practice because the detector must be moving, whereas TMRs can be measured with a stationary detector. TMRs for small fields are preferred for direct measurement which is why the TMR dataset in this study was measured in a solid water phantom using the MP512-EPI; these measurements were for 1×1 cm^2, 2×2 cm^2, 3×3 cm^2, 4×4 cm^2, 5×5 cm^2 and 10×10 cm^2 fields. The MP512-EPI was placed at a source to axis distance (SAD) of 100 cm and was provided with a full solid water phantom backscatter thickness of 10 cm, while the solid water slaps above the detector were placed from 0 to 30 cm, as shown in Figure 6.3. The TMRs that were scaled to a water-equivalent depth were compared to the data measured by Markus (ICCC dataset) in the water phantom for field sizes from 3×3 cm^2 to 10×10 cm^2, whereas the TMRs for small fields of 1×1 cm^2 and 2×2 cm^2 were compared to TMRs measured by the CC01 ionisation chamber and stereotactic diode field detector (SFD), as provided by Li *et al.* and Cheng *et al.* [260], [261].
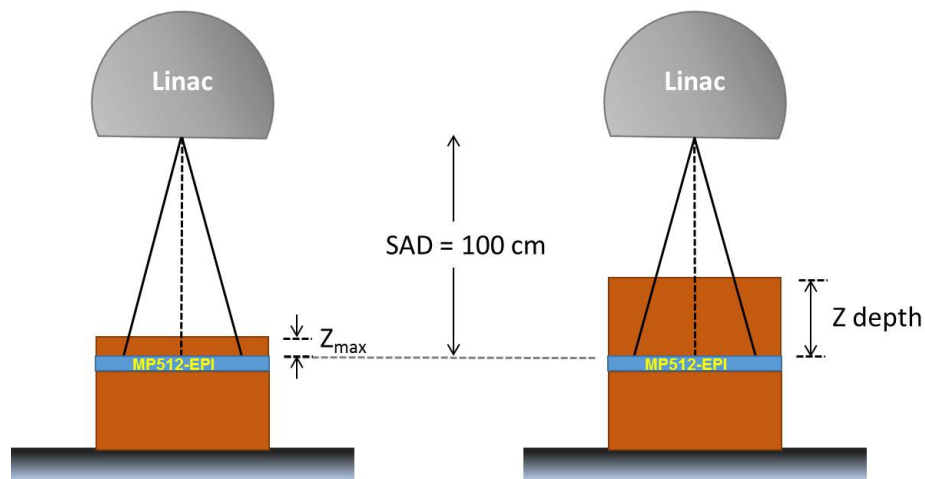
Figure 6.3: Geometry used for TMR measured by MP512-EPI at SAD of 100 cm for 6 MV photon beams.

6.3.3. Electron density of the CMRP phantom

The PMMA cylindrical phantom was scanned with the SOMATOM (Siemens Healthineers, Erlangen, Germany) at ICCC Wollongong hospital. Details of the scan protocol are described in **Chapter 5, section 5.2.4.** The CT data provided the mass and electron density of tissues that were involved with the accuracy of the treatment calculation and optimisation. The CT number (N_{CT}) or Hounsfield Units (HU) were calculated based on the linear attenuation coefficient within the material $\mu_{mat}(x, y)$ relative to the attenuation of water $\mu_{water}(x, y)$; this dose calculation can be described as Equation 6.6 [262].

$$N_{CT} = \left(\frac{\mu_{mat} - \mu_{water}}{\mu_{water}}\right) * 1000 \tag{6.6}$$

HU depended on the electron density and atomic number as well as the spectra energy used for the CT scan.

Over the past decade most treatment planning algorithms, such as the pencil beam (PB), and the analytical anisotropic algorithm (AAA) and collapsed cone (CC) modelled the heterogeneous correction of each voxel using an equivalent path length (EPL) based on the mass density obtained from the CT value [263]. The CT calibration phantom with known mass densities that are relative to human tissue was scanned to calculate the N_{CT} to the mass density calibration curve; a sample of the CT curve is shown in Figure 6.4. However, the EPL method overestimated the dose for bones and air, which is why J. Seco *et al.* introduced the electron density scaling method (eEPL) to correct the heterogeneous depth in the photon dose calculation [264]. The eEPL has been shown the excellent primary photon beams estimated within 1% for energies ranging from 4 to 20 MV; it is

also related to the mass density (ρ_{med}) and effective atomic number ($\left(\frac{Z}{A}\right)_{med}$) as given

by Equation 6.7 and 6.8.

$$\rho_{e_{med}} = \rho_{med} \times \left(\frac{Z}{A}\right)_{med} \tag{6.7}$$

$$eEPL = \sum_{med} l_{e_{med}} \frac{\rho_{e_{med}}}{\rho_{e_{water}}} \tag{6.8}$$

Where the electron density of the medium is $\rho_{e_{med}}$, and the physical length of the medium

is $l_{e_{med}}$.

According to Equation 6.8 the inhomogeneous correction factor based on the PDDs data

at particular field size (r) is calculated by Equation 6.9.

$$ICF = \frac{PDD_{(z_{eEPL}, r)}}{PDD_{(z_{phy}, r)}} \cdot \left(\frac{SSD + z_{eEPL}}{SSD + z_{phy}}\right)^2 \tag{6.9}$$

Where z_{eEPL} is the equivalent depth and z_{phy} is the physical depth.

In this study, eEPL was used to scale the dose distribution and generate the lookup table

for MP512-EPI measurements combined with the CMRP phantom. Table 6.1 shows the

physical mass density and electron density of each phantom used in this study.
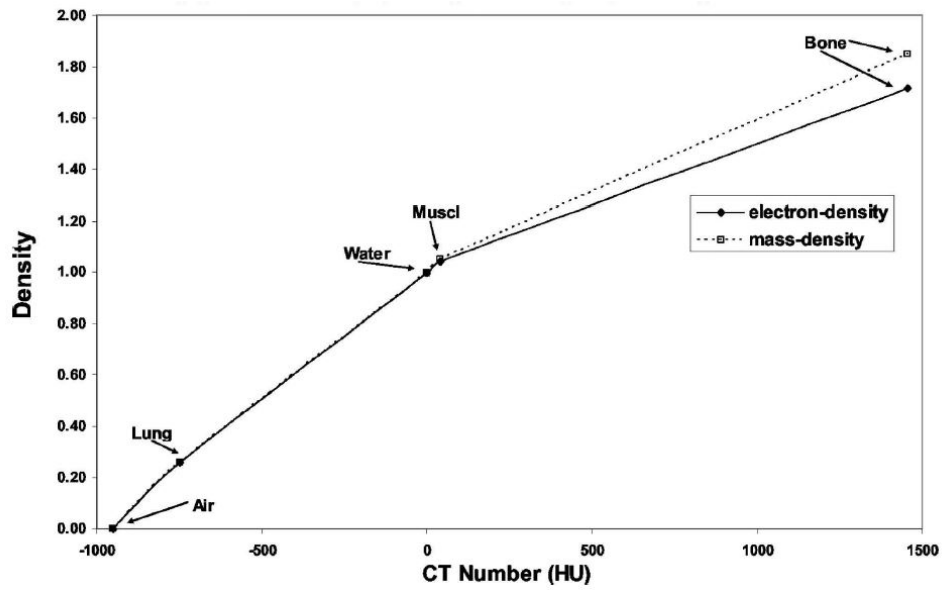
Figure 6.4: The N_{CT} to mass and electron density calibration curve normalised to water [264].

Table 6.1: Characteristic of phantom materials [264][265].

Phantom	Mass density $(g \cdot cm^{-3})$	Z_{eff} (Photoelectric)	$(Z/A)_{eff}$	Electron density relative to water
Water	1.000	7.42	0.555	1.000
Solid water phantom (GAMMEX-RMI457)	1.042	8.06	0.536	1.006
White water RW3	1.045	5.71	0.536	1.009
Plastic water CIRS	1.013	7.92	0.545	0.995
Polystyrene	1.060	5.69	0.538	1.028
PMMA cylindrical phantom	1.170	6.24	0.539	1.136

6.3.4. Equivalent square field calculation

The equivalent square radiation field is the field size that provides the same amount of radiation attenuation and scatter as the field size given with the same SSD. The equivalent

square is calculated to determine the appropriate PDDs and TMRs used in the dose distribution reconstruction. The equivalent square field (A_{eq}) can generally be computed using a simple equation and by following Day's rule (if the field size has the same area/perimeter; A/P) for a rectangular field with the width of x and side of y, as shown in Equation 6.10 [266][259].

$$A_{eq} = \frac{2xy}{x+y} = 4\left(\frac{A}{P}\right) \tag{6.10}$$

However, the IMRT and VMAT delivery that yielded the complex irregular fields must consider the scattering irradiation portion for the equivalent square field calculation. Several algorithms were used to calculate the irregular fields in the dose calculation software such as the ALFARD and Clarkson method [267], but this equation is complicated and time consuming. Equation 6.11 is based on the polar coordinate that proved to be a valid equation for comparing the equivalent field calculation to the experiment data [268][269]. Figure 6.5 shows the relationship between a circular field and a rectangular field, using the polar coordinates.

$$A_{eq} = \frac{2\sqrt{y1+y2}}{1.116}\left(\frac{x1}{y1}\right)^{\frac{\tan^{-1}\left(\frac{y1}{x1}\right)}{2\pi}}\left(\frac{x1}{y2}\right)^{\frac{\tan^{-1}\left(\frac{y2}{x2}\right)}{2\pi}}\left(\frac{x2}{y1}\right)^{\frac{\tan^{-1}\left(\frac{y1}{x2}\right)}{2\pi}}\left(\frac{x2}{y2}\right)^{\frac{\tan^{-1}\left(\frac{y2}{x2}\right)}{2\pi}} \times$$

$$exp\left(\frac{-1}{2\pi}\left(\int_{\tan^{-1}\left(\frac{y1}{x1}\right)-\frac{\pi}{2}}^{\tan^{-1}\left(\frac{y1}{x1}\right)}\ln(\cos\theta)\,d\theta + \int_{\tan^{-1}\left(\frac{y2}{x1}\right)-\frac{\pi}{2}}^{\tan^{-1}\left(\frac{y2}{x1}\right)}\ln(\cos\theta)\,d\theta + \right.\right.$$

$$\left.\int_{\tan^{-1}\left(\frac{y1}{x2}\right)-\frac{\pi}{2}}^{\tan^{-1}\left(\frac{y1}{x2}\right)}\ln(\cos\theta)\,d\theta + \int_{\tan^{-1}\left(\frac{y2}{x2}\right)-\frac{\pi}{2}}^{\tan^{-1}\left(\frac{y2}{x2}\right)}\ln(\cos\theta)\,d\theta - (1 - \right.$$

$$\left.\left. e^{-\mu t}\right)\sum_{i=1}^{n}\iint shield\ ith\frac{dxdy}{x^2+y^2}\right)\right) \tag{6.11}$$
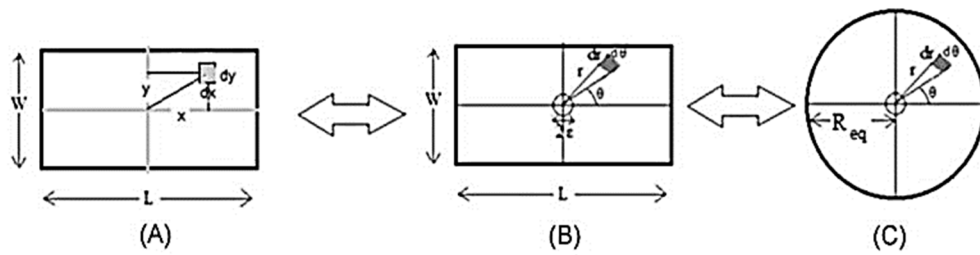
Figure 6.5: The relative field size equivalent using the polar coordinates [268].

6.3.5. Verifying the dose reconstruction for a small static field

The 3D reconstruction method using MP512-EPI in combination with a CMRP phantom can be concluded, and is shown in Figure 6.6. The accuracy of dose reconstruction using the implemented data (PDDs, OARs, and TMRs) measured by MP512-EPI was tested on a static 3×3 cm^2 open field at 6 MV photon beams. This size field was selected because it is suitable for an active detector area (5×5 cm^2) that could ultimately be compared to FWHM and the penumbra. Moreover, a smaller field size could not be verified because the smallest field size data that could implemented to the TPS (Pinnacle V9.6) at CMRP was 3×3 cm^2. The MP512-EPI was aligned at the isocentre of the CMRP phantom and the detector was irradiated with a 100 MU dose at 600 MU/min with the gantry at zero degrees. The cross beam profiles were reconstructed using the PDD and TMR dataset at physical depths of 1.5, 5, 10, 20, and 25 cm, which corresponded to the water-equivalent depth (electron densities corrected) of 1.704, 5.68, 11.36, 22.72 and 28.4, respectively. The reconstructed cross beam profiles were compared to the dose profiles obtained from The TPS.
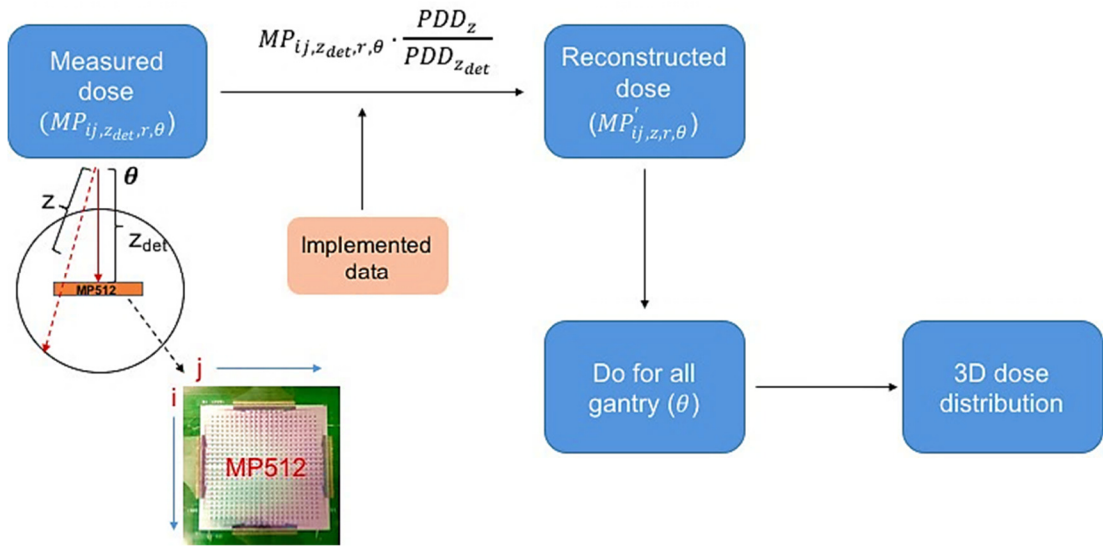
Figure 6.6: Summary of the 3D dose reconstruction based on the algorithm by Allgaier et al. [149].

6.4. Results

6.4.1. PDDs curve and off-axis ratio (OAR)

Figure 6.7 shows the PDD curves of the central axis pixels as a function of water-equivalent depth for different size fields. The PDDs curve measured by MP512-EPI was scaled to the water-equivalent depth using the mass density presents in Equation 6.3 and the shape preserving interpolant function from MATLAB. The PDDs measurement using MP512-EPI also contained the off-axis ratio dataset, as shown in Figure 6.8 and Figure 6.9. The PDD and OAR dataset will be installed as a matrix of field sizes and depths.
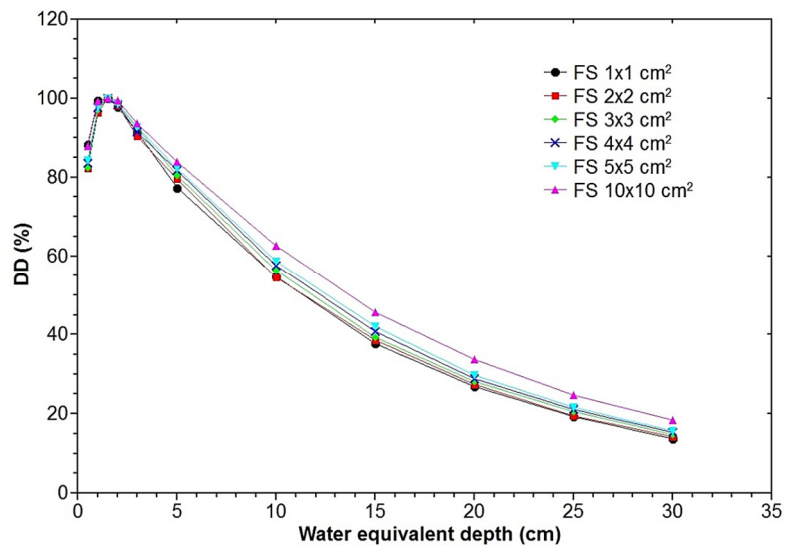
Figure 6.7: Central-axis percentage depth dose (PDD) curves measured by MP512-EPI at an SSD of 85 cm and normalised to a dose at Dmax for 6 MV photon beams ranging from 1×1 cm^2 to 10×10 cm^2.
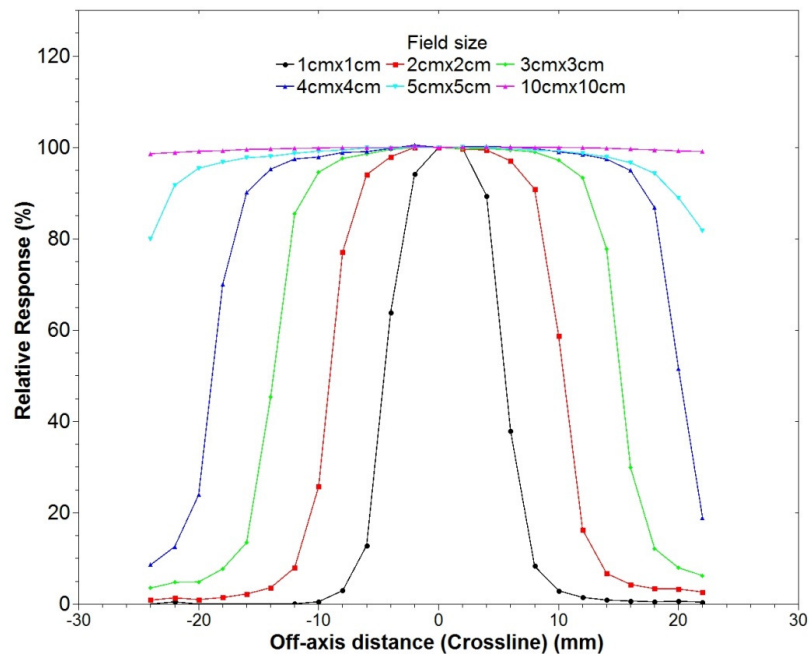
Figure 6.8: The off-axis ratio (MP$_{13j, 10,r}$) measured by MP512-EPI for different size fields at a depth of 10 cm and SSD of 85 cm.

MPi,j	1	2	3	4	5	6	7	8	9	10	11	12	13	14	15	16	17	18	19	20	21	22	23	24
1	0	0	0	0	0	0	0	0	0	2.68438	1.09E-06	1.50608	3.17291	2.40455	1.52087	1.80293	0	0	0	0	0	0	0	0
2	0	1.4161	1.56203	1.65869	1.87456	2.07792	2.35701	3.04816	3.01771	2.98726	4.02068	3.99513	3.90809	3.74398	1.75844	1.75844	1.68986	1.64128	1.60237	1.54639	1.34754	1.227	1.07816	0
3	0	1.45424	1.66324	1.74558	1.98947	2.21178	2.51182	3.24574	3.26781	3.28729	3.44068	3.48239	3.30557	2.91144	2.16483	2.04899	2.01017	2.03131	5.44626	2.95879	2.33361	1.22181	1.09073	0
4	0	1.52753	1.6743	1.84154	2.10873	2.53348	2.75497	2.93225	3.20642	3.89198	3.95306	4.02649	4.30548	3.83737	4.00539	4.17341	2.67354	2.46002	2.3222	2.70425	3.19729	1.36747	1.18072	0
5	0	1.53739	1.72256	2.01194	2.41155	3.09801	3.77458	4.11396	4.49158	5.4321	5.36902	5.39552	5.74863	5.1177	4.41382	4.32404	4.20181	3.88213	3.4638	2.77011	3.22573	1.81078	1.29497	0
6	0	1.67447	1.90704	2.27072	2.91191	4.20792	6.54402	8.77109	9.64844	10.009	9.99376	10.0361	9.97546	9.82724	9.44457	9.11592	9.02092	8.4227	7.39841	5.57328	3.2516	2.59923	2.13329	0
7	0	1.81661	2.12024	2.64624	3.84299	7.85621	19.3825	29.7161	31.7586	33.2207	33.3294	33.486	34.3316	34.1858	34.2431	34.3004	33.9931	34.1799	37.6777	18.1747	5.15607	7.50E-07	2.25729	0
8	0	1.96268	2.33487	3.05294	5.00218	13.7001	57.9018	74.8819	79.6559	81.2433	80.7971	80.1702	81.089	81.8828	82.3027	80.8306	79.9396	79.4067	73.1119	32.4386	7.80074	4.32762	2.69868	0
9	0	2.33816	2.62165	3.46774	5.86866	16.6262	69.0507	89.6982	94.5327	95.315	95.579	94.606	95.021	95.5231	96.2676	96.2604	95.6932	93.2067	85.1646	38.1274	9.01783	4.83044	1.93425	0
10	0.93438	2.30522	2.88062	3.5231	6.02781	17.2139	69.77	91.8132	96.8281	98.1136	98.5817	98.513	98.3669	98.1289	97.7367	97.1843	96.4722	95.3241	87.4363	40.1394	10.1109	4.46925	2.72055	1.76755
11	2.39379	2.27228	3.08717	3.58251	6.18365	17.0127	70.1456	92.9915	97.812	99.3984	98.8121	98.2257	99.049	99.4789	99.5521	99.2927	98.604	96.5073	87.9966	41.4668	11.2847	5.9767	4.17942	3.60077
12	2.54983	2.56264	3.20966	4.35822	6.95269	18.0546	70.2539	93.3568	97.437	98.6776	99.49	99.958	99.0841	99.5068	99.6036	99.1991	98.3118	96.0817	87.6442	42.0877	12.0535	6.46583	4.46179	3.97684
13	2.52556	2.853	3.01473	4.9456	7.14631	18.4649	69.6855	92.7457	97.1785	98.1174	98.7223	98.8526	99.6614	99.0845	99.5284	98.7295	97.0728	96.1006	87.7607	41.9298	11.6291	6.2311	4.55978	3.7338
14	1.63678	2.78998	2.57283	3.75534	6.29208	17.0308	69.4868	93.057	97.7322	98.918	99.2086	99.4677	100	99.6673	99.4982	99.3347	98.189	96.1589	87.9709	42.2194	11.3561	5.85053	4.10349	3.32631
15	0.9841	2.05582	1.68923	3.66835	6.16487	16.6775	70.0904	93.9062	98.6943	100.533	99.0933	99.2601	99.8946	98.9692	99.6421	100.58	99.3915	96.6331	88.1834	41.9725	11.4242	4.27718	2.61725	1.65859
16	0.42925	1.37461	1.29775	3.6324	6.11279	15.5949	68.7168	93.1581	97.4718	99.1321	99.2096	99.1761	99.8578	99.1567	99.4999	100.66	99.5856	97.3838	89.031	41.654	11.5505	3.77514	2.42524	1.25695
17	0	1.83055	1.76446	3.60358	6.06319	15.5469	67.7763	92.105	97.0544	98.5902	98.3203	98.274	99.0851	98.1893	99.0073	99.0802	99.0516	96.6994	89.0438	41.2226	11.6185	5.21524	3.54895	0
18	0	2.2865	2.58788	3.53798	5.94343	15.8791	64.7111	91.4403	95.3294	97.0504	96.8337	96.1707	97.4179	97.236	97.2015	97.1864	97.1434	94.8155	87.2029	40.4643	11.3223	6.94402	3.20819	0
19	0	2.11781	2.50455	3.322	5.34088	14.1729	60.3962	86.1231	89.6047	90.9553	90.8584	91.0796	91.3008	90.7891	90.9678	90.6584	90.6972	86.9605	80.687	39.1648	8.36336	3.55713	2.15823	0
20	0	1.97303	2.25624	2.93021	5.03247	10.0749	38.1369	55.8743	58.26	59.1017	58.7693	58.6784	58.5795	58.0673	56.9015	56.3153	56.1767	53.4305	49.348	23.9278	6.03108	2.86141	1.82332	0
21	0	1.80022	2.05191	2.49969	3.30056	6.18975	10.7302	14.2937	16.0042	17.334	17.6558	17.5558	17.4558	18.3113	16.5417	15.7007	15.0193	15.1864	13.5232	8.27713	4.43132	2.20197	1.52521	0
22	0	1.69524	1.82694	2.10867	2.59135	3.41198	3.97047	4.45138	6.04109	7.08312	7.61383	7.89876	8.10778	8.18899	6.97114	6.13721	6.09052	6.00448	5.81155	4.3641	3.22353	1.78905	1.37408	0
23	0	1.59154	1.67925	1.88344	2.18395	2.60223	2.97268	3.34029	3.83491	4.73419	5.18933	5.03473	5.30691	5.57909	5.18128	4.0322	3.68884	3.8862	4.08356	3.34552	2.54994	1.81014	1.39613	0
24	0	0	0	0	0	0	0	0	3.70851	4.14553	3.17929	3.87674	5.00744	3.84548	3.02064	0	0	0	0	0	0	0	0	0

(a)
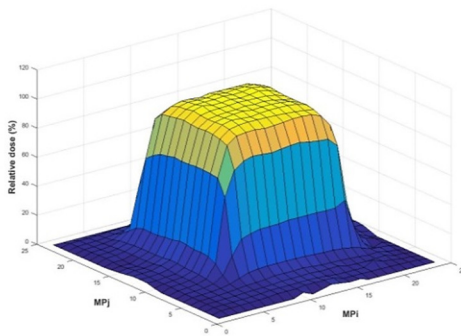
(b)
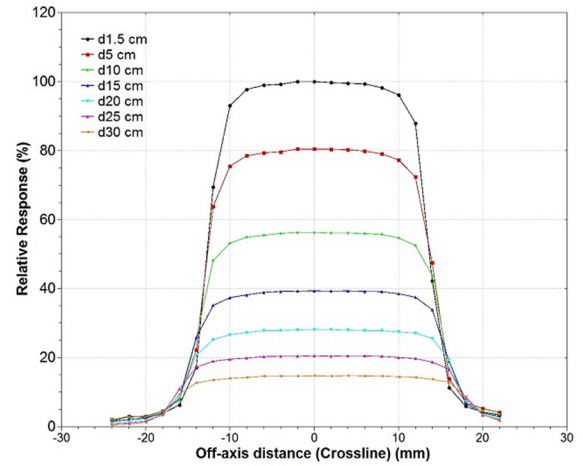
(c)

Figure 6.9: The off-axis ratio of field size $3 \times 3 cm^2$ for 6 MV photon beams measured by MP512-EPI at SSD 85 cm; (a) 2D response map of the off-axis data for each pixel $MP_{(ij)}$ at depth 1.5 cm, (b) the off-axis present in the 3D matrix and (c) the off-axis ratio of $MP_{(13,j)}$ at different depths.

6.4.2. Tissue maximum ratio (TMR) data

Figure 6.10 shows a comparison of central isocentric TMR curves measured by MP512-EPI and different detectors for various size fields. The difference in percentage relative to D_{max} between MP512-EPI, the CC01 ionisation chamber, SFD, and the Markus

chamber are shown in Table 6.2. The TMRs measured by MP512-EPI showed the average relative error to D_{max} was within ±1.5% in comparison to the reference detectors. The maximum under estimation was 1.09% for a 10×10 cm^2 field at a water-equivalent depth of 30 cm.

Table 6.2: The relative errors (Dmax) of the tissue maximum ration (TMR) measured by the MP512-EPI, Markus, CC01 and SFD.

WED (cm)	Field sizes (cm × cm)						
	1×1	2×2		3×3	4×4	5×5	10×10
	MP-CC01	MP-CC01	MP-SFD	MP-Markus	MP-Markus	MP-Markus	MP-Markus
1.5	0.00	0.00	0.00	0.00	0.00	0.00	0.00
5	0.60	-0.10	-0.30	-0.86	0.01	0.05	-0.25
10	-0.10	-0.40	0.00	-0.29	-0.27	-0.14	0.57
15	0.00	-0.60	-0.50	0.51	-0.01	-0.72	0.05
20	-0.50	-1.00	0.30	0.64	-0.38	-0.53	-0.69
25	-0.20	-0.90	0.20	0.24	-0.05	-0.69	-1.08
30	-0.60	-0.70	0.10	0.35	0.28	-0.30	-1.09
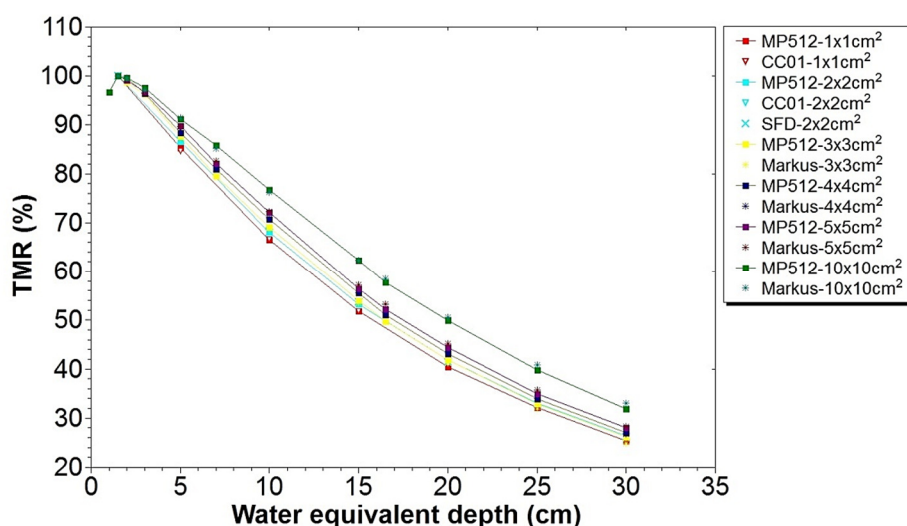
Figure 6.10: The tissue maximum ratio curves for different size fields as measured by MP512-EPI, Markus, CC01, and SFD.

6.4.3. Verifying the dose reconstruction for a small static field

Figure 6.11 shows a comparison of the cross beam profiles of a reconstructed dose along the central axis ($MP_{13,j}$) of a 3×3 cm^2 open field for 6 MV photon beams based on PDD and TMR dataset, where the dose was obtained from TPS at different depths. The results showed an excellent agreement along the cross beam profiles. The dose agreements in the centre of the beam for all depths were almost within ±2%, except for the physical depth of 1.5 cm that had an error up to 2.3% for the dose reconstruction based on PDD data corrected. The FWHM and penumbra for both methods showed excellent agreement within 0.0875±0.62% and 0.0962±0.85 mm. The different agreement between TPS, PDD, and TMR corrected methods were summarised and shown in Table 6.3.

Table 6.3: The different agreement of cross beam profiles between the reconstructed and TPS for different physical depths.

Physical depth (cm)	FWHM (%)		Penumbra (mm)	
	PDD corrected	TMR corrected	PDD corrected	TMR corrected
1.5	0.4547	-0.1414	-1.3670	0.7530
5.0	0.7911	0.9420	-1.0960	1.1540
10.0	0.1596	0.1596	-1.0760	1.0760
20.0	-0.6554	0.6115	-0.6320	0.3650
25.0	-1.2980	-0.1489	-0.4420	0.3030

(a)

(b)

(c)

(d)

(e)
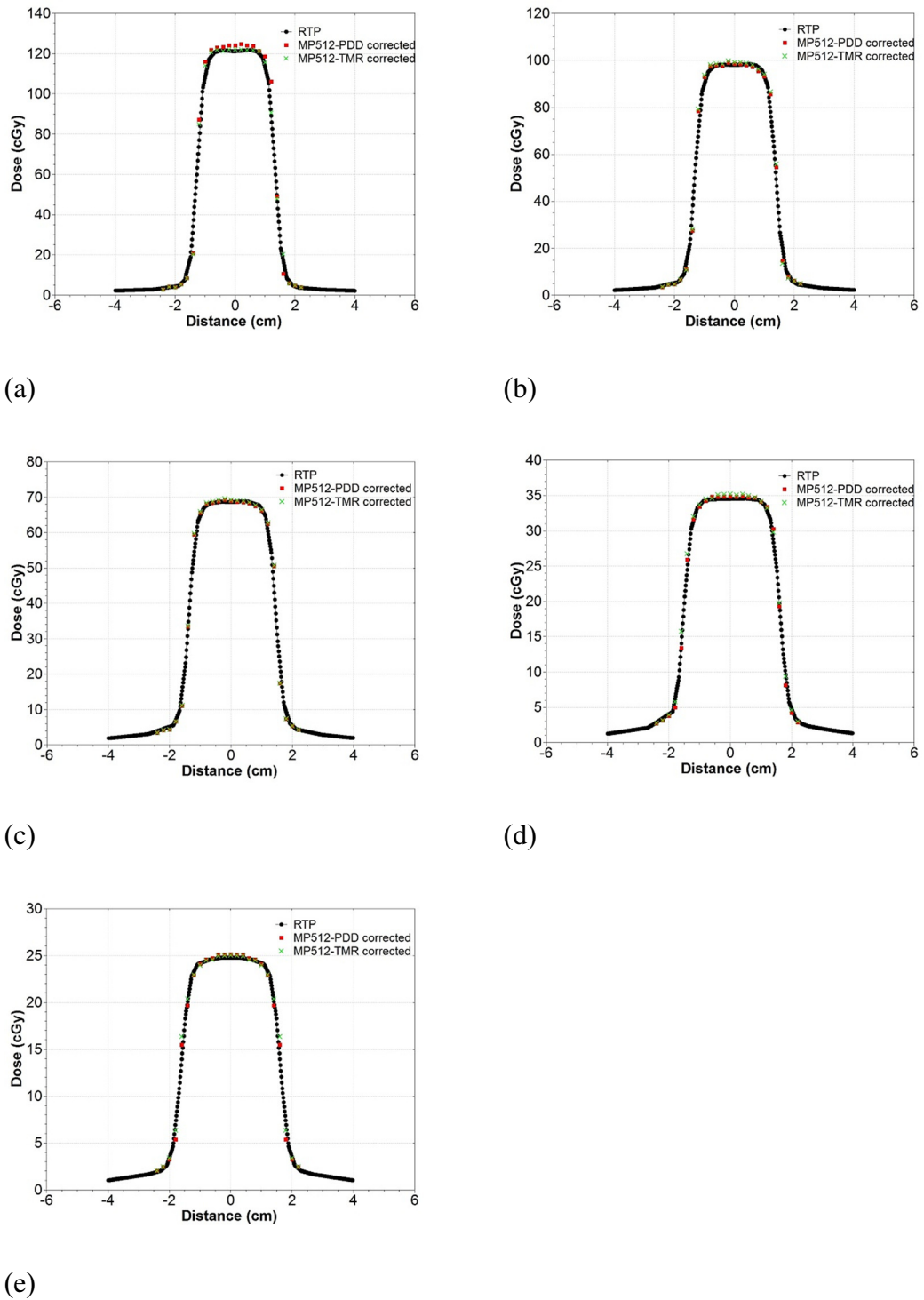
Figure 6.11: The cross beam profiles reconstructed along the central axis ($MP_{13,j}$) of a 3×3 cm^2 open field for 6 MV photon beams were compared to those obtained from TPS at a physical depth of (a) 1.5 cm, (b) 5 cm, (c) 10 cm, (d) 20 cm and (e) 25 cm.

6.5. Conclusions

Verifying the 3D dose distribution involved many steps, such as the efficiency of the detector, design of the phantom, the data implemented and the reconstructed algorithms. This chapter is the primary step for reconstructing a 3D dose using MP512-EPI in conjunction with CMRP phantom, and based on the PDD and TMR calculation methods. In this study we found that reconstructing a 3D dose using the implemented data measured by MP512-EPI was very accurate compared to the TPS for a static 3×3 cm^2 open beam. Reconstructing a dose using TMR data showed better agreement than PDD data, particularly at a physical depth of 1.5 cm because the SSD effect may have influenced these results since we know the PDD depended on SSD. Although the PDD was measured at SSD 85 cm, the maximum depth was not 1.5 cm (approximate water-equivalent depth of 1.44 cm), and the depth close to the surface of the phantom and different scattering from the non-flat surface may be involved. However, this study only showed the cross beams profiles of a 3×3 cm^2 field. The accuracy of the dose reconstruction for various static size fields, especially those smaller than 3×3 cm^2, as well as the complex fields, should be verified. A high spatial resolution of 2 mm of MP512 can provide a high dose reconstruction voxel up to $2\times2\times2$ mm^3 without using the linear interpolation method. This characteristic of MP512-EPI makes the device superior to a commercial detector array for reconstructing doses in small field treatment such as SRS and SBRT. The method of reconstruction and implemented data demonstrated in this study could be further modified and developed for complicated patient dose verification. However, the active area of MP512-EPI is only 5×5 cm^2 so obtaining a small 3D dose volume and CMRP phantom size seems to be inappropriate. Further study of the small rotating phantom will be developed for used in conjunction with MP512-EPI. The accuracy of the rotatable phantom function must be investigated and the full dose measurement using the rotating

phantom and 3D dose reconstruction within the patient CT will be verified. The dose agreement could be moved on from 2D gamma analysis to 3D gamma or DVH-based matric comparison.

Chapter 7

Conclusion and future work

Intricate treatment delivery using a small field such as SRS and SBRT is being used more used extensively but the accuracy of dose distribution must be verified before or during treatment. However, the criticality of a small field means that an appropriate detector and dose algorithms to measure 2D and 3D dose distributions must be developed. This thesis has studied and investigated a high spatial 2D detector array called MagicPlate-512 that was developed as a verification tool for use in small fields. Two detectors were investigated in this thesis, the MP512-Bulk and the MP512-EPI. These devices were successfully characterised as fully dosimetric, so they were then used in conjunction with CMRP for pre-treatment verification of IMRT and VMAT. This chapter summarises the potential outcomes using the MP512-Bulk and MP512-EPI detectors, including a discussion of the advantages and limitations of these device systems. This chapter also presents future study and methods of developing these devices for small field dosimetry.

7.1 The angular dependence study

This study extended the dosimetric characterisation of MP512 presented by Abdullah *et al*. [170]. The MP512-Bulk is a monolithic 2D detector array based on a p-type silicon substrate; it has 512 sensitive pixels arranged to cover an area of 52×52 mm^2 at 2 mm pitches. Each sensitive pixel area is 0.5×0.5 mm^2. The detector was investigated in terms of the effect that field size and energy has on the angular dependence of MP512. An angular correction factor was also developed and verified. The design of MP512 with its

high z material and silicon bulk length of 52 mm limited its use in rotation beam delivery where the irradiation beam is not perpendicular to the MP512 plane. The relative angular response of the MP512-Bulk demonstrated its maximum deviation at an incident beam angle parallel to the detector plane of up to 18.5±0.5% and 15.5±0.5% for 6 MV and 10 MV photon beams, respectively. The angular response of MP512 does not depend on the field size but it does depend on the photon energy. The angular correction method and correction factor with a reference field size of 10×10 cm^2 showed excellent results. The corrected cross beam profiles compared to the dose measured by EBT3 yielded agreements to within 2% for all field sizes and all incident beam angles, except for a 1×1 cm^2 for 6 MV photon beams at an incident angle of 90°. The sophisticated electron scattering in the detector at a parallel beam angle for a small field of less than or equal to 1×1 cm^2 needs further investigation using the Monte Carlo.

7.2 The dosimetric characteristics of MP512-EPI

The MP512-EPI dosimeter was developed based on the high resistivity an epitaxial layer grown on the top of a low resistivity p+ substrate while keeping the arrangement and size of sensitive pixels the same as the MP512-Bulk. The MP512-EPI dosimeter and fast acquisition system based on FPGA has proven to be very useful as a QA device for small field dosimetry. The MP512-EPI dosimeter that was fabricated on a high resistivity 100 Ω cm p-Si epitaxial layer was superior to the MP512-Bulk in terms of radiation hardness, while keeping it full dosimetric characteristics within ±2%, unlike the reference detectors such as the ionisation chamber and gafchromic EBT3 films. Moreover, the MP512-EPI provided excellent long-term reproducibility within ±0.9% for one year without recalibration. EPI-Although the MP512 response had a reduction at a minimum dose per pulse of 2.11×10^{-4} Gy/pulse (SSD 370 cm) up to 8 %. At a typical dose per pulse or SAD

set up for IMRT and VMAT delivery its response revealed it to be dose per pulse independent. The use of MP512-EPI in conjunction with the appropriate air gap provided accurate output factor measurements for field sizes down to 1×1 cm^2. Increasing its thickness from 470 µm (MP512-Bulk) to 535 µm (MP512-EPI) and with a resistivity value of 100 Ω cm did not affect the relative angular response, which demonstrated the percentage difference between two detectors to be within ±2% for both energies. The dose per pulse dependence revealed the effect on PDD when measured by the MP512-EPI, where the depth was more than 20 cm, but the percentage difference relative to the Dmax comparison to IC measurement was within ±2%, and can be improve by correction with the dose per pulse factor.

7.3. 2D and 3D dose reconstruction

The MP512-EPI dosimeter was verified as a QA device for clinical IMRT and VMAT treatment delivery. The 2D dose distribution was measured using MP512-EPI in conjunction with a CMRP cylindrical phantom with different material insertions. The homogeneous and inhomogeneous insertions represented the brain and lung tissue, respectively. Small lesions (GTV) of less than 3 cm^3 were used to plan with the Pinnacle V14. Gamma indexes of 1%/1mm, 2%/2mm and 3%/3mm were used as comparisons between the 2D dose distribution reconstruction of MP512-EPI, RTP dose calculation, and gafchromic EBT3 film dose measurement. The 2D dose distribution was computed using the angular correction method set out in Chapter 3. For the VMAT case, sample angles of 1°, 5°, and 10° were calculated and verified. The 2D dose distribution reconstructed by MP512-EPI demonstrated excellent agreement with the TPS dose calculation and EBT3 measurements. Due to the high spatial resolution (2 mm) of MP512-EPI, the percentage passing rate with a tolerance of 2%/2mm was almost 95%

for all plan deliveries. A more delicate sample angle of angular correction improved the dose agreement at the peripheral region to provide a low dose distribution, but the 2D dose distribution verification cannot present clinically relevant results.

The MP512-EPI dosimeter was also implemented as a 3D dose verification tool. The implemented data and 3D dose reconstruction algorithm were developed and the PDDs and TMRs measured by MP512-EPI in a solid water phantom demonstrated an excellent dataset using the 3D dose algorithm based on the method introduced by Allgaier *et al*. [149]. The reconstructed cross beam profiles of MP512-EPI agreed with the dose obtained from the Pinnacle V9.6 in terms of the central dose, FWHM, and the penumbra for all depths, but this study was only verified for a static 3×3 cm^2 open field; a smaller field and a clinical IMRT or VMAT delivery should also be validated.

7.4. Future work

The design of MP512-EPI with its small active area limited its use for fields larger than 52×52 mm^2, so future work will be directed towards the development of a Quadro MP512-EPI detector with a four tiled MP512-EPI that allows for a sensitive area 10×10 cm^2 while maintaining the same spatial and temporal resolutions.

Further development of the MP512-EPI and the acquisition system would be implemented for 3D dose distribution verification. The DVH matrix will be applied as a comparison method. A rotating phantom would be designed and developed to fit the MP512-EPI, it would have a suitable size and be combined with the rotation validation system. All the data discussed in Chapter 6 will play a big role in the specific domain development which we expect to use as a software application for the proposed a fast 3D dose reconstruction operating in real time measurements. In addition, the validation of 3D dose reconstruction developed in this thesis using high spatial resolution 2D detectors

placed in rotation phantom and software for that will be investigated further by comparison of reconstructed doses with the TPS and some commercial quasi-3D dose verification devices such as ArcCheck and Delta4. Additionally obtained 3D dose will be compared with the actual 3D dose measurement using gel dosimetry.

Bibliography

[1]   R. D. Timmerman and B. D. Kavanagh, "Stereotactic body radiation therapy.," *Curr. Probl. Cancer*, vol. 29, no. 3, pp. 120–57, 2005.

[2]   P. O. Lopez *et al.*, "ICRP publication 112: A report of preventing accidental exposures from new external beam radiation therapy technologies," *Ann. ICRP*, vol. 39, no. 4, 2009.

[3]   T. D. Solberg *et al.*, "Quality and safety considerations in stereotactic radiosurgery and stereotactic body radiation therapy: Executive summary," *Pract. Radiat. Oncol.*, vol. 2, no. 1, pp. 2–9, 2012.

[4]   J. U. Wuerfel, "Dose measurements in small fields," *Med. Phys. Int.*, vol. 1, no. 1, pp. 81–90, 2013.

[5]   L. Potters *et al.*, "American Society for Therapeutic Radiology and Oncology and American College of Radiology practice guideline for the performance of stereotactic body radiation therapy.," *Int. J. Radiat. Oncol. Biol. Phys.*, vol. 60, no. 4, pp. 1026–32, Nov. 2004.

[6]   S. H. Benedict *et al.*, "Stereotactic body radiation therapy: The report of AAPM Task Group 101," *Med. Phys.*, vol. 37, no. 8, p. 4078, 2010.

[7]   L. Leksell, "Occasional review Stereotactic radiosurgery," *J. Neurol. Neurosurg. Psychiatry*, vol. 46, no. April, pp. 797–803, 1983.

[8]   A. J. Hamilton, B. A. Lulu, H. Fosmire, B. Stea, and J. R. Cassady, "Preliminary Clinical Experience with Linear Accelerator-based Spinal Stereotactic Radiosurgery," *Neurosurgery*, vol. 36, no. 2, 1995.

[9]   H. Blomgren and R. U. T. Svanstrom, "Stereotactic radiotherapy of malignancies

in the abdomen," *Acta Oncol. (Madr).*, vol. 33, no. 6, pp. 677–683, 1994.

[10] S. Chawla, R. Abu-Aita, A. Philip, T. Lundquist, P. Okunieff, and M. T. Milano, "Stereotactic radiosurgery for spinal metastases: case report and review of treatment options.," *Bone*, vol. 45, no. 4, pp. 817–21, Oct. 2009.

[11] P. S. Swift, "Radiation for spinal metastatic tumors.," *Orthop. Clin. North Am.*, vol. 40, no. 1, p. 133–44, vii, Jan. 2009.

[12] K. a Ahmed *et al.*, "Stereotactic body radiation therapy in spinal metastases.," *Int. J. Radiat. Oncol. Biol. Phys.*, vol. 82, no. 5, pp. e803-9, Apr. 2012.

[13] C. B. Simone, B. Wildt, A. R. Haas, G. Pope, R. Rengan, and S. M. Hahn, "Stereotactic Body Radiation Therapy for Lung Cancer," *CHEST J.*, vol. 143, no. 6, p. 1784, 2013.

[14] S. W. Davis, D. A. Rahn III, and A. P. Sandhu, "Stereotactic body radiation therapy (SBRT) for non-small cell lung cancer (NSCLC): current concepts and future directions," *Transl. Cancer Res.*, vol. 3, no. 8, pp. 303–312, 2014.

[15] G. C. Sharp, S. B. Jiang, S. Shimizu, and H. Shirato, "Prediction of respiratory tumour motion for real-time image-guided radiotherapy.," *Phys. Med. Biol.*, vol. 49, no. 3, pp. 425–440, 2004.

[16] C. P. Kamerling, M. F. Fast, P. Ziegenhein, M. J. Menten, S. Nill, and U. Oelfke, "Real-time 4D dose reconstruction for tracked dynamic MLC deliveries for lung SBRT," *Med. Phys.*, vol. 43, no. 11, pp. 6072–6081, 2016.

[17] S. S. Vedam, P. J. Keall, V. R. Kini, and R. Mohan, "Determining parameters for respiration-gated radiotherapy.," *Med. Phys.*, vol. 28, no. 10, pp. 2139–2146, 2001.

[18] A. Hutchinson and P. Bridge, "4DCT radiotherapy for NSCLC: a review of planning methods.," *J. Radiother. Pract.*, vol. 14, no. 1, pp. 70–79, 2015.

[19] A. Bezjak, *RTOG 0813: Seamless Phase I/Ii Study of Stereotactic Lung*

Radiotherapy (SBRT) for Early Stage, Centrally Located,Non-Small Cell Lung Cancer (NSCLC) in Medically Inoperable Patients. 2011.

[20] S. Ryu *et al.*, *Radiation Therapy Oncology Group RTOG 0631 Phase II / III Study Of Image-Guided Radiosurgery / SBRT For Localized Spine Metastasis*. 2013.

[21] A. R. Schulz, C. Huntzinger, S. Blacksburg, and K. Rozenzweig, "Stereotactic body radiation therapy (SBRT) for early stage primary liver cancer (HCC)," *Appl. Radiat. Oncol.*, no. March 2012, pp. 12–18, 2012.

[22] M. Scorsetti, E. Clerici, and T. Comito, "Stereotactic body radiation therapy for liver metastases," *J. Gastrointest. Oncol.*, vol. 5, no. 3, pp. 190–197, 2014.

[23] U. Selek, "Spinal Stereotactic Body Radiotherapy," *turknorosirurji.org.tr*, pp. 261–271, 2010.

[24] W. Kilby, J. R. Dooley, G. Kuduvalli, S. Sayeh, and C. R. Maurer, "The CyberKnife Robotic Radiosurgery System in 2010," *Technol. Cancer Res. Treat.*, vol. 9, no. 5, p. 433—452, Oct. 2010.

[25] Y. S. Kim, "Cyberknife robotic radiosurgery system for cancer treatment," *J. Korean Med. Assoc.*, vol. 51, no. 7, pp. 630–637, 2008.

[26] R. L. Dodd, M.-R. Ryu, P. Kamnerdsupaphon, I. C. Gibbs, S. D. J. Chang, and J. R. J. Adler, "CyberKnife Radiosurgery for Benign Intradural Extramedullary Spinal Tumors," *Neurosurgery*, vol. 58, no. 4, 2006.

[27] A. treatment in INDIA, "CyberKnife Radiosurgery - World's Most Advanced Technology at AdvancedTreatmentinindia affiliated Hospitals in India." [Online]. Available: http://www.advancedtreatmentinindia.com/cyberKnife-radiosurgery-in-india.php.

[28] A. Brahme, J.-E. Roos, and I. Lax, "Solution of an integral equation encountered in rotation therapy," *Phys. Med. Biol.*, vol. 27, no. 10, p. 1221, 1982.

Bibliography

[29] Q. J. Wu *et al.*, "Impact of collimator leaf width and treatment technique on stereotactic radiosurgery and radiotherapy plans for intra- and extracranial lesions.," *Radiat. Oncol.*, vol. 4, no. 3, pp. 1–10, 2009.

[30] BRAINLAB, "Novalis comprehensive radiosuregery solution." [Online]. Available: https://www.brainlab.com/en/radiosurgery-products/novalis/.

[31] B. Sells, "Novalis Tx RapidArc." [Online]. Available: https://www.flickr.com/photos/bernd-seils/3925782984.

[32] K. Otto, "Volumetric modulated arc therapy: IMRT in a single gantry arc," *Med. Phys.*, vol. 35, no. 1, pp. 310–317, 2008.

[33] L. Ding *et al.*, "Volume Modulated Arc Therapy (VMAT) for pulmonary Stereotactic Body Radiotherapy (SBRT) in patients with lesions in close approximation to the chest wall.," *Front. Oncol.*, vol. 3, no. February, p. 12, 2013.

[34] M. P. Carol, "Peacock™: A system for planning and rotational delivery of intensity-modulated fields," *Int. J. Imaging Syst. Technol.*, vol. 6, no. 1, pp. 56–61, Mar. 1995.

[35] M. Fuss, C. Shi, and N. Papanikolaou, "Tomotherapeutic stereotactic body radiation therapy: Techniques and comparison between modalities.," *Acta Oncol.*, vol. 45, no. 7, pp. 953–60, 2006.

[36] Technologie Avanzate, "Tomotherapy QA systems." [Online]. Available: http://www.tecnologieavanzate.com/prodotto-18/catalogue/dosimetria-relativa-12/tomotherapy-qa-systems-16.

[37] IAEA, "Absorbed Dose Determination in External Beam Radiotherapy," 2000.

[38] I. J. Das, G. X. Ding, and A. Ahnesjö, "Small fields: Nonequilibrium radiation dosimetry," *Med. Phys.*, vol. 35, no. 1, p. 206, 2008.

[39] M. Tyler *et al.*, "Characterization of small-field stereotactic radiosurgery beams

with modern detectors.," *Phys. Med. Biol.*, vol. 58, no. 21, pp. 7595–608, 2013.

[40] R. Alfonso *et al.*, "A new formalism for reference dosimetry of small and nonstandard fields.," *Med. Phys.*, vol. 35, no. 11, pp. 5179–5186, 2008.

[41] P. H. Charles *et al.*, "A practical and theoretical definition of very small field size for radiotherapy output factor measurements.," *Med. Phys.*, vol. 41, no. 4, p. 41707, Apr. 2014.

[42] W. U. Laub and T. Wong, "The volume effect of detectors in the dosimetry of small fields used in IMRT.," *Med. Phys.*, vol. 30, no. 3, pp. 341–347, 2003.

[43] O. A Sauer and J. Wilbert, "Measurement of output factors for small photon beams.," *Med. Phys.*, vol. 34, no. 6, pp. 1983–1988, 2007.

[44] P. Metcalfe, T. Kron, A. Elliott, and T. Wong, "dosimetry of 6-MV x-ray beam penumbra." pp. 1439–1445, 1993.

[45] PTW, "Small Field Dosimetry Application Guide," pp. 12–13, 2012.

[46] Bjarngard BE, "On Fano's and O'connor's theorems," *Radiat Res*, vol. 109, no. 2, pp. 184–9, 1987.

[47] IPEM, "Small Field MV Photon Dosimetry." p. 196, 2010.

[48] D. a Low, J. M. Moran, J. F. Dempsey, L. Dong, and M. Oldham, "Dosimetry tools and techniques for IMRT.," *Med. Phys.*, vol. 38, no. 3, pp. 1313–1338, 2011.

[49] F. H. Attix, *Introduction to radiological physics and radiation dosimetry*. Wiley-VCH, 2014.

[50] P. R. Almond *et al.*, "AAPM's TG-51 protocol for clinical reference dosimetry of high-energy photon and electron beams.," *Med. Phys.*, vol. 26, no. 9, pp. 1847–1870, 1999.

[51] W. Lechner, H. Palmans, L. Sölkner, P. Grochowska, and D. Georg, "Detector comparison for small field output factor measurements in flattening filter free

photon beams," *Radiother. Oncol.*, vol. 109, no. 3, pp. 356–360, 2013.

[52] E. Pappas *et al.*, "Small SRS photon field profile dosimetry performed using a PinPoint air ion chamber, a diamond detector, a novel silicon-diode array (DOSI), and polymer gel dosimetry. Analysis and intercomparison.," *Med. Phys.*, vol. 35, no. 10, pp. 4640–4648, 2008.

[53] PTW technical note, "Detectors for Small Field Dosimetry", http://www.ptw.de/uploads/media/Detectors_for_Small_Field_Dosimetry_Note_en_63420000_00.pdf, 2010.

[54] C. Martens, C. De Wagter, and W. De Neve, "The value of pinpoint ion chamber for characterization of small field segments used in intensity modulated radiotherapy," *Phys. Med. Biol.*, vol. 45, 2000.

[55] PTW, "PTW detectors for small field dosimetry," 2017. [Online]. Available: http://www.ptw.de/small_field_dosimetry.html.

[56] IBA, "Ionization Chambers and Diode Detectors for Relative and Absolute Dosimetry Air Ionization Chambers," 2013.

[57] G. Rikner and E. Grusell, "General specifications for silicon semiconductors for use in radiation dosimetry.," *Phys. Med. Biol.*, vol. 32, no. 9, pp. 1109–1117, 1987.

[58] J. Shi, W. E. Simon, and T. C. Zhu, "Modeling the instantaneous dose rate dependence of radiation diode detectors.," *Med. Phys.*, vol. 30, no. 9, pp. 2509–2519, 2003.

[59] A. B. Rosenfeld, T. Kron, F. D'Errico, and M. Moscovitch, "Advanced Semiconductor Dosimetry in Radiation Therapy," *AIP Conf. Proc.*, vol. 1345, no. 1, pp. 48–74, 2011.

[60] W. Jong, J. H. D. Wong, and N. Ung, "Characterization of MOSkin detector for in vivo skin dose measurement during megavoltage radiotherapy," *J. Appl. Clin.*

Med. Phys., vol. 15, pp. 120–132, 2014.

[61] P. A Jursinic, "Angular dependence of dose sensitivity of surface diodes.," *Med. Phys.*, vol. 36, no. 6, pp. 2165–2171, 2009.

[62] N. Jornet, M. Ribas, and T. Eudaldo, "In vivo dosimetry: intercomparison between p-type based and n-type based diodes for the 16-25 MV energy range.," *Med. Phys.*, vol. 27, no. 6, pp. 1287–1293, 2000.

[63] G. Casse, "Radiation hardness of p-type silicon detectors," *Nucl. Instruments Methods Phys. Res. Sect. A Accel. Spectrometers, Detect. Assoc. Equip.*, vol. 612, no. 3, pp. 464–469, 2010.

[64] G. Rikner and E. Grusell, "Effects of radiation damage on the silicon lattice," *Phys. Med. Biol.*, vol. 1261, no. 28, 1983.

[65] P. A. Jursinic, "Dependence of diode sensitivity on the pulse rate of delivered radiation.," *Med. Phys.*, vol. 40, no. 2, p. 21720, 2013.

[66] F. Marsolat *et al.*, "Diamond dosimeter for small beam stereotactic radiotherapy," *Diam. Relat. Mater.*, vol. 33, pp. 63–70, 2013.

[67] M. J. Guerrero, D. Tromson, M. Rebisz, C. Mer, B. Bazin, and P. Bergonzo, "Requirements for synthetic diamond devices for radiotherapy dosimetry applications," *Diam. Relat. Mater.*, vol. 13, no. 11–12, pp. 2046–2051, 2004.

[68] J. M. Larraga-GutierreZ, P. Ballesteros-Zebadï, M. Rodrïguez-Ponce, O. A. Garcï-Garduno, and O. O. G. De La Cruz, "Properties of a commercial PTW-60019 synthetic diamond detector for the dosimetry of small radiotherapy beams," *Phys. Med. Biol.*, vol. 60, no. 2, pp. 905–924, 2015.

[69] S. Almaviva *et al.*, "Synthetic single crystal diamond dosimeters for Intensity Modulated Radiation Therapy applications," *Nucl. Instruments Methods Phys. Res. Sect. A Accel. Spectrometers, Detect. Assoc. Equip.*, vol. 608, no. 1, pp. 191–

194, 2009.

[70] M. Heydarian, P. W. Hoban, W. A. Beckham, I. M. Borchardt, and A. H. Beddoe, "Evaluation of a PTW diamond detector for electron beam measurements," *Phys. Med. Biol.*, vol. 38, no. 8, pp. 1035–1042, 1993.

[71] ESTAR, "National Institute of standards and technology (NIST)." [Online]. Available: http://physics.nist.gov/PhysicRefData/Star/Text/ESTAR.html.

[72] M. Marinelli, G. Prestopino, C. Verona, and G. Verona-Rinati, "Experimental determination of the PTW 60019 microDiamond dosimeter active area and volume," *Med. Phys.*, vol. 43, no. 9, pp. 5205–5212, 2016.

[73] W. U. Laub and R. Crilly, "Clinical radiation therapy measurements with a new commercial synthetic single crystal diamond detector," *J. Appl. Clin. Med. Phys.*, vol. 15, no. 6, pp. 92–102, 2014.

[74] I. Das, Y. Akino, and P. Francescon, "TU-F-BRE-05: Experimental Determination of K Factor in Small Field Dosimetry," *Med. Phys.*, vol. 41, no. 6Part27, p. 469, 2014.

[75] P. Mancosu *et al.*, "Evaluation of a synthetic single-crystal diamond detector for relative dosimetry on the Leksell Gamma Knife Perfexion radiosurgery system," *Med. Phys.*, vol. 42, no. 9, pp. 5035–5041, 2015.

[76] J. Dosimetry, "Dosimetry of cone-defined stereotactic radiosurgery fields with a commercial synthe ... Pagina 1 di 1 Dosimetry of cone-defined stereotactic radiosurgery fields with a commercial synthetic diamond detector," p. 75952, 2014.

[77] S. Russo *et al.*, "Multicenter evaluation of a synthetic single-crystal diamond detector for CyberKnife small field size output factors," *Phys. Medica*, vol. 32, no. 4, pp. 575–581, 2016.

[78] PTW, "microDiamond Synthetic Diamond detector." [Online]. Available: http://www.ptw.de/2732.html.

[79] A. S. Beddar, T. R. Mackie, and F. H. Attix, "Water-equivalent plastic scintillation detectors for high-energy beam dosimetry: I. Physical characteristics and theoretical consideration.," *Phys. Med. Biol.*, vol. 37, no. 10, pp. 1883–900, 1992.

[80] A. S. Beddart, T. R. Mackie, and F. H. Attix, "Water-equivalent plastic scintillation detectors for high- energy beam dosimetry: II. Properties and measurements A," *Phys. Med. Biol*, vol. 37, no. 10, pp. 1883–1900, 1992.

[81] J. M. Fontbonne *et al.*, "Scintillating fiber dosimeter for radiation therapy accelerator," *IEEE Trans. Nucl. Sci.*, vol. 49 I, no. 5, pp. 2223–2227, 2002.

[82] P. Z. Y. Liu, "Plastic scintillation dosimetry: comparison of three solutions for cerenkov challenge," *Phys. Med. Biol*, vol. 56, p. 5805, 2011.

[83] L. M. Moutinho, I. F. Castro, L. Peralta, M. C. Abreu, and J. F. C. A. Veloso, "Development of a scintillating optical fiber dosimeter with silicon photomultipliers," *Nucl. Instruments Methods Phys. Res. Sect. A Accel. Spectrometers, Detect. Assoc. Equip.*, vol. 735, pp. 640–643, 2014.

[84] T. C. Zhu, L. Ding, C. R. Liu, J. R. Palta, W. E. Simon, and J. Shi, "Performance evaluation of a diode array for enhanced dynamic wedge dosimetry.," *Med. Phys.*, vol. 24, no. 7, pp. 1173–1180, 1997.

[85] B. Petrovic, A. Grzadziel, L. Rutonjski, and K. Slosarek, "Linear array measurements of enhanced dynamic wedge and treatment planning system (TPS) calculation for 15 MV photon beam and comparison with electronic portal imaging device (EPID) measurements," *Radiol. Oncol.*, vol. 44, no. 3, pp. 199–206, Sep. 2010.

[86] J. H. D. Wong *et al.*, "The use of a silicon strip detector dose magnifying glass in

stereotactic radiotherapy QA and dosimetry.," *Med. Phys.*, vol. 38, no. 3, pp. 1226–1238, 2011.

[87]   S. Pai *et al.*, "Radiographic film for megavoltage beam dosimetry.," *Med. Phys.*, vol. 34, no. 6, pp. 2228–2258, 2007.

[88]   T. M. Bogucki, W. R. Murphy, C. W. Baker, S. S. Piazza, and A. G. Haus, "Processor quality control in lase imaging systems," *Med. Phys.*, vol. 4, 1997.

[89]   P. Papaconstadopoulos, G. Hegyi, J. Seuntjens, and S. Devic, "A protocol for EBT3 radiochromic film dosimetry using reflection scanning.," *Med. Phys.*, vol. 41, no. 12, p. 122101, 2014.

[90]   R. Dreindl, D. Georg, and M. Stock, "Radiochromic film dosimetry: Considerations on precision and accuracy for EBT2 and EBT3 type films," *Z. Med. Phys.*, vol. 24, no. 2, pp. 153–163, 2014.

[91]   V. Casanova Borca *et al.*, "Dosimetric characterization and use of GAFCHROMIC EBT3 film for IMRT dose verification.," *J. Appl. Clin. Med. Phys.*, vol. 14, no. 2, p. 4111, 2013.

[92]   J. Eduardo Villarreal-Barajas and R. F. H. Khan, "Energy response of EBT3 radiochromic films: Implications for dosimetry in kilovoltage range," *J. Appl. Clin. Med. Phys.*, vol. 15, no. 1, pp. 331–338, 2014.

[93]   E. E. Wilcox and G. M. Daskalov, "Evaluation of GAFCHROMIC® EBT film for CyberKnife® dosimetry," *Med. Phys.*, vol. 34, no. 6, p. 1967, 2007.

[94]   N. Hardcastle, A. Basavatia, A. Bayliss, and W. A. Tomé, "High dose per fraction dosimetry of small fields with Gafchromic EBT2 film," *Med. Phys.*, vol. 38, no. 7, pp. 4081–4085, 2011.

[95]   M. Fuss, E. Sturtewagen, C. De Wagter, and D. Georg, "Dosimetric characterization of GafChromic EBT film and its implication on film dosimetry

quality assurance.," *Phys. Med. Biol.*, vol. 52, no. 14, pp. 4211–25, Jul. 2007.

[96] J. E. Morales, M. Butson, S. B. Crowe, R. Hill, and J. V. Trapp, "An experimental extrapolation technique using the Gafchromic EBT3 film for relative output factor measurements in small x-ray fields," *Med. Phys.*, vol. 43, no. 8, pp. 4687–4692, 2016.

[97] D. S. Sharma *et al.*, "Experimental determination of stereotactic cone size and detector specific output correction factor," *Br. J. Radiol.*, vol. 90, no. 1077, Aug. 2017.

[98] C. R. Blackwell *et al.*, "Radiochromic Film Dosimetry: Recommendation of AAPM Radiation Therapy Committe Task Group 55," vol. 25, no. 63, pp. 2093–2115, 1998.

[99] S. Amerio *et al.*, "Dosimetric characterization of a large area pixel-segmented ionization chamber," *Med. Phys.*, vol. 31, no. 0094–2405; 2, pp. 414–420, 2004.

[100] M. Stasi *et al.*, "D-IMRT verification with a 2D pixel ionization chamber: dosimetric and clinical results in head and neck cancer," *Phys. Med. Biol.*, vol. 50, no. 19, pp. 4681–4694, 2005.

[101] S. Alashrah, S. Kandaiya, S. Y. Yong, and S. K. Cheng, "Characterization of a 2D ionization chamber array for IMRT plan verification," *Nucl. Instruments Methods Phys. Res. Sect. A Accel. Spectrometers, Detect. Assoc. Equip.*, vol. 619, no. 1–3, pp. 181–185, Jul. 2010.

[102] R. Boggula, M. Birkner, F. Lohr, V. Steil, F. Wenz, and H. Wertz, "Evaluation of a 2D detector array for patient-specific VMAT QA with different setups," *Phys. Med. Biol.*, vol. 56, no. 22, pp. 7163–7177, 2011.

[103] J. G. Li, G. Yan, and C. Liu, "comparison of two commercial detector arrays for IMRT qualty assurance," *J. Appl. Clin. Med. Phys.*, vol. 10, no. 2, pp. 1–11, 2009.

[104] J. Herzen *et al.*, "Dosimetric evaluation of a 2D pixel ionization chamber for implementation in clinical routine.," *Phys. Med. Biol.*, vol. 52, pp. 1197–1208, 2007.

[105] M. Hussein, E. J. Adams, T. J. Jordan, C. H. Clark, and A. Nisbet, "A critical evaluation of the PTW 2D-ARRAY seven29 and OCTAVIUS II phantom for IMRT and VMAT verification," *J. Appl. Clin. Med. Phys.*, vol. 14, no. 6, pp. 274–292, 2013.

[106] S. a Syamkumar, S. Padmanabhan, P. Sukumar, and V. Nagarajan, "Characterization of responses of 2d array seven29 detector and its combined use with octavius phantom for the patient-specific quality assurance in rapidarc treatment delivery.," *Med. Dosim.*, vol. 37, no. 1, pp. 53–60, Jan. 2012.

[107] T. S. Stelljes *et al.*, "Dosimetric characteristics of the novel 2D ionization chamber array OCTAVIUS Detector 1500," *Med. Phys.*, vol. 42, no. 4, pp. 1528–1537, 2015.

[108] A. Van Esch, K. Basta, M. Evrard, M. Ghislain, F. Sergent, and D. P. Huyskens, "The Octavius1500 2D ion chamber array and its associated phantoms: Dosimetric characterization of a new prototype," *Med. Phys.*, vol. 41, no. 9, p. 91708, 2014.

[109] B. Poppe, T. S. Stelljes, H. K. Looe, N. Chofor, D. Harder, and K. Willborn, "Performance parameters of a liquid filled ionization chamber array.," *Med. Phys.*, vol. 40, no. 8, p. 82106, 2013.

[110] P. A. Jursinic and B. E. Nelms, "A 2-D diode array and analysis software for verification of intensity modulated radiation therapy delivery," *Med. Phys.*, vol. 30, no. 5, p. 870, 2003.

[111] P. a Jursinic, R. Sharma, and J. Reuter, "MapCHECK used for rotational IMRT measurements: step-and-shoot, TomoTherapy, RapidArc.," *Med. Phys.*, vol. 37,

no. 6, pp. 2837–2846, 2010.

[112] D. S. Saini, "IMRT QA with 2-dimensional Diode Array of Detectors," *October*, 2004.

[113] P. A. Jursinic and B. E. Nelms, "A 2-D diode array and analysis software for verification of intensity modulated radiation therapy delivery," *Med. Phys.*, vol. 30, no. 5, pp. 870–9, 2003.

[114] Q. L. Li, X. W. Deng, L. X. Chen, and S. M. Huang, "The angular dependence of a 2 - dimensional diode array and the feasibility of its application in verifying the composite dose distribution of intensity - modulated radiation therapy," *Chin. J. Cancer*, pp. 617–620, 2010.

[115] SUN NUCLEAR coroporation, "MapCHECK2&3 DVH the gold standard for 2D arrays," 2017. [Online]. Available: https://www.sunnuclear.com/solutions/patientqa/mapcheck.

[116] IBA, "iba-dosimetry." [Online]. Available: http://www.iba-dosimetry.com/solutions/radiation-therapy/patient-qa/matrixx-universal-detector-array/.

[117] A. Van Esch, T. Depuydt, and D. P. Huyskens, "The use of an aSi-based EPID for routine absolute dosimetric pre-treatment verification of dynamic IMRT fields," *Radiother. Oncol.*, vol. 71, no. 2, pp. 223–234, 2004.

[118] T. Fuangrod *et al.*, "Investigation of a real-time EPID-based patient dose monitoring safety system using site-specific control limits," *Radiat. Oncol.*, vol. 11, no. 1, p. 106, 2016.

[119] B. J. M. Heijmen *et al.*, "Portal dose measurement in radiotherapy using an electronic portal imaging device (EPID)," *Phys. Med. Biol.*, vol. 40, no. 11, p. 1943, 1995.

Bibliography

[120] K. L. Pasma, M. Kroonwijk, J. C. J. De Boer, A. G. Visser, and B. J. M. Heijmen, "Accurate portal dose measurement with a fluoroscopic electronic portal imaging device (EPID) for open and wedged beams and dynamic multileaf collimation," *Phys. Med. Biol.*, vol. 43, no. 8, p. 2047, 1998.

[121] A. Van Esch, B. Vanstraelen, J. Verstraete, G. Kutcher, and D. Huyskens, "Pretreatment dosimetric verification by means of a liquid-filled electronic portal imaging device during dynamic delivery of intensity modulated treatment fields," *Radiother. Oncol.*, vol. 60, no. 2, pp. 181–190, 2001.

[122] P. Winkler, A. Hefner, and D. Georg, "Dose-response characteristics of an amorphous silicon EPID," *Med. Phys.*, vol. 32, no. 10, pp. 3095–3105, 2005.

[123] M. G. Herman *et al.*, "Clinical use of electronic portal imaging: Report of AAPM Radiation Therapy Committee Task Group 58," *Med. Phys.*, vol. 28, no. 5, pp. 712–737, 2001.

[124] M. Sabet, P. Rowshanfarzad, F. W. Menk, and P. B. Greer, "Transit dosimetry in dynamic IMRT with an a-Si EPID," *Med. Biol. Eng. Comput.*, vol. 52, no. 7, pp. 579–588, 2014.

[125] H. Gustafsson, P. Vial, Z. Kuncic, C. Baldock, and P. B. Greer, "EPID dosimetry: Effect of different layers of materials on absorbed dose response," *Med. Phys.*, vol. 36, no. 12, pp. 5665–5674, 2009.

[126] H. Fricke and E. Hart, "Chemical dosimetry," *Radiat. Dosim.*, vol. 2, 1955.

[127] G. Ibbott, "Applications of gel dosimetry," *J. Phys. Conf. Ser.*, vol. 3, pp. 58–77, 2004.

[128] C. Baldock, P. Harris, A. Piercy, and B. Healy, "Experimental determination of the diffusion coefficient in two-dimensions in ferrous sulphate gels uisng the finite element method," *Australas. Phys. Eng.Sci. Med.,* vol. 24, pp. 19–30, 2001.

[129] L. J. Schreiner, "Review of Fricke gel dosimeters," *J. Phys. Conf. Ser.*, vol. 3, pp. 9–21, 2004.

[130] C. Baldock *et al.*, "Polymer gel dosimetry.," *Phys. Med. Biol.*, vol. 55, no. 5, pp. R1–R63, 2010.

[131] M. McJury *et al.*, "Radiation dosimetry using polymer gels: methods and applications," *Br. J. Radiol.*, vol. 73, no. 873, pp. 919–929, 2000.

[132] S. Back, S. Ceberg, and H. Gustafsson, "Gel Dosimetry for Verification of Dynamic Radiotherapy," *Radiother. Oncol.*, vol. 92, p. S126, 2009.

[133] C. Baldock, "Review of gel dosimetry: a personal reflection," *J. Phys. Conf. Ser.*, vol. 755, no. February, 2016.

[134] J. Adamovics and M. J. Maryanski, "Characterisation of PRESAGE[TM]: A new 3-D radiochromic solid polymer dosemeter for ionising radiation," *Radiat. Prot. Dosimetry*, vol. 120, no. 1–4, pp. 107–112, 2006.

[135] J. Adamovics and M. J. Maryanski, "A new approach to radiochromic three-dimensional dosimetry-polyurethane," *J. Phys. Conf. Ser.*, vol. 3, pp. 172–175, 2004.

[136] a Thomas, J. Newton, J. Adamovics, and M. Oldham, "WE-E-BRB-08: Commissioning and Benchmarking a 3D Dosimetry System for Clinical Use," *Med. Phys.*, vol. 38, no. 6, p. 3817, 2011.

[137] M. Alqathami, A. Blencowe, G. Qiao, D. Butler, and M. Geso, "Optimization of the sensitivity and stability of the PRESAGE[TM] dosimeter using trihalomethane radical initiators," *Radiat. Phys. Chem.*, vol. 81, no. 7, pp. 867–873, 2012.

[138] T. Gorjiara *et al.*, "Investigation of radiological properties and water equivalency of PRESAGE® dosimeters," *Med. Phys.*, vol. 38, no. 4, pp. 2265–2274, 2011.

[139] G. Li *et al.*, "Evaluation of the ArcCHECK QA system for IMRT and VMAT

verification," *Phys. Medica*, vol. 29, no. 3, pp. 295–303, 2013.

[140] J. Qian *et al.*, "Dose reconstruction for volumetric modulated arc therapy (VMAT) using cone-beam CT and dynamic log files.," *Phys. Med. Biol.*, vol. 55, no. 13, pp. 3597–3610, 2010.

[141] V. Feygelman, G. Zhang, C. Stevens, and B. E. Nelms, "Evaluation of a new VMAT QA device, or the 'X' and 'O' array geometries.," *J. Appl. Clin. Med. Phys.*, vol. 12, no. 2, p. 3346, 2011.

[142] R. Thiyagarajan *et al.*, "Analyzing the performance of ArcCHECK diode array detector for VMAT plan," *Reports Pract. Oncol. Radiother.*, vol. 21, no. 1, pp. 50–56, 2016.

[143] R. Thiyagarajan *et al.*, "Analyzing the performance of ArcCHECK diode array detector for VMAT plan," *Reports Pract. Oncol. Radiother.*, vol. 21, no. 1, pp. 50–56, 2016.

[144] J. L. Bedford, Y. K. Lee, P. Wai, C. P. South, and A. P. Warrington, "Evaluation of the Delta4 phantom for IMRT and VMAT verification.," *Phys. Med. Biol.*, vol. 54, no. 9, pp. N167–N176, 2009.

[145] A. N. Gutiérrez and O. Calvo, "Diode Arrays and QA of Advanced Techniques," *J. Phys. Conf. Ser.*, vol. 250, p. 12049, 2010.

[146] V. Feygelman, D. Opp, K. Javedan, a. J. Saini, and G. Zhang, "Evaluation of a 3D Diode Array Dosimeter for Helical Tomotherapy Delivery QA," *Med. Dosim.*, vol. 35, no. 4, pp. 324–329, 2010.

[147] T. Pham and J. Luo, "Clinical Implementation of a 3D Dosimeter for Accurate IMRT and VMAT Patient Specific QA," *Open J. Biophys.*, vol. 3, no. February, pp. 99–111, 2013.

[148] C. K. McGarry, B. F. O'Connell, M. W. D. Grattan, C. E. Agnew, D. M. Irvine,

and A. R. Hounsell, "Octavius 4D characterization for flattened and flattening filter free rotational deliveries.," *Med. Phys.*, vol. 40, no. 9, p. 91707, Sep. 2013.

[149] B. Allgaier, E. Schüle, and J. Würfel, "Dose reconstruction in the OCTAVIUS 4D phantom and in the patient without using dose information from the TPS," *PTW D913.200.06/00*, no. October, pp. 0–7, 2013.

[150] M. van Zijtveld, M. L. P. Dirkx, H. C. J. de Boer, and B. J. M. Heijmen, "3D dose reconstruction for clinical evaluation of IMRT pretreatment verification with an EPID.," *Radiother. Oncol.*, vol. 82, no. 2, pp. 201–7, Feb. 2007.

[151] T. R. McNutt, "Modeling dose distributions from portal dose images using the convolution/superposition method," *Med. Phys.*, vol. 23, no. 8, p. 1381, 1996.

[152] SUN NUCLEAR coroporation, "EPIDose." [Online]. Available: http://www.dta.com.es/index_htm_files/epidose.pdf.

[153] N. Narloch, "On the clinically relevant detector resolution and error detection capability of COMPASS 3D plan verification," vol. 38, no. February, pp. 1–12, 2011.

[154] F. Clemente-Gutiérrez and C. Pérez-Vara, "Dosimetric validation and clinical implementation of two 3D dose verification systems for quality assurance in volumetric-modulated arc therapy techniques," *J. Appl. Clin. Med. Phys.*, vol. 16, no. 2, pp. 198–217, 2015.

[155] D. Harder, "The influence of a novel transmission detector on 6 MV x-ray beam characteristics," *Phys. Med. Biol.*, vol. 54, no. 3, pp. 3173–3183, 2009.

[156] D. Harder, "The influence of a novel transmission detector on 6 MV x-ray beam characteristics," *Phys. Med. Biol.*, vol. 54, no. 3, pp. 3173–3183, 2009.

[157] J. Thoelking, Y. Sekar, J. Fleckenstein, F. Lohr, F. Wenz, and H. Wertz, "Characterization of a new transmission detector for patient individualized online

plan verification and its influence on 6MV X-ray beam characteristics," *Z. Med. Phys.*, vol. 26, no. 3, pp. 200–208, 2016.

[158] J. Thoelking *et al.*, "Patient-specific online dose verification based on transmission detector measurements," *Radiother. Oncol.*, vol. 119, no. 2, pp. 351–356, 2016.

[159] B. Poppe *et al.*, "DAVID—a translucent multi-wire transmission ionization chamber for *in vivo* verification of IMRT and conformal irradiation techniques," *Phys. Med. Biol.*, vol. 51, no. 5, pp. 1237–1248, 2006.

[160] M. K. Islam *et al.*, "An integral quality monitoring system for real-time verification of intensity modulated radiation therapy," *Med. Phys.*, vol. 36, no. 12, pp. 5420–5428, 2009.

[161] B. R. Paliwal, M. Zaini, T. McNutt, E. J. Fairbanks, and R. Kitchen, "A consistency monitor for radiation therapy treatments," *Med. Phys.*, vol. 23, no. 10, pp. 1805–1807, 1996.

[162] B. Poppe, H. K. Looe, N. Chofor, A. Rühmann, D. Harder, and K. C. Willborn, "Clinical performance of a transmission detector array for the permanent supervision of IMRT deliveries," *Radiother. Oncol.*, vol. 95, no. 2, pp. 158–165, 2010.

[163] B. Poppe, H. K. Looe, N. Chofor, A. Rühmann, D. Harder, and K. C. Willborn, "Clinical performance of a transmission detector array for the permanent supervision of IMRT deliveries," *Radiother. Oncol.*, vol. 95, no. 2, pp. 158–165, 2010.

[164] Scandidos, "Delta Discover[4]," http://delta4family.com/products, 2017

[165] T. Li, Q. J. Wu, T. Matzen, F. F. Yin, and J. C. O'Daniel, "Diode-based transmission detector for IMRT delivery monitoring: A validation study," *J. Appl. Clin. Med. Phys.*, vol. 17, no. 5, pp. 235–244, 2016.

[166] E. Grusell and G. Rikner, "Radiation damage induced dose rate non-linearity in an n-type silicon detector.," *Acta Radiol. Oncol.*, vol. 23, no. 6, pp. 465–469, 1984.

[167] E. Grusell and G. Rikner, "Linearity with dose rate of low resistivity p-type silicon semiconductor detectors," *Phys. Med. Biol.*, vol. 38, no. 6, p. 785, 1993.

[168] J. H. D. Wong *et al.*, "Characterization of a novel two dimensional diode array the 'magic plate' as a radiation detector for radiation therapy treatment.," *Med. Phys.*, vol. 39, no. 5, pp. 2544–58, May 2012.

[169] K. Al Shukaili *et al.*, "A 2D silicon detector array for quality assurance in small field dosimetry: DUO:," *Med. Phys.*, vol. 44, no. 2, pp. 628–636, 2017.

[170] A. H. Aldosari *et al.*, "A two dimensional silicon detectors array for quality assurance in stereotactic radiotherapy : MagicPlate-512," *Med. Phys.*, vol. 91707, no. 41, p. 91707, 2014.

[171] G. Rikner, "Silcon diodes as detectors in relative dosimetry of photon, electron and proton radiation fields," *Thesis, Uppsala Univ.*, 1983.

[172] D. Marre and G. Marinello, "Comparison of p-type commercial electron diodes for in vivo dosimetry.," *Med. Phys.*, pp. 50–56, 2004.

[173] E. G. G. Rikner, "Effects of radiation damage on p-type silicon detectors," *Phys. Med. Biol.*, vol. 28, no. 11, pp. 1261–1267, 1987.

[174] G. Hall, "Radiation damage to silicon detectors," *Nucl. Instruments Methods Phys. Res. Sect. A Accel. Spectrometers, Detect. Assoc. Equip.*, vol. 368, no. 1, pp. 199–204, 1995.

[175] E. Grusell and G. Rikners, "Evaluation of temperature effects in p-type silicon detectors," *Phys. Med. Biol.*, vol. 31, no. 5, pp. 527–534, 1986.

[176] D. Wilkins, X. a Li, J. Cygler, and L. Gerig, "The effect of dose rate dependence of p-type silicon detectors on linac relative dosimetry.," *Med. Phys.*, vol. 24, no. 6,

pp. 879–881, 1997.

[177] E. Fretwurst *et al.*, "Bulk damage effects in standard and oxygen-enriched silicon detectors induced by 60 Co-gamma radiation," *Nucl. Instruments Methods Phys. Res. Sect. A Accel. Spectrometers, Detect. Assoc. Equip.*, vol. 514, no. 1, pp. 1–8, 2003.

[178] J. Stahl, E. Fretwurst, G. Lindström, and I. Pintilie, "Deep defect levels in standard and oxygen enriched silicon detectors before and after 60 Co-γ-irradiation," *Nucl. Instruments Methods Phys. Res. Sect. A Accel. Spectrometers, Detect. Assoc. Equip.*, vol. 512, no. 1, pp. 111–116, 2003.

[179] G. Lindström *et al.*, "Epitaxial silicon detectors for particle tracking—Radiation tolerance at extreme hadron fluences," *Nucl. Instruments Methods Phys. Res. Sect. A Accel. Spectrometers, Detect. Assoc. Equip.*, vol. 568, no. 1, pp. 66–71, 2006.

[180] T. C. Dos Santos, W. F. P. Neves-Junior, J. A. C. Gonalves, C. M. K. Haddad, and C. C. Bueno, "Evaluation of rad-hard epitaxial silicon diode in radiotherapy electron beam dosimetry," *Radiat. Meas.*, vol. 46, no. 12, pp. 1662–1665, 2011.

[181] W. F. P. Neves-junior and C. C. Bueno, "Performance Of Epi Diodes As Dosimeters For Photon," pp. 3–7, 2011.

[182] M. Bruzzi *et al.*, "Epitaxial silicon devices for dosimetry applications," *Appl. Phys. Lett.*, vol. 90, no. 17, p. 172109, 2007.

[183] M. Petasecca, F. Moscatelli, D. Passeri, and G. U. Pignatel, "Numerical simulation of radiation damage effects in p-type and n-type FZ silicon detectors," *IEEE Trans. Nucl. Sci.*, vol. 53, no. 5, pp. 2971–2976, 2006.

[184] C. Talamonti, M. Bruzzi, M. Bucciolini, L. Marrazzo, and D. Menichelli, "Preliminary dosimetric characterization of a silicon segmented detector for 2D dose verifications in radiotherapy," *Nucl. Instruments Methods Phys. Res. Sect. A*

Accel. Spectrometers, Detect. Assoc. Equip., vol. 583, no. 1, pp. 114–118, 2007.

[185] A. Brahme, "Correction for the angular dependence of a detector in electron and photon beams," vol. 24, no. October, pp. 301–304, 1985.

[186] H. Bouchard, Y. Kamio, H. Palmans, J. Seuntjens, and S. Duane, "Detector dose response in megavoltage small photon beams. I. Theoretical concepts," *Med. Phys. Med. Phys*, vol. 42, no. 10, pp. 6033–6047, 2015.

[187] P. Björk, T. Knöös, and P. Nilsson, "Comparative dosimetry of diode and diamond detectors in electron beams for intraoperative radiation therapy.," *Med. Phys.*, vol. 27, no. 11, pp. 2580–8, 2000.

[188] P. C. Lee, J. M. Sawicka, and G. P. Glasgow, "Patient dosimetry quality assurance program with a commercial diode system.," 1994.

[189] Q. L. Li, X. W. Deng, L. X. Chen, and S. M. Huang, "The angular dependence of a 2 - dimensional diode array and the feasibility of its application in verifying the composite dose distribution of intensity - modulated radiation therapy," *Chin. J. Cancer*, vol. 29, no. 6, pp. 617–620, 2010.

[190] H. Jin, V. P. Keeling, D. A. Johnson, and S. Ahmad, "Interplay effect of angular dependence and calibration field size of MapCHECK 2 on RapidArc quality assurance," *J. Appl. Clin. Med. Phys.*, vol. 15, no. 3, pp. 80–92, 2014.

[191] P. H. Charles *et al.*, "The effect of very small air gaps on small field dosimetry," *Phys. Med. Biol.*, vol. 57, no. 21, pp. 6947–6960, 2012.

[192] K. Utitsarn *et al.*, "Optimisation of output factor measurements using the magic plate 512 silicon dosimeter array in small megavoltage photon fields," *J. Phys. Conf. Ser.*, vol. 777, p. 12022, 2017.

[193] Texas Instrument, "64 Channel Analog Front End for Digital X-Ray Detector AFE0064," no. September, 2009.

[194] M. Träxler, J. Ackermann, M. Juda, and D. Hirsch, "Polymethyl methacrylate (PMMA)," *Kunststoffe Int.*, vol. 101, no. 10, pp. 42–44, 2011.

[195] S. Devic *et al.*, "Linearization of dose–response curve of the radiochromic film dosimetry system," *Med. Phys.*, vol. 39, no. 8, pp. 4850–4857, 2012.

[196] MICROTEX, "MicroTex ScanMarker i800." [Online]. Available: http://www.microtek.com/products.php?KindID=3&ID=38.

[197] M. Martisíková, B. Ackermann, and O. Jäkel, "Analysis of uncertainties in Gafchromic EBT film dosimetry of photon beams.," *Phys. Med. Biol.*, vol. 53, no. 24, pp. 7013–27, 2008.

[198] G. Massillon-JL, "Energy Dependence of the New Gafchromic EBT3 Film:Dose Response Curves for 50 KV, 6 and 15 MV X-Ray Beams," *Int. J. Med. Physics,Clinical Eng. Radiat. Oncol.*, vol. 1, no. 2, pp. 60–65, 2012.

[199] D. Cusumano, M. L. Fumagalli, M. Marchetti, L. Fariselli, and E. De Martin, "Dosimetric verification of stereotactic radiosurgery/stereotactic radiotherapy dose distributions using Gafchromic EBT3," *Med. Dosim.*, vol. 3, pp. 1–6, 2015.

[200] G. Rikner and E. Grusell, "Selective shielding of a p-Si detector for quality independence.," *Acta Radiol. Oncol.*, vol. 24, no. 1, pp. 65–69, 1984.

[201] I. J. Das and F. M. Kahn, "Backscatter dose perturbation at high atomic number interfaces in megavoltage photon beams," *Med. Phys.*, vol. 16, no. 3, pp. 367–375, 1989.

[202] B. L. Werner, I. J. Das, F. M. Khan, and A. S. Meigooni, "Dose perturbations at interfaces in photon beams," *Med. Phys.*, vol. 14, no. 4, pp. 585–595, 1987.

[203] H. Bouchard, Y. Kamio, H. Palmans, J. Seuntjens, and S. Duane, "Detector dose response in megavoltage small photon beams. II. Pencil beam perturbation effects," *Med. Phys. Med. Phys*, vol. 42, no. 10, pp. 6048–6061, 2015.

[204] I. Fuduli *et al.*, "Multichannel Data Acquisition System comparison for Quality Assurance in external beam radiation therapy," *Radiat. Meas.*, vol. 71, pp. 338–341, 2014.

[205] Frank Honniger, "Radiation Damage in Silicon - Defect analysis and Detector Properties," p. 196, 2007.

[206] J. A. C. Gonçalves, T. C. Dos Santos, W. F. P. Neves, C. M. K. Haddad, and C. C. Bueno, "Feasibility study of using epitaxial silicon diodes for clinical electron and photon beams dosimetry," *IEEE Nucl. Sci. Symp. Conf. Rec.*, pp. 228–232, 2012.

[207] A. H. Aldosari *et al.*, "Characterization of an innovative p-type epitaxial diode for dosimetry in modern external beam radiotherapy," *IEEE Trans. Nucl. Sci.*, vol. 60, no. 6, pp. 4705–4712, 2013.

[208] J. Shi, W. E. Simon, L. Ding, and D. Saini, "Important issues regarding diode performance in radiation therapy applications," *Proc. 22nd Anu. EMBS Int. Conf.*, pp. 1710–1713, 2000.

[209] A. B. Rosenfeld, "Electronic dosimetry in radiation therapy," *Radiat. Meas.*, vol. 41, pp. 134–153, 2006.

[210] I. J. Das *et al.*, "Accelerator beam data commissioning equipment and procedures: report of the TG-106 of the Therapy Physics Committee of the AAPM.," *Med. Phys.*, vol. 35, no. 9, pp. 4186–4215, 2008.

[211] B. J. Gerbi, "Measurement of dose in the buildup region using fixed-separation plane-parallel ionization chambers," *Med. Phys.*, vol. 17, no. 1, pp. 17–26, Jan. 1AD.

[212] D. E. Mellenberg, "Determination of build-up region over-response corrections for a Markus-type chamber.," *Med. Phys.*, vol. 17, no. 6, pp. 1041–1044, 1990.

[213] J. A. Rawlinson, D. Arlen, and D. Newcombe, "Design of parallel plate ion

chambers for buildup measurements in megavoltage photon beams," *Med. Phys.*, vol. 19, no. 3, pp. 641–648, 1992.

[214] D. E. Velkley, D. J. Manson, J. A. Purdy, and G. D. Oliver, "Build-up region of megavoltage photon radiation sources," *Med. Phys.*, vol. 2, no. 1, pp. 14–19, 1975.

[215] F. Q. Chen, R. Gupta, and P. Metcalfe, "Intensity modulated radiation therapy (IMRT) surface dose measurements using a PTW advanced Markus chamber," *Australas. Phys. Eng. Sci. Med.*, vol. 33, no. 1, pp. 23–34, 2010.

[216] D. Wilkins, X. A. Li, J. Cygler, and L. Gerig, "The effect of dose rate dependence of p-type silicon detectors on linac relative dosimetry," *Med. Phys.*, vol. 24, no. 6, p. 879, 1997.

[217] Varian Medical Systems, "C-Series CLINAC clinical User Guide. Delivery systems.," 1999.

[218] A. S. Saini and T. C. Zhu, "Dose rate and SDD dependence of commercially available diode detectors.," *Med. Phys.*, vol. 31, no. 4, pp. 914–924, 2004.

[219] A. J. D. Scott, S. Kumar, A. E. Nahum, and J. D. Fenwick, "Characterizing the influence of detector density on dosimeter response in non-equilibrium small photon fields," *Phys. Med. Biol.*, vol. 57, no. 14, pp. 4461–4476, 2012.

[220] N. Stansook *et al.*, "Technical Note:Angular dependence of a 2D monolithic silicon diode array for small field sodimetry," *Med. Phys.*, pp. 1–9, 2017.

[221] N. Stansook *et al.*, "The angular dependence of a two dimensional monolithic detector array for dosimetry in small radiation fields," *J. Phys. Conf. Ser.*, vol. 777, p. 12020, 2017.

[222] G. Cranmer-Sargison, S. Weston, N. P. Sidhu, and D. I. Thwaites, "Experimental small field 6 MV output ratio analysis for various diode detector and accelerator combinations," *Radiother. Oncol.*, vol. 100, no. 3, pp. 429–435, 2011.

Bibliography

[223] P. H. Charles *et al.*, "Monte Carlo-based diode design for correction-less small field dosimetry.," *Phys. Med. Biol.*, vol. 58, no. 13, pp. 4501–12, 2013.

[224] VARIAN, "the Truebeam System," 2013. [Online]. Available: https://www.varian.com/sites/default/files/resource_attachments/TrueBeamBrochure_RAD10119D_September2013.pdf.

[225] G. Rinaldin *et al.*, "Quality assurance of Rapid Arc treatments: Performances and pre-clinical verifications of a planar detector (MapCHECK2).," *Phys. Med.*, vol. 30, no. 2, pp. 184–90, 2014.

[226] S. Stathakis, "IMRT and VMAT Patient Specific QA Using 2D and '3D' Detector Arrays."

[227] J. Gimeo-Olmos, "Octavius 4D 1000 SRS , a new instrument for SBRT VMAT IMRT verification , commissioning and clinical implementation Purpose / Objective," p. 1000.

[228] One Technology Way, "ADIS1609 High Accuracy , Dual-Axis Digital Inclinometer and Accelerometer data-sheets," 2012.

[229] P. Suwannakoon, "Description of Millennium MLC Controller Diagnostics Commands," *Varian Med. Syst.*, 1999.

[230] Engineering, "Densities of wood species," *The engineering toolbox*. [Online]. Available: www.engineerungtoolbox.com/wood-density_40.html.

[231] E. G. H. John E. Jordan, Merita A. Bania, Kristine A. Blckham, Robert J. Feiwell, Steven W. Hetts, "Acr – Asnr Practice Parameter for the Performance of Computed Tomography (Ct) of the Brain," *Am. Coll. Radiol.*, vol. 1076, no. Revised 2008, pp. 1–9, 2014.

[232] T. R. Mackie, J. W. Scrimger, and J. J. Battista, "A convolution method of calculating dose for 15-MV x rays," *Med. Phys.*, vol. 12, no. 2, pp. 188–196, 1985.

Bibliography

[233] A. Ahnesjö, "Collapsed cone convolution of radiant energy for photon dose calculation in heterogeneous media," *Med. Phys.*, vol. 16, no. 4, p. 577, 1989.

[234] T. McNutt, "Dose Calculations Collapsed Cone Convolution Superposition and Delta Pixel Beam," *Pinnacle White Pap.*, pp. 1–10, 2002.

[235] P. medical Systems, "Photon beam physics and measured data requirements," in *Pinnacle3 Physics reference guide*, 2009, pp. 17–18.

[236] W. Takahashi *et al.*, "Evaluation of heterogeneity dose distributions for Stereotactic Radiotherapy (SRT): Comparison of commercially available Monte Carlo dose calculation with other algorithms," *Radiat. Oncol.*, vol. 7, no. 1, pp. 1–8, 2012.

[237] M. J. Butson *et al.*, "Verification of lung dose in an anthropomorphic phantom calculated by the collapsed cone convolution method," *Phys. Med. Biol.*, vol. 45, no. 11, 2000.

[238] R. Munjal, P. Negi, A. Babu, S. Sinha, A. Anand, and T. Kataria, "Dose prediction accuracy of collapsed cone convolution superposition algorithm in a multi-layer inhomogenous phantom," *J. Med. Phys.*, vol. 31, no. 2, p. 67, 2006.

[239] S. Kry, "Couch attenuation impacts dose," *medicalphysicsweb review*, p.1, 2012.

[240] D. Wagner and H. Vorwerk, "Treatment couch modeling in the treatment planning system eclipse," *J. Cancer Sci. Ther.*, vol. 3, no. 1, pp. 007–012, 2011.

[241] Varian Medical System, "Exact ® IGRT couch specifications."

[242] H. Li, A. K. Lee, J. L. Johnson, R. X. Zhu, and R. J. Kudchadker, "Characterization of dose impact on IMRT and VMAT from couch attenuation for two Varian couches.," *J. Appl. Clin. Med. Phys.*, vol. 12, no. 3, p. 3471, 2011.

[243] I. B. Mihaylov, P. Corry, Y. Yan, V. Ratanatharathorn, and E. G. Moros, "Modeling of carbon fiber couch attenuation properties with a commercial

treatment planning system.," *Med. Phys.*, vol. 35, no. 11, pp. 4982–4988, 2008.

[244] C. Wu *et al.*, "On using 3D γ-analysis for IMRT and VMAT pretreatment plan QA," *Med. Phys.*, vol. 39, no. 6, pp. 3051–3059, 2012.

[245] D. A Low, W. B. Harms, S. Mutic, and J. a Purdy, "A technique for the quantitative evaluation of dose distributions.," *Med. Phys.*, vol. 25, no. 5, pp. 656–661, 1998.

[246] D. A Low, "Gamma Dose Distribution Evaluation Tool," *J. Phys. Conf. Ser.*, vol. 250, p. 12071, 2010.

[247] N. D. D. U. D. P. Hplu, D. Rnvdo, S. Vxfk, F. Iru, and P. Txdolw, "Dosimetric comparison of tools for intensity modulated radiaation therapy with gamma analysis: a phantom study," *EPJ Web Conf.*, vol. 1, pp. 5–8, 2015.

[248] G. A. Ezzell *et al.*, "IMRT commissioning: Multiple institution planning and dosimetry comparisons, a report from AAPM Task Group 119," *Med. Phys.*, vol. 36, no. 11, pp. 5359–5373, 2009.

[249] S. McCormack, J. Diffey, and A. Morgan, "The effect of gantry angle on megavoltage photon beam attenuation by a carbon fiber couch insert.," *Med. Phys.*, vol. 32, no. 2, pp. 483–487, 2005.

[250] C. F. Njeh, T. W. Raines, and M. W. Saunders, "Determination of the photon beam attenuation by the BrainLAB imaging couch: angular and field size dependence," *J. Appl. Clin. Med. Phys.*, vol. 10, no. 3, pp. 16–27, 2009.

[251] B. Vanderstraeten *et al.*, "Accuracy of patient dose calculation for lung IMRT: A comparison of Monte Carlo, convolution/superposition, and pencil beam computations.," *Med. Phys.*, vol. 33, no. 9, pp. 3149–3158, 2006.

[252] B. E. Nelms *et al.*, "VMAT QA: Measurement-guided 4D dose reconstruction on a patient," *Med. Phys.*, vol. 39, no. 7, pp. 4228–4238, 2012.

[253] C. Stambaugh, D. Opp, S. Wasserman, G. Zhang, V. Feygelman, and S. Wassrman,

"Evaluation of semiempirical VMAT dose reconstruction on a patient dataset based on biplanar diode array measurements," *J. Appl. Clin. Med. Phys.*, vol. 15, no. 2, pp. 1–12, 2014.

[254] PTW, "OCTAVIUS 4D IMRT Dosimetry," 2015. [Online]. Available: http://www.ptw.de/verisoft_octavius_4d.html.

[255] R. C. Tailor, V. M. Tello, C. B. Schroy, M. Vossler, and W. F. Hanson, "A generic off-axis energy correction for linac photon beam dosimetry," *Med. Phys.*, vol. 25, no. 5, p. 662, 1998.

[256] D. Georg, G. Kragl, S. af Wetterstedt, P. McCavana, B. McClean, and T. Knöös, "Photon beam quality variations of a flattening filter free linear accelerator," *Med. Phys.*, vol. 37, no. 1, p. 49, 2010.

[257] CNMC, "Dosimetry PhantomS | Plastic Slab Phantoms Virtual Water ™ Phantom Materials," p. 1.

[258] BJR Supp 25, "Central axis depth dose data for use in radiotherapy," *Br. J. Radiol.*, vol. Supplement, 1996.

[259] F. M. Khan, *The physics of radiation therapy*, Third. Philadelphia: Lippincott Williams &Wilkins, 2003.

[260] C.-W. Cheng, S. Hyun Cho, M. Taylor, and I. J. Das, "Determination of zero-field size percent depth doses and tissue maximum ratios for stereotactic radiosurgery and IMRT dosimetry: Comparison between experimental measurements and Monte Carlo simulation," *Med. Phys.*, vol. 34, no. 8, pp. 3149–3157, 2007.

[261] L. Chen *et al.*, "Measurements and comparisons for data of small beams of linear accelerators.," *Ai Zheng*, vol. 28, no. 3, pp. 328–332, 2009.

[262] H. H. Huizenga and P. R. Storchi, "The use of computerd tomography numbers in dose calculations for radiation therapy," *Acta Radiol. Oncol.*, vol. 24, pp. 509–519,

1985.

[263] A. Ahnesjö and M. M. Aspradakis, "Dose calculations for external photon beams in radiotherapy," *Phys. Med. Biol.*, vol. 44, no. 11, p. R99, 1999.

[264] J. Seco and P. M. Evans, "Assessing the effect of electron density in photon dose calculations.," *Med. Phys.*, vol. 33, no. 2, pp. 540–552, 2006.

[265] Y. Watanabe and C. Constantinou, "Phantom Materials in Radiology," in *Encyclopedia of medical devices and instrumentation Vol. 5*, no. April 2006, 2006, pp. 252–269.

[266] M. J. Day and E. G. Aird, "The equivalent-field method for dose determinations in rectangular fields.," *Br. J. Radiol. Suppl.*, vol. 17, p. 105, 1983.

[267] G. S. J. Tudor and S. J. Thomas, "Equivalent diameters of elliptical fields," *Br. J. Radiol.*, vol. 77, no. 923, pp. 941–943, 2004.

[268] M. J. Tahmasebi Birgani, N. Chegeni, M. Zabihzadeh, and N. Hamzian, "An analytical method to calculate equivalent fields to irregular symmetric and asymmetric photon fields," *Med. Dosim.*, vol. 39, no. 1, pp. 54–59, 2014.

[269] S. A. Shafiei, H. Hasanzadeh, and S. A. Shafiei, "A simple calculation method for determination of equivalent square field," *J. Med. Physics/Association Med. Phys. India*, vol. 37, no. 2, p. 107, 2012.

Appendix A

Autodesk drawing

The detector holders for CMRP cylindrical phantom were designed for particular materials. The 3D design Autodesk^{TM} AUTOCAD 2016 (California, USA) was used to create the drawings.

A.1. MP512 holder for solid water phantom

The PMMA frame was used in conjunction with the solid water phantom in the work described in **Chapter 4**.
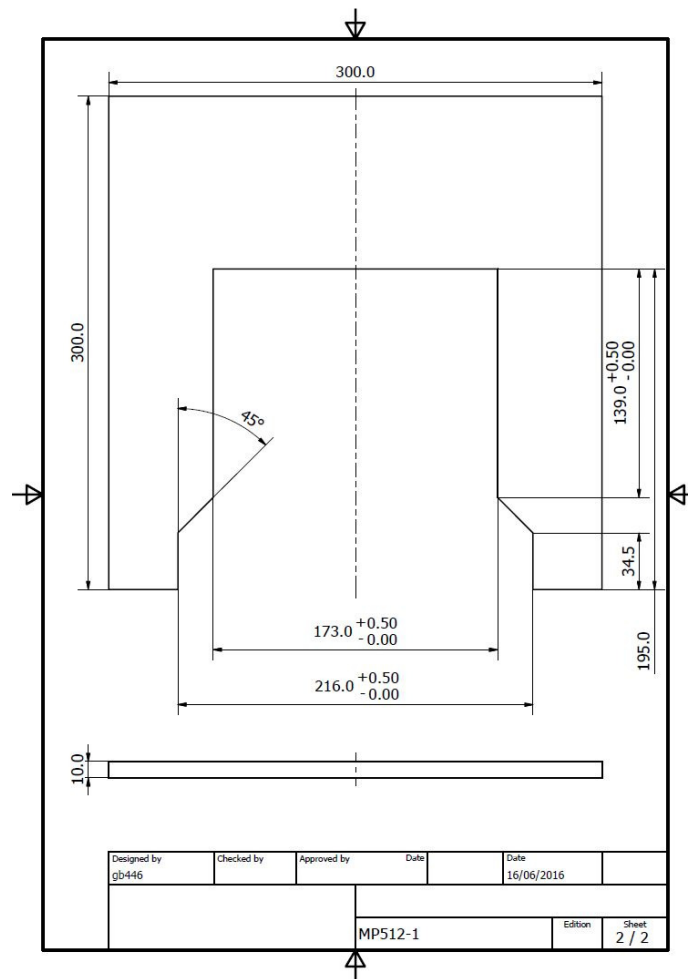
A.2. Inhomogeneous holder for CMRP phantom

A.2.1. Upper part

The inhomogeneous holder was designed to hold the MP512 inside the CMRP cylindrical phantom. The redwood material represents lung tissue; it was used in the patient specific verification described in **Chapter 5**.

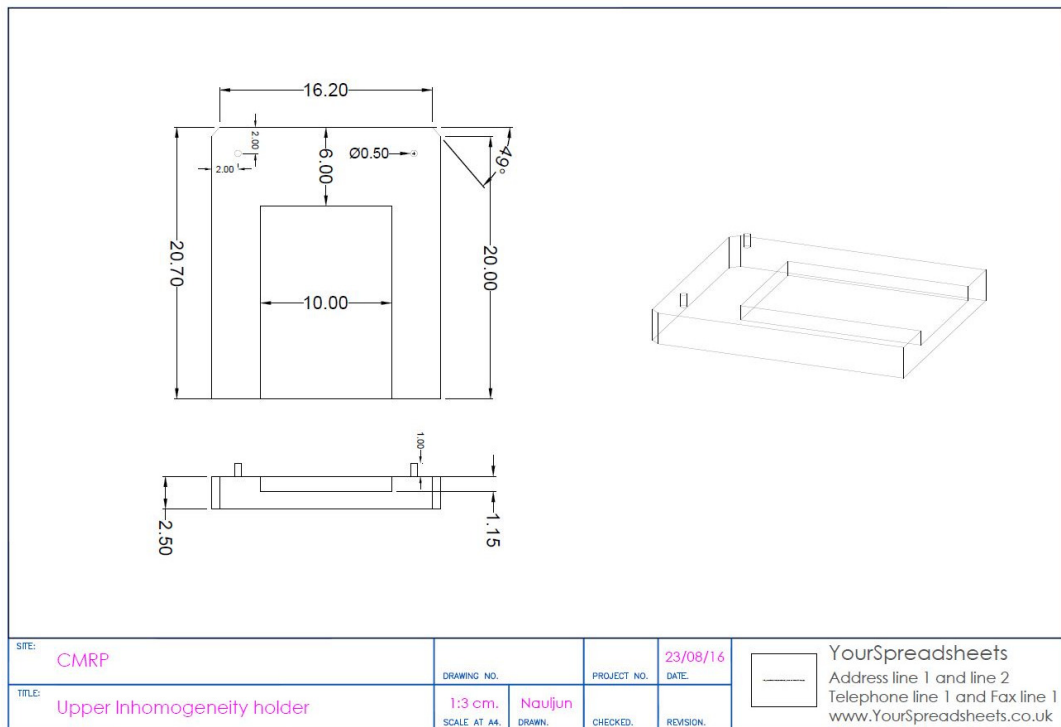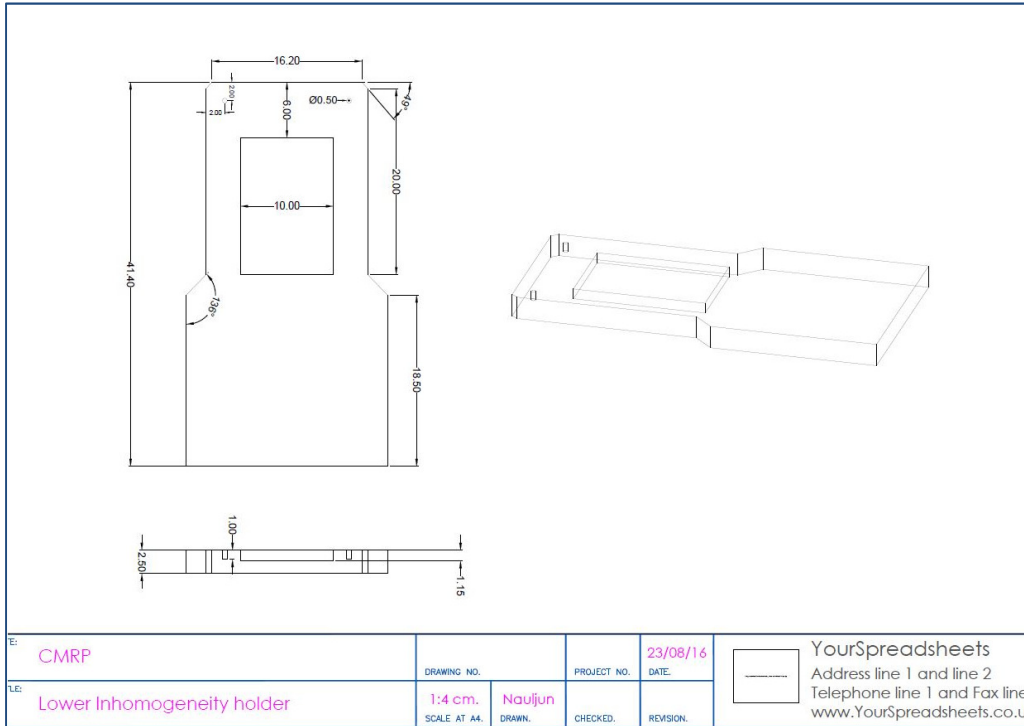## A.2.1. Lower part

Appendix B

Matlab Scripts

Matlab scripts were written using Matlab 2016 (The MathsWorks Inc.) to manage the MP512 data involved in **Chapter 3** and **Chapter 5**.

B.1. Mapping function script

This script was used to map the MP512 data into matrix arrays.

function [Map] = mappingFunction(Input)

%% read 1x512 input data from Input512.xlsx file (file name can be changed)

% Input contains a 1x512 matrix of MP512

%% read 24x24 array from map.xlsx file (file name can be changed)

Map = xlsread('map.xlsx');

%% mapping

for i = 1:1:24

   for j = 1:1:24

     if Map(i,j) == 0

       Map(i,j) = 0;

    else

      %% transform 1x512 to 24x24

      Map(i,j) = Input(1,Map(i,j));

    end

```
        end

end

%%  replace NaN

for i = 1:1:24

  for j = 1:1:24

    if isnan(Map(i,j))


       Map(i,j) = 0;

    end

  end

end

end
```

B.1. Angular correction script

The scripts were used to correct the angular dependence of MP512, as described in Chapter 3 and Chapter 5.

B.1.1. Angular sampling script

function [samplingIndex, samplingData, convertedIndex] = Sampling(index, data, samplingSize)


```
  if size(index,1) ~= size(data,1)

    error('size of index and data is not compatible');

  end

  if size(index,2) > 1

    error('index has more than 1 column');
```

```matlab
end

if size(data,2) ~= 512

    error('data must be 512 columns')

end


%re-adjust index: for negative value do this (180 - x) + 180

fprintf('convert negative index: (180 - index) + 180\n')

fprintf('negative index: %d\n', sum(index<0));


%converted Inclinometer index corresponding to LINAC index

convertedIndex = index;

for i = 1:size(convertedIndex,1)

    if convertedIndex(i,1) < 0

        convertedIndex(i,1) = (180 + convertedIndex(i,1)) + 180;

    end

end

%find number output row

outputRow = 360 / samplingSize;

lower = 0;

upper = samplingSize;

clear samplingIndex;

clear samplingData;

for i = 1:outputRow

    samplingIndex(i,1) = lower;

    samplingIndex(i,2) = upper;
```

```
        samplingData( i,: )  =  sum( data( convertedIndex  >=  lower  &  convertedIndex  <
upper,:));


    lower = upper;

    upper = upper + samplingSize;

  end

end
```

B.1.2. Application of angular correction factor applying

dataFileName = 'InhomoVMAT/Inhomo_VMAT3_Decoded.txt'; *%folder/filename*

indexFileName = 'InhomoVMAT/Inhomo_VMAT3_angles.aux'*;*

load('sumCF_6X_10de.mat');

% load('CF_6X_ctrPoint.mat');

load('ERMap_m.mat')

%% import data

data = importDecodedData512(dataFileName);

index = importIndexAngle(indexFileName);

%% adjust data

data(1, :) = []; *%cut first raw due to unstable reading of inclinometer where gantry start*
movement, have to check

data(:, 171)= 0*; %replace zero to channel that error reading this number can be changed*
depend on raw data show

data = (data.*100)./65535; *% where 65535 = 2^16 -1 (16 bit) and data is a percentage response of data bit reading*

% index(1, :) = []; %cut first raw due to unstable reading of inclinometer where gantry strat movement

%% find baseline

BS = 10; *% first part: before beam start this number can be changed*

BP = 35000*; %BP = second part after beam stop this number can be changed*

baseline = cutBaseline(data, BS, BP);

data = data - baseline; *%cut baseline each raw*

%% sampling angle and cut baseline

samplingSize = 10; *% this value can be change*

[samplingIndex, samplingData, convertedIndex] = Sampling(index, data, samplingSize);

%% Begin matrix angular correction

[correctedData2, mapData2] = ApplyCorrectionFactor(samplingData, sumCF_6X_10de,2);

mapData2(isnan(mapData2)) = 0;

mapData2 = mapData2./ERMap_man; *%ER = equivalization factor (20x20 cm2, d10)*

mapData2 = mapData2 .* 0.00038; *% Converted MP512 response to dose(cGy) using FC(10x10cm2 ,d1.5cm)*

[mapData2]= MP_fixNan(mapData2);

B.2. Gamma analysis

The 2D gamma index was used to compare the dose distribution of MP512 reconstruction, EBT3 measurements and TPS calculations. This gamma index was calculated based on Low's equation.

%Run script

MP = In_VMAT2_1de_predict; %add MP512 name

MP2 = MP2:23,2:23); %wing pixel was cut

%newMP = fillDead(MP2,k);

film = VMAT1_D; %add Film name

flim2 = medfilt2(film);

flim2(1,1) = film(1,1);

flim2(1,137) = film(1,137);

flim2(137,1) = film(137,1);

flim2(137,137) = film(137,137);

[Vq_MP, Vq_wflim] = AdjustScale(film, MP2, 2,0.35278,11,1);

[GammaMap numpass avg numWithinField] = GammaCompare(Vq_wflim./mean(Vq_wflim(:)), Vq_MP./mean(Vq_MP(:)),41, 41,0.5, 0.03, 0.3, 0.1,10);

fprintf('-------result-------\n');

fprintf('Gamma pass-rate:%4g\n',numpass*100);

fprintf('Average gamma :%4g\n',avg);

subplot(1,3,1) , imagesc(film) , subplot(1,3,2) ,imagesc(MP) , subplot(1,3,3) , imagesc(GammaMap);

subplot(1,3,1) , contour(film) , subplot(1,3,2) ,contour(MP) , subplot(1,3,3) , contour(GammaMap);

%imagesc(GammaMap);

%Adjust scale

function [Vq_MP, Vq_film] = AdjustScale(film, MP, Mpx,Fpx,exSize,exPx)

%{

%INPUT parameters and detial

film = IMRT1_fD;   % original film data

MP = comImRT1_PDnet;   % original MP5121 data

Fpx=0.35278;   % pixel size spacing of film data

Mpx=2;   % pixel size spacing of MP512 data

exSize = 20;   % output image size (i.e 20X20 mm)

exPx = 1;   % pixel size spacing of output image(i.e0.5mm)

%OUPUT

Vq_MP   % converted MP images

Vq_film   % converted film images

For example:

[Vq_MP, Vq_film] = AdjustScale(film2, newMP, 2,0.35278,20,1);

%film2 is film with median filter (3X3)

%}

% read image size

fsize = size(film,1);

msize = size(MP,1);

% Create Mesh grid

[Mxgrid,Mygrid] = meshgrid(-1*Mpx*msize/2+(Mpx/2):Mpx:+Mpx*msize/2-(Mpx/2));

[Fxgrid,Fygrid] = meshgrid(-1*Fpx*fsize/2+(Fpx/2):Fpx:+Fpx*fsize/2-(Fpx/2));

[Nxgrid,Nygrid] = meshgrid(-1*exSize+(exPx/2):exPx:+exPx*exSize-(exPx/2));

% 2D interp

Vq_film = interp2(Fxgrid,Fygrid,film, Nxgrid, Nygrid);

Vq_MP = interp2(Mxgrid, Mygrid, MP, Nxgrid, Nygrid);

% GammaCompare

% GammaMapsub will carry the calculated gamma values for the truncated

% images. GammaMap2 will be the Gamma values for the full image.

GammaMapsub = NaN;

GammaMap = zeros(size(Image1));

% Find the threshold limits for truncation

[validmask_y validmask_x] = find(Mask);

min_x = min(validmask_x)-rad;

max_x = max(validmask_x)+rad;

min_y = min(validmask_y)-rad;

max_y = max(validmask_y)+rad;

if min_x < 1

```matlab
        min_x = 1;

    end

    if min_y < 1

        min_y = 1;

    end

    if max_x > size(Image1,2)

        max_x = size(Image1,2);

    end

    if max_y > size(Image1,1)

        max_y = size(Image1,1);

    end

    % Truncate the images to avoid needless calculations

    Im1 = Image1(min_y:max_y,min_x:max_x);

    Im2 = Image2(min_y:max_y,min_x:max_x);

    % Shift the image by varying amounts. Determine the minimum gamma value

    % for all shifts

    for i=-rad:rad

        for j=-rad:rad

            % circshift function wraps elements from top to bottom as necessary

            % The entire image is shifted at once

            Im2_shift = circshift(Im2,[i j]);

            dist = sqrt((res_y*i)^2 + (res_x*j)^2);

            DoseDiff = Im2_shift - Im1;

            % Compute the gamma map for this particular shift value

            Gamma_temp = sqrt((dist./DTA_tol).^2 + (DoseDiff./Dose_tol).^2);
```

% Accumulate the map of the minimum values of gamma at each point

GammaMapsub = min(GammaMapsub,Gamma_temp);

    end

end

% Put the truncated gamma map back into its proper location within the full

% gamma map

GammaMap(min_y:max_y,min_x:max_x) = GammaMapsub;

% Remove any edge effects from the circular shifting by multiplying by the mask values.

This will negate any calculated gamma values around the edges of the distribution where

this effect would arise

GammaMap = GammaMap .* Mask;

% Ensure that NaN values outside the mask do not affect the calculation

GammaMap(~Mask) = 0.0;

% Compute statistics

numWithinField = nnz(Mask);

numpass = nnz(GammaMap<1 & Mask)./numWithinField;

avg = sum(GammaMap(:))./numWithinField;